ADSORPTION AND PHOTOCATALYTIC STUDIES ON ACTIVATED CARBON AND ITS COMPOSITE: AN EXPERIMENTAL AND THEORETICAL INSIGHT TO UNDERSTAND THE MECHANISM

by

SHISAK SHARMA

Ph.D. REGN. NO. Ph.D./CHE/00351

Submitted to

NAGALAND UNIVERSITY

In partial fulfillment of the requirements for the Degree

of

DOCTOR OF PHILOSOPHY IN CHEMISTRY

DEPARTMENT OF CHEMISTRY

NAGALAND UNIVERSITY

LUMAMI-798627

NAGALAND, INDIA

2026

ADSORPTION AND PHOTOCATALYTIC STUDIES ON ACTIVATED CARBON AND ITS COMPOSITE: AN EXPERIMENTAL AND THEORETICAL INSIGHT TO UNDERSTAND THE MECHANISM

by

SHISAK SHARMA

Ph.D. REGN. NO. Ph.D./CHE/00351

Submitted to

NAGALAND UNIVERSITY

In partial fulfillment of the requirements for the Degree

of

DOCTOR OF PHILOSOPHY IN CHEMISTRY

DEPARTMENT OF CHEMISTRY

NAGALAND UNIVERSITY

LUMAMI-798627

NAGALAND, INDIA

2026

ADSORPTION AND PHOTOCATALYTIC STUDIES ON ACTIVATED CARBON AND ITS COMPOSITE: AN EXPERIMENTAL AND THEORETICAL INSIGHT TO UNDERSTAND THE MECHANISM

by

SHISAK SHARMA

and

PROF. DIPAK SINHA

(Supervisor)

Submitted

In partial fulfillment of the requirements for the Degree

of

DOCTOR OF PHILOSOPHY IN CHEMISTRY

DEPARTMENT OF CHEMISTRY

NAGALAND UNIVERSITY

LUMAMI-798627

NAGALAND, INDIA

2026

Dedicated

To

My Family

नागालैण्डविश्वविद्यालय
NAGALAND UNIVERSITY
(संसद द्वारा पारित अधिनियम 1989, क्रमांक 35 के अंतर्गत स्थापित केंद्रीय विश्वविद्यालय)
(A Central University established by an Act of Parliament No.35 of 1989)
मुख्यालय : लुमामी, जिला : जुन्हेबोटो (नागालैण्ड), पिनकोड – 798627
Hqrs: Lumami, Dist. Zunheboto (Nagaland), Pin Code – 798627
वेबसाइट / Website : www.nagalanduniversity.ac.in

Department of Chemistry

DECLARATION

Nagaland University

2026

I, **Mr. Shisak Sharma**, bearing Registration No. **Ph.D./CHE/00351** with effect from **31/08/2019**, hereby declare that the contents of the thesis entitled **"Adsorption and Photocatalytic Studies on Activated Carbon and its Composite: An Experimental and Theoretical Insight to Understand the Mechanism"** is the result of my research on the subject. I also declare that the contents of this thesis did not form basis of the award of any previous degree to me or to the best of my knowledge to anybody else, and that the thesis has not been submitted by me for any research degree in any other university/institute.

This Ph. D. thesis is submitted in compliance with the UGC Regulation 2016 dated May 05, 2016 (Minimum Standard and Procedure for Award of M. Phil. /Ph. D. Degree) to the Nagaland University for the degree of Doctor of Philosophy in Chemistry.

(**Prof. Dipak Sinha**)	(**Head**)	(**Shisak Sharma**)
Supervisor	Department of Chemistry Nagaland University	Scholar

नागालैण्डविश्वविद्यालय
NAGALAND UNIVERSITY
(संसद द्वारा पारित अधिनियम 1989, क्रमांक 35 के अंतर्गत स्थापित केंद्रीय विश्वविद्यालय)
(A Central University established by an Act of Parliament No.35 of 1989)
मुख्यालय : लुमामी, जिला : जुन्हेबोटो (नागालैण्ड), पिनकोड – 798627
Hqrs: Lumami, Dist. Zunheboto (Nagaland), Pin Code – 798627
वेबसाइट / Website : www.nagalanduniversity.ac.in

Prof. Dipak Sinha
(FRSC,FNESA, BOYSCAST FELLOW)
Department of Chemistry

CERTIFICATE

This is to certify that **Mr. Shisak Sharma**, a registered Research Scholar for Ph.D. degree in Chemistry under Nagaland University, bearing Registration No. **Ph.D./CHE/00351; dated: 31/08/2019**, has carried out his research work under my guidance and supervision. His thesis entitled **"Adsorption and Photocatalytic Studies on Activated Carbon and its Composite: An Experimental and Theoretical Insight to Understand the Mechanism"** embodies the original research work and has fulfilled all the requirements according to the rules/regulations of Nagaland University.

Further, to the best of my knowledge, the present research work has not been submitted to any University/Institution for the award of any degree or diploma.

(Prof. Dipak Sinha)
Supervisor

ADSORPTION AND PHOTOCATALYTIC STUDIES ON ACTIVATED CARBON AND ITS COMPOSITE: AN EXPERIMENTAL AND THEORETICAL INSIGHT TO UNDERSTAND THE MECHANISM

by

SHISAK SHARMA
DEPARTMENT OF CHEMISTRY
NAGALAND UNIVERSITY

ABSTRACT

of

The Thesis submitted in Fulfillment of the Requirements for the Award of Degree of Doctor of Philosophy in Chemistry

To

NAGALAND UNIVERSITY
LUMAMI-798627, NAGALAND, INDIA

2026

ABSTRACT

Nowadays, the quality of water resources is a critical aspect of sustainable development. The rapid expansion of industrialization, along with the growing modernity and urbanization of society, is a significant human-caused factor contributing to water pollution and the ensuing decline of aquatic ecosystems. Among these contaminants, phenolic compounds, including 2-chlorophenol (2CP), catechol (CT), resorcinol (RS), 4-nitrophenol (4-NP), and bisphenol A (BPA), are classified as priority pollutants because of their high toxicity, chemical stability, resistance to biodegradation, and endocrine-disrupting properties. These compounds are associated with carcinogenicity, mutagenicity, hormonal imbalance, developmental disorders, and other chronic health effects, posing severe threats to aquatic organisms and human health, even at trace concentrations. Their ubiquitous detection in surface and groundwater highlights the urgent need for effective, sustainable, and environmentally benign remediation strategies.

Conventional wastewater treatment procedures often suffer from limitations such secondary pollution, inadequate removal, high operating costs, and the production of hazardous byproducts. Adsorption and photocatalytic degradation have become viable substitutes in this regard. Adsorption is known for its ease of use, great effectiveness, and viability from an economic standpoint when it comes to eliminating contaminants from aqueous systems. However, it predominantly transfers contaminants from one phase to another without achieving complete mineralization. On the other hand, photocatalysis enables the oxidative degradation of organic pollutants into less harmful or mineralized products but may be limited by issues such as rapid electron–hole recombination and restricted visible-light activity of pristine semiconductors. Therefore, integrating adsorption with photocatalysis provides a synergistic method, wherein pollutants are first concentrated onto the adsorbent surface and subsequently degraded through catalytic processes.

In view of this, the present thesis focuses on the development of biomass-derived activated carbon (AC) and its semiconductor-based nanocomposites for the effective adsorption and degradation of phenolic contaminants from aqueous solution. AC was synthesized from locally available *Croton caudatus* biomass through KOH chemical

activation to obtain a porous, high-surface-area adsorbent enriched with surface functional groups. Furthermore, AC was employed as a supporting matrix for the fabrication of heterojunction photocatalysts, including ZrO_2–ZnO and Co-doped ZnO systems, to enhance charge separation, improve light absorption, and suppress recombination of electron-hole pairs. Density functional theory (DFT) simulations were also performed to support experimental studies by offering molecular-level understanding of adsorption energetics, interaction processes, and catalytic pathways. The integration of experimental and theoretical approaches enabled a comprehensive understanding of both adsorption and photocatalytic processes.

To thoroughly address the above objectives, the thesis entitled "**Adsorption and Photocatalytic Studies on Activated Carbon and its Composite: An Experimental and Theoretical Insight to Understand the Mechanism"** is structured into the following chapters:

Chapter 1 provides a detailed overview of water pollution with particular attention on the environmental and health impacts of phenolic contaminants. The chapter discusses conventional treatment technologies and highlights the limitations that necessitate the development of advanced remediation strategies. The chapter also discusses the fundamental concepts of heterogeneous photocatalysis and adsorption, the physicochemical and structural properties of AC, and the rationale for integrating AC with ZnO-based semiconductor materials. The limitations of pristine ZnO, including rapid electron–hole recombination, photocorrosion, agglomeration and restricted visible-light activity, are critically addressed, thereby establishing the need for heterojunction formation with ZrO_2, transition metal modification and AC supporting system. The chapter also introduces Density Functional Theory (DFT) as a complementary tool to elucidate adsorption mechanisms and catalytic processes at the molecular level, and outlines the aims and objectives of the present study.

Chapter 2 outlines the materials and experimental methodologies employed for the synthesis, characterisation, and assessment of AC and its nanocomposites. The preparation of biomass-derived AC, adsorption experiments and modeling approaches, hydrothermal synthesis of photocatalysts, photocatalytic degradation studies, and analytical techniques for mechanistic investigation are all outlined. The chapter further

introduces a computational framework utilizing DFT simulations to augment experimental results.

Chapter 3 presents the synthesis and application of activated carbon derived from *Croton caudatus* biomass (CCAC) for the adsorption of 2CP from aqueous solution. The CCAC was prepared via KOH chemical activation and systematically characterized to evaluate its structural, morphological, and surface chemical properties. Batch adsorption studies were conducted to examine the influence of operational parameters, and the adsorption behavior was analyzed using equilibrium isotherm, kinetic, and thermodynamic models. The adsorption process was found to follow Langmuir isotherm and pseudo-second-order (PSO) kinetics, indicating monolayer adsorption governed by chemisorption mechanisms. Thermodynamic evaluation confirmed the spontaneous and exothermic nature of the process. Regeneration and reuse experiments demonstrated the recyclability and practical applicability of the developed adsorbent even after five cycles. Furthermore, DFT simulations were performed to elucidate the interaction mechanism between 2CP and oxygen-containing functional (OCF) groups present on the CCAC surface. The theoretical findings revealed that carboxyl functional groups significantly enhance adsorption strength, and the presence of multiple functional groups further improves adsorption performance. A comparative and cost analysis established the economic feasibility of the synthesized biomass-derived AC for wastewater treatment applications.

Chapter 4 extends the adsorption investigation to additional phenolic derivatives, namely CT and RS, in order to evaluate the versatility and adsorption performance of CCAC adsorbent toward structurally distinct pollutants. By examining dihydroxybenzene isomers with different hydroxyl group orientations, this study provides deeper insight into structure–adsorption relationships and the influence of functional group positioning on adsorption behavior. Systematic batch adsorption studies were conducted to evaluate the influence of pH, contact time, temperature, adsorbent dosage, and co-existing inorganic ions. Equilibrium data were best described by the Langmuir isotherm model, indicating monolayer adsorption, while kinetic studies followed a PSO model, suggesting chemisorption-controlled interactions.

Thermodynamic analysis confirmed the spontaneous and endothermic nature of the adsorption process. Regeneration studies demonstrated the reusability and stability of the adsorbent over multiple cycles. Furthermore, DFT simulations provided molecular-level insights into adsorption mechanisms, highlighting the dominant role of hydrogen bonding and π–π interactions. Among various oxygen-containing functional groups, carboxyl-functionalized AC exhibited the strongest interaction with both CT and RS.

Chapter 5 advances the remediation strategy from adsorption to photocatalytic degradation through the development of a novel CCAC/ZrO_2–ZnO nanocomposite synthesized via a hydrothermal method. In this approach, biomass-derived AC was integrated with ZrO_2–ZnO heterojunction photocatalysts to enhance charge separation efficiency, suppress electron–hole recombination, and improve light absorption characteristics. The photocatalytic performance of the synthesized nanocomposite was evaluated for the degradation of 4-NP under UV irradiation. Systematic optimization of operational parameters was performed, and the degradation kinetics followed pseudo-first-order (PFO) behavior consistent with the Langmuir–Hinshelwood model. Comparative catalytic efficiency tests confirmed the superior performance of the composite relative to pristine ZnO and ZrO_2. Reusability and photostability studies demonstrated sustained catalytic activity over several cycles, indicating structural stability and practical applicability. Total organic carbon analysis and LC–MS investigations confirmed substantial mineralization and elucidated the degradation pathway of 4-NP through reactive oxygen species mechanisms. The photocatalyst was further validated under real wastewater conditions, demonstrating effective degradation in complex matrices. DFT simulations provided theoretical insight into electronic structure modifications and enhanced reactivity of the composite system. Additionally, molecular docking studies against bacterial targets suggested potential antibacterial interactions, offering broader implications for environmental and biomedical applications.

Chapter 6 extends the photocatalytic investigation toward a visible-light-responsive system to enhance sustainability and practical applicability, as visible light constitutes the major fraction of the solar spectrum, whereas UV radiation represents only a minor

portion. To overcome the wide band gap limitation of pristine ZnO (3.3 eV), cobalt doping was employed to narrow the band gap to 2.1 eV, enabling visible-light activation. A porous carbon/Co–ZnO heterojunction was synthesized via hydrothermal anchoring of Co-doped ZnO nanoparticles onto CCAC supporting materail. Structural and optical characterization confirmed successful heterojunction formation, improved charge separation, and enhanced light absorption. Under visible-light irradiation, the composite achieved 99.67 % BPA degradation within 60 min, following PFO kinetics. Radical scavenging studies identified hydroxyl radicals as the dominant reactive species. Mineralization and LC–MS analyses confirmed progressive breakdown of BPA into less harmful intermediates, while toxicity predictions indicated reduced ecological risk compared to the parent compound. Density Functional Theory (DFT) calculations further elucidated reactive sites and supported the proposed degradation mechanism. Overall, this study demonstrates a sustainable, biomass-derived, visible-light-active photocatalyst with strong potential for solar-driven wastewater treatment applications.

Chapter 7 consolidates the overall contributions of this thesis, highlighting the successful transformation of waste *Croton caudatus* biomass into value-added carbonaceous materials for environmental remediation. The work demonstrates a systematic progression from adsorption-based pollutant removal to advanced heterojunction photocatalytic mineralization, supported by molecular-level theoretical validation. Overall, the thesis establishes a sustainable framework that converts low-cost biomass waste into multifunctional, reusable materials capable of both pollutant adsorption and photocatalytic degradation, offering a value-added environmental solution for advanced wastewater treatment.

The future scope of this work is also outlined in this chapter. Future research will focus on exploring alternative biomass precursors to optimize pore structure and surface functionality, as well as developing multi-doped and ternary semiconductor systems to enhance visible-light activity and charge separation efficiency. Further studies will address the simultaneous removal of mixed emerging contaminants, including pharmaceuticals, microplastics, and per and polyfluoroalkyl substances (PFAS), under realistic wastewater conditions. Advanced electrochemical and spectroscopic

techniques will be employed to better understand charge transfer dynamics and catalytic mechanisms, thereby supporting scale-up and practical implementation.

नागालैण्डविश्वविद्यालय
NAGALAND UNIVERSITY
(संसद द्वारा पारित अधिनियम 1989, क्रमांक 35 के अंतर्गत स्थापित केंद्रीय विश्वविद्यालय)
(A Central University established by an Act of Parliament No.35 of 1989)
मुख्यालय : लुमामी, जिला : जुन्हेबोटो (नागालैण्ड), पिनकोड – 798627
Hqrs: Lumami, Dist. Zunheboto (Nagaland), Pin Code – 798627
वेबसाइट / Website : www.nagalanduniversity.ac.in

Department of Chemistry

COURSE WORK COMPLETION CERTIFICATE

This is to Certify that **Mr. Shisak Sharma**, a registered Research Scholar for Ph.D. degree in Chemistry under Nagaland University, bearing Ph.D. Registration No. **Ph.D./CHE/00351**, **dated: 31/08/2019**, has satisfactorily completed all the courses offered in the Pre-Ph.D. Course Work Programme in the Department of Chemistry, Nagaland University, Hqrs. Lumami.

The Course Includes:

CHEM-601: Research Methodology

CHEM-602: Advance in Chemistry

CHEM-603: Literature Review, Report Writing and Presentation

Head
Department of Chemistry
Nagaland University

Sl. No. : 19- 65765

NAGALAND UNIVERSITY

STATEMENT OF MARKS

Ph. D COURSE WORK EXAMINATION, 2020

DEPARTMENT OF CHEMISTRY

The following are the marks secured by Shisak Sharma
Roll No. 19PhD04 *of Ph.D Course Work Examination held in* 2020

Subject(s)/Paper(s)	Max. Marks	Minimum Qualifying Marks	Marks Secured
Paper No. Chem-601 Research Methodology	100	35	71
Paper No. Chem-602 Advance in Chemistry	100	35	73
Paper No. Chem-603 Literature Review, Report Writing and Presentation	100	35	78
Total Aggregate Marks			222
Average Pass Mark – 55 %			

Result	Division	Percentage
Passed	**I Division**	74 %

Marks compared by

COE/Dy. Reg. (AR (Exams)
Assistant Registrar (Exams)
Nagaland University
Hqrs. Lumami

NAGALAND UNIVERSITY

HEAD QUARTERS : LUMAMI

Ph. D COURSE WORK EXAMINATION

This is to certify that Mr/Ms Shisak Sharma

of Nagaland University bearing Roll No. 19.Ph.D.04 *is qualified in the Ph.D Course Work Examination in the Department of* Chemistry *Nagaland University held in the Year* 2020

30/10/20
Head of Department

Dean
School of Science

ACKNOWLEDGEMENT

"Great things are never done by one person; they are done by a team of people."

– Steve Jobs

I take this opportunity to express my sincere appreciation and heartfelt gratitude to all those who have supported and accompanied me throughout my Ph.D. journey.

Firstly, I would like to express my sincere gratitude to my Supervisor, **Prof. Dipak Sinha**, for his invaluable guidance, continuous support, and encouragement throughout my Ph.D. research. His mentorship and constructive suggestions have been instrumental in the successful completion of this thesis.

I gratefully acknowledge the **Department of Chemistry, Nagaland University**, for providing the necessary facilities and academic environment to carry out this research. I also thank the **UGC Non-NET Fellowship** for financial assistance during my research tenure.

I extend my appreciation to **Prof. Ambrish Singh (Head, Department of Chemistry)** and all faculty members of the Department of Chemistry for their guidance and encouragement.

I sincerely thank **Dr. Mayur Mausoom Phukan (Department of Forestry)** and **Dr. Shanta Sinha (Department of Physics)** for their support in sample analysis.

My appreciation also goes to all the teaching faculty members and administrative staff of **Nagaland University** for their cooperation, guidance, and encouragement throughout my research period.

I am truly grateful to **Mr. S. Bendangtemsu, Ms. Sunepjungla, Ms. Temsuienla Amer, Mr. Puloto, Mr. Johnny Yanthan, Mr. Phyobemo Patton, Ms. Lovi, Ms. Kylie, and Mr. Renbeni** for their immense support and encouragement throughout my research journey.

I extend my heartfelt thanks to my respected seniors — **Dr. Chubaakum Pongener, Dr. Parimal Chandra Bhomick, Dr. Aola Supong, Dr. Mridushmita Baruah, Dr.**

Soremo L. Ezung, and Dr. Supongtoshi Jamir — for their guidance, advice, and continuous encouragement.

Special thanks are due to my lab mates — **Mr. Suraj Kumar, Mr. Raplang Steven Umdor, Ms. Imotila T. Longchar, and Ms. Priyakshi Bora** — for their cooperation, encouragement, and the pleasant working environment they helped create.

I also sincerely thank my fellow research scholars from other laboratories and departments, and my hostel mates for their support, encouragement, and cherished friendship.

Finally, I owe my deepest gratitude to my beloved family for their endless patience, unconditional love, understanding, and unwavering support, without which this achievement would not have been possible.

Above all, I offer my profound gratitude to the **Almighty God** and His servants for their blessings, guidance, strength, and prayers throughout my research journey.

(Shisak Sharma)

CONTENTS

APPENDIXES

Appendix A *Plagiarism Similarity Report*

Appendix B *Curriculum Vitae*

LIST OF FIGURES

LIST OF SCHEMES

LIST OF TABLES

LIST OF ABBREVIATIONS

Abbreviations	Meaning
AC	Acitvated carbon
AOP	Advanced oxidation process
BOD	Biological oxygen demand;
BPA	Bisphenol A
CAB	Croton caudatus biomass
CB	Conduction band
CCAC	*Croton caudatus* activated carbon
CHO(AC)	Carbonyl functionalized activated carbon;
COOH(AC)	Carboxyl functionalized activated carbon,
CPs	Chlorophenols
CT	Catechol
DDW	Double distilled water
DFT	Density functional theory
DHFR	Dihydrofolate reductase
D-R	Dubinin–Radushkevich
EC	Electrical conductivity;
EDCs	Endocrine-disrupting chemicals
FWHM	Full width at half-maximum
GAC	Granular activated carbon
ID	Intraparticle diffusion
L-H	Langmuir-Hinshelwood
MQW	Ultrapure milli-Q water;
MVD	Molegro virtual docker
NP	Nitrophenol
OFGs	Oxygen functional groups
OH(AC)	Hydroxyl functionalized activated carbon;
p_AC	Pristine/unmodified activated carbon;

PAC	Activated carbon
PFO	Pseudo-first-order
pH_{zpc}	Zero-point charge
PSO	Pseudo-second-order
RMSE	Root mean square error
ROS	Reactive oxygen species
RS	Resorcinol
TDS	Total dissolved solids
TH	Total hardness
TOC	Total organic carbon;
VB	Valence band
WNAC	Waste newspaper-derived activated carbon
Wt %	Weight percentage;
$\bullet O_2^-$	Superoxide radicals
•OH	Hydroxyl radicals
h^+	Holes
K_{ap}	Apparent reaction rate constant
Q_{max}	Adsorption capacity

CHAPTER 1

INTRODUCTION

This chapter presents advances in the development of biomass-derived activated carbon and activated carbon-based nanocomposites for the removal of hazardous phenolic contaminants from wastewater. Synthesized activated carbon was produced by chemical activation followed by incorporation into semiconductor photocatalysts to improve degrading efficiency. The study addresses the limitations of pristine ZnO, including rapid electron–hole recombination and restricted visible-light activity, through heterostructure formation *via* transition metal modification and activated carbon as supporting material. The synthesized materials were assessed for the adsorption and the photocatalytic degradation of phenolic derivatives. Experimental studies were supplemented by density functional theory (DFT) simulations to clarify adsorption processes and chemical reactivity interactions.

1.1 Introduction

Water is an essential natural resource for sustaining earth's ecosystem. Nonetheless, the supply of safe and clean water has become increasingly limited in many parts of the world [1]. The rapid development of the world population, agricultural demands, rising industrialization, modern technological society, and a variety of geological, environmental, and climatic factors are all contributing to increased water pollution [2,3]. In recent years, a wide range of toxic contaminants, including phenolic compounds, endocrine-disrupting substances, dyes, personal care products, pesticides, and pharmaceuticals, have been found at hazardous concentrations in drinking water, groundwater, and surface water posing serious risks to both environmental sustainability and public health [4-6].

Among the diverse classes of organic pollutants, phenol and substituted phenols are classified as priority organic pollutants due to their high toxicity, limited biodegradability, and adverse impacts on human health and aquatic life even at lower concentrations [7,8]. Exposure to phenolic chemicals has been associated to carcinogenesis, mutagenesis, endocrine disruption, and nervous system disorders [9,10]. The European Union and the United States Environmental Protection Agency have listed these compounds as a priority pollutant, with a maximum permitted concentration of 1 ppm in water bodies [11,12]. Given the severity of water contamination caused by elevated concentrations of toxic substances, the development of efficient, cost-effective, and ecologically benign treatment methods is necessary before being discharged into the aquatic environment. Various conventional and sophisticated treatment approaches have been developed to remove phenolic pollutants from wastewater, including biological treatment, membrane filtration, chemical oxidation, ion-exchange processes, coagulation-flocculation, and adsorption [13-15]. Figure 1.1 depicts commonly used physicochemical techniques for wastewater treatment. Among these methods, adsorption is considered one of the most effective wastewater treatment techniques for the removal of phenolic contaminants, owing to its simple operation, minimal or no pre-treatment requirements, environmental friendliness, absence of harmful by-products, and cost-effectiveness [16,17]. Adsorption is the process by which a material accumulates on a surface or contact. Adsorption takes place at the interface of a solid adsorbent and polluted water in water

treatment systems. The substance being removed from water is known as the adsorbate, and the material that facilitates its absorption is known as the adsorbent [18].

Figure 1.1. An overview of wastewater treatment techniques.

Activated carbon (AC)-based adsorption is widely used for the effective removal of organic pollutants from aqueous media due to its extremely porous structure, large surface area, and various surface chemical properties [19-21]. Despite its efficiency, the large-scale commercial application of AC can be hindered because of its high manufacturing value, which are mostly caused by the use of costly and non-renewable precursors such as petroleum wastes, coal, peat, and lignite [22-24]. To address this limitation, current research efforts have shifted toward the use of low-cost and widely available precursors, such as agricultural wastes and waste biomass, for the long-term generation of AC. Biomass-derived AC is being considered as an alternative to expensive commercial AC due to its availability, renewability, and low cost [25,26].

AC is commonly used as a co-adsorbent and support material for photocatalysts in wastewater treatment using photocatalytic degradation processes [27]. Its efficiency as a catalytic support is due to its large specific surface area, high aspect ratio, and strong capacity to evenly scatter catalytically active metal particles, which are necessary characteristics for improved catalytic performance [28]. Although each approach has certain benefits and drawbacks, photocatalysis has received a lot of attention as an advanced oxidation process (AOP) that entirely mineralize persistent organic pollutants into environmentally friendly intermediates under room

temperature [29-31]. Numerous semiconductor photocatalysts have been extensively studied for the breakdown of organic contaminants in aquatic environments. Among the most commonly investigated materials are titanium dioxide (TiO_2), tungsten trioxide (WO_3), silicon dioxide (SiO_2), zirconium dioxide (ZrO_2), iron oxide (Fe_2O_3), zinc oxide (ZnO), and molybdenum disulfide (MoS_2) [32].

Furthermore, the efficient design and optimization of wastewater treatment systems depend on a comprehensive understanding of the mechanisms controlling the removal of pollutants. In this regard, several studies have been conducted to gain deeper insights into the adsorption and catalytic mechanisms between AC and AC-based nanocomposites using density functional theory (DFT). For instance, Jan et al. [33] examined the impact of several surface functional groups on the adsorption behavior of azo dyes, such as –OH, –COOH, $–NO_2$, $–CH_2$ or $–CH_3$, –C≡C, –C=O, and $–SO_3$. In another study by Kebir et al. [34], the influence of various surface functional groups on AC was carried out for oxytetracycline adsorption, revealing a significant improvement in adsorption performance and a strong correlation with experimental data. Additionally, the chemical reactivity of basic dyes in correlation with AC was examined using DFT-based descriptors by De Souza et al. [35]. Similarly, Al-Kahtani et al. [36] studied the photocatalytic degradation process of bisphenol A (BPA) utilizing a ZnS/NSDC nanocomposite and then corroborated the experimental results by DFT calculations. The synthesized nanocomposite demonstrates exceptional characteristics and can serve as a reusable photocatalyst for the breakdown of BPA in aqueous solutions. The mechanisms involved in the elimination processes will be computed using the Gaussian 09/16 W program *via* DFT approach for the adsorption and its catalytic activity.

Given the growing significance of wastewater treatment, it is necessary to investigate the utilization of AC in adsorption processes and its nanocomposite derivatives in photocatalysis for the effective removal of phenolic contaminants from aqueous systems.

1.2 Activated carbon

AC can be described as carbonaceous materials that possess high porosity, notable

physicochemical stability, an abundance of functional groups, significant adsorptive capability, and a high degree of surface reactivity [37]. AC is a tasteless, amorphous, microcrystalline, non-graphitic type of carbon, appearing as a black solid substance similar to powdered or granular charcoal. “Activated carbon” denotes carbonaceous substances characterized by significant porosity, exceptional physicochemical stability, substantial adsorptive capacity, robust mechanical strength, pronounced surface reactivity, and a highly developed pore morphology [38]. AC typically has several heteroatoms, including oxygen, sulfur, hydrogen, nitrogen, halogens, and other elements, integrated into its structure as surface-bound functional groups [39,40].

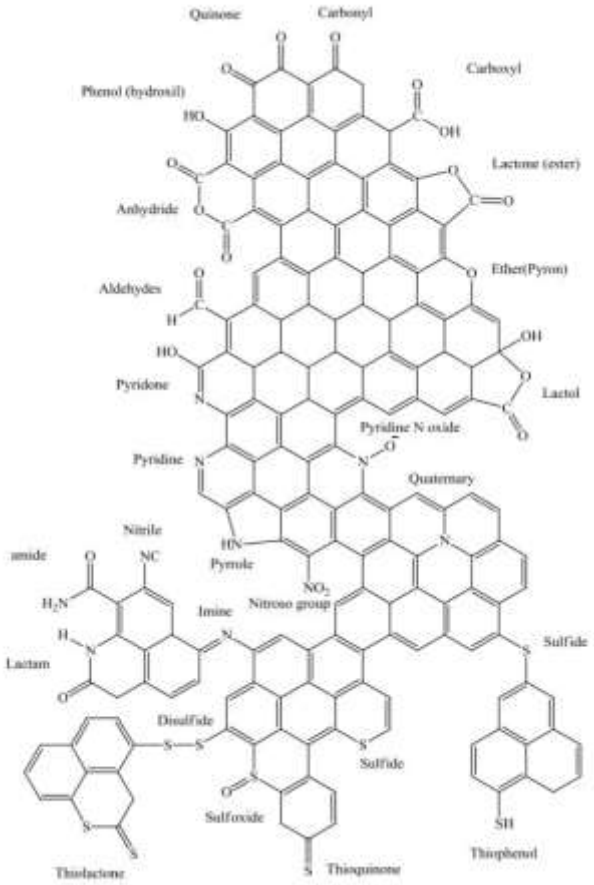

Figure 1.2. Several functional groups present on the activated carbon surface [44].

These functional groups may be introduced through chemical treatments during the activation process or may be the result of the carbonization of biomass precursors. The surface chemistry of AC may be modified via oxidation or nitrogen doping to produce carbon-based materials enriched with oxygen and nitrogen. Oxygen-containing

functional groups, including as carboxyl, carbonyl, phenolic, and lactone groups, can be synthesized utilizing activating agents such potassium hydroxide (KOH), sodium hydroxide (NaOH), and sulfuric acid (H_2SO_4) [41,42]. Nitrogen-containing groups, including amide, amine, pyridinic, and pyrrolic functionalities, can be integrated by activation procedures utilizing ammonia, urea, or melamine solutions in ethanol [43]. Figure 1.2 depicts various functional groups that may be found on the surface of AC.

Cuhadaroglu and Uygun [45] observe that AC does not possess a definitive chemical formula owing to its variable composition and structural heterogeneity. AC may be categorized into different forms based on its physical qualities, including powdered activated carbon (PAC), granular activated carbon (GAC), extruded activated carbon, activated carbon fibers, and activated carbon cloths. Owing to these versatile properties, AC is widely known as a highly adaptable carbonaceous material with numerous applications in supercapacitors, batteries, gas separation, wastewater treatment, energy storage systems, air purification, and catalytic processes.

In recent years, AC has been widely employed for environmental protection, with more rigorous pollution control legislation substantially enhancing its demand for air and water treatment applications. Due to its extensive adsorption capacity, AC efficiently removes many harmful and persistent pollutants from water sources, such as pesticides, herbicides, chlorinated hydrocarbons, heavy metal ions, and phenolic compounds [46,47].

Although AC exhibits excellent removal efficiency, challenges associated with regeneration and reuse under conventional conditions, along with relatively high operational costs, limit its practical applications [48]. As a result, significant efforts have been focused on creating low-cost adsorbents from waste materials for water filtration via batch and column adsorption methods [49]. The development of better AC with higher quality and performance has been driven by continuous developments in manufacturing processes and the research of alternate precursor materials.

1.2.1 Crystalline structure of AC

ACs possess a microcrystalline structure comprised of fused hexagonal carbon atom rings [50]. The microcrystalline structure of AC differs from that of graphite in terms of interlayer spacing. Graphite has an interlayer spacing of 0.335 nm, whereas AC has

an interlayer spacing of 0.34 to 0.35 nm. The microcrystallite layers in ACs exhibit reduced orderliness. The disorder in microcrystallite layers is attributable to the existence of heteroatoms and unoccupied lattice sites in ACs [51]. Biscoe and Warren introduced the word "turbostratic" to describe the disordered variant of the graphitic structure found in AC [52]. Figure 1.3 illustrates the contrast between the three-dimensional structure of graphite and the turbostratic structure of AC.

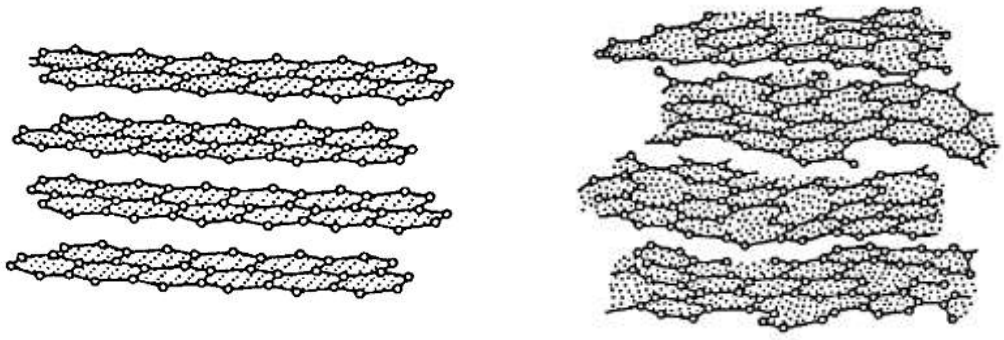

(a) **(b)**

Figure 1.3. Comparison of the three-dimensional crystal lattice of (a) graphite and (b) turbostratic structure.

1.2.2 Porous structure of AC

AC possesses a highly developed internal surface distinguish by a polydisperse porous structure including pores of various shapes and sizes. The most often utilized AC possesses a surface area usually between 500 and 1500 m^2/g and a pore volume approximately ranging from 0.7 to 1.8 cm^3/g. Nonetheless, the pore volume and surface area may reach up to 3000 m^2/g and 1 cm^3/g, respectively [53,54]. The International Union for Pure and Applied Chemistry (IUPAC) categorizes pores into three kinds based on size: micropores with an average diameter under 2 nm, mesopores with diameters ranging from 2 to 50 nm, and macropores with an average diameter above 50 nm [55].

Figure 1.4 depicts a porous structure characterized by macropores that connect directly to the external surface, mesopores that extend from the macropores, and micropores that further branch from the mesopores. The overall surface area of AC predominantly pertains to the surface area of micropores, so the majority of adsorption occurs within these micropores. Conversely, the mesopores and macropores function as transport pathways for the adsorbate to access the micropores. All pores possess walls, thereby

including two types of surfaces: an interior or microporous surface and an exterior surface. The internal or microporous surface denotes the walls of the micropores, whereas the external surface comprises the walls of the mesopores and macropores, together with the margins and the outward-facing aromatic sheets [56].

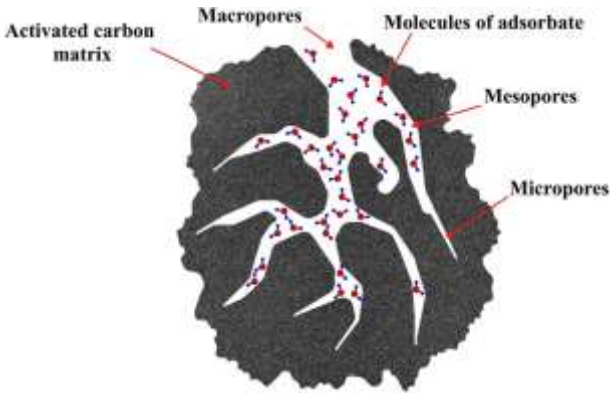

Figure 1.4. Schematic of activated carbon with different types of pores [57].

1.2.3 Raw material for the synthesis of AC

AC may be derived from both naturally occurring and synthesized carbonaceous substances, according to by Girgis et al. [58]. AC is often categorized according to the precursor type, since the features of the initial material substantially affect the structural characteristics, physicochemical properties, and overall efficacy of the produced AC [59,60]. Cagnon et al. [61] highlighted that the inherent structure of the precursor is crucial in influencing the ultimate characteristics of AC. Commercial AC has traditionally been produced using non-renewable and quite costly resources such as lignite, coal, wood, peat, and petroleum wastes [62]. As a result, there has been a growing focus on the use of affordable, renewable agricultural residues and lignocellulosic biomass for the synthesis of AC. A diverse array of biomass precursors, including corn cobs, hazelnut shells, mulberry pruning residues, olive stones, jojoba seeds, Chinese fir sawdust, coconut shells, kenaf fibers, bamboo, rice husks, groundnut shells, paper mill sludge, Prosopis juliflora, sugarcane bagasse, jackfruit peel, and other agro-industrial by-products has been investigated as sustainable alternatives [63,64]. Despite their availability, renewability, and cost-effectiveness, these biomass sources possess a significant amount of volatile matter, which is advantageous for generating a highly porous structure of AC. The majority of biomass resources are disposed of as waste without appropriate use from a commercial perspective.

Consequently, transforming agro-waste or biomass into value-added goods like AC might reduce waste disposal expenses and mitigate adverse environmental impacts.

1.2.4 Preparation of AC

The activation process generates or increases porosity on the surface of AC, as seen in Figure 1.5. AC can be manufactured either directly from dried raw materials or through a two-step activation process including the carbonization of the precursor followed by activation [65]. Based on the activation technique used, ACs are typically manufactured by two methods: (i) physical or gas activation, and (ii) chemical activation.

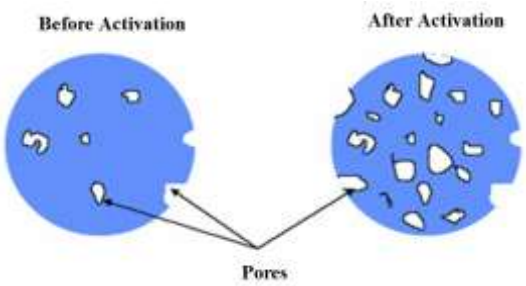

Figure 1.5. Two-dimensional representation of carbon activation [66].

(i) Physical activation

Physical activation is a two-step procedure. The raw precursor is initially pyrolyzed in an inert environment at temperatures over 400 °C to remove a wide range of volatile components. Thereafter, the carbonized substance undergoes activation at high temperatures (600–1200 °C) employing oxidizing agents such steam, carbon dioxide, nitrogen, or their combinations [67,68]. This process generates AC characterized by a robust porous structure and commendable mechanical strength, generally regarded as a cost-efficient and eco-friendly technique due to the lack of chemical activating agents [69,70]. However, physical activation has limitations, including prolonged activation durations, high energy requirements, and a reduced adsorption capacity of the produced AC [71].

(ii) Chemical activation

Chemical activation, often known as wet oxidation, can be performed in either a one- or two-step procedure. The one-step process involves immediately impregnating the dried precursor with chemical agents that oxidize and dehydrate it, followed by a

period of high temperature treatment [72]. The two-step approach entails the initial carbonization of dried raw material at temperatures ranging from 400-600 °C to generate char, succeeded by chemical impregnation and subsequent high-temperature activation [71]. To eliminate any remaining chemicals or by-products, the activated material is washed extensively with either acidic or alkaline solutions, and then rinsed with water. Chemical activation involves the incorporation of activating agents into the carbon matrix, which helps to promote the creation of pores. The washing procedure is essential for removing imbedded chemical species and creating a well-defined porous structure in the final AC [73]. Typical activating agents are metal salts like $FeCl_3$, $ZnCl_2$, and $MgCl_2$; alkaline chemicals such as Na_2CO_3, K_2CO_3, NaOH, and KOH; and acidic agents like HNO_3, HCl, H_3PO_4, and H_2SO_4 [74,75]. These compounds engage with the carbonaceous matrix, yielding gaseous products that facilitate pore formation [76]. Furthermore, they serve as oxidizing or dehydrating agents, facilitating pyrolytic breakdown and augmenting carbon output by minimizing tar and ash production [77,78]. Activating agents are of great importance in the development of surface functional groups and pore structures. KOH is considered one of the most efficient agents for generating AC with a high specific surface area [79]. Chemical activation is preferred over physical activation because it produces a more homogeneous pore structure and a larger surface area [80]. Furthermore, the comparatively lower activation temperature and reduced processing duration render chemical activation economically beneficial [81].

1.2.5 Effect of activating agents

The surface area and pore volume of AC can be substantially improved by employing appropriate chemical activating agents. Phosphoric acid (H_3PO_4), KOH, and zinc chloride ($ZnCl_2$) are some of the most often used agents for enhancing the texture characteristics of AC [82,83]. The activation process using $ZnCl_2$ facilitates the creation of inter- and intra-particle voids, resulting in AC distinguished by a large surface area and increased porosity [84]. Phosphoric acid is recognized for enhancing carbon production and producing a porous structure comprising both micropores and mesopores [85]. KOH activation mostly promotes the development of intricate microporous structures, yielding AC with a high specific surface area [86-88].

1.2.6 Effect of impregnation ratio

The impregnation ratio, defined as the weight ratio of activating agent to precursor, is considered an important attribute in chemical activation processes. Giraldo and Moreno-Pirajan [89] indicated that the impregnation ratio markedly affects the formation of porosity in AC. Utilizing $ZnCl_2$ and KOH as activating agents in ratios of 2:1 to 3:1 (activating agent: precursor) resulted in an increase in both surface area and total pore volume when the ratio was elevated from 2 to 3. The increase in porosity was ascribed to the elimination of tar from the cross-linked carbon structure caused by the chemical treatment [90].

Singh et al. [91] established that KOH activation at 600 °C with an impregnation ratio of 1:2 yielded AC with optimal surface area and porosity. In another work, Akpen et al. [92] synthesized AC from the seeds of two mango types (local and dausha) utilizing anhydrous $ZnCl_2$ at impregnation ratios of 1:2 and 1:3 for the purpose of wastewater color removal. The adsorption performance ranked as follows: local 1:2 > local 1:3 > dausha 1:2 > dausha 1:3, demonstrating that the impregnation ratio significantly influences adsorption efficiency. Sagili et al. [93] examined grape industrial waste treated with $ZnCl_2$ and found that elevated impregnation ratios enhanced mesopore formation, whereas diminished ratios facilitated micropore development. This behavior was elucidated by the augmented swelling and heightened release of volatile substances at elevated ratios, resulting in pore expansion [94]. In contrast, reduced impregnation ratios restricted pore expansion and promoted micropore formation by decreasing tar accumulation. Various investigations have similarly validated that the impregnation ratio significantly influences the surface area and pore structure of AC [95,96].

1.2.7 Effect of temperature on surface area and pore volume

The activation temperature is an important variable influencing the textural properties of AC. The ideal temperature range is contingent upon several elements, including the characteristics of the precursor, the nature of the activation substance, the heating approach, and the mixing process. Excessively high activation temperatures may cause a decrease in specific surface area and carbon yield, most likely due to the increased transformation of cross-linked solid-phase structures into volatile gaseous products

[97,98]. Conversely, inadequate activation temperatures might provide suboptimal porosity, since the energy supplied may be insufficient to commence full pyrolysis, resulting in partial reactions [99].

1.2.8 Applications of AC

AC is a diverse and highly effective adsorbent extensively utilized in several industrial sectors of industry. In addition to its use in solar cells, gas-phase adsorption, solvent recovery, separation and purification technologies, catalytic processes, biomedical applications, pollution control, spill remediation, supercapacitors, energy storage devices, and batteries, AC is also employed in the removal of color, odor, and undesirable organic and inorganic contaminants from water [100-102]. The remarkable adsorption capability of AC is mostly due to its large surface area, advanced porous architecture, and elevated surface reactivity. Furthermore, the adjustability of its physicochemical features enhances its use across many domains [103].

AC is widely utilized for the removal of biological, organic, and inorganic contaminants from wastewater. Numerous research has shown that biomass-derived ACs are highly effective in treating water. Wang et al. [104] reported an adsorption capacity of 934.57 mg/g for methylene blue with AC obtained from distillers' grains. Nasser et al. [105] investigated palm fruit bunch particles for the adsorption of basic dye (BR18), attaining a maximum adsorption capacity (q_{max}) of 242 mg/g. AC derived from argan nutshells had a maximum adsorption capacity of 1250 mg/g for bisphenol A at 293 K [106]. Supong et al. [107] performed experimental and theoretical studies on the adsorption of phenol and dinitrophenol with AC derived from *Tithonia diversifolia*, achieving removal efficiencies of 99.98 % and 97.81 %, respectively. Khalil et al. [108] similarly generated AC from sugarcane bagasse, exhibiting robust adsorption capabilities for phenolic chemicals. Bhomick et al. [109] synthesized activated biocarbon from Pinus kesiya cones using $ZnCl_2$ activation, resulting in an 89 % elimination of Alizarin Red S dye. Nourouzi et al. [110] examined waste newspaper-derived activated carbon (WNAC) for the adsorption of glyphosate from aqueous solutions.

1.3 Adsorption process

Adsorption is a surface phenomena that facilitates the transfer of molecules from a gaseous or liquid phase to a solid surface. The molecules or atoms on the solid surface have residual surface energy due to unbalanced forces, and when certain substances collide with the solid surface, they are drawn by these unbalanced forces and remain on the solid surface. The adsorption process can be classified as physisorption or chemisorption based on the characteristics of the adsorption forces. In physisorption, the adsorbate molecules adhere to the adsorbent surface by weak van der Waals forces [111]. Physical adsorption often occurs at low temperatures, characterized by a rapid adsorption rate, minimal adsorption heat, and a lack of selectivity. Chemisorption, conversely, pertains to the sharing or exchange of electrons between the surface of the adsorbent and the adsorbed molecule. A chemical bond formed between the adsorbate and the adsorbent surface as result of the reaction. Physical adsorption and chemical adsorption are interrelated often occur simultaneously [112].

Adsorption isotherms models are used to represent the adsorption process at equilibrium. These models demonstrate the interaction between adsorbent and adsorbate and measure the quantity of material adhered to the surface. The predominant adsorption isotherms are the Langmuir, Freundlich, Temkin and Dubinin–Radushkevich (D-R) isotherm [113,114]. Another significant aspect of the adsorption process is the explore of adsorption kinetics, which describes the absorption rate of adsorbate, the nature of the adsorption mechanism, and the rate-controlling step. Several kinetic models, including the pseudo-first-order, pseudo-second-order, and Weber and Morris intraparticle diffusion model, are employed to study the kinetics of adsorption [115-117]. Moreover, thermodynamic investigations elucidate the influence of temperature on numerous thermodynamic parameters, including Gibbs free energy, enthalpy, and entropy [118]. Chapter 2 provides an extensive overview of adsorption isotherms, kinetic models, and thermodynamic parameters, respectively.

1.4 Photocatalysis

Photocatalysis is the process of accelerating or modifying a chemical reaction in the presence of a photocatalyst under ultraviolet or visible light irradiation [119]. Due to its cost-effectiveness, negligible secondary pollution, high efficiency, and ease of

operation, it has become a very promising method for the degradation of phenolic substances [120]. Photocatalytic materials produce very reactive species when exposed to light, especially hydroxyl radicals (•OH) [121], which may oxidize organic contaminants and then mineralize them into water (H_2O) and carbon dioxide (CO_2) [122]. Both homogeneous and heterogeneous systems are commonly used to describe photocatalysis, depending on the phase relationship between the photocatalyst and the reactants [123]. Homogeneous photocatalysis involves the simultaneous presence of the photocatalyst and the reactants, allowing light irradiation to produce reactive hydroxyl radicals. The Photo-Fenton process ($UV/Fe^{2+}/H_2O_2$) and ozone-based photolysis ($UV/O_3/H_2O_2$) are two of the most often used homogeneous systems [124]. In contrast, heterogeneous photocatalysis occurs when reactants and photocatalysts interact in distinct phases, usually solid-liquid or solid-gas systems [125]. Due to its cost-effectiveness, reusability, ease of catalyst separation, and operational simplicity, this approach is commonly considered an excellent destructive technology for pollutant removal [126]. Semiconductor metal oxides are commonly employed in heterogeneous systems to break down harmful organic pollutants by using air oxygen as the oxidant and light as the energy source [127]. The current research focuses on synthesizing heterogeneous catalysts made of semiconductor metal oxides and using them to degrade pollutants.

1.4.1 Mechanism of heterogeneous photocatalysis

Below is a description of the mechanism that underlies heterogeneous photocatalysis, which breaks down very harmful and toxic chemicals into carbon dioxide (CO_2) and water (H_2O) [128].

(i) Excitation of the semiconductor

The structure of a semiconductor metal oxide consists of a valence band (VB) and a conduction band (CB), with the electrons located in the VB [129]. Bandgap energy is the energy that is present between the two bands. Electrons (e^-) in the VB are stimulated to the CB when the semiconductor metal oxide is exposed to light with an energy equal to or higher than the bandgap energy, creating a hole (h^+) in the VB (Equation 1.1). While holes at the top of the VB take part in oxidation processes, photo-induced electrons at the bottom of the CB engage in reduction activities [130].

$$\text{Metal oxide} + hv \longrightarrow \text{Metal oxide } e^-_{CB} + h^+_{CB} \quad (1.1)$$

(ii) Formation of hydroxyl radical

During the photoreduction process, the photoexcited electron in the CB (e^-_{CB}) engages with oxygen (O_2) adsorbed on the metal oxide (MO) surface, resulting in the generation of reactive superoxide radicals ($\bullet O_2^-$), as illustrated in Equation (1.2.)

$$e^-_{CB} + O_2 \longrightarrow \bullet O_2^- \quad (1.2)$$

The superoxide radical persists in its interaction with water molecules to produce H_2O_2, which subsequently decomposes and releases the •OH radical (Equation 1.5) [131]. The $\bullet O_2^-$ radical then interacts with water molecules to produce H_2O_2, which ultimately decomposes, releasing the •OH radical (Equation 1.5).

$$\bullet O_2^- + H^+ \longrightarrow \bullet OHH \quad (1.3)$$

$$\bullet OHH + \bullet OHH \longrightarrow H_2O_2 + \bullet O_2 \quad (1.4)$$

$$H_2O_2 + \bullet OHH \longrightarrow \bullet OH + \bullet OH \quad (1.5)$$

The hole (h^+_{VB}) can undergo photo-oxidation with water to produce the reactive hydroxyl radical (•OH) (Equation 1.6) [132].

$$h^+_{VB} + \bullet OH \longrightarrow \bullet OH \quad (1.6)$$

(iii) Recombination reaction

The generated hole (h^+_{VB}) and electron (e^-_{CB}) may recombine without taking part photoreaction, thus releasing the absorbed light energy as heat [133].

(iv) Photodegradation of phenolic compounds

Phenolic contaminants adsorbed on semiconductor photocatalysts are oxidized by the hydroxyl radicals (•OH) produced. Due to their high oxidation potential (approximately 2.8 V relative to the standard hydrogen electrode), these highly reactive •OH species efficiently decompose organic pollutants, ultimately transforming them into mineralized byproducts such as CO_2 and H_2O, as illustrated in Equation (1.6) [134].

$$\text{Phenolic compound} + \bullet OH \longrightarrow CO_2 + H_2O \quad (1.6)$$

A schematic illustration of the photocatalytic mechanism is depicted in Figure 1.6.

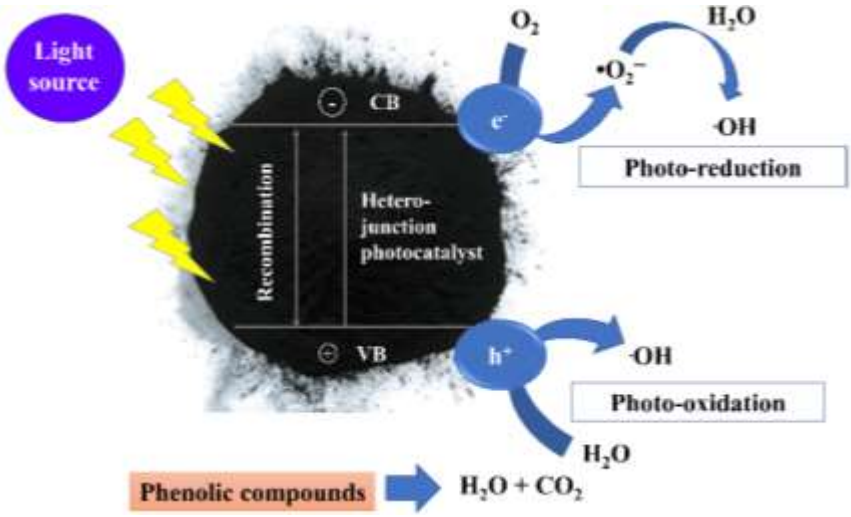

Figure 1.6. Photocatalytic degradation mechanism.

1.4.2 Semiconductor materials as photocatalysts

Extensive study has recently been undertaken on several semiconductor (metal oxide) photocatalysts and their physicochemical characteristics. An efficient metal oxide photocatalyst must demonstrate excellent photostability, chemical and biological inertness, low toxicity, and the capacity to utilize both ultraviolet and visible light. Furthermore, it must have an appropriate bandgap energy to effectively facilitate photocatalytic processes [135]. Table 1.1 provides a summary of the most common semiconductor metal oxides used as photocatalysts.

Table 1.1. Bandgap energy and wavelength of photocatalysts.

Semiconductor	Bandgap (eV)	Wavelength (nm)
ZnO	3.37	362
TiO_2	3.20	413
WO_3	2.80	443
Bi_2O_3	2.80	400
Fe_2O_3	2.20	539
CdS	2.40	514
CuS	2.20	570
ZnS	3.60	344
CuO	2.00	570
$BiVO_4$	2.40	500
Ag_3PO_4	2.45	365
g-C_3N_4	2.70	450

To function effectively as a photocatalyst, a semiconductor must possess an array of essential properties. Photocatalyst must be able to absorb photons and produce electron–hole pairs, while reducing the recombination of these charge carriers. Furthermore, the material must have a better structural and chemical stability. The redox potentials of the hydroxyl radical (•OH/H_2O) system must reside inside the semiconductor's bandgap to facilitate efficient oxidation-reduction processes [136]. A semiconductor must possess specific characteristics to function effectively as a photocatalyst: it must absorb photons, generate electron-hole pairs, minimize recombination of these pairs, exhibit long-term stability, and have oxidation-reduction potentials of the OH and H_2O pairs within the semiconductor material's bandgap domain [137].

Photocatalytic methods use semiconductor metal oxides like TiO_2, SnO_2, Bi_2O_3, ZrO_2, and ZnO, as well as metal sulfides like ZnS, PbS, and CdS, to degrade pollutants. These materials use solar radiation for energy and atmospheric oxygen (O_2) as an oxidizing agent [138]. Zinc oxide (ZnO) is commonly considered as a potential material among metal oxide photocatalysts because of its high photoactivity, strong oxidative capacity, low cost, operational efficacy under ambient settings, and non-toxicity [139]. As a result, ZnO was chosen as the photocatalyst in this investigation, and the next section provides a brief description of its structural characteristics and properties.

1.4.3 Zinc oxide as a photocatalyst

Zinc oxide (ZnO) is categorized as an II–VI semiconductor due to zinc and oxygen's positions in Groups 2 and 6 of the periodic table, respectively. Due to its exceptional optical features, chemical sensing capabilities, semiconducting behavior, electrical conductivity, and piezoelectric qualities, ZnO is one of the most thoroughly studied metal oxides. Figure 1.7 demonstrates that ZnO occurs in three crystalline forms: hexagonal wurtzite, cubic zinc blende, and rock salt formations. The wurtzite phase is the most thermodynamically stable at ambient temperature. It demonstrates a tetrahedral coordination geometry wherein each Zn atom is connected to four oxygen atoms and vice versa [140]. ZnO is an n-type semiconductor that has a broad bandgap of about 3.37 eV, a high exciton binding energy of over 60 meV, and significant

absorption in the deep violet to near-ultraviolet (UV) spectrum at ambient temperature [141]. The characteristics of ZnO may change as it is reduced to the nanoscale or doped with foreign elements. ZnO has garnered considerable attention for the breakdown and total mineralization of water pollutants due to its low cost, high quantum efficiency, appropriate bandgap, robust redox potential, and efficient photocatalytic properties [142]. The principal physical and chemical features of wurtzite ZnO are summarized in Table 1.2.

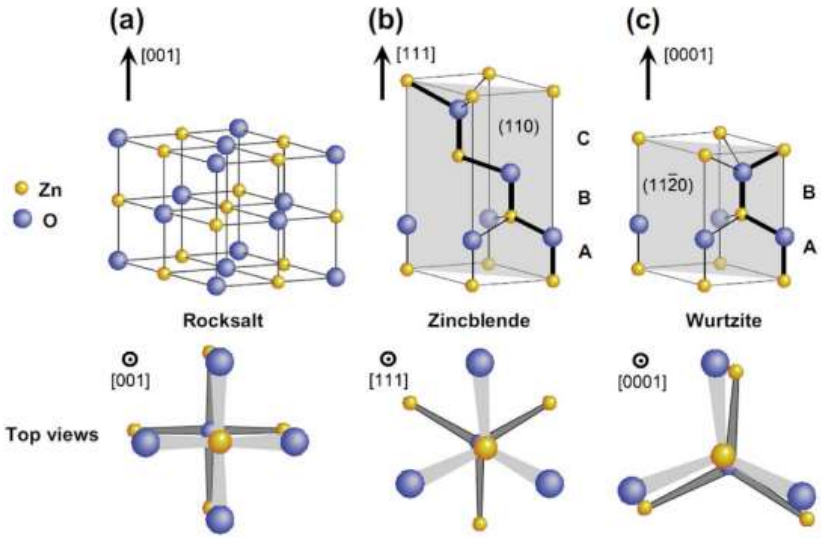

Figure 1.7. Different crystals forms of ZnO [143].

Table 1.2. Physical and chemical properties of wurtzite ZnO.

Properties	**ZnO nanoparticles**
Molar mass (g/mol)	81.39
Light absorption (nm)	<320
Atoms per unit cell (Z)	4
Lattice parameters	a = 3.25Å, c = 5.205Å
Color	White powder
Odor	Odorless
Density (g/cm^3) @ RT	5.6
Melting point (K)	2248
Flash point (K)	1709
Solubility	Insoluble in water
Refractive index	2.0041

Band gap (eV)	3.37, Direct jump
Exciton binding energy (meV)	50
Thermal Conductivity (W/m/K)	0.7,1-1.5

1.4.4 Limitations in ZnO photocatalysis

ZnO has several limits even though it is widely used as an antibacterial agent in radiation-driven degradation of organic contaminants, wastewater treatment, and antifouling systems. The photo-instability of pure ZnO in aqueous conditions and the quick recombination of photogenerated electron-hole pairs are severe issues that drastically reduce its photocatalytic performance [144]. Moreover, pure ZnO nanoparticles tend to cluster at elevated concentrations, have a relatively low specific surface area in bulk form, and demonstrate improved colloidal stability in water, complicating their subsequent separation and recovery after treatment [145].

To address these issues, subsequent studies have focused on coupling or doping ZnO with other metals or metal oxides that further increase its efficiency [146,147]. The integration of these materials serves numerous significant functions:

(i) The inclusion of appropriate hybrid materials allows for excellent trapping of photoexcited electrons and their transport to the semiconductor surface. The production of ZnO-based metal oxide-metal oxide heterostructures can greatly limit the recombination of photogenerated electron-hole pairs, thereby increasing photocatalytic effectiveness [148].

(ii) A suitable work function is an essential need for the included foreign material. Several factors including energy level alignment, interfacial placement, and the efficiency of electron transport from the semiconductor conduction band to the adsorbed electrolyte species primarily determine the overall performance of the hybrid system [149].

(iii) The supporting material should have a large surface area and a significant adsorption affinity for the target pollutants. Enhanced adsorption promotes effective degradation while reducing the development of intermediate byproducts during the photocatalytic process.

(iv) The matrix should enable for the photocatalyst's fast and efficient recovery, allowing it to be reused immediately or after regeneration.

1.4.5 AC as supporting material

To address the inherent limitations of ZnO-based photocatalysis, AC is commonly used as a supporting material. ZnO-modified AC has a higher surface area, porosity, and cation exchange capacity than the pure photocatalyst [150]. AC has a highly porous structure, hydrophilic surface functional groups, and hydrophobic graphitic domains, making it ideal for both adsorption and catalysis [151]. AC typically has a large specific surface area (500-2000 m^2/g) and strong surface reactivity [152]. As a result, in the current work, a ZnO/AC nanocomposite was created and used as an efficient photocatalytic system for pollutant degradation.

The incorporation of AC and ZnO addresses several practical limitations associated with standalone ZnO photocatalysts, such as particle aggregation in suspension, challenges in implementing ZnO in continuous flow systems, and difficulties in post-reaction separation and recovery of fine ZnO powders. The use of AC as a supporting matrix not only increases dispersion and stability, but it also considerably improves the photocatalytic performance of the pure semiconductor [153]. The primary benefits of using AC as a support for ZnO are as follows:

(i) It has a large specific surface area and enables efficient charge separation between the VB and CB. This improved separation allows charge carriers to migrate to the surface and interact with pre-adsorbed redox species, resulting in increased photocatalytic efficiency.

(ii) The intermediates produced during photocatalysis can be successfully adsorbed onto the surface of AC, allowing for continued degradation in following cycles and increasing the overall availability and efficiency of the photocatalyst [154].

(iii) The photocatalytic efficacy of the nanocomposite can be greatly improved by coupling semiconductors with AC, since this integration reduces photogenerated electron-hole pair recombination [155].

(iv) ZnO/AC composites have a higher electron transfer capacity, better dispersion stability, smaller crystallite sizes, and a lesser tendency for aggregation and surface passivation.

1.4.6. Heterojunction formation of ZnO photocatalyst

ZnO is widely regarded as a promising semiconductor photocatalyst owing to its att-

ractive physicochemical properties. Nevertheless, its practical photocatalytic performance is subject to several limitations. A foremost drawback is its susceptibility to photocorrosion and instability under prolonged light irradiation. Moreover, the rapid recombination of photogenerated electron–hole pairs significantly reduces its photocatalytic efficiency [156].

Another drawback of ZnO is its relatively wide bandgap, which confines its photoresponse to the ultraviolet region, limiting its efficient use of solar light in the visible spectrum [157]. Reduced bandgap energy is consequently required to enable visible-light-driven photodegradation. To overcome these issues, numerous modification procedures have been attempted, such as metal and nonmetal doping, noble metal deposition, and coupling with other semiconductors or carbon-based materials. These alterations improve charge separation by allowing the trapping and transport of photoexcited electrons on the semiconductor surface, hence increasing total photocatalytic activity [158].

In recent years, ZnO/metal heterojunction systems have received a lot of interest in photocatalysis because they collaborate the distinctive characteristics of metals and semiconductors while producing improved optical, electrical, and catalytic properties through synergistic interactions. To enhance ZnO photocatalytic performance, significant research efforts have been directed toward the production of ZnO-based nanocomposites. Several hybrid systems, such as ZnO-CuO, ZnO-Fe_2O_3, ZnO-NiO, and ZnO-ZrO_2, were effectively synthesized. These adjustments increase the photoresponse range and enable more effective separation of photogenerated electron-hole pairs, improving overall photocatalytic performance [159,160].

For example, ZnO/Cu_2O/Si nanohybrid was synthesized using a simple, cost-effective, all-solution processing technique at a low temperature [162]. This ternary hybrid achieved an 81.6 % elimination of MB in 120 min under visible light illumination, significantly outperforming both the pure Si nanowires and the binary nanohybrids. Similarly, a work conducted by Yuan et al. [163] involves the creation of g-C_3N_4/CeO_2/ZnO nanoscale heterostructures for the degradation of MB under visible light. Shen et al. [161] proposed the synergistic VPC-PSA mechanism that for use in the Cu/ZnO/CoFe-CLDH composite system as shown in Figure 1.8.

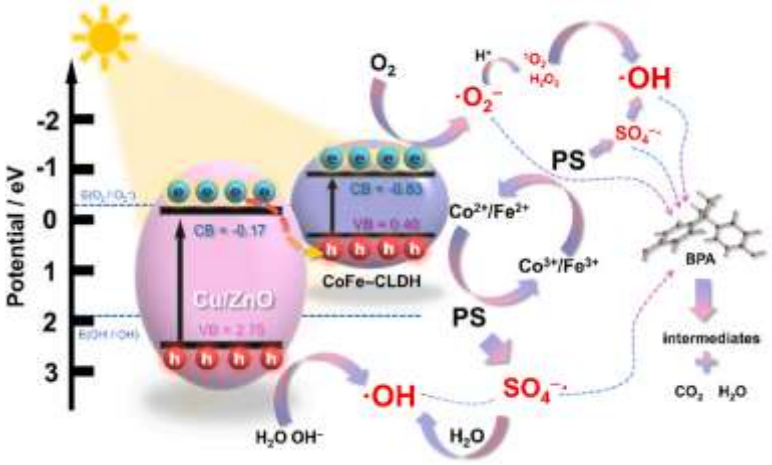

Figure 1.8. Schematic representation of synergistic VPC-PSA procedure enhances Cu/ZnO/CoFe-CLDH catalytic mechanism for ROS generation and BPA degradation [161].

1.5 Overview of selected phenolic derivatives for degradation studies

This study examined the photocatalytic degradation of phenolic chemicals, particularly 4-nitrophenol (4-NP) and bisphenol A (BPA). The production of many different types of industrial chemicals relies on phenolic compounds as essential intermediates, including colors, medicines, insecticides, polymers, resins, and disinfectants [164]. These chemicals are commonly found in industrial effluents and surface water bodies because of their widespread use in various sectors. Phenolic pollutants are highly toxic, persistent, and resistant to biodegradation, even at low concentrations. Their presence in aquatic environments poses serious risks to both human health and ecosystems [165]. Exposure to phenolic compounds can cause skin and eye irritation, headaches, nausea, liver and kidney damage, endocrine disruption, and other chronic health complications [166]. The efficient removal of phenolic contaminants from water sources is now an urgent environmental concern due to their toxicity, persistence, and prevalence. A brief overview of the phenolic pollutants that were studied in this thesis are described in Chapter 2.

1.6 Density functional theory study

Quantum chemical calculations have become an essential tool for studying the structural and electrical characteristics of molecular systems. Molecular energy, charge distribution, dipole moment, bonding properties, and other physicochemical

factors, especially for tiny and medium-sized molecules, may be thoroughly investigated using these computational approaches. Understanding adsorption mechanisms and bolstering the formulation and interpretation of experimental investigations are greatly enhanced by the insights gained from such computations. Quantum chemical calculations have become a significant method to understand the structure and characteristics properties of molecules in recent times. These calculations may provide extensive information on molecular energy, charge, dipole moment, chemical bond, and other properties for most small and medium molecular systems. The calculated results have significant implications for the investigation of adsorption mechanisms and the advancement of experimental research [167]. Even though the experimental studies provide valuable information, there are phenomena and system insights that cannot be observed through pure experimental methods. Furthermore, because of the complexity of the system and the coupling of various interactions, some experimental data are difficult to interpret. As a result, an approach that goes beyond experimentation is required to forecast the unobservable features and enhance the interpretation of the experimental results [168]. Quantum mechanical methods offer effective solutions to issues that are not entirely resolved through experimental techniques. Theoretical techniques may predict a wide variety of molecular characteristics and behaviors, such as the relative energies and stabilities of molecules and solid-state systems [169]. Depending on the underlying quantum mechanical framework, computational methods are widely classified as ab initio methods, semi-empirical or empirical approaches, molecular mechanics, and molecular dynamics simulations [170].

Density Functional Theory (DFT) was used in the current investigation, which is classified as ab initio and provides the best balance of computing efficiency and accuracy [171]. Ab initio methods, also known as first-principles approaches, allow the estimation of numerous system attributes based simply on basic structure knowledge, without the need of modifiable empirical parameters [172]. As a result, these methods offer a strong and complementary framework for studying molecular and material systems in comparison to traditional experimental techniques and solely theoretical quantum (field) models.

In ab initio methods, the molecular Schrödinger equation is solved without the use of empirical or semi-empirical parameters, resulting in all results being directly derived from fundamental theoretical principles. Nevertheless, this does not indicate that the solutions are precise; rather, the approximations are meticulously defined within a first-principles framework, with an anticipated and qualitatively understood margin of error [173]. Ab initio calculations are increasingly important tools for both experimentalists and theorists. They contribute to a better knowledge of material characteristics, valid predictions of empirically observed events, and the rational design and development of novel materials [174].

DFT is now recognized as one of the most successful and extensively used methods for identifying the electrical structure of matter. In addition to electronic structure computations, DFT may be used to evaluate a variety of molecular features, such as optimal geometries, total energies, vibrational frequencies, electrical and magnetic properties, and reaction pathways [175,176]. DFT techniques have been used in a variety of computer programs, including VASP, Quantum ESPRESSO, SIESTA, and Gaussian [177]. In the current investigation, all DFT-based computations were performed using the Gaussian 09/16W software package.

1.7 Present study

AC is well known as an abundant and versatile adsorbent with lots of applications in water treatment. AC also has the benefit of being able to be coupled with photocatalysts, increasing the efficiency with which organic pollutants are removed. Nonetheless, the exorbitant cost and non-renewability of traditional precursor materials limit their large-scale utilization. Similarly, single semiconductor photocatalysts such as ZnO have intrinsic limitations. Long-term light irradiation causes photocorrosion and structural instability in ZnO. Furthermore, the photogenerated electron-hole pairs undergo fast recombination, considerably reducing their photocatalytic efficacy. Another significant drawback of ZnO is its broad bandgap, which confines its photoactivity predominantly to the UV region, hindering its effective use in visible light irradiation.

To accomplish visible-light-responsive photocatalysis, two major concerns need to be addressed: narrowing bandgap and electron-hole recombination inhibition. Lowering

the bandgap increases photocatalytic effectiveness by extending light absorption into the visible spectrum and reducing charge carrier recombination. Therefore, the nanocomposite was further modified through transition metal doping to improve its visible-light-driven photocatalytic efficiency for the degradation of aqueous pollutants.

Consequently, the present investigation focuses on the synthesis of AC and AC-based heterojunction photocatalyst for the removal of phenolic compounds from wastewater. AC was produced from locally available waste biomass which was then activated using chemical activating agent (e.g., KOH). On the other hand, the photocatalyst-supported AC nanocomposite, including AC coupled with ZnO/ZrO_2 and Co-doped ZnO/AC was manufactured by a hydrothermal process. The physicochemical characteristics of the produced materials were thoroughly investigated utilizing a variety of analytical techniques. The produced AC was used for the adsorption of 2-chlorophenol, and catechol and resorcinol, while its nanocomposite materials were applied for the photocatalytic degradation of 4-nitrophenol and bisphenol A from aqueous solutions. Theoretical investigations utilizing DFT simulations were conducted to understand the adsorption mechanism and assess the chemical reactivity of both the adsorbent material and the target contaminants. The outline of the work undertaken in this thesis is presented in Figure 1.9.

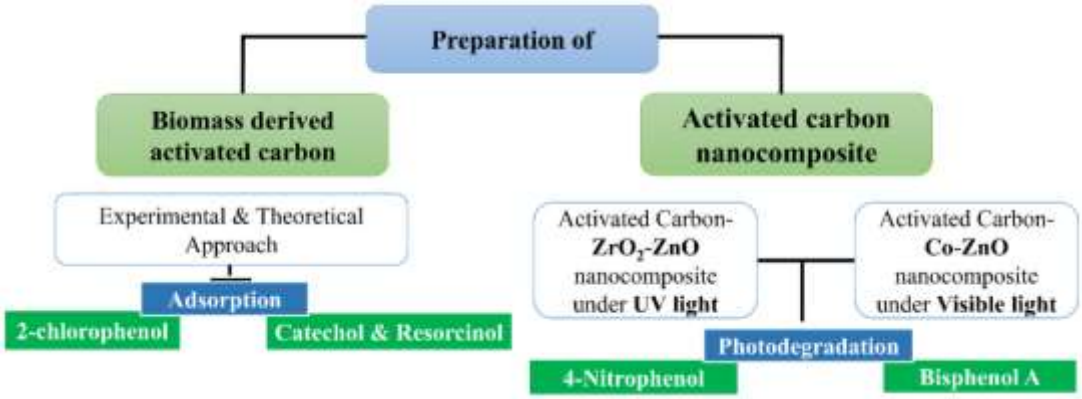

Figure 1.9. Scheme of the present study.

1.8 Aims and objectives of the work

The objectives of the present work are as follows:

1. Preparation of AC adsorbent from locally available biomass via KOH chemical activation.
2. Preparation of AC with transition metal/ semiconductor materials using hydrothermal method.
3. Characterization of synthesized material using various analytical techniques.
4. Application studies for the adsorption & photodegradation of phenolic compounds.
5. Computational approaches to understand the reaction mechanism between the adsorbent & adsorbate.

The outline of the thesis is presented in Figure 1.10.

Chapter 1	**Introduction**
Chapter 2	**Materials and methods**
Chapter 3	**Activated carbon adsorbent derived from waste biomass, " Croton caudatus" for efficient removal of 2-chlorophenol from aqueous solution: kinetics, isotherm, thermodynamics and DFT simulation**
Chapter 4	**Exploring the adsorption of catechol and resorcinol onto Croton caudatus activated carbon: An integrated experimental and theoretical approach**
Chapter 5	**Highly efficient photocatalytic degradation of organic pollutants using novel carbon integrated ZrO_2-ZnO nanocomposites: kinetics, molecular docking, DFT simulation and real wastewater application**
Chapter 6	**Harnessing synergistic effects in porous carbon/Co–ZnO heterojunction for enhanced visible-light photocatalytic removal of bisphenol A**
Chapter 7	**Summary and conclusions**

Figure 1.10. Outline of the thesis work.

References

[1] P. O. Ukaogo, U. Ewuzie, C. V. Onwuka, Environmental pollution: causes, effects, and the remedies, in: Microorg. Sustain. Environ. Heal. (2020) 419–430.

[2] V. Saxena, Water quality, air pollution, and climate change: investigating the environmental impacts of industrialization and urbanization, Water Air Soil Pollut., 236 (2025) 73.

[3] S. V. Rathod, P. Saras, S. M. Gondaliya, Environmental pollution: threats and challenges for management, in: Eco-restoration of Polluted Environment, CRC Press (2024) 1–34.

[4] S. Thakur, A. Chandra, V. Kumar, S. Bharti, Environmental pollutants: endocrine disruptors/pesticides/reactive dyes and inorganic toxic compounds, in: Biotechnol. Environ. Sustain., Springer Nature Singapore (2025) 55–100.

[5] P. K. Singh, U. Kumar, I. Kumar, A. Dwivedi, P. Singh, S. Mishra, C. S. Seth, R. K. Sharma, Critical review on toxic contaminants in surface water ecosystem: sources, monitoring, and its impact on human health, Environ. Sci. Pollut. Res., 31 (2024) 56428–56462.

[6] D. Boro, M. Chirania, A. K. Verma, D. Chettri, A. K. Verma, Comprehensive approaches to managing emerging contaminants in wastewater: identification, sources, monitoring and remediation, Environ. Monit. Assess., 197 (2025) 1–29.

[7] A. Mohd, Presence of phenol in wastewater effluent and its removal: an overview, Int. J. Environ. Anal. Chem., 102 (2022) 1362–1384.

[8] T. Ruan, P. Li, H. Wang, T. Li, G. Jiang, Identification and prioritization of environmental organic pollutants: from an analytical and toxicological perspective, Chem. Rev., 123 (2023) 10584–10640.

[9] A. A. Sokan-Adeaga, M. A. Sokan-Adeaga, E. D. Sokan-Adeaga, A. N. Oparaji, H. Edris, E. O. Tella, F. A. Balogun, M. Aledeh, O. E. Amubieya, Environmental toxicants and health adversities: a review on interventions of phytochemicals, J. Public Health Res., 12 (2023) 22799036231181226.

[10] E. A. Nnamani, A. A. Bayode, O. B. Otitoju, M. O. Alfred, M. O. Omorogie, Environmental profiling of endocrine disrupting chemicals in ground water sources: an African perspective, RSC Adv., 15 (2025) 26673–26692.

[11] V. Nikolopoulou, N. A. Alygizakis, M.-C. Nika, M. Oswaldova, P. Oswald, M. Kostakis, A. Koupa, N. S. Thomaidis, J. Slobodnik, Screening of legacy and emerging substances in environmental matrices using wide-scope target and suspect screening, Sci. Total Environ., 805 (2022) 150253.

[12] J. Kaur, I. Thakur, S. K. Mehta, Safe level (threshold) of emerging contaminants in drinking water, in: Emerg. Contam. Water, Springer Nature Switzerland (2025) 485–507.

[13] A. Labidi, H. Ren, A. Sial, H. Wang, E. Lichtfouse, C. Wang, Coal ash for removing toxic metals and phenolic contaminants from wastewater: a brief review, Crit. Rev. Environ. Sci. Technol., 53 (2023) 2006–2029.

[14] S. Ho, Low-cost adsorbents for the removal of phenol/phenolics, pesticides, and dyes from wastewater systems: a review, Water, 14 (2022) 3203.

[15] G. Bal, A. Thakur, Distinct approaches of removal of dyes from wastewater: a review, Mater. Today Proc., 50 (2022) 1575–1579.

[16] H. N. Tran, Adsorption technology for water and wastewater treatments, Water, 15 (2023) 2857.

[17] F. I. da Silva Aires, D. N. Dari, I. S. Freitas, J. L. da Silva, J. R. de Matos Filho, K. M. dos Santos, V. C. Bizerra, Advanced and prospects in phenol wastewater treatment technologies: unveiling opportunities and trends, Discover Water, 4 (2024) 20.

[18] M. A. Albedah, M. R. Hamoudi, S. H. Sadon, E. Oussama, Q. H. Le, Study of phenol removal from wastewater petroleum industry using molecular dynamics method for two-dimensional adsorbents, Eng. Anal. Bound. Elem., 147 (2023) 69–75.

[19] Y. Tang, G. Xu, S. Liu, M. Li, J. He, X. Wen, Activated carbon microspheres with high surface area for efficient organic contaminants removal, Colloids Surf. A, 669 (2023) 131479.

[20] B. Wang, J. Lan, C. Bo, B. Gong, J. Ou, Adsorption of heavy metal onto biomass-derived activated carbon, RSC Adv., 13 (2023) 4275–4302.

[21] C. H. V. Brito, D. C. S. Gloria, E. B. Santos, R. A. Domingues, G. T. Valente, N. C. S. Vieira, M. Gonçalves, Porous activated carbon/graphene oxide composite for efficient adsorption of pharmaceutical contaminants, Chem. Eng. Res. Des., 191 (2023) 387–400.

[22] H. H. Shah, M. Amin, F. Pepe, E. Mancusi, A. G. Fareed, Overview of environmental and economic viability of activated carbons derived from waste biomass for adsorptive water treatment applications, Environ. Sci. Pollut. Res., 32 (2025) 19084–19109.

[23] M. Hamood-ur-Rehman, M. Hussain, P. Akhter, F. Jamil, Versatile eco-friendly activated carbon–based green catalysts: energy and environmental applications, ChemBioEng Rev., 12 (2025) e70005.

[24] T. Khandaker, T. Islam, A. Nandi, M. A. A. M. Anik, M. S. Hossain, M. K. Hasan, M.S. Hossain, Biomass-derived carbon materials for sustainable energy applications: a comprehensive review, Sustain. Energy Fuels, 9 (2025) 693–723.

[25] R. Devi, V. Kumar, S. Kumar, M. Bulla, A. Jatrana, R. Rani, A. K. Mishra, P. Singh, Recent advancement in biomass-derived activated carbon for wastewater treatment, energy storage, and gas purification: a review, J. Mater. Sci., 58 (2023) 12119–12142.

[26] R. Chakraborty, K. Vilya, M. Pradhan, A. K. Nayak, Recent advancement of biomass-derived porous carbon based materials for energy and environmental remediation applications, J. Mater. Chem. A, 10 (2022) 6965–7005.

[27] B. Orero, F. Ntuli, T. Lekgoba, A. Ochieng, UV photodegradation of textile dyes using TiO_2–ZnO supported on banana peel activated carbon, Int. J. Environ. Sci. Technol., 20 (2023) 9537–9554.

[28] J. Gautam, A. M. Kale, J. Rawal, P. Varma, S. J. Lee, S. Y. Lee, S. J. Park, Biomass-derived carbon photocatalysts for organic pollutant degradation: strategies and perspectives, Carbon Neutralization, 5 (2026) e70109.

[29] Q. Zou, B. Wang, B. Gao, T. Jiang, Q. Feng, M. Chen, J. Zhang, X. Zhang, Roles and mechanisms of carbonaceous materials in advanced oxidation coupling processes for degradation of organic pollutants in wastewater: a review, Biochar, 5 (2023) 86.

[30] S. Noor, A. Ashar, M. B. Taj, Z. A. Bhutta, Advanced oxidation processes for remediation of persistent organic pollutants, in: Adv. Oxid. Process. Wastewater Treat., CRC Press (2022) 203–212.

[31] P. V. Nidheesh, C. Couras, A. V. Karim, H. Nadais, A review of integrated advanced oxidation processes and biological processes for organic pollutant removal, Chem. Eng. Commun., 209 (2022) 390–432.

[32] K. Byrappa, A. S. Dayananda, C. P. Sajan, B. Basavalingu, M. B. Shayan, K. Soga, M. Yoshimura, Hydrothermal preparation of ZnO:CNT and TiO_2:CNT composites and their photocatalytic applications, J. Mater. Sci., 43 (2008) 2348–2355.

[33] S. U. Jan, A. Ahmad, A. A. Khan, S. Melhi, I. Ahmad, G. Sun, C.-M. Chen, R. Ahmad, Removal of azo dye from aqueous solution by low-cost coal-derived activated carbon: adsorption kinetics, isotherms and DFT simulation, Environ. Sci. Pollut. Res., 28 (2021) 10234–10247.

[34] M. Kebir, R. Bourzami, N. Nasrallah, S. E. I. Lebouachera, F. Dergal, R. Ladji, L. Khezami, Pharmaceutical pollutants adsorption onto activated carbon: isotherm,

kinetic investigations and DFT modeling approaches, C. R. Chim., 25 (2022) 9–25.

[35] T. N. V. de Souza, S. M. L. de Carvalho, M. G. A. Vieira, M. G. C. da Silva, D. D. S. B. Brasil, Adsorption of basic dyes onto activated carbon: experimental and theoretical investigation using DFT-based descriptors, Appl. Surf. Sci., 448 (2018) 662–670.

[36] A. A. Al-Kahtani, S. M. Alshehri, M. Naushad, Ruksana, T. Ahamad, Fabrication of highly porous N/S doped carbon embedded with ZnS as highly efficient photocatalyst for degradation of bisphenol, Int. J. Biol. Macromol., 121 (2019) 415–423.

[37] Z. Heidarinejad, M. H. Dehghani, M. Heidari, G. Javedan, I. Ali, M. Sillanpää, Methods for preparation and activation of activated carbon: a review, Environ. Chem. Lett., 18 (2020) 393–415.

[38] M. A. Yahya, Z. Al-Qodah, C. W. Z. Ngah, Agricultural bio-waste materials as sustainable precursors for activated carbon production: a review, Renew. Sustain. Energy Rev., 46 (2015) 218–235.

[39] S. Liu, P. Qi, S. Xu, P. Jin, B. Li, W. Yu, B. Young, Insights into nitrogen-doped sulfur-existed carbonaceous material toward acetaminophen removal by peroxymonosulfate activation, J. Environ. Chem. Eng., 10 (2022) 107853.

[40] A. Maurya, Carbonaceous supports for Schiff base metal complexes: strategies for enhanced catalytic efficiency, iScience, (2026) in press.

[41] N. E. Williams, O. A. Oba, N. P. Aydinlik, Modification, production, and methods of KOH-activated carbon, ChemBioEng Rev., 9 (2022) 164–189.

[42] N. Samghouli, I. Bencheikh, K. Azoulay, S. Jansson, S. El Hajjaji, Mechanistic and reactional activation study of carbons for emerging pharmaceutical pollutant adsorption, Environ. Monit. Assess., 197 (2025) 259.

[43] S. Rong, L. Zhang, Z. Yue, Z. Song, W. Tang, X. Zhu, T. Wang, X. Zhou, S. Cheng, X. Xia, Directional introduction of pyridine nitrogen functional groups in activated carbon catalysts for hydrogen production: experimental and DFT calculation, Chem. Eng. J., 453 (2023) 139744.

[44] G. F. Jahromi, A. Ghahreman, Effect of surface modification with different acids on functional groups of AF-5 catalyst and its catalytic effect on atmospheric leaching of enargite, Colloids Interfaces, 3 (2019) 45.

[45] D. Cuhadaroglu, O. A. Uygun, Production and characterization of activated carbon from bituminous coal by chemical activation, Afr. J. Biotechnol., 7 (2008) 3703–3710.

[46] A. A. Tahmasebi, A. S. Beni, A. Azhdarpoor, Z. Moeini, Application of granular and biological activated carbon columns for removal of organochlorine and organophosphorus pesticides, J. Water Process Eng., 56 (2023) 104383.

[47] S. Singh, G. Tailor, C. Mehta, D. Das, Role of activated carbon and nanomaterials in removal of pesticides from contaminated water, in: Pesticide Removal Methods from Wastewater, Apple Academic Press (2025) 41–61.

[48] S. S. Ray, D. Sangeetha, R. Vijayaraghavan, Enhanced activity and reusability of ZnO-loaded magnetic activated carbon for removal of organic pollutants under sunlight, J. Chem. Pharm. Res., 7 (2015) 157–173.

[49] M. E. Gamal, H. A. Mousa, M. H. El-Naas, R. Zacharia, S. Judd, Bio-regeneration of activated carbon: a comprehensive review, Sep. Purif. Technol., 197 (2018) 345–359.

[50] Z. G. Zhao, Adsorption of phenylalanine from aqueous solution onto active carbon and silica gel, Chin. J. Chem., 10 (1992) 325–330.

[51] S. Bubanale, M. Shivashankar, History, method of production, structure and applications of activated carbon, Int. J. Eng. Res., 6 (2017).

[52] J. Biscoe, B. E. Warren, An X-ray study of carbon black, J. Appl. Phys., 13 (1942) 364–371.

[53] J. Saleem, U. B. Shahid, M. Hijab, H. Mackey, G. McKay, Production and applications of activated carbons as adsorbents from olive stones, Biomass Convers. Biorefin., (2019).

[54] F. Çeçen, Ö. Aktaş, Activated carbon for water and wastewater treatment, Wiley-VCH (2011).

[55] R. C. Bansal, M. Goyal, Activated carbon adsorption, CRC Press, Boca Raton (2005).

[56] H. Marsh, F. Rodríguez-Reinoso, Activated carbon, Elsevier (2006).

[57] J. Serafin, B. Dziejarski, Activated carbons—preparation, characterization and their application in CO_2 capture: a review, Environ. Sci. Pollut. Res., 31 (2024) 40008–40062.

[58] B. S. Girgis, S. S. Yunis, A. M. Soliman, Characteristics of activated carbon from peanut hulls in relation to preparation conditions, Mater. Lett., 57 (2002) 164–172.

[59] N. A. Rashidi, Y. H. Chai, I. S. Ismail, M. F. H. Othman, S. Yusup, Biomass as activated carbon precursor and potential in supercapacitor applications, Biomass Convers. Biorefin., 15 (2025) 29597–29611.

[60] M. Iwanow, T. Gärtner, V. Sieber, B. König, Activated carbon as catalyst support: precursors, preparation, modification and characterization, Beilstein J. Org. Chem., 16 (2020) 1188–1202.

[61] B. Cagnon, X. Py, A. Guillot, F. Stoeckli, G. Chambat, Contributions of hemicellulose, cellulose and lignin to the mass and porous properties of chars and steam-activated carbons, Bioresour. Technol., 100 (2009) 292–298.

[62] N. Muttil, S. Jagadeesan, A. Chanda, M. Duke, S. K. Singh, Production, types, and applications of activated carbon derived from waste tyres: an overview, Appl. Sci., 13 (2022) 257.

[63] A. Chakraborty, J. Panda, A. K. Mishra, S. Sivakumar, L. V. Srinivasan, A. Nongbet, S. S. Mohanty, Jackfruit waste for sustainable biorefinery products: a step towards bio-economic advancement, Biomass Convers. Biorefin., 15 (2025) 9801–9823.

[64] A. R. Monteiro, A. P. Battisti, G. A. Valencia, C. J. de Andrade, Production of high-added-value bioproducts from non-conventional biomasses: an overview, Biomass, 3 (2023) 123–137.

[65] J. Serafin, B. Dziejarski, Activated carbons—preparation, characterization and their application in CO_2 capture: a review, Environ. Sci. Pollut. Res., 31 (2024) 40008–40062.

[66] N. B. Amari, Master's thesis, University Sains Malaysia (2008).

[67] N. Radenahmad, A. T. Azad, M. Saghir, J. Taweekun, M. S. A. Bakar, M. S. Reza, A. K. Azad, A review on biomass-derived syngas for SOFC-based combined heat and power applications, Renew. Sustain. Energy Rev., 119 (2020) 109560.

[68] A. U. Rajapaksha, M. Vithanage, M. Ahmad, D. C. Seo, J. S. Cho, S. E. Lee, S. S. Lee, Y. S. Ok, Enhanced sulfamethazine removal by steam-activated invasive plant-derived biochar, J. Hazard. Mater., 290 (2015) 43–50.

[69] J. Pallarés, A. González-Cencerrado, I. Arauzo, Production and characterization of activated carbon from barley straw by physical activation with carbon dioxide and steam, Biomass Bioenergy, 115 (2018) 64–73.

[70] N. Byamba-Ochir, W. G. Shim, M. S. Balathanigaimani, H. Moon, Highly porous activated carbons from Mongolian anthracite by direct NaOH activation, Appl. Surf. Sci., 379 (2016) 331–337.

[71] W. Ao, J. Fu, X. Mao, Q. Kang, C. Ran, Y. Liu, H. Zhang, Z. Gao, J. Li, G. Liu, J. Dai, Microwave-assisted preparation of activated carbon from biomass: a review, Renew. Sustain. Energy Rev., 92 (2018) 958–979.

[72] G. Jolly, L. Dupont, M. Aplincourt, J. Lambert, Improved Cu and Zn sorption on oxidized wheat lignocellulose, Environ. Chem. Lett., 4 (2006) 219–223.

[73] C. Pongener, P. Bhomick, S. U. Bora, R. L. Goswamee, A. Supong, D. Sinha, Sand-supported bio-adsorbent column of activated carbon for removal of coliform bacteria and Escherichia coli from water, Int. J. Environ. Sci. Technol., 14 (2017) 1897–1904.

[74] T. Kokulnathan, B. Sriram, S. Pandiyarajan, S. Ramanathan, T. Sakthi Priya, Introduction to biowaste-derived materials: synthesis, characterization, and properties, in: Biomass-Derived Carbon Materials: Production and Applications (2022) 27–61.

[75] P. Saha, M. Z. Islam, S. S. Shah, M. N. Shaikh, T. Maiyalagan, M. A. Aziz, A. S. Ahammad, Harnessing marine biomass-derived carbon for electrochemical energy storage, Battery Energy, 4 (2025) e20240055.

[76] B. Zhang, Y. Jiang, R. Balasubramanian, Synthesis, formation mechanisms and applications of biomass-derived carbonaceous materials: a critical review, J. Mater. Chem. A, 9 (2021) 24759–24802.

[77] H. E. P. Santana, M. Jesus, J. Santos, A. C. Rodrigues, P. Pires, D. S. Ruzene, I. P. Silva, D. P. Silva, Lignocellulosic biomass gasification: perspectives, challenges, and methods for tar elimination, Sustainability, 17 (2025) 1888.

[78] Y. Gao, Q. Yue, B. Gao, A. Li, Insight into activated carbon from different chemical activating agents: a review, Sci. Total Environ., 746 (2020) 141094.

[79] I. Okman, S. Karagöz, T. Tay, M. Erdem, Activated carbons from grape seeds by chemical activation with potassium carbonate and potassium hydroxide, Appl. Surf. Sci., 293 (2014) 138–142.

[80] F. Rodríguez-Reinoso, M. Molina-Sabio, Activated carbons from lignocellulosic materials by chemical and/or physical activation: an overview, Carbon, 30 (1992) 1111–1118.

[81] M. I. Din, S. Ashraf, A. Intisar, Comparative study of different activation treatments for the preparation of activated carbon: a mini-review, Sci. Prog., 100 (2017) 299–312.

[82] J. Wang, S. Kaskel, KOH activation of carbon-based materials for energy storage, J. Mater. Chem., 22 (2012) 23710–23725.

[83] G. Singh, K. S. Lakhi, I. Y. Kim, P. Srivastava, R. Naidu, A. Vinu, Synthesis of activated mesoporous biocarbons with extremely high surface area for high-pressure CO_2 adsorption, ACS Appl. Mater. Interfaces, 9 (2017) 29782–29793.

[84] B. Li, J. Hu, H. Xiong, Y. Xiao, Application and properties of microporous carbons activated by $ZnCl_2$: adsorption behavior and activation mechanism, ACS Omega, 5 (2020) 9398–9407.

[85] G. Chu, J. Zhao, Y. Huang, D. Zhou, Y. Liu, M. Wu, H. Peng, Q. Zhao, B. Pan, C. E. W. Steinberg, Phosphoric acid pretreatment enhances specific surface area of biochars by micropore generation, Environ. Pollut., 240 (2018) 1–9.

[86] R. L. Tseng, S. K. Tseng, F. C. Wu, C. C. Hu, C. C. Wang, Effects of micropore development on physicochemical properties of KOH-activated carbons, J. Chin. Inst. Chem. Eng., 39 (2008) 37–47.

[87] Y. Li, J. Mei, L. Wu, Q. Xu, Z. Li, Ultrahigh surface area hierarchical porous carbon derived from biomass via new KOH activation strategy for supercapacitors, Int. J. Hydrog. Energy, 49 (2024) 67–80.

[88] Z. Zhang, C. Jiang, D. Li, Y. Lei, H. Yao, G. Zhou, K. Wang, Micro–mesoporous activated carbon possessing large surface area and ultra-high pore volume for VOC adsorption, Carbon, 170 (2020) 567–579.

[89] L. Giraldo, J. C. Moreno-Piraján, Synthesis of mesoporous activated carbon from coffee waste and its application for adsorption of zinc and mercury ions, E-J. Chem., 9 (2012) 938–948.

[90] T. Di, Y. Xia, B. Pei, T. Zhu, T. Zhao, T. Li, L. Li, Preparation of porous carbon from hyper-cross-linked asphalt/coal tar and its high desulfurization performance, Langmuir, 36 (2020) 11117–11124.

[91] G. Singh, I. Y. Kim, K. S. Lakhi, P. Srivastava, R. Naidu, A. Vinu, Single-step synthesis of activated biocarbons with high surface area and excellent CO_2 adsorption capacity, Carbon, 116 (2017) 448–455.

[92] G. D. Akpen, I.L. Nwaogazie, T.G. Leton, Optimum conditions for color removal from wastewater using mango seed shell-based activated carbon, Indian J. Sci. Technol., 4 (2011) 890–894.

[93] H. Sayılı, F. Güzel, Y. Önal, Conversion of grape industrial waste to activated carbon and its performance in cationic and anionic dye adsorption, J. Clean. Prod., 93 (2015) 84–93.

[94] S. Timur, I. C. Kantarli, E. Ikizoglu, J. Yanik, Preparation of activated carbons from oregano stalks by chemical activation, Energy Fuels, 20 (2006) 2636–2641.

[95] A. Kumar, H. M. Jena, High surface area microporous activated carbons prepared from fox nut (*Euryale ferox*) shell by $ZnCl_2$ activation, Appl. Surf. Sci., 356 (2015) 753–761.

[96] S. Uçar, M. Erdem, T. Tay, S. Karagöz, Preparation and characterization of activated carbon produced from pomegranate seeds by $ZnCl_2$ activation, Appl. Surf. Sci., 255 (2009) 8890–8896.

[97] G. A. Adebisi, Z. Z. Chowdhury, P. A. Alaba, Equilibrium, kinetic and thermodynamic studies of lead and zinc ion adsorption onto palm oil mill effluent-derived activated carbon, J. Clean. Prod., 148 (2017) 958–968.

[98] Q. Liang, Y. Liu, M. Chen, L. Ma, B. Yang, L. Li, Q. Liu, Optimized preparation of activated carbon from coconut shell and municipal sludge, Mater. Chem. Phys., 241 (2020) 122327.

[99] A. Nayak, B. Bhushan, V. Gupta, P. Sharma, Chemically activated carbon from lignocellulosic wastes for heavy metal remediation: effect of activation conditions, J. Colloid Interface Sci., 493 (2017) 228–240.

[100] H. Treviño-Cordero, L. G. Juárez-Aguilar, D. I. Mendoza-Castillo, V. Hernández-Montoya, A. Bonilla-Petriciolet, M. A. Montes-Morán, Synthesis and adsorption properties of activated carbons from Prunus domestica and Jacaranda mimosifolia biomass for removal of heavy metals and dyes, Ind. Crops Prod., 42 (2013) 315–323.

[101] R. H. Gumus, I. Okpeku, Production and characterization of activated carbon from snail shell waste (Helix pomatia), Adv. Chem. Eng. Sci., 5 (2015) 51–61.

[102] A. Dobashi, Y. Shu, T. Hasegawa, J. Maruyama, S. Iwasaki, Y. Shen, H. Uyama, Preparation of activated carbon by KOH activation from Amygdalus pedunculata shell for electric double-layer capacitor application, Electrochemistry, 83 (2015) 351–353.

[103] C. Nieto-Draghi, G. Fayet, B. Creton, X. Rozanska, P. Rotureau, J.-C. de Hemptinne, P. Ungerer, B. Rousseau, C. Adamo, A general guidebook for theoretical prediction of physicochemical properties of chemicals for regulatory purposes, Chem. Rev., 115 (2015) 13093–13164.

[104] H. Wang, R. Xie, J. Zhang, J. Zhao, Preparation and characterization of distillers' grain-based activated carbon as low-cost methylene blue adsorbent: mass transfer and equilibrium modeling, Adv. Powder Technol., 29 (2018) 27–35.

[105] M. M. Nasser, Kinetics of basic dye removal using palm fruit bunch, Adsorp. Sci. Technol., 15 (1997) 609–617.

[106] M. Zbair, K. Ainassaari, A. Drif, S. Ojala, M. Bottlinger, M. Pirilä, R. L. Keiski, M. Bensitel, R. Brahmi, Preparation and characterization of activated carbon from argan nut shell for bisphenol A removal, Environ. Sci. Pollut. Res., 25 (2018) 1869–1882.

[107] A. Supong, P. C. Bhomick, R. Karmaker, S. L. Ezung, L. Jamir, U. B. Sinha, D. Sinha, Experimental and theoretical insight into adsorption of phenol and 2,4-dinitrophenol onto *Tithonia diversifolia* activated carbon, Appl. Surf. Sci., 529 (2020) 147046.

[108] K. M. S. Khalil, M. Khairy, O. A. S. Allam, M. K. Khalil, Formation of improved activated carbons from sugarcane bagasse for adsorption of phenolic pollutants, Int. J. Environ. Sci. Technol., 19 (2022) 3103–3116.

[109] P. C. Bhomick, A. Supong, M. Baruah, C. Pongener, Pine cone biomass as precursor for activated biocarbon for anionic dye adsorption: isotherm, kinetic, thermodynamic and regeneration studies, Sustain. Chem. Pharm., 10 (2018) 41–49.

[110] M. M. Nourouzi, T. G. Chuah, T. S. Y. Choong, Adsorption of glyphosate onto activated carbon derived from waste newspaper, Desalin. Water Treat., 24 (2010) 321–326.

[111] J. Dai, J. Yuan, Physisorption to chemisorption transition of NO_2 on graphene induced by substrate and van der Waals forces: a first-principles study, Chem. Phys., 405 (2012) 161–166.

[112] I. I. Salame, T. J. Bandosz, Role of surface chemistry in adsorption of phenol on activated carbons, J. Colloid Interface Sci., 264 (2003) 307–312.

[113] M. Faraj, M. Erhayem, Langmuir, Freundlich, Temkin and Dubinin–Radushkevich isotherm studies of methylene blue adsorption onto Morus nigra roots powder, J. Pure Appl. Sci., 17 (2018).

[114] T. A. Saleh, Isotherm models of adsorption processes on adsorbents and nanoadsorbents, in: Interface Sci. Technol., 34 (2022) 99–126.

[115] É. C. Lima, M. A. Adebayo, F. M. Machado, Kinetic and equilibrium models of adsorption, in: Carbon Nanomaterials as Adsorbents for Environmental and Biological Applications, Springer (2015) 33–69.

[116] E. D. Revellame, D. L. Fortela, W. Sharp, R. Hernandez, M. E. Zappi, Adsorption kinetic modeling using pseudo-first- and pseudo-second-order rate laws: a review, Cleaner Eng. Technol., 1 (2020) 100032.

[117] L. Largitte, R. J. C. E. R. Pasquier, A review of adsorption kinetic models and their application to lead adsorption by activated carbon, Chem. Eng. Res. Des., 109 (2016) 495–504.

[118] W. Konicki, M. Aleksandrzak, E. Mijowska, Equilibrium, kinetic and thermodynamic studies on adsorption of cationic dyes using graphene oxide, Chem. Eng. Res. Des., 123 (2017) 35–49.

[119] S. W. Verbruggen, TiO_2 photocatalysis for gas-phase pollutant degradation: morphological design to plasmonic enhancement, J. Photochem. Photobiol. C, 24 (2015) 64–82.

[120] D. Pathania, A. Sharma, S. Kumar, A. Kumar, Bio-synthesized Cu–ZnO heteronanostructure for catalytic degradation of chlorpyrifos under solar illumination, Chemosphere, 277 (2021) 130315.

[121] A. Buthiyappan, A. R. Abdul Aziz, W. M. A. W. Daud, Recent advances in catalytic advanced oxidation processes for textile effluent treatment, Rev. Chem. Eng., 32 (2016) 1–47.

[122] L. Lin, W. Jiang, L. Chen, P. Xu, H. Wang, Treatment of produced water with photocatalysis: advances and prospects, Catalysts, 10 (2020) 1–18.

[123] A. Kumar, G. Pandey, Factors affecting photocatalytic degradation of hazardous materials: a review, Mater. Sci. Eng. Int. J., 1 (2017) 106–114.

[124] M. Muruganandham, R. P. S. Suri, S. Jafari, M. Sillanpää, G. Lee, J. J. Wu, M. Swaminathan, Recent developments in homogeneous advanced oxidation processes, Int. J. Photoenergy, 2014 (2014) 1–21.

[125] D. D. Thongam, H. Chaturvedi, Advances in nanomaterials for heterogeneous photocatalysis, Nano Express, 2 (2021) 012005.

[126] K. H. H. Aziz, F. S. Mustafa, K. M. Omer, S. Hama, R. F. Hamarawf, K. O. Rahman, Heavy metal pollution in aquatic environments: low-cost removal approaches, RSC Adv., 13 (2023) 17595–17610.

[127] A. O. Ibhadon, P. Fitzpatrick, Heterogeneous photocatalysis: recent advances and applications, Catalysts, 3 (2013) 189–218.

[128] M. M. Mahlambi, C. J. Ngila, B. B. Mamba, Environmental photocatalytic degradation using TiO_2 nanoparticles: a review, J. Nanomater., 2015 (2015) 1–29.

[129] W. Wang, J. C. Yu, P. K. Wong, Photocatalysts for solar-induced water disinfection: developments and opportunities, Mater. Sci. Forum, 734 (2013) 63–89.

[130] X. Xiao, S. Tu, M. Lu, H. Zhong, C. Zheng, X. Zuo, J. Nan, Reaction mechanism of photocatalytic degradation of organic contaminants: semiconductor photo-induced electrocatalysis, Appl. Catal. B, 198 (2016) 124–132.

[131] W. H. Glaze, J.W. Kang, Advanced oxidation processes: kinetic model for oxidation with ozone and hydrogen peroxide, Ind. Eng. Chem. Res., 28 (1989) 1573–1580.

[132] J. C. Colmenares, R. Luque, Heterogeneous photocatalytic nanomaterials: prospects and challenges, Chem. Soc. Rev., 43 (2014) 765–778.

[133] R. Daghrir, P. Drogui, D. Robert, Modified TiO_2 for environmental photocatalytic applications: a review, Ind. Eng. Chem. Res., 52 (2013) 3581–3599.

[134] E. M. Cuerda-Correa, M. F. Alexandre-Franco, C. Fernández-González, Advanced oxidation processes for antibiotic removal from water, Water, 12 (2020) 1–51.

[135] L. A. C. Santiago, A. L. M. Salazar, J. V. Moreno, O. R. Hernández, B. P. Martínez, Fe–Zn–Ti systems as photocatalysts for hydroxyl radical production, Int. J. Hydrog. Energy, 47 (2022) 31888–31902.

[136] L. Yang, H. Zhou, T. Fan, D. Zhang, Semiconductor photocatalysts for water oxidation: status and challenges, Phys. Chem. Chem. Phys., 16 (2014) 6810–6826.

[137] Q. Wang, K. Domen, Particulate photocatalysts for light-driven water splitting: mechanisms and design strategies, Chem. Rev., 120 (2019) 919–985.

[138] C. Han, M. Yang, B. Weng, Y.J. Xu, Improving photocatalytic activity of ZnO by carbon coupling, Phys. Chem. Chem. Phys., 16 (2014) 16891–16903.

[139] X. Gu, C. Li, S. Yuan, M. Ma, Y. Qiang, J. Zhu, ZnO-based heterojunctions for environmental photocatalysis, Nanotechnology, 27 (2016) 1–21.

[140] C. B. Ong, L. Y. Ng, A. W. Mohammad, ZnO nanoparticles as solar photocatalysts: synthesis and applications, Renew. Sustain. Energy Rev., 81 (2018) 536–551.

[141] S. Agarwal, L. K. Jangir, K. S. Rathore, M. Kumar, K. Awasthi, Morphology-dependent structural and optical properties of ZnO nanostructures, Appl. Phys. A, 125 (2019) 553.

[142] S. S. Kumar, P. Venkateswarlu, V. R. Rao, G. N. Rao, Synthesis and optical properties of zinc oxide nanoparticles, Int. Nano Lett., 3 (2013) 1–6.

[143] S. Mustapha, M. M. Ndamitso, A. S. Abdulkareem, J. O. Tijani, D. T. Shuaib, A. O. Ajala, A. K. Mohammed, TiO_2 and ZnO nanoparticles immobilized on clay for wastewater treatment: a review, Appl. Water Sci., 10 (2020) 1–36.

[144] Y. Zhai, Y. Chang, A. Tang, K. Lu, Photostability in organic solar cells: mechanisms and strategies, J. Mater. Chem. A, (2025).

[145] R. D. C. Soltani, G. S. Khoramabadi, H. Godini, Z. Noorimotlagh, ZnO/SiO_2 nanocomposite for photocatalytic degradation of textile dye, Desalin. Water Treat., 56 (2015) 2551–2558.

[146] R. Medhi, M. D. Marquez, T. R. Lee, Visible-light-active doped metal oxide nanoparticles: synthesis and applications, ACS Appl. Nano Mater., 3 (2020) 6156–6185.

[147] P. Singh, R. Kumar, R. K. Singh, Transition metal-doped ZnO nanoparticles and applications, Ind. Eng. Chem. Res., 58 (2019) 17130–17163.

[148] P. Biswas, R. Bandyopadhyaya, Water disinfection using silver nanoparticle-impregnated activated carbon, Water Res., (2016).

[149] K. Qi, B. Cheng, J. Yu, W. Ho, Improvement of photocatalytic and antibacterial activities of ZnO, J. Alloys Compd., 727 (2017) 792–820.

[150] M. Baruah, A. Supong, P. Chandra, B. Rituparna, K. Chubaakum, Batch sorption–photodegradation using TiO_2/activated carbon nanocomposite, Nanotechnol. Environ. Eng., 3 (2020) 1–13.

[151] M. J. Sweetman, S. May, N. Mebberson, P. Pendleton, K. Vasilev, S. E. Plush, J. D. Hayball, Activated carbon, carbon nanotubes and graphene for water purification, J. Carbon Res., 3 (2017) 1–29.

[152] A. Mohammad-Khah, R. Ansari, Activated charcoal: preparation, characterization and applications, Int. J. Chem. Tech. Res., 1 (2009) 859–864.

[153] S. Alhan, M. Nehra, N. Dilbaghi, N. K. Singhal, K. H. Kim, S. Kumar, ZnO@activated carbon nanocomposites for Cd^{2+} removal, Environ. Res., 173 (2019) 411–418.

[154] J. Ge, Y. Zhang, S. J. Park, Carbonaceous photocatalysts with enhanced performances: a mini review, Materials, 12 (2019) 1–26.

[155] F. Khan, M. S. Kahan, S. Kamal, M. Arshad, S. I. Ahmad, S. A. A. Nami, Graphene oxide-based nanocomposites for photodegradation of dyes, J. Mater. Chem. C, 8 (2020) 15940–15955.

[156] O. Benton, S. Apollo, B. Naidoo, A. Ochieng, Photodegradation of molasses wastewater using TiO_2–ZnO nanohybrid on activated carbon, Chem. Eng. Commun., 203 (2016) 1443–1454.

[157] P. Kumar, S. Kaushal, S. Kumar, J. Dalal, K. M. Batoo, D. S. Ahlawat, Recent advancements in pure and doped zinc oxide nanostructures for UV photodetector applications, Physica B, (2025) 417177.

[158] M. A. M. Adnan, N. M. Julkapli, S. B. A. Hamid, ZnO hybrid photocatalysts for water pollutant degradation, Rev. Inorg. Chem., 36 (2016) 77–104.

[159] Y. Liu, L. Sun, J. Wu, T. Fang, R. Cai, A. Wei, ZnO/Fe_2O_3 nanotube composites: preparation and photocatalytic activity, Mater. Sci. Eng. B, 194 (2015) 9–13.

[160] A. I. Vaizoğullar, ZnO/ZrO_2 composites: synthesis and photocatalytic degradation of oxytetracycline, Mater. Technol., 34 (2019) 433–443.

[161] J. Shen, A. Shi, J. Lu, X. Lu, H. Zhang, Z. Jiang, Cu-doped ZnO/CoFe-LDH composite for bisphenol A degradation, Environ. Pollut., 323 (2023) 121186.

[162] P. H. Hsiao, T. C. Li and C. Y. Chen, ZnO/Cu_2O/Si nanowire arrays as ternary heterostructure-based photocatalysts with enhanced photodegradation performances, Nanoscale Res. Lett., 2019, **14**, 244.

[163] Y. Yuan, G. F. Huang, W. Y. Hu, D. N. Xiong, B. X. Zhou, S. Chang and W. Q. Huang, Construction of g-C_3N_4/CeO_2/ZnO ternary photocatalysts with enhanced photocatalytic performance, J. Phys. Chem. Solids, 2017, **106**, 1–9.

[164] A. B. Hamzat, A. A. Adegbite, T. O. Olabiyi, M. A. Lere-Aliu, A. Y. Oriji, Environmental effects of phenolic compound additives, in: Environ. Footprint Bioplastic Additives, CRC Press (2025) 192–207.

[165] M. Mukherjee, T. Chakraborty, S. Banerjee, S. Pandit, Biodegradation of phenol and phenolic compounds, in: Adv. Bio-syst. Technol. Wastewater Treat., Springer (2024) 207–224.

[166] D. J. Bhuyan, A. Basu, Phenolic compounds: potential health benefits and toxicity, in: Utilisation of Bioactive Compounds from Agricultural and Food Production Waste, CRC Press (2017) 27–59.

[167] Q. Yin, L. Si, R. Wang, Z. Zhao, H. Li, Z. Wen, DFT study on functional groups of carbonaceous surface for ammonium adsorption, Chemosphere, 287 (2022) 132294.

[168] S. L. Ezung, M. Baruah, A. Supong, S. Sharma, D. Sinha, Experimental and theoretical insight into adsorption of 2,4-dichlorophenol on bamboo sheath activated carbon, Sustain. Chem. Pharm., 26 (2022) 100643.

[169] S. Kumar, S. Sharma, R. Karmaker, D. Sinha, DFT study on platinum group doped graphene, Mater. Today Commun., 26 (2021) 101755.

[170] P. Deglmann, A. Schäfer, C. Lennartz, Application of quantum calculations in the chemical industry, Int. J. Quantum Chem., 115 (2015) 107–136.

[171] A. Latif, A. Latif, M. Mohsin, I. A. Bhatti, Density functional theory for nanomaterials: structural and spectroscopic applications, J. Mol. Model., 31 (2025) 211.

[172] X. Gonze, B. Amadon, P.-M. Anglade, J.-M. Beuken, F. Bottin, P. Boulanger, F. Bruneval, ABINIT: first-principles approach to material properties, Comput. Phys. Commun., 180 (2009) 2582–2615.

[173] Q. Cui, M. Elstner, Density functional tight binding: semi-empirical methods in ab initio era, Phys. Chem. Chem. Phys., 16 (2014) 14368–14377.

[174] A. Jain, Y. Shin, K. A. Persson, Computational predictions of energy materials using DFT, Nat. Rev. Mater., 1 (2016) 1–13.

[175] P. He, X. Zhang, X. Peng, X. Jiang, J. Wu, N. Chen, Interaction of elemental mercury with defective carbon cluster, J. Hazard. Mater., 300 (2015) 289–297.

[176] C. Lee, W. Yang, R. G. Parr, Development of the Colle–Salvetti correlation-energy functional, Phys. Rev. B, 37 (1988) 785–789.

[177] M. Abu Radia, S. A. Saafan, Overview of density functional theory for beginners in computational materials science, Egypt. J. Solids, 47 (2025) 110–138.

CHAPTER 2

MATERIALS AND METHODS

This chapter describes the materials and procedures utilized for the synthesis, characterisation, and evaluation of activated carbon and its nanocomposites for wastewater treatment applications. Detailed analytical methods were employed to investigate structural, morphological, surface, and optical characteristics. Batch adsorption test were performed to assess pollutant removal efficacy, and the experimental results were evaluated utilizing isotherm, kinetic, and thermodynamic models to understand the adsorption mechanism. Experiments on photocatalytic degradation were conducted to evaluate catalytic efficacy and mineralization efficiency. Furthermore, density functional theory (DFT) simulations were utilized to elucidate the interaction processes and its chemical reactivity between the adsorbent surface and target contaminants.

2.1 Chemicals and reagents

Chemicals including zinc acetate dihydrate ($Zn(CH_3COO)_2 \cdot H_2O$), zirconium dioxide (ZrO_2), cobalt nitrate hexahydrate ($Co(NO_3)_2 \cdot 6H_2O$), zinc oxide (ZnO), potassium hydroxide (KOH), sodium hydroxide (NaOH), hydrochloric acid (HCl), and ethanol were utilized in the experimental work. Phenolic compounds such as 2-chlorophenol (ClC_6H_4OH), catechol, and resorcinol, 4-nitrophenol ($C_6H_5NO_3$) and bisphenol A were used for adsorption and degradation studies. All the chemicals and reagents utilized in the present work are of analytical grade and used without further purification. All testing experiments were conducted using double distilled water (DDW) from the Milli-Q system (18.2 MΩ cm).

2.2 Raw precursor for the preparation of activated carbon

The raw materials employed in the current investigation were chosen based on their availability, abundance, and environmental safety. Croton caudatus, a locally available biomass at Nagaland University (26° 13′29.60″ N | 94° 28′ 35.0″ E), India, was used as a precursor for the synthesis of activated carbon. The collected biomass was chopped into small pieces, extensively cleaned to eliminate any remaining impurities, and dried in a hot air oven at 105 °C for 24 hours. The dried biomass was then chemically activated to produce activated carbon. The next section describes in detail the biomass materials utilized in this investigation.

Croton caudatus

Croton caudatus (*Euphorbiaceae* family) is a scandent shrub found across tropical and subtropical Asia and Australia, including southern China, the Indian subcontinent, and Southeast Asia. The plant develops as a climbing shrub with long, flexible stems and is usually found along forest edges and in disturbed areas. *Croton caudatus* is a valuable and renewable biomass resource because to its widespread availability and rapid growth. The plant has been recognized for its traditional medicinal and utilitarian uses, but it is still mostly discarded for material applications [1,2]. *Croton caudatus* was chosen as an appropriate raw precursor for the synthesis of activated carbon in the present study due to its lignocellulosic content, local availability, and eco-friendliness (Figure 2.1).

Figure 2.1. Picture showing *Croton caudatus* plant.

2.3 Synthesis of activated carbon

In the current work, activated carbon derived from biomass material was produced by a two-step activation procedure. The raw precursor was first carbonized, then chemically activated with the KOH activating agent. This method results in porous material with increased yield and greater surface area. The production of activated carbon was labeled as CCAC (*Croton caudatus* activated carbon) and is described thoroughly in Chapters 3.

2.4 Characterisation of CCAC

Characterization of activated carbon is a crucial step prior to its application in any treatment process. The physical and chemical characteristics of the produced activated carbon were investigated comprehensively in this work utilizing a variety of analytical methods. Proximate analysis, which included the evaluation of moisture content, ash content, volatile matter, and fixed carbon, followed the American Society for Testing and Materials recommendations [3]. Furthermore, ultimate analysis was carried out to identify the elemental composition of the activated carbon.

(i) Proximate analysis

The proximate analysis involves heating activated carbon at different temperatures to measure moisture, volatile matter, fixed carbon, and ash content. The experimental protocols are outlined below.

(ii) Moisture content

A silica crucible was pre-heated at 110 °C for 1 hour, then cooled to room temperature in a desiccator. The activated carbon sample was then inserted in the pre-weighed silica crucible and dried at a higher temperature periodically. The drying sample was reweighed at 10-minute intervals until a consistent weight was achieved. Moisture content is computed using the Equation (2.1), which is the ratio of change in original weight expressed in percentage [3].

$$\text{Moisture content (\%)} = \frac{(C-D)}{(C-B)} \text{ X } 100 \qquad (2.1)$$

where B= crucible mass (g), C= crucible mass with original sample (g) and D = crucible mass after sample heating (g).

(iii) Ash content

A silica crucible was preheated in a muffle furnace at 650 ℃ for 1 hour before cooling to ambient temperature in a desiccator. The pre-weighed crucible with 1g of activated carbon was then heated in the furnace at 650 ℃. The sample was weighed every three hours until a consistent weight was reached [4].

$$\text{Ash content (\%)} = \frac{(D-B)}{(C-B)} \text{ X } 100 \quad (2.2)$$

(iv) Volatile matter

A silica crucible initially overheated at 900 °C in a muffle furnace for 10 minutes before cooling to room temperature in a desiccator. After that, around 1 g of activated carbon was added to the preheated crucible, and it was partially covered and heated to 900 °C for 10 min. Once heated, the sample-containing crucible was taken out and left to cool for 1 hour in a desiccator [3]. The volatile matter content was determined using the Equation (2.3).

$$\text{Volatile matter (\%)} = \frac{(C-D)}{(C-B)} \text{ X } 100 \quad (2.3)$$

(v) Fixed carbon

The fixed carbon content, indicated as a percentage, was determined by subtracting the total percentages of volatile matter, moisture content, and ash content from 100 %. The fixed carbon of the activated carbon was calculated using the equation below.

Fixed Carbon (%) = 100 – (volatile matter % + ash content % + moisture content %) (2.4)

(vi) Ultimate analysis

The carbon, hydrogen, nitrogen, and oxygen content of the activated carbon sample was determined *via* ultimate analysis. CHNS/O elemental analyzer was used in the current investigation to study the prepared sample.

2.5 Description of pollutants considered for adsorption studies

The subsequent section presents a concise overview of the pollutants examined in this study, namely 2-chlorophenol, catechol and resorcinol.

(i) 2-chlorophenol

Chlorophenols (CPs) are a kind of phenolic derivatives in which chlorine atom are covalently substituted in the ortho, meta, or para positions of the phenol ring. 2CPs are widely employed in a variety of applications, including pesticide and dye manufacture, water disinfection, preservative production, petrochemical industries, agriculture, biocides, cosmetics and pharmaceuticals [5]. The presence of 2CPs in water is associated with a foul odor, an unpleasant taste, and a deterioration in drinking water quality [6]. 2CPs have garnered substantial interest in recent years due to their low biodegradability and evident poisonous, carcinogenic, and mutagenic qualities. Once discharged into the environment, these chemicals frequently accumulate in wastewater, surface water, and groundwater, posing significant threats to human health and the environment even at low doses below 0.1 μg/L [7].

Figure 2.2. Chemical structure of 2-chlorophenol.

Furthermore, human exposure to such pollutant can cause long-term health problems, such as gastrointestinal diseases (e.g., diarrhea), nervous system damage, aberrant urine coloring, increased respiration rate, and sensations like nausea and vomiting. The toxicity of chlorophenols rises with the level of chlorination. Although these chemicals have important biocidal properties, they become extremely toxic at large doses [8]. As a result, the successful removal of 2CPs from wastewater has remained a persistent difficulty, emphasizing the need of developing efficient treatment strategies to eradicate these chemicals before they enter the aquatic environment. The structural representation of 2CP is presented in Figure 2.2.

(ii) Catechol and resorcinol

Catechol (CT) and resorcinol (RS) are dihydroxybenzene isomers that are commonly used in industrial solvents [9]. Catechol (1,2-dihydroxybenzene) is utilized extensively in the production of photographic and fur dyes, as a polymerization inhibitor, antioxidant, and food ingredient. In addition, catechol is often used in chemical labs to

detect and quantify different metal ions [10]. Resorcinol (1,3-dihydroxybenzene) is widely utilized in the production of synthetic fibers, resins, polymers, and colors [11]. These compounds are frequently detected in effluents released by industries such as petroleum refineries, cosmetics, textile processing, and pharmaceutical manufacture [12]. Following their discharge into the environment, they are regularly found in soil, surface water, and groundwater, posing serious threats to human health and ecological systems.

(a) Catechol **(b) Resorcinol**

Figure 2.3. Chemical structure of catechol and resorcinol.

They are categorized as pollutants because of their limited biodegradability, high toxicity, increased oxygen consumption, and carcinogenic potential, even at low levels. Furthermore, persistent exposure to these pollutants can cause eye and skin irritation, gastrointestinal diseases such as diarrhea and stomach discomfort, pulmonary edema, DNA damage and vascular collapse. CT is more hazardous than RS, and both substances are regarded more toxic than phenol because they can alter erythrocyte function at low doses [13]. Consequently, there is a need to develop simple and economically viable strategies for the effective monitoring and removal of these contaminants from the environment. The molecular structure of catechol and resorcinol are depicted in Figure 2.3.

2.6 Batch adsorption experiments for adsorption studies

Batch adsorption tests were carried out to determine the removal of 2-chlorophenol, and catechol and resorcinol from aqueous solutions. In each experiment, a desired amount of adsorbent was introduced to a 250 mL Erlenmeyer conical flask containing a specified volume of phenolic solution (50 mL) at varying initial concentration. The pH of the solution was adjusted by adding 0.1M of NaOH or HCl. The mixture was then stirred on a rotary shaker at 180 rpm for a set amount of time under regulated temperature. Following adsorption, the solutions were filtered and the residual phenolic concentrations were measured with a UV-visible spectrophotometer (Model: Lambda 35, PerkinElmer) at the corresponding wavelengths. All tests were conducted in triplicate to ensure data quality. The adsorption capacity (q_e) and removal efficiency (R %) of phenolic compounds were calculated using the following equations.

$$\% \text{ Removal} = 100 \times \frac{C_i - C_e}{C_I} \quad (2.5)$$

$$q_e = V \times \frac{C_i - C_e}{M_s} \quad (2.6)$$

where, the initial and equilibrium concentrations of adsorbate in aqueous phase are expressed by C_i and C_e (mg/L) respectively, volume of the solution by V (L), and the mass of CCAC by M_s (g).

A detailed discussion of batch mode adsorption experiments for the removal of phenolic compounds is provided in Chapters 3 and 4.

2.7 Description of adsorption models

Adsorption models are essential to evaluate adsorbent performance, offering insights into removal efficiency, pollutant absorption rates, and the thermodynamic properties of the adsorption system [14]. Moreover, these models enhance comprehension of the fundamental adsorption mechanisms. Therefore, the experimental adsorption data were analyzed in the present study using a variety of established mathematical models and equations to understand the adsorption behavior. The isotherm, kinetic, and thermodynamic models utilized in this study are outlined in the subsequent sections.

2.7.1 Isotherm models

Adsorption isotherms are vital for understanding the interaction of pollutants and adsorbent surfaces, and they play an important role in improving adsorption system design for contaminant removal from aqueous medium [15]. These models offer important insights into the surface properties of the adsorbent, the nature of the adsorption process, and the affinity between the adsorbent and adsorbate. An adsorption isotherm highlights the correlation between the equilibrium quantity of adsorbate per unit mass of adsorbent (q_e) and the equilibrium concentration of the adsorbate in solution (C_e) at a constant temperature. The correlation between q_e and C_e is often examined by fitting the empirical data to one or more equilibrium isotherm models. To comprehend adsorption behavior, a variety of isotherm models have been utilized. The Langmuir, Freundlich, Temkin, and Dubinin–Radushkevich (D-R) isotherm models are among the most frequently used in studies that involve activated carbon for water treatment.

(i) Langmuir isotherm

The Langmuir isotherm model, initially introduced by Irving Langmuir, proposes that adsorption takes place at distinct homogenous active sites on the adsorbent surface, with no interaction between adsorbate molecules occupying adjacent sites [16]. The model defines monolayer adsorption, characterized by the formation of a singular layer of adsorbate molecules on the surface, often linked to chemisorption phenomena. Equation (2.7) and Equation (2.8) presents the linearized and non-linearized form of the Langmuir isotherm.

$$\text{Linearized form}, \frac{C_e}{q_e} = \frac{1}{Q_m K_L} + \frac{1}{Q_m} C_e \quad (2.7)$$

$$\text{Non} - \text{Linearized form}, q_e = \frac{Q_m K_L C_e}{1 + K_L C_e} \quad (2.8)$$

where, C_e is the equilibrium concentration of the adsorbate in the solution (mg/L), and q_e indicates the quantity of adsorbate adsorbed per unit mass of the adsorbent at equilibrium (mg/g). The constant K_L represents the Langmuir isotherm parameter related to the affinity between the adsorbate and the adsorbent (L/mg), whereas Q_m denotes the maximum monolayer adsorption capacity of the adsorbent (mg/g).

Another significant parameter associated with the Langmuir isotherm is the dimensionless separation factor (R_L), which is an indicator of the adsorption process's favorability [17]. The mathematical expression for R_L is presented in Equation (2.9).

$$R_L = \frac{1}{1 + K_L C_O} \quad (2.9)$$

The nature of the adsorption process is determined by the value of R_L. Adsorption is described as favorable ($0<R_L<1$), linear ($R_L=1$), irreversible ($R_L=0$), and unfavorable ($R_L>1$), respectively [18].

(ii) Freundlich isotherm

The Freundlich isotherm model is appropriate for characterizing multilayer adsorption phenomena and characterizes adsorption that takes place on heterogeneous surfaces with a non-uniform distribution of adsorption energies [19]. Equation (2.10) and Equation (2.11) represents the Freundlich isotherm in its linear and non-linear form.

$$\text{Linear form}, \log q_e = \log K_F + \left(1/n\right) \log C_e \quad (2.10)$$

$$\text{Non} - \text{linear form}, q_e = K_F C_e^{\frac{1}{n}} \quad (2.11)$$

where, C_e = adsorbate concentration at equilibrium (mg/L), q_e = amount of adsorbate per gram of adsorbent at equilibrium (mg/g), and K_F = Freundlich adsorption capacity constant (mg/g) (L/mg), '1/n' and 'n' indicating Freundlich adsorption intensity.

Adsorption intensity is denoted by the Freundlich adsorption intensity 'n'. The adsorption intensity increases as the 'n' value increases. Furthermore, the adsorption process is considered to adhere to a conventional Langmuir isotherm when the value of '1/n' is less than unity, while the cooperative nature of the adsorption process is indicated when the value of "1/n" is greater than unity [20].

(iii) Temkin isotherm

The Temkin isotherm model proposes that the heat of adsorption declines linearly with increasing surface coverage as a result of adsorbate-adsorbent interactions, and that the binding energies are evenly distributed throughout the surface [21]. The linearized form of the Temkin isotherm is delineated in Equation (2.12).

$$q_e = \frac{RT}{b_T} \ln(A_T C_e) \quad (2.12)$$

where, b_T corresponds to the Temkin constant associated with the heat of sorption (kJ/mol), whereas A_T is the Temkin equilibrium binding constant (L/mg). The symbol R represents the universal gas constant (8.314 J/mol/K), whereas T specifies the absolute temperature at 298 K.

(iv) Dubinin–Radushkevich (D-R) isotherm

The Dubinin–Radushkevich (D–R) isotherm model is utilized to assess porosity, apparent free energy, and the overall characteristics of the adsorption process [22]. This model is very effective in differentiating between physical and chemical adsorption interactions. The mean free energy of adsorption (E) obtained from the D–R model elucidates the fundamental adsorption process. An E value between 1-8 kJ/mol indicates physisorption, while values ranging from 8 to 16 kJ/mol signify

chemisorption [23]. The linear representation of the D-R isotherm model is expressed by Equation (2.13).

$$\ln q_e = \ln q_{DR} + \beta_{\varepsilon^2} \tag{2.13}$$

$$\varepsilon = RT \ln \left[1 + \frac{1}{C_e}\right] \tag{2.14}$$

The mean free energy is subsequently computed using Equation (2.15).

$$E = \frac{1}{(2\beta)^{1/2}} \tag{2.15}$$

where q_e = amount of adsorbate per gram of adsorbent at equilibrium (mg/g), q_{DR} = theoretical monolayer adsorption capacity (mg/g), β = D-R constant, ε = Polanyi potential, E = mean free energy (kJ/mol), R = universal gas constant (8.314 J/mol/K) and T= Temperature at 298 K.

2.7.2 Kinetic models

Adsorption kinetic studies are important for assessing the adsorption process by determining the reaction order, rate constants, and potential rate-controlling stages [24]. This work employed three kinetic models, including pseudo-first-order, pseudo-second-order, and intraparticle diffusion to assess adsorption kinetics.

(i) Pseudo-first-order

The pseudo-first-order (PFO) kinetic model, initially proposed by Lagergren, provides a simplified framework for characterizing the adsorption of a solute from the liquid phase onto a solid surface [25]. This model posits that the rate-limiting step is determined by physical interactions, including van der Waals forces, π–π interactions, and hydrogen bonding [26]. Equation (2.16) and Equation (2.17) presents the linearized and non-linearized form of the PFO equation.

$$\text{Linearized form}, \log\ (q_e - q_t) = \log q_e - \frac{k_1}{2.303}\ t \tag{2.16}$$

$$\text{Non} - \text{linearized form}, q_t = q_e\left(1 - e^{-k_1 t}\right) \tag{2.17}$$

where, q_e = equilibrium adsorption capacity (mg/g), q_t =adsorption capacity at time t (mg/g), k_1 = rate constant of PFO (1/min).

(ii) Pseudo-second-order

The pseudo-second-order (PSO) kinetic model, based on adsorption equilibrium capacity, is commonly used to elucidate the chemisorption mechanism of the adsorption process. This model proposes that the adsorption rate is directly proportional to the quantity of occupied active sites on the adsorbent surface [27]. The linear and non-linear form of the PSO kinetic equation is presented in Equation (2.18) and Equation (2.19).

$$\text{Linear form}, \frac{t}{q_t} = \frac{1}{k_2 q_e^2} + \frac{t}{q_e} \quad (2.18)$$

$$\text{Non} - \text{linear form}, q_t = \frac{q_e^2 k_2 t}{1 + q_e k_2 t} \quad (2.19)$$

where, q_e = equilibrium adsorption capacity (mg/g), q_t = adsorption capacity at time t (mg/g), k_2 = rate constant of PSO (1/min).

(iii) Intraparticle diffusion

The intraparticle diffusion (ID) model, proposed by Weber and Morris (1963), was utilized to clarify the diffusion mechanism and identify the rate-controlling stage of the adsorption process [28]. This model describes adsorption as including two principal stages: the migration of adsorbate molecules from the bulk solution to the external surface of the adsorbent, succeeded by their diffusion into the interior pores of the adsorbent [29]. The ID concept is mathematically expressed in Equation (2.20) [30].

$$q_t = k_{id} t^{0.5} + c \quad (2.20)$$

where q_t = amount of adsorption at any time, t = time, k_{id} = intra-particle diffusion rate constant (mg/g.min$^{1/2}$) and c = thickness of the boundary layer.

2.7.3 Thermodynamics

The effect of temperature on the adsorption process was assessed by thermodynamic analysis. These investigations elucidate the changes in internal energy attributed to adsorption [31]. The thermodynamic parameters, namely the variations in enthalpy (ΔH°) and entropy (ΔS°), were ascertained from the slope and intercept of the linear

graph of ln K_d against 1/T, as described by Equation (2.21). The change in Gibbs free energy (ΔG°) at various temperatures was determined utilizing Equation (2.23).

$$\ln K_d = \frac{\Delta S}{R} - \frac{\Delta H}{RT} \quad (2.21)$$

$$K_d = \frac{q_e}{C_e} \quad (2.22)$$

$$\Delta G = -RT \ln K_L \quad (2.23)$$

where, K_d = thermodynamic distribution coefficient, q_e = adsorbed concentration on the adsorbent, C_e = initial concentration at equilibrium, T (K) = absolute temperature, R = gas constant (8.314 J/mol/K).

2.7.4 Model validation

The most favorable isotherm and kinetic models were determined by statistical error analysis utilizing the residual root mean square error (RMSE) and chi-square (χ^2) tests to evaluate the goodness of fit between the experimental and calculated data [32].

$$\chi^2 = \sum_{i=1}^{m} \frac{(q_e - q_c)^2}{q_c} \quad (2.24)$$

The χ^2 values were computed utilizing the Equation (2.24). The experimental and calculated adsorption capabilities from batch investigations are represented by q_e and q_c, respectively, with 'm' denoting the number of observations. A low χ^2 value signifies a strong correlation between the experimental data and the model predictions, indicating an effective fit of the kinetic or isotherm model. The values of the RMSE were determined using the Equation (2.25).

$$RMSE = \sqrt{\frac{1}{m-2}} \sum_{i=1}^{m} (q_e - q_c)^2 \quad (2.25)$$

where a lower RMSE value suggests a more accurate curve fitting [33].

2.8 Synthesis of photocatalysts and supporting material

The synthesis route and operational conditions influence the structural, morphological, electrical, optical, and stoichiometric characteristics of nanomaterials [34]. As a result, choosing a suitable synthesis process is important to producing a highly active photocatalyst. This study examined photocatalytic degradation employing

nanocomposite photocatalysts, including ZrO_2-ZnO, CCAC/ZrO_2-ZnO, and CCAC/Co-ZnO, respectively.

2.8.1 Synthesis of ZrO_2-ZnO and Co-ZnO nanocomposite supported on CCAC

Metal oxide nanocomposites have been synthesized using a variety of techniques, including co-precipitation, microemulsion, polyol, and reverse micelle methods [35-38]; however, these approaches are frequently associated with low efficiency, particle agglomeration, poor crystallinity, and broad particle size distributions [39]. The present research used a hydrothermal approach to develop high-purity and uniformly sized ZrO_2-ZnO and Co-ZnO nanocomposites.

Hydrothermal synthesis is one of the most widely used methods for the preparation of metal oxide nanocomposites [40]. During this process, higher temperature and pressure are generated within a sealed hydrothermal autoclave, which significantly alter the physicochemical properties of water, thereby increasing the mobility and solubility of reactant species and promoting crystallization reactions [41]. Owing to its simplicity, low reaction temperatures, and one-step processing capability, hydrothermal synthesis is considered a promising method for the fabrication of nanomaterials [42]. In this work, ZrO_2-ZnO and Co-ZnO nanocomposites based on CCAC were obtained using the hydrothermal approach. Chapters 5 and 6 provide detailed synthesis processes for CCAC/ZrO_2-ZnO and CCAC/Co-ZnO nanocomposites, respectively.

2.9 Photocatalytic reactor

In the present study, photocatalytic reactions were carried out in a photocatalytic reactor (63 x 44 x 44 cm) enclosed within a black box, as illustrated in the schematic diagram (Figure 2.4). The photocatalytic reactor consisted of a double-jacketed glass tank with two ports: one for adding samples and the other for inserting a condenser to condense heated vapors, in the borosilicate glass outer jacket. The inner jacket consisted of a Pyrex glass jar holding a 450 W mercury lamp (UV source) producing radiation at 325 nm with an intensity of 1500 mW cm^{-2}, positioned 5 cm away from the reaction mixture. For visible-light tests, a high-pressure mercury lamp (350 W) with a maximum wavelength of 520 nm was put at the same distance as the reaction solution. A magnetic stirrer placed beneath the double-jacketed tank ensured uniform

mixing of the reaction system. The temperature was kept stable by continually pumping water through the outer jacket with a pump. In addition, an exhaust fan was put in the reactor chamber to ensure that air circulated throughout the system.

Figure 2.4. Schematic representation of experimental photocatalytic reactor.

2.10 Description of pollutants considered for photodegradation studies

The subsequent section presents a concise overview of the pollutants examined in this study, namely 4-nitrophenol, and bisphenol A.

(i) 4-nitrophenol

Nitrophenols are anthropogenic, inhibitory, and biorefractory organic compounds. They have been widely used in the chemical industry for pesticides, drugs, and colors [43]. 4-Nitrophenol (4-NP) is a phenolic molecule with a benzene ring that has both nitro ($–NO_2$) and hydroxyl (–OH) functional groups on it. According to the European Economic Union and the United States Environmental Protection Agency, 4-NP is classified as a priority pollutant due to its high toxicity, with a maximum permissible concentration of 1 ppm in water [44]. 4-NP poses significant health hazards to humans, animals, and aquatic organisms, even at minimal concentrations. Exposure to such pollutant may lead to many acute and chronic health impacts, including gastrointestinal and respiratory illnesses, organ damage to the liver and kidneys, skin and eye irritation, and cardiovascular disorders. Additional side effects may include increased saliva production, decreased hunger, deterioration of proteins, and interference with the neurological and circulatory systems [45,46]. Given these serious health risks, it is critical to treat 4-NP-containing wastewater thoroughly before it is discharged into aquatic environments. The chemical structure of 4-NP is depicted in Figure 2.5.

Figure 2.5. Molecular structure of 4-nitrophenol.

(ii) Bisphenol A

Bisphenol A (BPA) is a commonly found endocrine-disrupting chemical (EDC) in groundwater, surface water, industrial effluent, and landfill leachate. Its ubiquitous occurrence is primarily due to its extensive use as a precursor in the production of epoxy resins, polycarbonate plastics, and a variety of polymeric materials, such as

rubber additives, food packaging products, dental sealants, PVC pipelines, and specialty chemicals [47,48]. BPA is composed of two phenolic rings connected by an acetone-derived bridge, which is the source of the identifier "A" (acetone). BPA is consistently released into the environment due to its extensive usage in industries, adversely affecting ecosystems and human health. Besides its effects on the endocrine system, BPA is also known to have carcinogenic and genotoxic properties. Experimental studies indicate that BPA exposure may promote the development of cancer cells, especially in breast and prostate tissues [49]. Furthermore, it has been associated with reproductive problems, obesity, and developmental anomalies. The persistence and toxicity of BPA are significantly affected by its physicochemical properties, such as its considerable aqueous solubility (~200 mg/L at 25 °C), chemical stability, and resistance to biodegradation, facilitating its accumulation in aquatic environments even at trace concentrations (pM–nM levels) [50-52]. In response to these concerns, the United States Environmental Protection Agency (USEPA) has incorporated BPA into the Drinking Water Contaminant Candidate List 5 [53]. Consequently, the development of strategies that are highly effective in the removal of BPA from aqueous environments continues to be a critical priority. The chemical structure of BPA is depicted in Figure 2.6.

Figure 2.6. Molecular structure of bisphenol A.

2.11 Photocatalytic degradation experiments

Batch-mode photocatalytic degradation tests were conducted in a reactor system to remove 4-nitrophenol and bisphenol A [54-56]. The degradation investigations were carried out with constant water circulation at room temperature during the reaction time. After reaching equilibrium, the pollutant concentration was measured and used as the starting concentration to ensure that adsorption by the nanocomposite did not interfere the overall photocatalytic activity. Following that, photocatalytic degradation was initiated, and at regular intervals of 10 min, 3.5 mL aliquots were taken out, centrifuged, and monitored with a UV-visible spectrophotometer at the corresponding λ_{max} values. The degradation efficiency (R %) of the target pollutants was calculated using Equation (2.5).

Batch photocatalytic degradation experiments were carried out with various operating parameters, as described in Chapters 5 and 6.

2.12 Liquid chromatography–mass spectrometry and total organic carbon analyses

Liquid chromatography-mass spectrometry (LC-MS) is a powerful analytical method commonly used to identify degradation intermediates in aquatic environments [57]. Liquid chromatography enables the separation of complex multicomponent mixtures, while mass spectrometry provides structural identification of individual compounds with high molecular specificity and detection sensitivity. In the current investigation, an LC-MS system was used to detect the degradation products produced during the photocatalytic activity.

Total organic carbon (TOC) measurement is a prevalent method for assessing the extent of mineralization in photocatalytic degradation processes [58]. TOC analysis assesses the total carbon content in organic compounds within the solution. TOC analyzers are versatile and can be used to analyze a wide range of liquid samples, including drinking water, wastewater, surface water, and industrial process water. The measurement is expressed as the concentration of carbon in parts per million (ppm) or milligrams per litre (mg/L) [59]. Therefore, it provides direct evidence of the conversion of organic pollutants into inorganic end-products such as CO_2 and H_2O.

In this investigation, the extent of complete mineralization is confirmed by a reduction in TOC in contrast to a mere transformation into intermediate by-products. The mineralization efficiency was calculated using the Equation (2.26).

$$\text{Mineralization} = \frac{\text{TOC}_{\text{initial}} - \text{TOC}_{\text{final}}}{\text{TOC}_{\text{initial}}} \times 100 \quad (2.26)$$

2.13 Photodegradation kinetics

(i) Langmuir Hinshelwood kinetic model

To describe heterogeneous photocatalytic degradation of organic contaminants in aquatic environments, the Langmuir-Hinshelwood (L-H) kinetic model is the most commonly used model. This approach proposes that the reactive species are initially chemisorbed onto the surface of the catalyst prior to the reaction [60]. Moreover, the

overall reaction rate is governed by the surface oxidation step under conditions of maximum catalyst coverage. The L-H rate equation is presented as follows:

$$\ln\left(\frac{C_0}{C_t}\right) = K_{ap}t \quad (2.27)$$

where K_{ap} is the apparent reaction rate constant, calculated from the slope of the graph of $\ln(C_0/C_t)$ vs time, C_0 = initial concentration, and C_t = concentration at time t, respectively.

(ii) Half-life time reaction

The half-life of a reaction is utilized to determine the rate of a first-order kinetic process. The half-life ($t_{1/2}$) is determined using Equation (2.28).

$$t_{\frac{1}{2}} = \frac{ln\ 2}{k_{ap}} = \frac{0.693}{k_{ap}} \quad (2.28)$$

where $t_{1/2}$ is the half-life time of reactions calculated from k_{ap} (min) [61].

2.14 Density functional theory study

Theoretical simulations employing the density functional theory (DFT) approach were conducted understand the potential interactions between the adsorbate and activated carbon. DFT was applied for its conceptual simplicity and computational efficiency in simulating molecular interactions.

All geometry optimizations, frequency evaluations, and energy calculations were conducted utilizing the Gaussian 09/16 software package [62,63]. The calculations utilized the B3LYP hybrid functional with the 6-31G/LanL2DZ basis set, incorporating a dielectric constant of ε = 80 to replicate an aquatic environment. GaussView 05/06 was utilized to build the molecular structures, which were then optimized in their electronic ground states after a variety of structural models of activated carbon were studied. The adsorption energy ($E_{adsorption}$) of the adsorbate on the carbon surface was computed utilizing Equation (2.29).

$$E_{adsorption} = E_{system} - (E_{adsorbent} + E_{adsorbate}) \quad (2.29)$$

where, E_{system}= Total energy of the adsorbent and adsorbate, $E_{adsorbent}$ = Total energy of the adsorbent (AC), $E_{adsorbate}$ = Total energy of the adsorbate. Moreover, a higher value

of negative $E_{adsorption}$ indicates a more stable arrangement, whereas a positive $E_{adsorption}$ value denotes unfavorable adsorption [64] .

The underlying adsorption mechanisms can be better understood by the use of DFT in adsorption investigations. This research promotes the systematic advancement of highly effective adsorbents for targeted contaminant elimination and enhances the comprehension of the interactions, bonding properties, and reactivity between the adsorbate and the adsorbent surface.

To enhance understanding of chemical reactivity and to gain deeper insight into adsorption and degradation mechanisms, quantum chemical descriptors, including HOMO-LUMO energy gap, chemical potential, chemical softness and hardness, electronegativity, electrophilicity index, maximum charge transfer, electrostatic potential surfaces, and Fukui function analysis were assessed to evaluate the reactivity of both the photocatalyst and the pollutant. Detailed discussions of these parameters are provided in Chapters 5 and 6.

2.15 Analytical instruments used for characterization

The synthesized CCAC, CCAC/ZrO_2-ZnO and CCAC/Co-ZnO nanocomposites were studied using various analytical techniques. These include, CHNS elemental analyzer (Model: EA3000, Eurovector), Fourier Transform Infrared Spectroscopy (FT-IR; Model: Spectrum Two, Perkin Elmer), Brunauer-Emmett-Teller Surface Area Analysis (BET; Model: Smart Sob 93, Smart Instruments), Scanning Electron Microscopy (SEM; Model: JSM 6390LV, JEOL), X-Ray Diffraction (XRD; Model: ULTIMA IV, Rigaku), Transmission Electron Microscopy (TEM; Model: JEM 2100, JEOL), Energy-Dispersive X-Ray (EDX; PHI 5000 Versa Probe III), X-Ray Photoelectron Spectroscopy (XPS; Model: PHI 5000 VersaProbe III, Physical Electronics), UV-Visible Diffuse Reflectance Spectroscopy (DRS; Shimadzu, and wavelength), Photoluminescence (PL; Horiba Fluoromax4CP spectrofluorometer), Liquid Chromatography–Mass Spectrometry (LC-MS; INKAR, Expression-S) Spectrophotometer and Total Organic Carbon (TOC; Shimazu Model 5000 A). Brief descriptions of the analytical equipment used in this work are provided below: -

(i) Fourier Transform Infrared Spectroscopy

Fourier transform infrared (FT-IR) spectroscopy is a widely employed method for detecting surface chemical functional groups in materials [65]. In this investigation, FT-IR spectra have been carried out to identify the functional groups on the surface of synthesized samples. For spectral analysis, pellets were prepared by thoroughly mixing activated carbon with KBr in a 1:100 ratio, followed by compression using a hydraulic pellet press. The spectra were collected using an FT-IR spectrometer with a spectral range of 4000-400 cm^{-1} and a resolution of 4 cm^{-1}.

(ii) BET Surface Area, average pore diameter and total pore volume

The Brunauer-Emmett-Teller (BET) technique is widely used to evaluate the specific surface area and pore properties of porous materials using multilayer gas adsorption. The present work employed a BET surface area analyzer to measure the specific surface area, average pore diameter and total pore volume of the synthesized materials through nitrogen (N_2) adsorption-desorption isotherms. Furthermore, the pore size distribution was measured using the Barrett-Joyner-Halenda (BJH) technique.

(iii) X-Ray Diffraction

X-ray diffraction (XRD) analysis is a widely used technique for determining the crystalline structure and degree of crystallinity of materials using their diffraction patterns. In this procedure, an incoming X-ray beam interacts with the sample, and the intensity and diffraction angles of the scattered X-rays are measured. The average crystallite size was calculated using the Scherrer equation [66].

$$D = 0.9\,\lambda/\beta\,\mathrm{Cos}\,\theta \qquad (2.30)$$

where λ denotes the X-ray radiation wavelength, θ is the Bragg's angle, and β is the full width at half-maximum (FWHM).

Powder X-ray diffraction (PXRD) was used in this research to collect the diffraction patterns of the synthesized materials and determine their crystalline or amorphous nature by comparing them to standard diffraction databases via JCPDS/ICDD reference number. PXRD measurements were performed on an X-ray diffractometer using CuK_α radiation at a scan rate of 0.2° min^{-1}.

(iv) Scanning Electron Microscopy

Scanning electron microscopy (SEM) is widely utilized for investigating the surface morphological properties of materials [67]. In this work, SEM was used to explore the surface morphology of CCAC, since surface characteristics play an important role in controlling the interactions between the adsorbent and adsorbate.

(v) Transmission Electron Microscopy

Transmission electron microscopy (TEM) is a powerful characterisation method that offers high spatial resolution information on material shape, particle size distribution, crystal structure, lattice strain, defects, and chemical composition at atomic scale [68]. TEM data is derived from interactions between the material and the incoming electron beam. The word "transmission" electron microscopy refers to the process of detecting electrons as they pass through the sample. To transmit electrons, TEM samples must be thin, often less than ~200 nm, depending on the material composition and desired information. The electron beam having energy around 100-300 keV is used. The chamber in TEM has to be housed containing vacuum. It allows to avoid any contamination while analysis. Therefore, TEM was utilized in this study to examine the morphology, particle size distribution, and surface texture of the synthesized nanocomposites.

(vi) High-Resolution TEM

High-resolution (HRTEM) is a sophisticated imaging technology that can resolve the fine structural characteristics (typically smaller than 4-5 nm) of materials at the atomic level precision. HRTEM provides detail information on the microstructure, including internal morphology, crystal structure, atomic arrangement, and the existence of defects and impurities [69]. HRTEM commonly used to study lattice imperfections such as vacancies and point defects, as well as to detect crystallographic patterns and material composition [70]. Additionally, it enables estimation of defect volume fractions, thereby contributing to a better understanding of the mechanical properties of materials. The highest resolution of TEM is 0.050 nm which is achieved through high end HRTEM. Herein, the present work utilised HRTEM interplanar spacing of the lattice fringes in the prepared nanomaterials.

(vii) Selected-Area Electron Diffraction

Selected area electron diffraction (SAED) is a crystallographic experimental technique typically performed using TEM. SAED is the diffraction pattern formed when the electrons are diffracted, which results in the formation of dark background and bright spots. SAED patterns provide valuable information about sample crystallinity, including whether they are amorphous, single crystalline, or polycrystalline, as well as the associated crystallographic planes [71]. Diffuse, continuous, and broad rings are characteristic of amorphous materials, whereas sharp, bright spot patterns indicate single crystalline structures. In contrast, randomly distributed or overlapping diffraction rings are indicative of polycrystalline materials. The present study used SAED patterns to evaluate the crystallinity and structural features of the synthesized materials.

(viii) Energy-Dispersive X-Ray Spectroscopy

Energy-dispersive X-ray spectroscopy (EDS/EDX) is a powerful, non-destructive analytical method used to qualitatively and quantitatively determine elemental composition in materials [72]. It is typically used in conjunction with SEM/TEM, which allows for simultaneous morphological imaging and elemental analysis, providing vital information for chemical composition. EDS analysis allows for elemental characterisation of materials in macro, micro, and nanoscale dimensions. The current work utilized EDS analysis to confirm the elemental composition of the synthesized materials.

(ix) X-Ray Photoelectron Spectroscopy

X-ray photoelectron spectroscopy (XPS) is a surface-sensitive analytical method that uses core-level binding energies to determine the elemental composition, chemical/electronic states, and stoichiometry of materials [73]. High-energy X-ray photons expel electrons from atoms' core orbitals, resulting in XPS spectra. In this investigation, an X-ray photoelectron spectrometer was used to investigate the elemental composition and oxidation states of the photocatalysts.

(x) UV-Visible Diffuse Reflectance Spectroscopy

The optical characteristics and band gap energy of photocatalysts may be effectively

investigated using UV–visible diffuse reflectance spectroscopy (UV–Vis DRS) [74]. This approach is based on measuring the electromagnetic radiation reflected by powder samples. In this work, the band gap energies of the photocatalysts were determined using a UV-visible diffuse reflectance spectrophotometer.

(xi) Photoluminescence

Photoluminescence (PL) spectroscopy is a non-destructive analytical method in which a material absorbs incoming photons and moves electrons from the ground state to the excited state on femtoseconds [75]. PL analysis was used to quantify the band gap energy of photocatalysts and analyze the recombination behavior of photogenerated electron-hole pairs in semiconductor materials for the present study. The photoluminescence spectra were obtained with a photoluminescence spectrophotometer.

(vii) Zero-point charge

The batch equilibrium technique was used to calculate the point of zero charge (pH_{zpc}) in the carbon and carbon-based nanomaterials. The point of zero charge (pH_{zpc}) refers to the pH where the net surface charge of CCAC and/or carbon-based nanocomposite (photocatalyst) material is zero. When the solution pH is lower than the pH_{zpc}, the surface of activated carbon becomes positively charged ($pH < pH_{zpc}$), whereas at higher pH values, the surface develops a negative charge ($pH > pH_{zpc}$) [76].

The batch equilibrium technique was used to estimate the pH_{zpc} for CCAC and/or carbon-based nanocomposite samples [77]. For this purpose, 0.1 g of the material was introduced to Erlenmeyer flasks with 50 mL of 0.1 M potassium nitrate (KNO_3) solution. Each suspension's pH was changed from 2 to 12 using 0.1 M HNO_3/ KOH. The flasks were then sealed and stirred on a mechanical shaker for 24 hours to reach balance. Following equilibration, the final pH values were recorded. The difference between initial and final pH values ($\Delta pH = pH_{initial} - pH_{final}$) was plotted against the initial pH. The pH_{zpc} was found as the pH at which ΔpH equals zero, corresponding to the point where the ΔpH versus pH starting curve meets with the baseline.

References

[1] R. N. Sahoo, S. Mahawar, A. Arya, Antimalarial response, traditional and other potential uses of *Croton* genera, in: *Antimalarial Medicinal Plants*, CRC Press, (2024) 188–213.

[2] E. Jajo, G. Ngaomei, V. Raihing, P. K. Singh, The Croton caudatus plant used for trapping crabs by the Rongmei tribe of Tamenglong district, Manipur, (2024) 17–21.

[3] ASTM, Standard method for chemical analysis of wood charcoal, Am. Soc. Test. Mater., (1990) 292–293.

[4] ASTM, Standard test method for total ash content of activated carbon (ASTM D2866–94), (2004) 1–2.

[5] A. H. Kamel, H. S. Abd-Rabboh, A. Hefnawy, Electrochemical sensors for chlorophenols monitoring, RSC Adv., 14 (2024) 20163–20181.

[6] O. B. Otitoju, M. O. Alfred, O. O. Ogunlaja, C. G. Olorunnisola, O. D. Olukanni, A. Ogunlaja, M. O. Omorogie, E. I. Unuabonah, Risk assessment of phenolic compounds in drinking water, Environ. Sci. Pollut. Res., 30 (2023) 76798–76817.

[7] N. L. Mhlongo, M. O. Akharame, O. Pereao, I. S. Human, B. O. Opeolu, Phenolic compounds occurrence and risk assessment, Front. Toxicol., 5 (2024) 1269601.

[8] M. B. Tahir, T. Nawaz, G. Nabi, M. Sagir, M. I. Khan, N. Malik, Role of nanophotocatalysts in wastewater treatment, Int. J. Environ. Anal. Chem., 102 (2022) 491–515.

[9] M. Khodari, A. Abd El-Rady, E. Rabee, N. Nabil, Electro analytical determination of dihydroxybenzene isomers, J. Chem. Eng., 8 (2014) 654–661.

[10] F. Behboodi-Sadabad, H. Zhang, V. Trouillet, A. Welle, N. Plumere, P. A. Levkin, Controlled polymerization and photopatterning of plant polyphenols, Chem. Mater., 30 (2018) 1937–1946.

[11] M. Patel, P. Rathva, M. Raj, L. Raj, Epoxy resin from renewable phenols and resorcinol, J. Polym. Environ., 33 (2025) 3987–4007.

[12] M. F. Hanafi, N. Sapawe, Water pollution from phenol and dyes – review, Mater. Today Proc., 31 (2020) 141–150.

[13] S. Agarwal, A. Rani, Adsorption of resorcinol onto fly ash composites, J. Environ. Chem. Eng., 5 (2017) 526–538.

[14] W. Lu, C. Zhang, Y. Du, B. Quan, Z. Qin, K. Cheng, A. Niyazi, P. Su, Applications of nanoadsorbents for fluoride removal from water, Sep. Purif. Rev., 53 (2024) 311–335.

[15] R. K. Gautam, M. C. Chattopadhyaya, Kinetics and equilibrium isotherm modeling: graphene-based nanomaterials for heavy metal removal, in: *Nanomaterials for Wastewater Remediation*, (2016).

[16] I. Langmuir, The adsorption of gases on plane surfaces of glass, mica and platinum, J. Am. Chem. Soc., 40 (1918) 1361–1403.

[17] K. R. Hall, L. C. Eagleton, A. Acrivos, T. Vermeulen, Pore- and solid-diffusion kinetics in fixed-bed adsorption, Ind. Eng. Chem. Fundam., 5 (1966) 212–223.

[18] M. A. Usman, R. A. Aftab, S. Zaidi, S. M. Adnan, R. A. K. Rao, Adsorption of aniline blue dye on activated pomegranate peel, Int. J. Environ. Sci. Technol., 19 (2022) 8351–8368.

[19] H. M. Freundlich, Over the adsorption in solution, J. Phys. Chem., 57 (1906) 385–470.

[20] J. Amrutha, G. Jeppu, C. R. Girish, B. Prabhu, K. Mayer, Multi-component adsorption isotherms: review and modeling studies, Environ. Process., 10 (2023) 38.

[21] M. I. Temkin, Adsorption equilibrium and kinetics on nonhomogeneous surfaces, Zh. Fiz. Khim., 15 (1941) 296–332.

[22] M. M. Dubinin, The potential theory of adsorption of gases and vapors, Adsorption, (1969).

[23] H. Demiral, C. Güngör, Adsorption of copper(II) from aqueous solutions on activated carbon from grape bagasse, J. Clean. Prod., 124 (2016) 103–113.

[24] J. Wang, X. Guo, Adsorption kinetics and isotherm models of heavy metals: overview, Crit. Rev. Environ. Sci. Technol., 53 (2023) 1837–1865.

[25] E. Mosaffa, A. Banerjee, H. Ghafuri, Sustainable high-efficiency dye removal using biochar, Environ. Sci.: Water Res. Technol., 9 (2023) 2643–2663.

[26] J. Wu, H. B. Liu, J. Wang, In-situ growth of Fe-MOF on magnetic materials for tetracycline removal, Appl. Surf. Sci., 681 (2025) 161520.

[27] Y. S. Ho, G. McKay, Pseudo-second order model for sorption processes, Process Biochem., 34 (1999) 451–465.

[28] W. J. Weber, J. C. Morris, Kinetics of adsorption on carbon from solution, J. Sanit. Eng. Div., 89 (1963) 31–60.

[29] D. Wu, M. Yang, J. Yu, M. Dyballa, P. Yang, M. Li, G. Hou, M. Hunger, W. Dai, Role of adsorption and diffusion in zeolite catalysts, Chem. Soc. Rev., 54 (2025) 9192–9244.

[30] O. A. Moamen, G. A. Murad, H. S. Hassan, Adsorption mechanism and mass transfer modeling of cesium and europium ions, Microporous Mesoporous Mater., 356 (2023) 112564.

[31] C. R. Girish, Determination of thermodynamic parameters in adsorption studies: review, Chem. Pap., 79 (2025) 5687–5706.

[32] E. Igberase, I. G. Mkhize, Efficient adsorption of methylene blue by chitosan derivative, Desalin. Water Treat., 321 (2025) 100943.

[33] D. K. Nguyen, Q. T. Nguyen, V. P. Dinh, Integrating artificial intelligence with kinetic studies for Cr(VI) removal, RSC Adv., 15 (2025) 42238–42253.

[34] J. K. Patra, K.-H. Baek, Green nanobiotechnology: factors affecting synthesis and characterization techniques, J. Nanomater., 2014 (2014) 219.

[35] S. Patil, S. Jagadale, Co-precipitation methods for the synthesis of metal oxide nanostructures, in: *Solution Methods for Metal Oxide Nanostructures*, Elsevier, (2023) 39–60.

[36] E. Khalili, S. A. Hassanzadeh-Tabrizi, ZnO–CdO nanocomposite: microemulsion synthesis and dye removal ability, J. Sol-Gel Sci. Technol., 81 (2017) 475–482.

[37] S. Murali, P. K. Dammala, B. Rani, R. Santhosh, C. Jadhao, N. K. Sahu, Polyol mediated synthesis of anisotropic ZnO nanomaterials and composite with rGO: application towards hybrid supercapacitor, J. Alloys Compd., 844 (2020) 156149.

[38] A. S. Chernukha, G. M. Zirnik, K. V. Matveev, Y. V. Boleiko, T. A. Markin, E. S. Anannikov, A.A. Loshkarev, S.A. Gudkova, D.A. Vinnik, Reverse micelle synthesis of metal oxides, J. Struct. Chem., 66 (2025) 569–585.

[39] T. Dippong, E.A. Levei, O. Cadar, Recent advances in synthesis and applications of MFe_2O_4 (M = Co, Cu, Mn, Ni, Zn) nanoparticles, Nanomaterials, 11 (2021) 1–33.

[40] Y. X. Gan, A.H. Jayatissa, Z. Yu, X. Chen, M. Li, Hydrothermal synthesis of nanomaterials, J. Nanomater., 2020 (2020) 1–3.

[41] A. S. Ganeshraja, A. S. Clara, K. Rajkumar, Y. Wang, Y. Wang, J. Wang, K. Anbalagan, Simple hydrothermal synthesis of metal oxides coupled nanocomposites: structural, optical, magnetic and photocatalytic studies, Appl. Surf. Sci., 353 (2015) 553–563.

[42] J. A. Darr, J. Zhang, N. M. Makwana, X. Weng, Continuous hydrothermal synthesis of inorganic nanoparticles: applications and future directions, Chem. Rev., 117 (2017) 11125–11238.

[43] Y. Ji, Y. Shi, Y. Yang, P. Yang, L. Wang, J. Lu, J. Li, L. Zhou, C. Ferronato, J. M. Chovelon, Sulfate radical oxidation of nitrophenols, J. Hazard. Mater., 361 (2019) 152–161.

[44] K. G. Pavithra, P. S. Rajan, J. Arun, K. Brindhadevi, Q. H. Le, A. Pugazhendhi, Review on phenols removal from wastewater, Environ. Res., 237 (2023) 117005.

[45] Q. Mei, H. Cao, D. Han, M. Li, S. Yao, J. Xie, J. Zhan, Q. Zhang, W. Wang, M. He, Degradation of p-nitrophenol by OH radicals, J. Hazard. Mater., 389 (2020) 121901.

[46] H. Zheng, Y. Guo, H. Zhu, D. Pan, L. Pan, J. Liu, p-Nitrophenol degradation in corona discharge system, Plasma Chem. Plasma Process., 33 (2013) 1053–1062.

[47] E. Baralla, V. Pasciu, M. V. Varoni, M. Nieddu, R. Demuro, M. P. Demontis, Bisphenols occurrence in bivalves, Sci. Total Environ., 785 (2021) 147263.

[48] P. Loganathan, S. Vigneswaran, J. Kandasamy, T. V. Nguyen, A. K. Cuprys, H. Ratnaweera, Bisphenols in water: occurrence and mitigation, Chemosphere, 328 (2023) 138560.

[49] M. H. Mahmoudian, A. Mesdaghinia, A. H. Mahvi, S. Nasseri, R. Nabizadeh, M. H. Dehghani, Photocatalytic degradation of BPA using magnetic nanoparticles, J. Environ. Health Sci. Eng., 20 (2022) 617–628.

[50] J. Chudzinska, B. Wozniak, M. Sprynskyy, I. Nowak, A. Feliczak-Guzik, Photoremoval of BPA using zeolites, Int. J. Mol. Sci., 24 (2023) 2878.

[51] Z. Song, Y. Zhang, X. Zhang, X. Zhou, Y. Chen, X. Duan, N. Ren, Kinetics of peracetic acid for BPA removal, Water Res., (2023) 120274.

[52] D. Roy, S. Neogi, S. De, Mechanistic investigation of photocatalytic degradation of bisphenol-A using MIL-88A (Fe)/MoS_2 Z-scheme heterojunction composite, Chem. Eng. J., 428 (2022) 131028.

[53] USEPA, Contaminant candidate list (CCL5) and regulatory determination, U.S. Environ. Prot. Agency, (2023).

[54] M. Baruah, A. Supong, P. C. Bhomick, R. Karmaker, C. Pongener, D. Sinha, Sorption–photodegradation using TiO_2/activated carbon nanocomposite, Nanotechnol. Environ. Eng., 5 (2020) 1–13.

[55] H. Elnakar, M. F. Khan, U. M. Ismail, Sequencing batch reactor enhancement for phenol removal, Desalin. Water Treat., 317 (2024) 100310.

[56] S. A. Rashid, W. T. Mohammed, Oxidation of phenol using silica oxide-titanium dioxide photocatalyst, Chem. Afr., 8 (2025) 3773–3788.

[57] W. Gao, H. Chen, X. Liu, L. Zhang, H. Ding, C. Deng, Enhanced sulfamethoxazole degradation using synergistic plasma system, J. Water Process Eng., 69 (2025) 106579.

[58] A. Shetty, A. Goyal, Total organic carbon analysis in water – review of current methods, Mater. Today Proc., 65 (2022) 3881–3886.

[59] R. Dhanabal, B. Ramya, J. Yamini, P. P. Pavai, P. G. Priya, Photocatalytic degradation of malachite green using ZnO nanoparticles, Catal. Lett., 155 (2025) 1–17.

[60] R. J. Baxter, P. Hu, Insight into the Langmuir–Hinshelwood mechanism preference, J. Chem. Phys., 116 (2002) 4379–4381.

[61] N. Guettai, H. A. Amar, Photocatalytic oxidation of methyl orange: kinetics study, Desalination, 185 (2005) 439–448.

[62] M. J. Frisch, G. W. Trucks, H. B. Schlegel, G. E. Scuseria, M. A. Robb, J. R. Cheeseman, G. Scalmani, V. Barone, B. Mennucci, G. A. Petersson, H. Nakatsuji, M. Caricato, X. Li, H. P. Hratchian, A. F. Izmaylov, J. Bloino, G. Zheng, J. L. Sonnenberg, M. Hada, M.Ehara, K. Toyota, R. Fukuda, J. Hasegawa, M. Ishida, T. Nakajima, Y. Honda, O. Kitao, H. Nakai, T. Vreven, J. A. Jr. Montgomery, J. E. Peralta, F. Ogliaro, M. Bearpark, J. J. Heyd, E. Brothers, K. N. Kudin, V. N. Staroverov, R. Kobayashi, J. Normand, K. Raghavachari, A. Rendell, J. C. Burant, S. S. Iyengar, J. Tomasi, M. Cossi, N. Rega, J. M. Millam, M. Klene, J. E. Knox, J. B. Cross, V. Bakken, C. Adamo, J. Jaramillo, R. Gomperts, R. E. Stratmann, O. Yazyev, A. J. Austin, R. Cammi, C. Pomelli, J. W. Ochterski, R. L. Martin, K. Morokuma, V. G. Zakrzewski, G. A. Voth, P. Salvador, J. J. Dannenberg, S. Dapprich, A. D. Daniels, O. Farkas, J. B. Foresman, J. V. Ortiz, J. Cioslowski, D. J. Fox, Gaussian 09, Revision A.02-SMP, Gaussian, Inc., Wallingford, CT. **(2009).**

[63] Q. Yin, L. Si, R. Wang, Z. Zhao, H. Li, Z. Wen, DFT study on functional groups of carbonaceous surface on ammonium adsorption, Chemosphere, 287 (2022) 132294.

[64] A. Supong, P. C. Bhomick, U. B. Sinha, D. Sinha, Experimental and theoretical investigation of 4-nitrophenol adsorption using DFT, Korean J. Chem. Eng., 36 (2019) 2023–2034.

[65] M. Z. Abidin, M. P. Junqueira-Gonçalves, V. V. Khutoryanskiy, K. Niranjan, Intensifying chitin hydrolysis by adjunct treatments – an overview, J. Chem. Technol. Biotechnol., 92 (2017) 2787–2798.

[66] H. K. Abid, A. B. Siddique, A. Abbas, M. A. Shaheen, A. Ali, M. Fatima, A. Shami, M. A. Alrayyani, F. A. Al-Joufi, M. A. Assiri, Biogenic synthesis of ZnO, CuO and ZnO/CuO nanocomposites for degradation of organic pollutants, Nanoscale Adv., 7 (2025) 6145–6157.

[67] B. Dery, L. Zaixiang, Scanning electron microscopy (SEM) as a tool for morphology analysis, Food Rev. Int., 39 (2023) 2007–2026.

[68] G. Li, H. Zhang, Y. Han, Applications of transmission electron microscopy in nanomaterials engineering, Chem. Rev., 123 (2023) 10728–10749.

[69] G.-T. Park, S.-B. Kim, J.-I. Yoon, N.-Y. Park, M.-C. Kim, S.-M. Han, D.-H. Kim, M.-S. Kim, Y.-K. Sun, Role of manganese in nano and microstructural engineering of Ni-rich cathodes, Adv. Energy Mater., 14 (2024) 2400130.

[70] J. Wang, Y. Li, C. Pua, D. Yao, W. He, X. Yang, X. Wang, M. Liu, X. Li, Atomic-scale strain field mapping methods for HR-TEM and HR-STEM images, Acta Mech. Solida Sin., (2025) 1–15.

[71] Z. Czigány, V.K. Kis, Improving accuracy of SAED acquisition and evaluation, Microsc. Res. Tech., 86 (2023) 144–156.

[72] A. Keyvani, N. Kamkar, R. Chaharmahali, M. Bahamirian, M. Kaseem, A. Fattah-alhosseini, Improving anti-corrosion properties of AZ31 Mg alloy using hydroxyapatite nanoparticles, Inorg. Chem. Commun., 158 (2023) 111470.

[73] S. Zafeiratos (Ed.), Applications of X-ray photoelectron spectroscopy to catalytic studies, World Scientific, (2023).

[74] P. R. Jubu, O.S. Obaseki, A. Nathan-Abutu, F. K. Yam, Y. Yusof, M. B. Ochang, Dispensability of conventional Tauc's plot for bandgap determination, Results Opt., 9 (2022) 100273.

[75] A. N. Tuama, L. H. Alzubaidi, M. H. Jameel, K. H. Abass, M. Z. H. bin Mayzan, Z. N. Salman, Impact of electron–hole recombination on ZnO photocatalysis, J. Sol-Gel Sci. Technol., 110 (2024) 792–806.

[76] V. Mozhiarasi, T. S. Natarajan, Bael fruit shell–derived activated carbon adsorbent: effect of surface charge and pollutant type for improved adsorption capacity, Biomass Convers. Biorefin., 14 (2024) 8761–8774.

[77] B. M. Babic, S. K. Milonjic, M. J. Polovina, B. V. Kaludierovic, Point of zero charge and intrinsic equilibrium constants of activated carbon cloth, Carbon, 37 (1999) 477–481.

CHAPTER 3

ACTIVATED CARBON ADSORBENT DERIVED FROM WASTE BIOMASS, "*CROTON CAUDATUS*" FOR EFFICIENT REMOVAL OF 2-CHLOROPHENOL FROM AQUEOUS SOLUTION: KINETICS, ISOTHERM, THERMODYNAMICS AND DFT SIMULATION

This chapter aims to prepare an activated carbon (AC)[1] adsorbent developed from *Croton caudatus* biomass material for the adsorption of 2-chlorophenol (2CP) from wastewater. Activated carbon was prepared by KOH activation at 2:1 impregnation ratio and 700 ^{o}C temperature using a muffle furnace under self-generated atmosphere for 2 hours. Several techniques and methodologies such as proximate analysis, ultimate (CHNS) analysis, BET, SEM, FT-IR, XRD and point of zero charge (pH_{pzc}) have been used to determine physicochemical properties of the activated carbon. Batch adsorption studies were conducted for 2-chlorophenol adsorption and the optimum adsorbent dose, initial concentration, pH, reaction time and temperature were found to be 0.15 g/L, 80 mg/L, 4, 60 min and 298K, respectively. The equilibrium isotherm study for 2-chlorophenol adsorption was fitted well to the Langmuir model with the adsorption capacity of 53.619 mg/g, while the adsorption kinetics was best described by pseudo-second order model. Thermodynamic parameters demonstrated a negative ΔH (exothermic) and negative ΔG (spontaneous) values. Studies on regeneration have shown that saturated carbon can be recycled up to five times with considerable removal efficiency. Besides, density functional theory (DFT) simulation revealed that the adsorption of 2-chlorophenol onto AC adsorbent is favorable. Among the oxygen-containing functional groups, the carboxyl group appeared to have a greater influence on the adsorption process than the hydroxyl and carbonyl groups with the highest negative

[1] AC refers to activated carbon derived from *Croton caudatus* biomass, hereafter labeled as CCAC in following chapters.

$E_{adsorption}$ of -42.16 kJ/mol. Furthermore, the inclusion of three oxygen-containing functional groups improves the adsorption capacity of AC towards 2CP relative to a single functional group.

The text of this chapter has been published as:

S. Sharma, S. L. Ezung, A. Supong, M. Baruah, S. Kumar, R. S. Umdor, D. Sinha, Activated carbon adsorbent derived from waste biomass "*Croton caudatus*" for efficient removal of 2-chlorophenol from aqueous solution: kinetics, isotherm, thermodynamics and DFT simulation, Chem. Eng. Res. Des., 190 (2023) 777–792.

3.1 Introduction

Water pollution has become a major issue due to the release of inorganic and organic contaminants from various domestic and industrial effluents. Among the various aromatic organic pollutants that are found in water, phenolic compounds such as chlorophenols (CPs) have attracted enormous attention in recent years due to their poor biodegradable, toxic, carcinogenic, and mutagenic nature [1,2]. CPs are a class of phenolic derivates in which the Cl atom is covalently bound to the phenol molecule at the ortho, meta and para position. The presence of CPs in water is associated with a foul odor, an unpleasant taste, and deterioration of water quality suitable for drinking [3,4]. CPs are extensively used in pesticide, dye manufacturing, water disinfection operations, preserver production, petrochemicals, agriculture, biocide, cosmetic, industrial, and medicinal applications [5–7]. Since these compounds have been released into the environment, they are typically found in wastewaters, surface water, and ground water, inflicting severe damage to human health and the ecosystem [8]. CPs are weakly acidic and possess the ability to penetrate human skin and are absorbed easily by the gastrointestinal tract [9]. Furthermore, human exposure to such a pollutant can induce long-term impacts such as diarrhea, human nervous system impairment, excretion of black urine, as well as increased respiration rate, vomiting, and nausea [10–12]. Additionally, the U.S. EPA Clean Water Act and European Decision 2455/2001/EC has labeled them a priority contaminant due to their acute toxicity, carcinogenic characteristics, structural stability, and environmental persistence, even at low doses below 0.1 μg/L [13,14].The toxicity of chlorophenol rises as the level of chlorination increases. Despite their helpful biocidal properties, they are hazardous at higher concentrations [15]. Owing to this, effective chlorophenol removal from wastewater has been a continual challenge.

A variety of water treatment technologies have been developed to treat pollutants, including physical, chemical, and biological methods [16]. Moreover, traditional and cutting-edge approaches have been used to address the issue of monochlorinated phenols in wastewater, and much research has been undertaken. These include chemical coagulation, electrochemical oxidation, modified surfactant natural zeolite, adsorption, photochemical treatment, solvent extraction, biological treatment with anaerobic sludge, reverse osmosis, photodegradation, fuel oil fly ash, membrane

separation and ozonation, respectively [17-24]. However, many of these methods are having its limitations unsuccessful and raise the overall cost of manufacturing because of their high energy consumption, complexity, low efficiency, challenging operational approaches, and the production of harmful by products. Adsorption, on the other hand, is considered one of the best available technologies due to its excellent efficiency, simplicity in design, and formation of fewer secondary components [25,26].

A variety of adsorbents have been investigated for removing phenolic derivates from wastewater, including clay, activated carbon, polymers, zeolites, and chitosan [27-30]. Notably, it was found that activated carbon (AC) is the most potent adsorbent among others because of its unique properties, including large porosity, enormous surface area, abundant functional groups, and significant chemical and thermal stability [31-34]. Moreover, the use of commercial AC has also been limited because of its expensive cost of raw material and low recyclability [35,36]. Therefore, utilizing diverse biomass resources to synthesize activated carbon emerged as an option with several advantages such as affordability, availability, environmental friendliness, and renewability [37,38]. In this regard, studies have been undertaken on the treatment of organic pollutants from wastewater with activated carbon. For example, 2-chlorophenol was removed from aqueous solutions with AC prepared using *Ricinus communis pericarp* [3]. As described by Ezung et al. [39], AC was developed from biomass of bamboo sheath, and its ability to remove 2,4-dichlorophenol from aqueous medium was studied. Supong et al. [31] reported that Bisphenol A could be removed effectively from wastewater using *Tithonia diversifolia* activated carbon. AC synthesized from Neem leaf was used as a potential adsorbent for the removal of 4-Nitrophenol, Phenol, and 4-CP, as suggested by Rincón-Silva et al. [40]. Biochar prepared from pine fruit shells for the adsorption of phenol was reported by Mohammed et al. [17]. Altıntıg et al. [41,42] have successfully synthesized the magnetic AC adsorbent such as Fe-AC and Fe_3O_4-AC for the efficient removal of dyes (methylene blue and malachite green) from aqueous media. The removal of rhodamine B using magnetic AC/CeO_2 nanocomposite has been reported by Tuzen et al. [43]. Thus, in this study, attempts were made to design a novel and less priced AC by utilizing locally available *Croton caudatus* biomass for the adsorption of 2-chlorophenol (2CP) from wastewater.

Density functional theory (DFT) has been used to study the adsorption mechanism between adsorbate and adsorbent over the years. For example, Supong et al. [44,45] reported the interaction of 2,4-dinitrophenol and cresol with AC surfaces containing different oxygen containing functional groups (–OH, –CHO and –COOH). Among the functional groups, the results were found that (AC)COOH functional group interacted more strongly with 2,4-dinitrophenol and cresol. The effect of SO_2 on Hg adsorption on carbonaceous surfaces were investigated using DFT method by Liu et al. [46]. Jan et al. [47] studied the effect of various functional groups (–OH, –COOH, $–NO_2$, $–CH_2$ or $–CH_3$, –C=C, –C=O, and $–SO_3$) for the adsorption of azo dye. Shen et al. [48] investigated the interactions of hydrogen sulphide (H_2S) with the active sites of armchair and zigzag surfaces of AC. It has been found that the adsorption of H_2S is attracted more strongly to zigzag edge sites than to armchair edge sites.

Studies using DFT simulation suggested that 2,4-dichlorophenol adsorption could be affected by several interactions on functionalized activated carbon surfaces (–CHO, –CO–, –CCO, –OH and –COOH). Among these, –OH functionalized group attached to AC surface tended to influence the adsorption process for the removal of 2,4-dichlorophenol [39]. However, the adsorption interactions between the surface of AC and 2CP molecules are still not well understood. Thus, DFT studies were utilized to investigate the impact of oxygen functional groups like hydroxyl (–OH), carbonyl (–CHO) and carboxyl (–COOH) groups on the mechanism of 2CP adsorption by the AC surface. This insight will be extremely useful in creating effective sorbents for the removal of 2CP from aqueous medium.

Therefore, the current study aimed to evaluate the removal of 2CP onto AC prepared from *Croton caudatus* biomass both experimentally and computationally. The produced adsorbent was then analyzed using various techniques and batch operation were performed. In addition to the regeneration studies, thermodynamic and kinetic equilibrium adsorption isotherms of adsorption were also investigated. Moreover, DFT studies were carried out to elucidate the bonding and reactivity of pristine activated carbon (p_AC) and functionalized activated carbon such as hydroxyl functionalized activated carbon –OH(AC), carbonyl functionalized activated carbon –CHO(AC), and carboxyl functionalized activated carbon –COOH(AC). Therefore, the results of this work may provide novel strategies and better understanding in selecting the suitable

chemical activating agent to tailor the carbon surface in the removal of phenolic chemicals from wastewater.

3.2 Materials and method

3.2.1 Materials

Croton caudatus biomass used in the study was gathered locally at Nagaland University (26° 13′29.60″ N | 94° 28′ 35.0″ E), India. The entire plant's resources were utilized to produce activated carbon. The collected material was cut into small pieces (average length of 1.5 cm) and rinsed multiple times with deionized water to eliminate any residues from the surface. The CCB was then oven-dried at 105°C for 24 hours to reduce the moisture content from the water. 2-Chlorophenol (ClC_6H_4OH, molecular weight= 128.56 g/mol, purity ≥ 98%) was supplied by Sigma (Sigma-Aldrich Chemicals Pvt. Ltd., Bangalore, India). Figure 3.1 depicts the structural representation of 2CP. A stock solution of 1000 mg/L of the adsorbate was obtained by adding the desired amount of 2CP in deionized water and then diluted to produce working solutions of different proportions. Analytical-grade chemicals (Merck Specialities Pvt. Ltd., Mumbai, India) were utilized for all the remaining work without further purification.

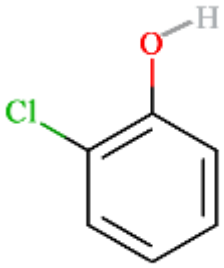

Figure 3.1. Chemical structure of 2-chlorophenol.

3.2.2 Preparation of activated carbon

The preparation of activated carbon was carried out into two stages with slight modification as described by Youssef et al. [49]. The dried raw material was initially carbonized at 500 °C for 1 hour in a muffle furnace. The carbonized sample were then grinded using mortar and pestle to attain uniform size carbon char (average size of ~1 mm). Afterwards, the powdered carbonized char was further immersed in potassium hydroxide (KOH) solution for activation. For chemical activation, a mixture of 40 g of

KOH pellets and 20 g of carbonized char was dissolved in 500 mL of deionized water maintaining the ratio of 2:1 (KOH: carbonized carbon) [31]. The KOH impregnated sample was magnetically agitated for 2 hours and dried at 110 °C overnight in an oven. The impregnated carbon sample was then pyrolyzed at 700 °C using a *muffle furnace under* self-generated atmosphere for 2 hours. The mixture was cooled to room temperature and then washed in a solution of 0.1 M hydrochloric acid (HCl), 0.1M sodium hydroxide (NaOH) and hot deionized water until the pH was between 6 and 7. The collected samples were dried in a 110°C hot air oven for 24 hours and the obtained activated carbon was labeled as CCAC (*Croton caudatus* activated carbon). Furthermore, the prepared sample were stored in air tight container prior to further use. The preparation procedure of CCAC is shown in Figure 3.2.

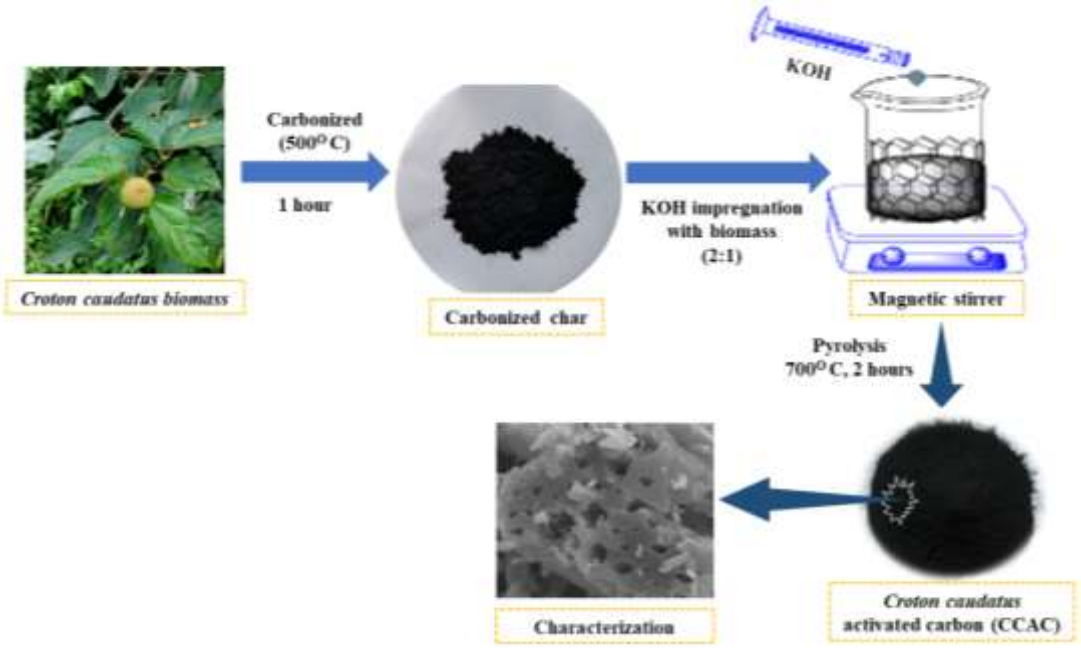

Figure 3.2. Schematic representation for the preparation of *Croton caudatus* activated carbon.

3.2.3 Activated carbon characterization

Proximate analysis of CCAC for determination of ash content, moisture content, fixed carbon and volatile matters was done by using standard ASTM D1762-84 method [50] while ultimate analysis was performed using CHNS elemental analyzer (Model: EA3000, Eurovector, Italy) to determine the carbon, hydrogen, nitrogen and sulphur contents. Pore structure and surface area measurements of CCAC were determined

through N_2 adsorption–desorption isotherm at 77K using a Surface Area Analyzer (Model: Smart Sob 93, Smart Instruments, India). X-ray diffraction analysis was carried out to determine the crystallinity or amorphous nature of CCAC. The analysis was performed by X-ray diffractometer (XRD; Model: ULTIMA IV, Rigaku, Japan) using CuK_α radiation with a diffraction angle (2θ) varied from 10º to 80º. The surface physical morphology of CCAC was observed through a scanning electron microscope (SEM; Model: JSM 6390LV, JEOL, USA) at an accelerating voltage of 20 kV. The surface functional groups of CCAC were identified through Fourier-transform infrared spectroscopy (FT-IR; Model: Spectrum Two, Perkin Elmer, USA). The spectrum data was recorded with a resolution of 4 cm^{-1} over the range of 500–4000 cm^{-1}. The 2CP residual concentration was determined using a UV Vis instrument (Lambda 365, PerkinElmer, USA) at the maximum absorbance of 273 nm. The point of zero charge (pH_{ZPC}) of the prepared activated carbon was determined by the batch equilibrium test [51].

3.2.4 Adsorption equilibrium experiments

The batch adsorption technique was carried out for the adsorptive removal of 2CP from wastewater. A number of batch equilibrium measurements were performed to study the effects of temperature, pH, initial concentration of adsorbate, adsorbent dosage, and contact time for the adsorption of 2CP on the activated carbon. All of the investigations have been carried out in Erlenmeyer flasks, and the concentration of 2CP was quantified using UV Vis spectrophotometer at its maximum absorbance of 273 nm. All of the measurements were done in triplicate intervals. The equilibrium capacity, q_e (mg/g) and removal % were calculated by Equation (3.1) and (3.2), respectively:

$$\% \text{ Removal} = 100 \times \frac{C_i - C_e}{C_i} \tag{3.1}$$

$$q_e = V \times \frac{C_i - C_e}{M_s} \tag{3.2}$$

where the initial and equilibrium concentrations of 2CP in aqueous phase are expressed by C_i and C_e (mg/L) respectively, 2CP solution volume is represented by V (L), and the mass of AC by M_s (g).

3.2.5 Statistical analysis

The best-fitting isotherm and kinetics model were confirmed by the residual root mean error (RMSE) and Chi-squared (χ^2) analysis that was used to evaluate the experimental data. The χ^2 values were calculated by [52]:

$$\chi^2 = \sum_{i=1}^{m} \frac{(q_e - q_c)^2}{q_c} \quad (3.3)$$

The q_e and q_c correspond to the estimated and calculated values from the batch experiments; m is the no. of observations to be determined. If the kinetic and isotherm model data are equivalent to the experimental results, then the value of χ^2 will be a relatively small number.

The RMSE values were calculated by [53]:

$$\text{RMSE} = \sqrt{\frac{1}{m-2}} \sum_{i=1}^{m} (q_e - q_c)^2 \quad (3.4)$$

where the lower RMSE value indicates better curve fitting.

3.3 Theoretical studies of 2CP adsorption onto activated carbon (AC)

3.3.1 Computational method

Simulations based on the DFT method were performed with the Gaussian 16W program to explore possible interactions between 2CP and activated carbon (AC). Gauss View 6.0 were used to design and visualize the structure of the pristine AC, functionalized AC and 2CP. Geometric optimizations and energy calculations in a dielectric medium (ε = 80) were also performed utilizing B3LYP/6-31G level theory. $E_{adsorption}$ of 2CP on AC's surface was computed using the equation

$$E_{adsorption} = E_{system} - (E_{adsorbent} + E_{adsorbate}) \quad (3.5)$$

where, E_{system}= Total energy of the adsorbent and adsorbate, $E_{adsorbent}$ = Total energy of the adsorbent (AC), $E_{adsorbate}$ = Total energy of the adsorbate (2CP). Moreover, a higher value of negative $E_{adsorption}$ indicates a more stable arrangement, whereas a positive $E_{adsorption}$ value denotes unfavorable adsorption [54].

3.3.2 Modeling of AC

An appropriate model must be generated to explore the interaction between 2CP and

An appropriate model must be generated to explore the interaction between 2CP and AC surfaces. A solid-state 13C Nuclear magnetic resonance (NMR) study indicated that the surface of activated carbon is composed of three- to seven-fused benzene structure [55]. Consequently, the AC surface was developed using arm-chair model comprised of six-fused benzene complex with arm-chair edge.

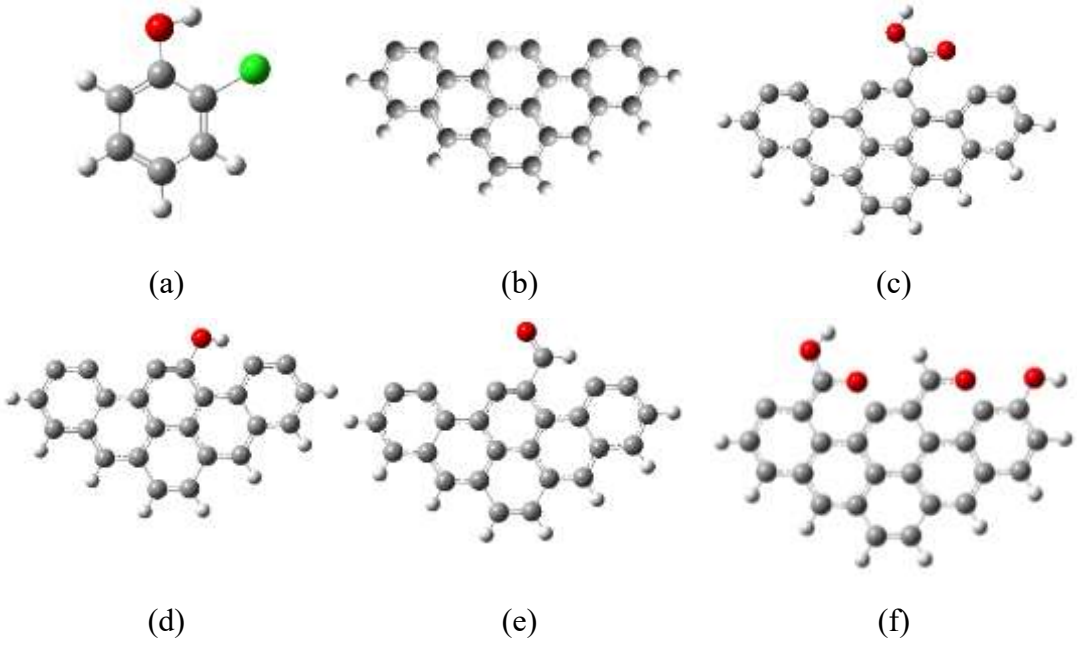

Figure 3.3. The optimized structures of (a) 2-CP (b) p_AC (c) –COOH(AC) (d) –OH(AC) (e) –CHO(AC) (f) OH+CHO+COOH(AC).

Furthermore, six-fused rings were selected since the calculations provide an acceptable balance between accuracy and computational cost. In the armchair model, the top C-atoms were unsaturated to develop an active site, while the rest were capped with H-atoms. To explore the influence of surface functional groups on 2CP adsorption, the active region of the carbon was embedded with oxygen containing functional groups –OH, –COOH, and –CHO. Figure 3.3 (a) depicts the optimized structure of 2-chlorophenol, while Figure 3.3 (b-e) present the optimized cluster models of activated carbon employed in this investigation. The models of activated carbon (AC) were designated as pristine-activated carbon (p_AC), –COOH embedded AC (–COOH(AC)), –OH embedded AC (–OH(AC)), and –CHO embedded AC (–CHO(AC)).

3.4 Results and discussion

3.4.1 Characteristics of CCAC

The results of the ultimate and proximate analyses of CCAC are shown in Table 3.3.1. The results of the ultimate analysis of prepared CCAC are as follows: 47.90 % carbon (C), 2.06 % hydrogen (H), 0.18 % sulphur (S), 1.70 % nitrogen (N) and 48.16 % oxygen (O). Ash content decreases the adsorption ability of activated carbon and the effectiveness of reactivation [56-58]. These results are in good agreement with the results reported by several other authors [59-61]. Egirani et al. [62] synthesized AC from palmae shells which contains 47.23 % carbon, 6.88 % hydrogen, 0.77 % nitrogen, 44.86 % oxygen, 0.25 % sulphur, respectively and was successfully used as an adsorbent for mercury removal with highest adsorption efficiency of 93 %. Similarly, Paluri et al. [63] also reported AC derived from banana root with carbon, hydrogen, nitrogen and oxygen contents of 47.52 %, 2.15 %, 5.69 % and 44.6 %, respectively, and utilized for the adsorption of methylene blue. In a study by Altintig et al. [64], activated carbon was made from acorn shells with a fixed carbon content of 31.32 % and an ash content of 8.46 % for removal of methylene blue. In comparison with several earlier reported results, the present synthesized AC derived from *Croton caudatus* has a moderate carbon content and a low ash level, thus making it a promising material for adsorption of 2CP from wastewater.

Table 3.1. Ultimate and proximate analyses results of CCAC.

Ultimate analysis (Wt%)		Proximate analysis (Wt%)	
C	47.90	Ash	6.10
H	2.06	Moisture	0.64
S	0.18	Volatile	52.90
N	1.70	Fixed carbon[b]	40.36
O[a]	48.16		

[a,b] Estimated by difference

The functional groups on the CCAC surface were studied using FTIR analysis, and the resultants are depicted in Figure 3.4. The band at 3451 cm^{-1} could be attributed to vibrations caused by O–H stretching of hydrogen bonded hydroxyl groups [65]. Two narrow bands at 2942 and 2825 cm^{-1} might be due to symmetric and asymmetric C–H stretching vibrations for alkanes, and alkyls respectively. The stretching vibrations of C=O in ester, acetyl, ketones, and aldehydes derivatives cause the development of a

band at 1751 cm^{-1}. There are two bands at 1636 cm^{-1} and 1433 cm^{-1} which correspond to the C=C and C–O stretching vibration of the carboxyl group [66,67]. The two bands at 1162 cm^{-1} and another at 1016 cm^{-1} indicate the stretching vibrations of C–O groups [68-70].

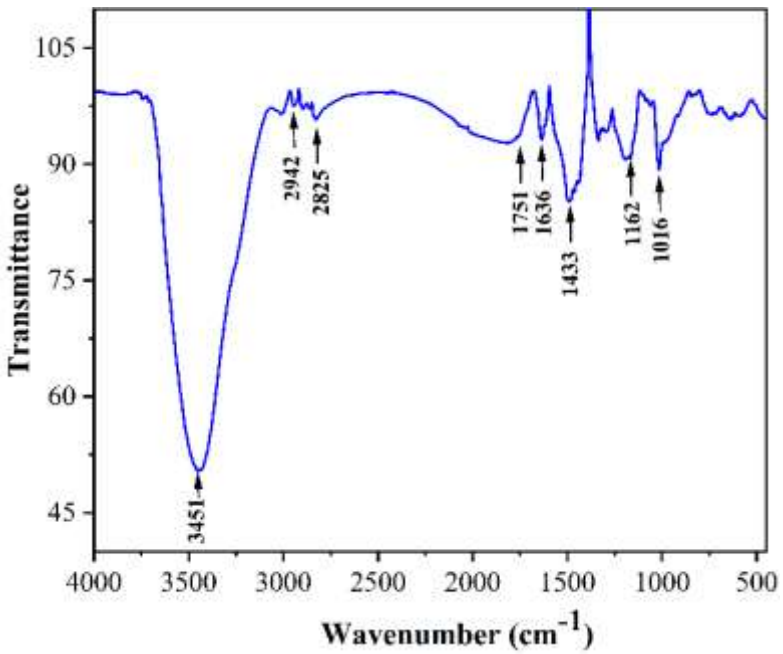

Figure 3.4. FTIR spectrum of *Croton caudatus* activated carbon.

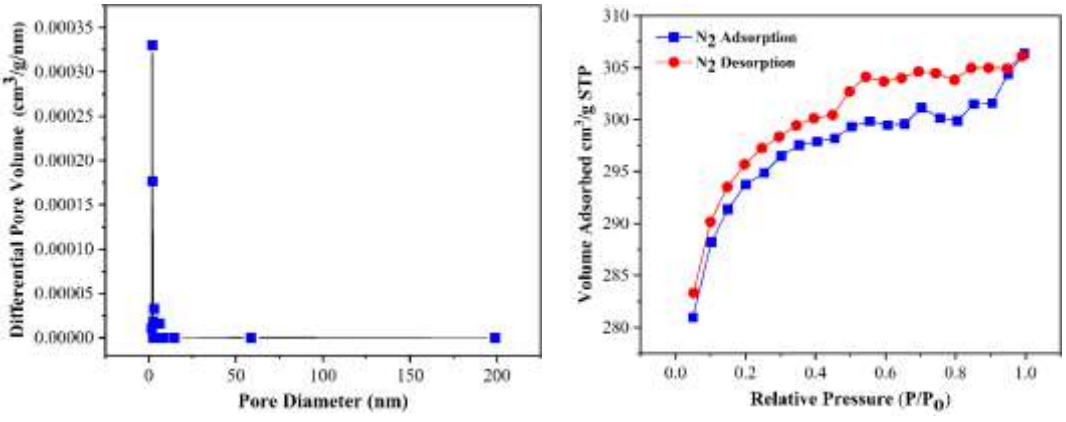

(a) **(b)**

Figure 3.5. (a) Pore size distribution (b) N_2 adsorption-desorption isotherm plot of *Croton caudatus* activated carbon.

The pore size distribution and N_2 adsorption–desorption isotherms of CCAC are shown in Figure 3.5. The prepared CCAC has a BET surface area of 846.29 m^2/g and a total pore volume of 0.019 cm^3/g, and an average pore diameter of 3.82 nm, respectively. According to IUPAC classification, type I isotherm can be associated with

microporous structure while type IV isotherm exhibited by mixture of mesoporous and microporous material [71]. Similar results have been reported by Ren et al. [72].

XRD was used to explore the amorphous or crystalline natures of the synthesized CCAC. The relatively broad diffraction peaks of this activated carbon and the absence of a sharp peak confirms that it has a mostly amorphous structure. As shown in Figure 3.6a, there are two broad asymmetric peaks that correspond to the diffraction of (002) and (101) planes at 2θ = 26° and 44° (JCPDS-00-001-0646) which indicate the formation of hexagonal graphite carbon, respectively [9]. Thus, the occurrence of such bands confirms the graphite like micro-crystallite nature of CCAC. The average crystallite size of the produced CCAC was calculated using the Debye Scherer equation [73],

$$D = \frac{K\lambda}{\beta \cos\theta} \tag{3.6}$$

where, D is the average crystalline size, λ and β represents the wavelength of X-ray radiation (CuK_α = 0.15 nm) and line width half maxima of the peaks, respectively, K is a constant taken as 0.89 and θ is the Braggs diffraction angle. The average crystallite size of CCAC adsorbent is found to be ~17.5 nm.

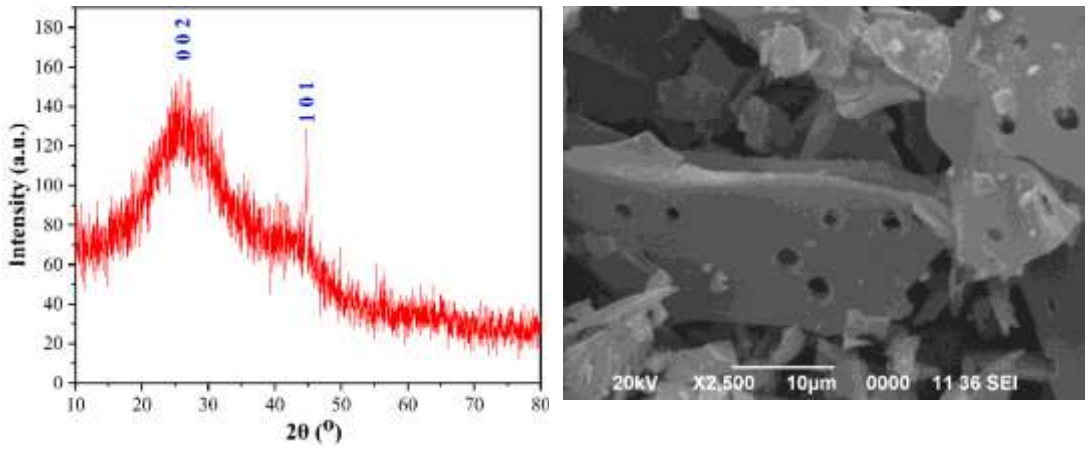

(a) **(b)**

Figure 3.6. (a) XRD diffraction pattern and (b) Scanning electron microscopy (SEM) micrograph of *Croton caudatus* activated carbon.

SEM is widely used to analyze the morphological characteristics and surface properties of adsorbent materials. The micrographs of CCAC in Figure 3.6b shows the pores of various sizes, shapes and dimensions scattered throughout the surface. The

CCAC sample shows an irregular surface structure, which might be due to the interaction of KOH with the precursor caused by the release of volatiles and the formation of cavities during the carbonization and activation processes.

3.4.2 Batch equilibrium studies

(i) Effect of CCAC dose

Adsorbent dosage is an essential adsorption parameter as it has a substantial impact on the adsorption capacity of the adsorbent and the removal efficiency of contaminants, which are interdependent; therefore, it is essential to select the appropriate adsorbent dosage. The influence of the CCAC dose on 2CP adsorption from water was studied at different CCAC doses in the range of 0.05-0.35 g/L. From the Figure 3.7, as the carbon dose varied from 0.05-0.15 g/L, the effectiveness of 2CP removal improved from 89.25 % to 98.50 %, whilst, a decrease in the adsorption capacity was seen from 71.40 mg/g to 26.27 mg/g.

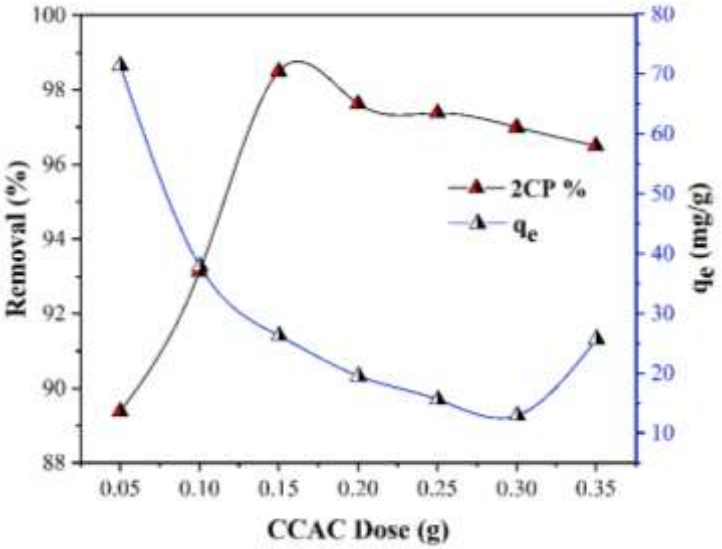

Figure 3.7. The effect of CCAC dose on 2CP adsorption (Initial 2CP concentration: 80 mg/L; Reaction time: 60 min; pH 4; Temperature: 298K).

These results clearly demonstrated that the removal efficiency and adsorption capacity were inversely related with adsorbent dosage. Adsorption capacity was reduced as adsorbent dosage was increased because the available surface area and adsorption active sites could not be effectively exploited in the presence of excess adsorbent [3], particularly when 98.50 % removal efficiency was obtained. Therefore, 0.15 g/L of adsorbent was chosen as the ideal dose for following studies.

(ii) Effect of 2CP concentration

The influence of starting concentration (40–140 mg/L) on 2CP removal and adsorption capacity from the aqueous phase was studied. As evident in Figure 3.8, 98.63 % removal rate was possible in the initial concentration of 80 mg/L, indicating that 2CP have been almost removed. Accordingly, a similar trend was observed with the rise in adsorption capacity from 12.57 mg/g to 26.30 mg/g. As initial concentrations rise till 140 mg/L, the removal efficiency slightly dropped to 90.40 % while q_e increased up to 42.17 mg/g. The removal efficiency for 2CP was obtained at a concentration of 80 mg/L [74]. Similar results have been reported by Daifullah et al. [75].

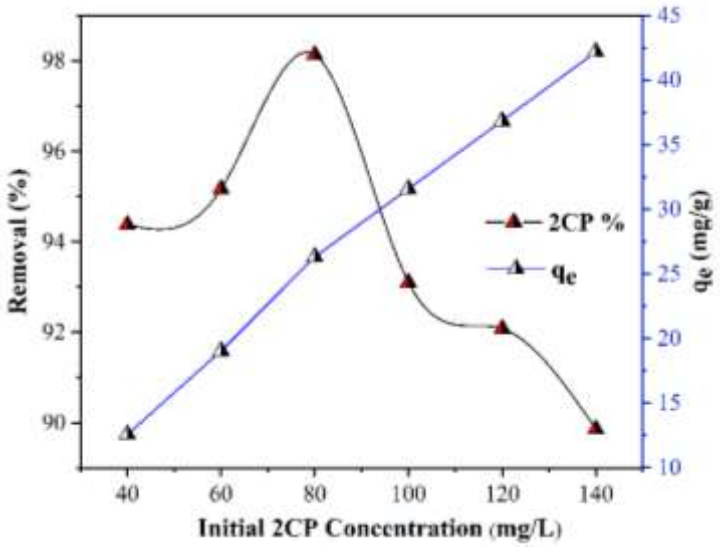

Figure 3.8. The effect of initial concentration on 2CP adsorption (CCAC dose: 0.15 g/L; Reaction time: 60 min; pH 4; Temperature: 298K).

(iii) Effect of reaction time

Figure 3.9 represents the influence of reaction time on adsorption efficiency of 2CP. A variation of reaction time (15–90 min) was evaluated at constant conditions (pH-4, 80 mg/L initial concentration, 298K temperature and 0.15 g/L adsorbent dose). During the initial stages, the absorption of 2CP increased significantly and then slowed as the equilibrium was reached that may be attributed due to the availability of a large number of readily accessible sites on the adsorbent surface. Eventually, the system reached equilibrium after about 60 min as the removal rate slowed down with reaction time [76,77]. Accordingly, 60 min was determined as the optimum reaction period to conduct additional adsorption tests.

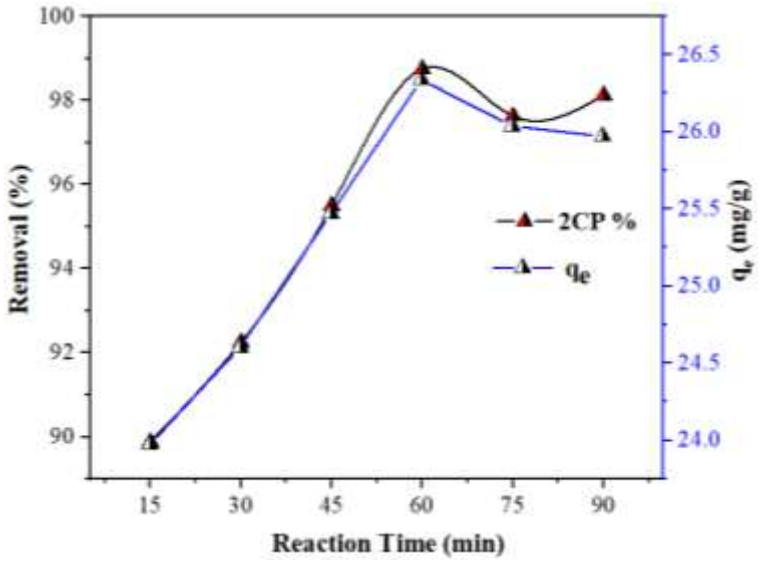

Figure 3.9. The effect of reaction time on 2CP adsorption (Initial 2CP concentration: 80 mg/L; CCAC dose: 0.15 g/L; pH 4; Temperature: 298K).

(iv) Effect of pH

The experiments with pH solutions varying from 2 to 12 were carried out to examine the impact of pH on the rate of adsorption. As depicted in Figure 3.10, the effectiveness of 2CP was determined to slightly rise with an increase in pH solution range between 2 and 4, but decline thereafter with increasing pH levels above 4. Usually, pH solutions have a substantial impact on the adsorbent's surface charge as well as the ionic strength of the adsorbate [78]. The pH_{zpc} of the CCAC was determined to be 7.1, while the pK_a of 2-chlorophenol was 8.56. Therefore, at a lower pH value (pK_{zpc}>pH), the protonated CCAC surface (pK_{zpc}>pH) formed strong interaction with unionized halogenated chlorophenol (pK_a>pH) resulting in optimum efficiency. However, at higher pH values (pK_{zpc}<pH), the adsorption process decreases due to the ionization of 2CP molecules (pK_a<pH). This could be due to electrostatic repulsion developed between the chlorophenolate anions, and negatively charged CCAC surface and between chlorophenolate - chlorophenolate anions in solution [79,80]. As a result, the maximum removal of 2-chlorophenol removal was found at pH 4 with the removal efficiency of 98.38% and adsorption capacity of 26.33 mg/g as compared to higher pH. Therefore, pH 4 was chosen as an optimum pH value for the remaining studies.

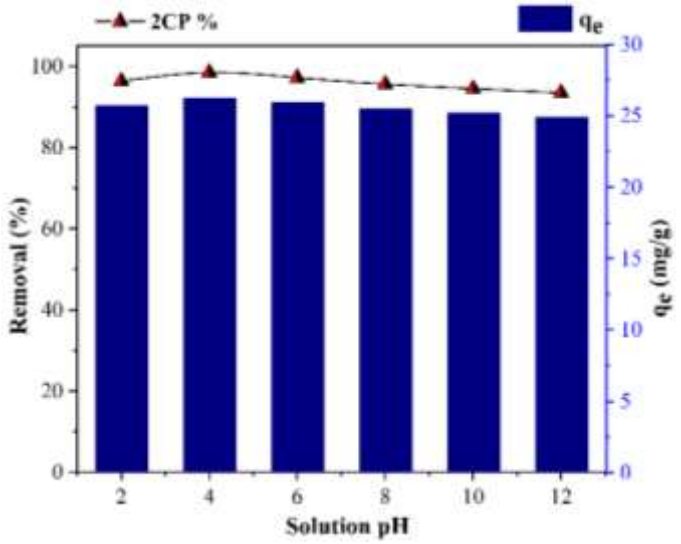

Figure 3.10. The effect of pH on 2CP adsorption (Initial 2CP concentration: 80 mg/L; CCAC dose: 0.15 g/L; Reaction time: 60 min; Temperature: 298K).

(v) Effect of temperature and adsorption's thermodynamics

The influence of temperature on 2CP adsorption by CCAC was examined using thermodynamic approach at temperatures of 298K, 308K, 318K, and 328K.

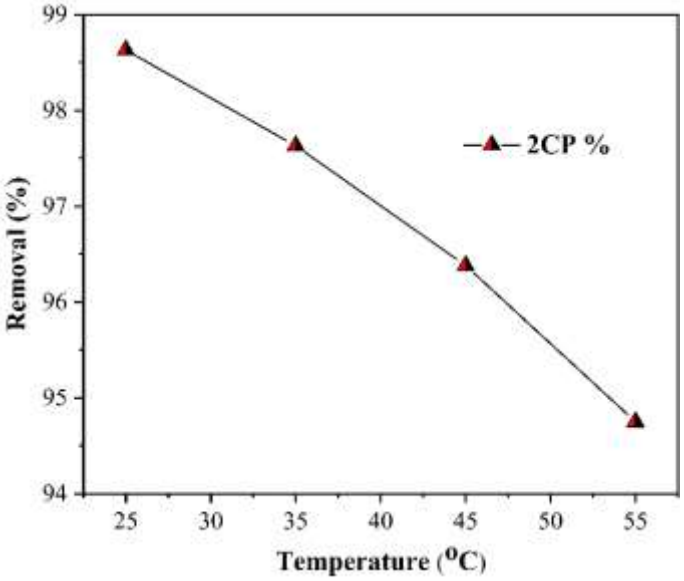

Figure 3.11. The effect of temperature on 2CP adsorption (CCAC dose: 0.15g/L, Initial 2CP concentration: 80 mg/L, Reaction time: 60 min, pH 4).

As observed from the plot (Figure 3.11), the amount of 2CP adsorbed by CCAC decreases with an increase in temperature, suggesting that the removal of 2CP was favorable at a lower temperature. Moreover, the decline in the adsorption efficiency with the rise in temperature could be due to the weakening of the adsorptive forces

between the adsorbent's active sites and the adsorbate species. Hence, the optimum temperature for the adsorption process is 298K.

The thermodynamic parameters of free energy change (G), enthalpy (H), and entropy (S) were used to determine the viability of the adsorption process. These can be computed by the following equations:

$$\ln K_d = \frac{\Delta S}{R} - \frac{\Delta H}{RT} \quad (3.7)$$

$$K_d = \frac{q_e}{C_e} \quad (3.8)$$

$$\Delta G = -RT \ln K_L \quad (3.9)$$

where, K_d = thermodynamic distribution coefficient, q_e = adsorbed 2CP concentration on CCAC, C_e = 2CP concentration at equilibrium, T (K) = absolute temperature, R = universal gas constant.

In this study, ΔS and ΔH values were calculated from the intercept and slope of the plot between ln K_d Vs 1/T, respectively. Table 3.3.2 shows the calculated values of ΔS, ΔH, and ΔG for adsorption of 2-chlorophenol onto CCAC. The negative values of ΔG at various temperatures (298K, 308K, 318K and 328K) indicated that the process of adsorption was feasible and occurred spontaneously.

Table 3.2. Thermodynamic parameters of 2CP adsorption onto CCAC adsorbent at different temperatures.

Adsorbent	ΔH (kJ/mol)	ΔS (kJ/mol/K)	ΔG (kJ/mol)			
			298K	308K	318K	328K
CCAC	-37.247	-0.099	-7.864	-6.703	-5.768	-4.893

Additionally, the magnitude of ΔG decreased with increasing temperatures, signifying that the spontaneous process was diminishing, making the adsorption unfavorable at higher temperatures. Thus, it is possible to conclude that the adsorption process is more favorable at lower temperatures. The negative ΔH value confirms an exothermic nature of the adsorption process, while the negative value of ΔS revealed the high orderliness at the solid/liquid interface during 2CP adsorption onto CCAC [81].

3.4.3 Adsorption isotherm models

Four isotherm models: Langmuir, Freundlich, Temkin, Dubinin - Radushkevich (D-R) were used to analyze a study of the equilibrium adsorptive behavior of 2CP onto the CCAC (Figure 3.12). The linearized form of isotherm parameters and their coefficient values were presented in Table 3.3.

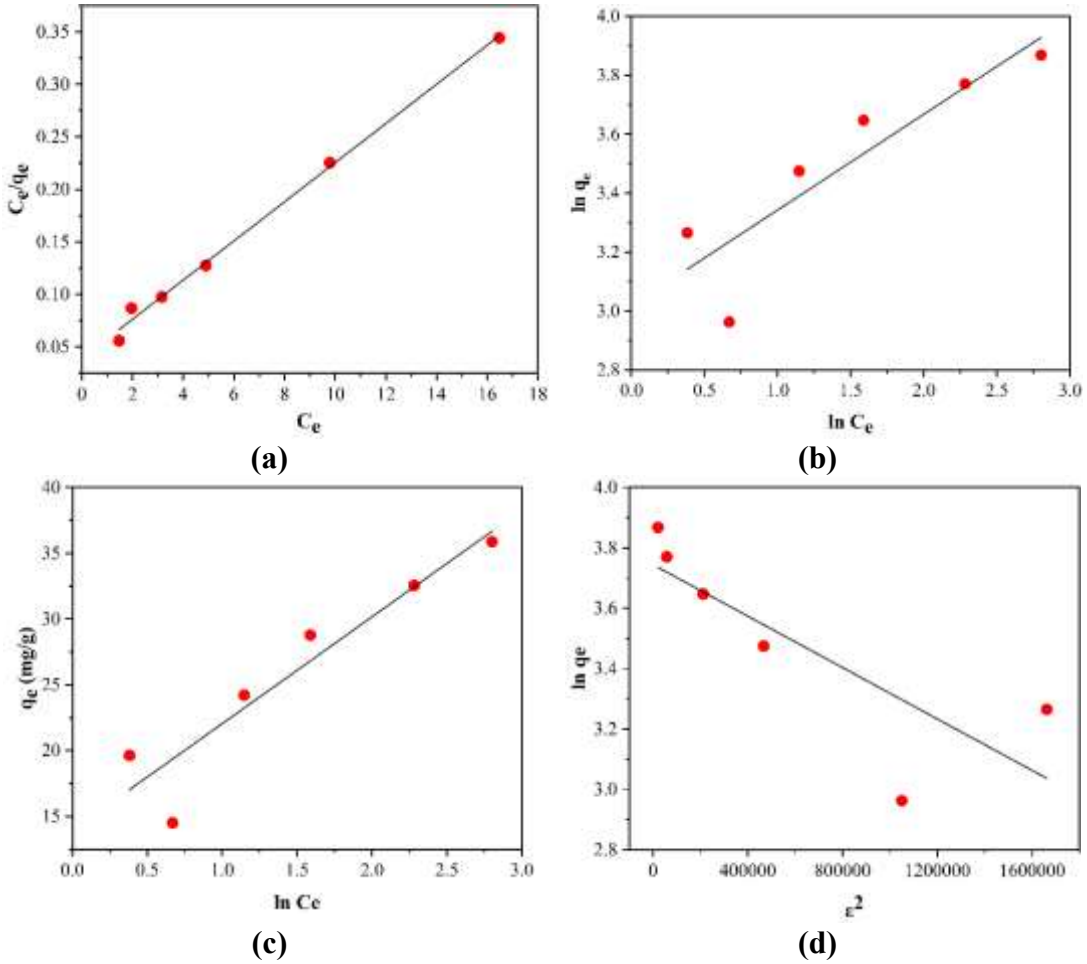

Figure 3.12. (a) Langmuir isotherm model (b) Freundlich isotherm model (c) Temkin isotherm model and (d) Dubinin - Radushkevich (D-R) isotherm model for 2CP adsorption onto CCAC adsorbent.

The R^2 value and χ^2 depicted in Table 3.3 signifies that the 2CP adsorption was described well by the Langmuir model; a possibility of 2CP monolayer formation on the CCAC surface with a Q_{max} value of 53.619 mg/g. The computed R_L value in this study was 0.958, indicating that the adsorption of 2CP onto CCAC occurs efficiently [82]. Moreover, the value of Freundlich constants 'n' was above unity thereby confirming that the adsorption was highly favorable [83]. However, the R^2 = 0.754

obtained in Freundlich mode indicates that the Langmuir isotherm model amazingly performs better in fitting the equilibrium data for 2CP. The result obtained was further analyzed using the Temkin isotherm model to determine equilibrium at room temperature.

Table 3.3. Adsorption isotherm models, its parameters and correlation coefficients of 2CP adsorption onto CCAC adsorbent.

Isotherms Models	Parameters	R^2	χ^2	RMSE
Langmuir, $\frac{C_e}{q_e} = \frac{1}{Q_{max} K_L} + \frac{1}{Q_{max}} C_e$ $R_L = \frac{1}{1 + K_L C_O}$	Q_{max}= 53.619 K_L=0.0007 R_L= 0.958	0.997	6.6 ×10^{-5}	0.058
Freundlich, $\ln q_e = \ln K_F + (1/n) \ln C_e$	1/n = 0.325 n = 3.078 K_F = 1.147	0.754	5.3 × 10^{-3}	0.073
Temkin, $q_e = \frac{RT}{b_T} \ln A_T + \frac{RT}{b_T} \ln C_e$	b_T = 8.118 A_T = 4.665	0.862	8.9244	2.987
Dubinin - Radushkevich (D-R), $\ln q_e = \ln q_{DR} + \beta_{\varepsilon^2}$ $\varepsilon = RT \ln [1 + \frac{1}{C_e}]$ $E = \frac{1}{(2\beta)^{1/2}}$	q_{DR}= 42.266 $\beta = 4.3 \times 10^{-7}$ E = 1.084	0.588	0.0473	0.218

C_e (mg/L) = 2CP concentration at equilibrium, q_e (mg/g) = amount of 2CP adsorbed at equilibrium, q_{max}(mg/g) = adsorption capacity, K_L (L/mg) = Langmuir isotherm constant, K_F (mg/g. (L/mg)$^{1/n}$) = Freundlich constant, 1/n = dimensionless heterogeneity constant, T (K) = absolute temperature, b_T (kJ/ mol) = constant correspond to heat of sorption, A_T (L/mg) = equilibrium binding constant, R = universal gas constant, q_{DR} (mg/g) = monolayer adsorption capacity, β (mol^2/kJ^2)= D-R constant of adsorption energy, ε = D-R isotherm constant, E (kJ/mol)= mean free energy

The calculated value of b_T corresponds to the heat of adsorption and A_T is shown in Table 3.3. Based on the results obtained, it was found that the Temkin's model was inadequate in explaining the adsorption mechanism. From D-R model, q_{DR} and mean free energy (E) was determined to be 42.266 mg/g and 1.08 kJ/mol. The R^2 value of 0.588 demonstrates that the D-R isotherm model does not fit the adsorption data.

Moreover, a chi-square test and RMSE analysis were used to validate the isotherm models. All four adsorption isotherm models were evaluated by comparing their R^2, χ^2 and RMSE values. The Langmuir model is well-suited for the adsorption of 2CP,

with a maximum correlation coefficient R^2 = 0.997 and lowest χ^2 (6.6 ×10^{-5}) and RMSE (0.056) values.

3.4.4 Adsorption kinetic studies

Adsorption kinetics describe the uptake rate that determines the adsorbate's residence period at the solid-liquid interface [84].

Table 3.4. Pseudo-first order, pseudo-second order, and intra-particle diffusion parameters for the adsorption of 2CP onto CCAC adsorbent.

Kinetic Models	Parameters	R^2	χ^2	RMSE
Pseudo-first order, $\ln(q_e - q_t) = \ln q_e - k_1 t$	$q_{e,\ exp}$ = 26.333 $q_{e,\ cal}$= 18.125 k_1 = 0.065	0.907	7.7 × 10^{-2}	0.279
Pseudo-second order, $\frac{t}{q_t} = \frac{1}{k_2 q_e^2} + \frac{t}{q_e}$	$q_{e,\ exp}$ = 26.333 $q_{e,\ cal}$= 26.653 k_2 = 0.0201	0.999	7.2 × 10^{-4}	0.027
Intra-particle diffusion, $q_t = k_{id} t^{0.5} + c$	k_{id} = 6.677 c =13.766	0.916	8 × 10^{-2}	0.299

q_e (mg/g) = equilibrium adsorption capacity, q_t (mg/g) = adsorption capacity at any time t (1/min), k_1 (1/min) = adsorption rate constant, k_2 (g/mg/min) = pseudo second order rate constant, k_{id} (mg/g/$min^{0.5}$) = rate constant of intra-particle diffusion

To investigate and predict the adsorption behavior of 2CP onto CCAC adsorbent, three types of kinetic models were considered i.e., pseudo-first order, pseudo-second order and intra particle diffusion models [85,86]. Figure 13 depicts the plot of kinetic studies for the 2CP adsorption onto CCAC adsorbent and the fitting parameters are tabulated in Table 3.4.

In the present work, the best fitting kinetic model was selected by analyzing the correlation coefficients (R^2), χ^2 and RMSE values between experimental data and theoretical values. From the plot of ln (q_e - q_t) vs t (min) (Figure 3.13a), the calculated data ($q_{e,\ cal}$= 18.125 mg/g) were significantly deviated from the experimental values ($q_{e,\ exp}$ = 26.333 mg/g), which indicates a poor applicability of the pseudo-first order. Contrary, the calculated q_e values ($q_{e,\ cal}$= 26.653 mg/g) was close similar to the experimental data ($q_{e,\ exp}$ = 26.333 mg/g) for the pseudo-second order (Figure 3.13b), suggesting its good applicability for this model. Weber and Morris' intra-particle

diffusion model was also used to analyze the adsorption kinetics on CCAC adsorbent for the removal of 2CP in aqueous medium [87].

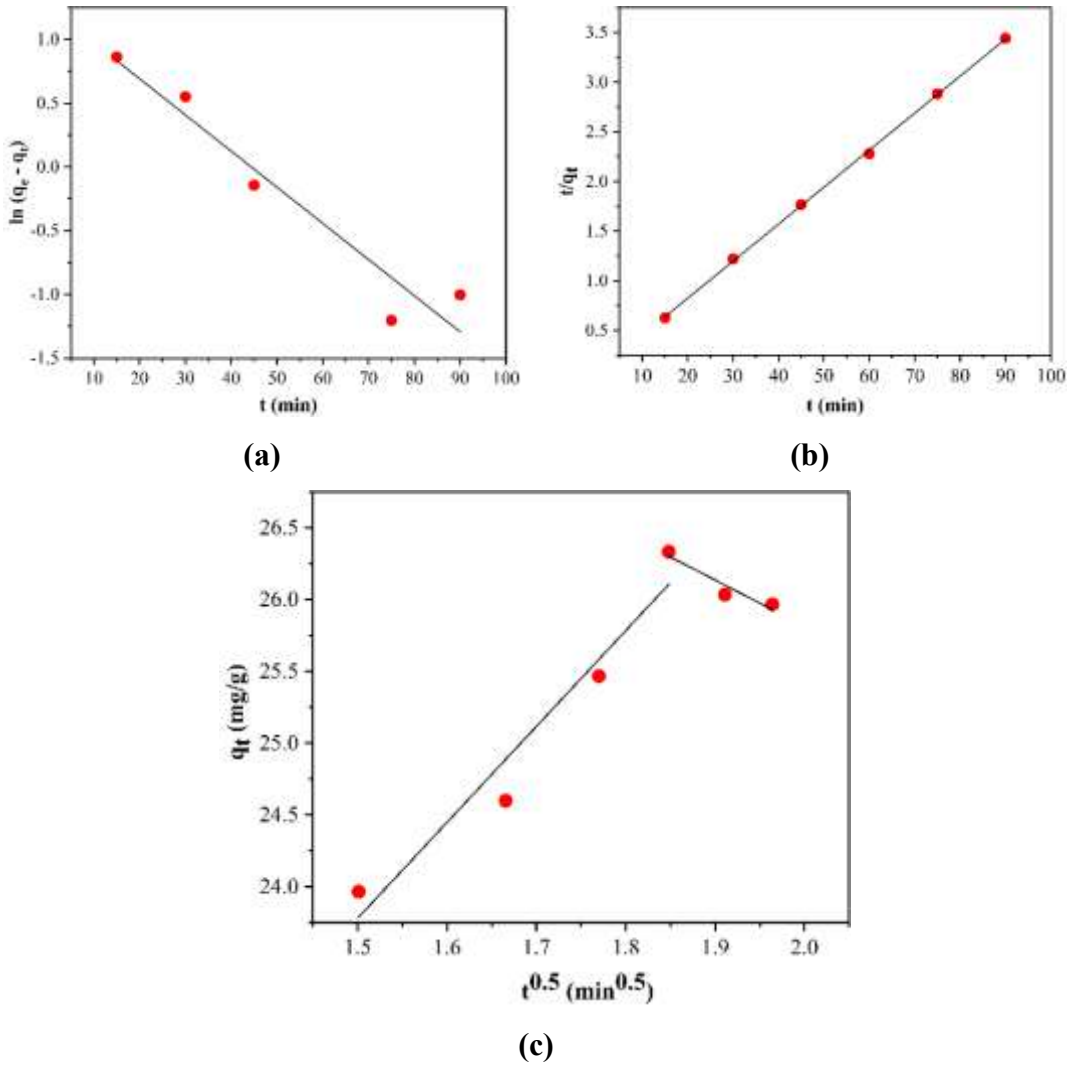

Figure 3.13. Kinetic model plots of (a) Pseudo-first order (b) Pseudo-second order and (c) Intraparticle diffusion for 2CP adsorption onto CCAC adsorbent.

The plot (Figure 3.13c) indicates that the adsorption process occurs in two stages. The first stage represents the quick absorption of 2CP over a period of time (reaction time: 60 min), but the rate of absorption slowed in the second phase. This might be caused by the boundary layer diffusion in the early phases of adsorption, followed by intra particle diffusion in the latter stages [88]. The linear plots moved further from the origin, thus suggests that intraparticle diffusion is not the only rate-limiting phase in the adsorption process, but rather that the adsorption process is controlled simultaneously by other kinetics processes.

In addition, the results in Table show that the lowest Chi-square (7.2×10^{-4}) and RMSE (0.027) value and highest correlation coefficients (R^2= 0.999) for pseudo-second order model was much higher as compared to pseudo-first order and intraparticle diffusion. Hence, the pseudo-second order model best explains the kinetic process for the adsorption of 2CP onto CCAC adsorbent. The obtained results are consistent with previous studies on adsorption of chlorophenolic compounds [89].

3.4.5 Theoretical studies

2CP adsorption on activated carbon is likely to involve a variety of interactions, including hydrogen bond formation, π–π interactions, electrostatic interactions, and electron donor-acceptor mechanisms [90]. However, among the many different forms of interactions that contribute to the adsorption process, one of the most essential types of interactions is the hydrogen bonding that occurs between the adsorbate and the activated carbon. So, the present study used DFT calculations to investigate the possibility of H-bond formation between activated carbon and the adsorbate [91]. An armchair model was used to examine the adsorption processes of both pristine active-

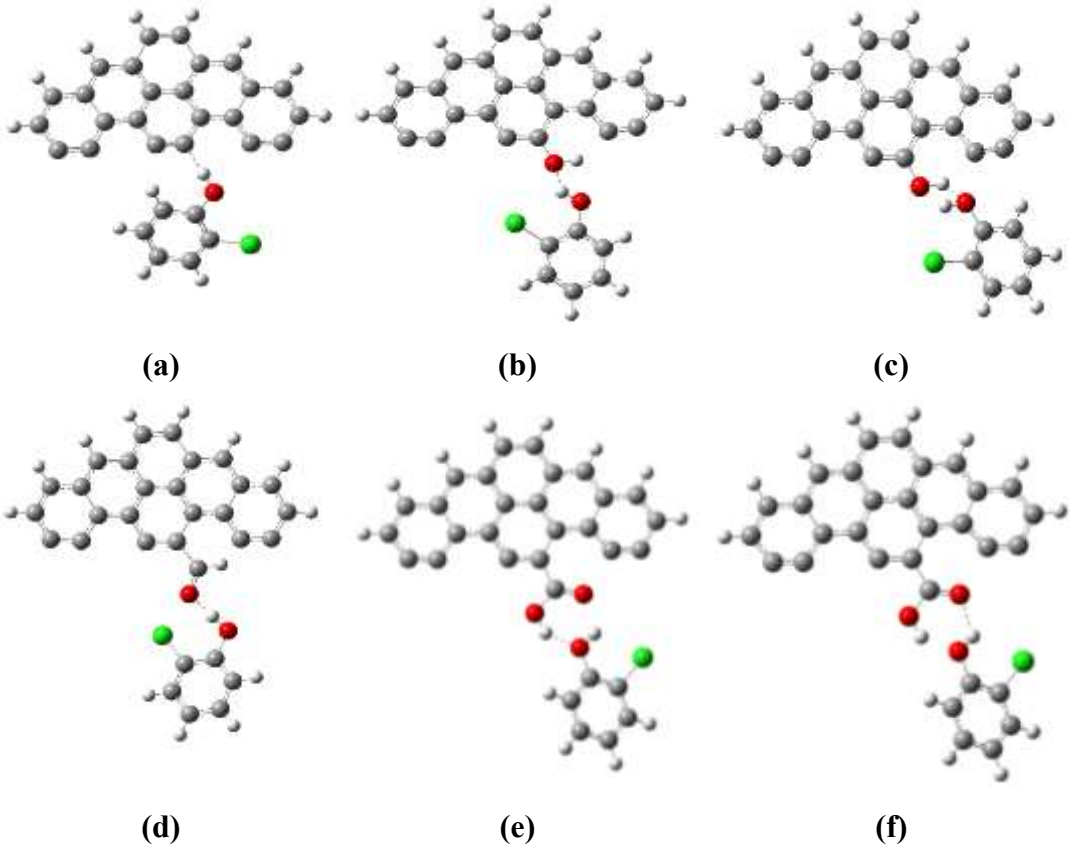

(g)

Figure 3.14. Optimized structures of 2CP interactions with AC: (a) (2CP)OH—C(p_AC) (b) (2CP)OH—OH(AC) (c) (2CP)HO—HO(AC) (d) (2CP)OH—OHC(AC) (e) (2CP)HO—HOOC(AC) (f) (2CP)OH—OCOH(AC) (g) (2CP)HO—HOOC+CHO+OH(AC).

ted carbon (p_AC) and functionalized activated carbon with 2-chlorophenol. Such study would be of tremendous use in the process of modifying the preparation of activated carbon. The optimized structures of 2CP interactions with p_AC and functionalized AC is presented in Figure 3.14. While the adsorption energies ($E_{adsorption}$) and bond length computed for various interactions are summarized in Table 3.5.

(i) 2CP adsorption on pristine activated carbon (p_AC)

To study the possible interaction of p_AC with 2CP, a bond was formed between the –OH group of 2CP and the –C atom of the pristine AC. The mode of interaction is represented as (2CP) OH—C(AC) and the optimized structure is shown in Figure 3.14a. The C-C bond distance of the pristine activated carbon where the oxygen atom of phenolic hydroxyl group was directly attached elongated from 0.124 nm to 0.137 nm and 0.124 nm to 0.136 nm upon phenol and DNP adsorption respectively. Upon adsorption of 2CP, the C–C bond length of the p_AC in which the H-atom of the chlorophenolic hydroxyl group was directly connected elongated from 0.121 to 0.125 nm and 0.141 to 0.142 nm. This evidence suggested that the electron density migrates to the adsorption sites, where it weakens the C–C bond of the activated carbon. Furthermore, the $E_{adsorption}$ was found to be -10.49 kJ/mol for the (2CP)OH—C(AC) system, indicating that the interaction between 2CP and activated carbon is favorable.

Table 3.5. The energy of adsorption and bond length between 2CP and AC adsorbent systems.

System	Mode of interaction	Adsorption energy (kJ/mol)	Bond distance (nm)
2CP + AC	(2CP)OH—C(AC)	-10.49	0.216 (H_{2CP}-C_{AC})
2CP + (AC)OH	(2CP)OH—OH(AC)	-24.63	0.181 (H_{2CP}-O_{AC})
	(2CP)HO—HO(AC)	-11.95	0.219 (O_{2CP}-H_{AC})
2CP + (AC)CHO	(2CP)OH—OHC(AC)	-29.00	0.172 (H_{2CP}-O_{AC})
2CP + (AC)COOH	(2CP)HO—HOOC(AC)	-42.16	0.171 (O_{2CP}-H_{AC})
	(2CP)OH—OCOH(AC)		0.194 (H_{2CP}-O_{AC})

(ii) 2CP adsorption on hydroxyl functionalized activated carbon –OH(AC)

The interaction between –OH functionalized AC and 2CP was investigated by applying two attachment modalities (i.e., (2CP)OH—OH(AC) and (2CP)HO—HO(AC) as depicted in Figure14(b-c). The $E_{adsorption}$ of (2CP)OH—OH(AC) and (2CP)HO—HO(AC) were -24.63 and -11.95 kJ/mol, respectively. On the other hand, the bond distance for H_{2CP}-O_{AC} interaction was 0.181 nm, whereas the bond distance for O_{2CP}-H_{AC} was 0.219 nm. The greater negative value of $E_{adsorption}$ and shorter bond length suggest that the (2CP)OH—OH(AC) type of interaction is more favored over (2CP)HO—HO(AC).

(iii) 2CP adsorption on carbonyl functionalized activated carbon –CHO(AC)

To comprehend the adsorption of 2CP onto–CHO functionalized activated carbon, the formation of a H-bond between the H-atom of (2CP)OH and the O-atom of functionalized CHO(AC) was examined (Figure 3.14d). The $E_{adsorption}$ of (2CP)OH—OHC(AC) is -29 kJ/mol, indicating that the adsorption of 2CP on –CHO functionalized AC is favorable.

(iv) 2CP adsorption on carboxyl functionalized activated carbon –COOH(AC)

The formation of two types of H-bonding between 2CP and –COOH functionalized AC facilitated the adsorption interaction of 2CP on the activated carbon surface with the function of –COOH as depicted in Figure 3.14(e-f). Two modes of H-bonds could be formed simultaneously: one between the O-atom of –COOH functionalized activated carbon and the H-atom of 2CP ((2CP)HO—HOOC(AC)), and the other

between the O-atom of 2CP and the H-atom of COOH functional AC ((2CP)OH—OCOH(AC)). After adsorption, the O_{2CP}-H_{AC} and H_{2CP}-O_{AC} bond distance were found to be 0.171 to 0.194 nm, whilst, the $E_{adsorption}$ correspond to -42.16 kJ/mol. From these results, the (2CP)HO—HOOC(AC) type of interaction was found to be more favored over (2CP)OH—OCOH(AC) upon 2CP adsorption.

(v) Adsorption energies of 2CP onto Croton caudatus activated carbon (CCAC)

The adsorption energies of 2CP and activated carbon surface functional groups were investigated and its schematic diagram are shown in Figure 3.15. In this work, the functional groups of the AC surface with the symbols COOH(AC), OH(AC), and CHO(AC) were taken into consideration. As can be seen from the plot, the interaction of 2-chlorophenol with COOH(AC) exhibited the maximum negative adsorption energy when compared to the CHO(AC) and OH(AC) systems.

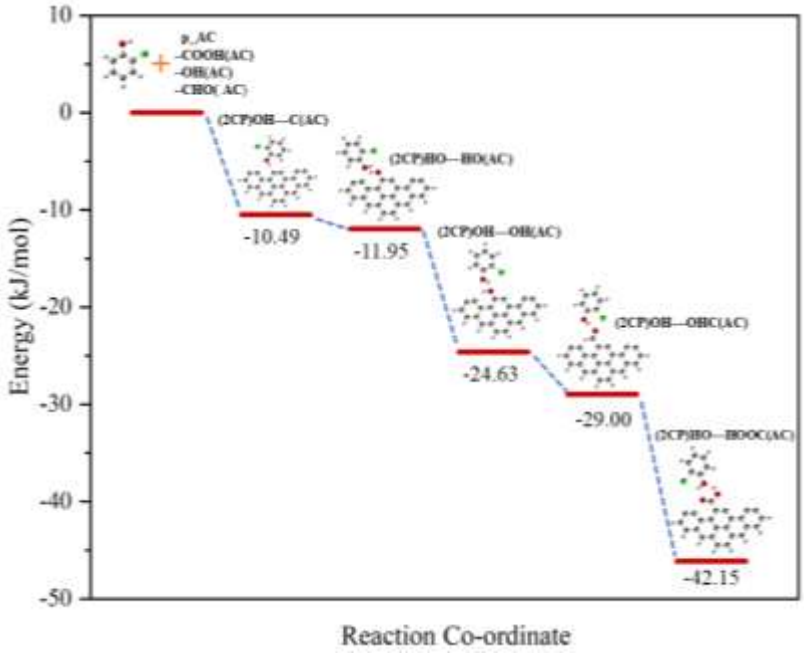

Figure 3.15. Energy diagram of 2CP adsorption on functionalized activated carbon.

Subsequently, it can be inferred that the inclusion of the carboxylic functional group into the activated carbon system will improve the adsorption interaction of 2-chlorophenol with the surface of activated carbon more of the CHO(AC) and OH(AC) groups.

The following sequence describes the relative energies and adsorption capacity of various configurations:

(2CP)HO—HOOC(AC)≈(2CP)OH—HOOC(AC)>(2CP)OH—
OHC(AC)>(2CP)OH—OH(AC)>(2CP)HO—HO(AC)>(2CP)OH—C(AC)

To study the overall influence of three-oxygenated functional groups on 2CP adsorption –OH, –CHO, and –COOH, were placed on the active sites of p_AC. The model for activated carbon used in this investigation was denoted as OH+CHO+COOH(AC). The optimized structure of OH+CHO+COOH(AC) as well as its potential interaction with 2-chlorophenol are depicted in Figure 3.3f and Figure 3.14g. The possible interaction of OH+CHO+COOH(AC) with 2CP was done via H-bonding (i.e., carboxyl hydrogen of OH+CHO+COOH(AC) formed a H-bond with the hydroxyl oxygen of the 2-chlorophenol molecule). It was revealed that the adsorption energy of the interaction between OH+CHO+COOH(AC) and 2CP was -47.17 kJ/ mol. This energy of adsorption is higher than that seen for the interaction of 2CP with various individual groups such as COOH(AC), OH(AC), and CHO(AC). Thus, the presence of multiple functional groups enhances the adsorption capabilities of AC towards 2CP as compared to the presence of single function group.

3.4.6 Comparative studies of adsorption capacity (Q_{max}) of prepared CCAC with other adsorbents

The relative efficacy of the produced CCAC for 2CP adsorption was compared with other adsorbent materials from aqueous medium. The maximum adsorption capacity

Table 3.6. Comparison studies of adsorption capacity of prepared CCAC with other adsorbents for 2CP removal.

Adsorbent	Q_{max} (mg/g)	Ref.
CCAC	**53.62**	**Present work**
Banana bunch	24.33	[92]
Schizophyllum commune fungus	46	[93]
Sargassum muticum	22	[94]
Paper mill sludge	0.34	[95]
Aspergillus niger	40.98	[96]
C. indica biomass	2.77	[97]
Rice straw	41.83	[98]
Granular-activated carbon (GAC)	18.83	[99]
Mesoporous SBA-15	25	[100]

(Q_{max}) of prepared CCAC determined using the Langmuir isotherm was compared to other adsorbents presented in the literature. The comparison results are listed in Table 3.6, and it can be seen that the proposed activated carbon has a considerably better adsorption capacity (Q_{max}) for 2CP. Therefore, AC derived from *Croton caudatus* could be a promising material for the adsorption phenolic chemicals from wastewater.

3.4.7 Regeneration and reuse of CCAC adsorbent

Regeneration studies are the most essential part of any adsorption process since it can reduce replacement and disposal costs and make the process more sustainable. In this study, 1 g/L of CCAC was stirred continuously with 50 mL of 2CP (1000 mg/L) for 24 hours to attained complete saturation. The saturated CCAC was desorbed in 0.1 M NaOH solution for two-hours while being stirred. After that, the solutions were filtered, washed, and dried in an oven at 110 °C. It was then utilized for 2CP adsorption in order to validate its reusability.

The desorption efficiencies of 2CP from regenerated CCAC appended as Figure 3.16. The plot shows that after the first cycle, the desorption efficiency of regenerated CCAC decreased from 92.50 % to 82.10 % in the fifth cycle. These results indicate that the regenerated CCAC could be used for several times. However, more research may be needed to enhance the regenerated carbon capacity and make the process more sustainable.

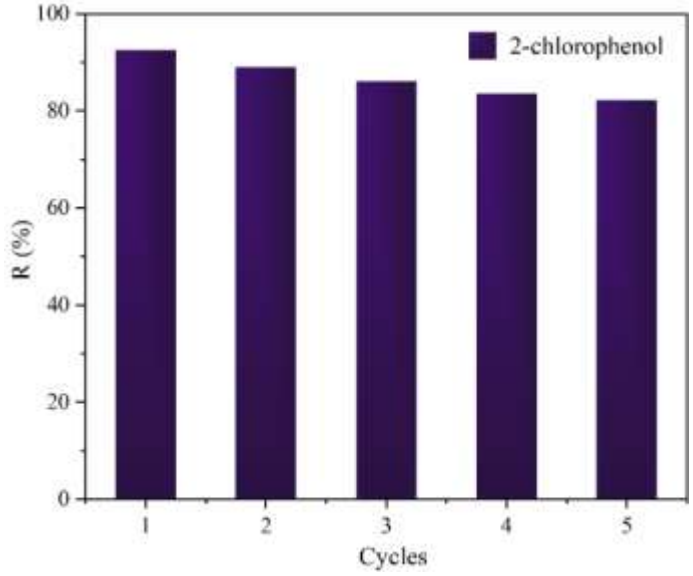

Figure 3.16. Desorption efficiencies of regenerated CCAC (initial 2CP concentration: 80 mg/L, CCAC dose: 0.15g/L, pH:4, 298K and contact time: 60 min).

3.4.8 Cost analysis

The estimated cost to produce 250 g of CCAC was computed, which includes the cost of electric current, KOH, water, HCl, and starting precursor. Table 3.7 and Table 3.8 provide the approximate and comparative cost analyses of the prepared and commercially activated carbon, respectively.

Table 3.7. Operating cost estimation for the production of 250 g CCAC.

Materials	Consumption (approx.)	Cost (approx.) (US **$**)
KOH	250 g	3.62
HCl	250 mL (0.1M HCl)	0.01 (**$** 6.67/500 mL)
Precursor	1500 g	0
Electric current	14 kWh	0.51
Water	53 L	0.19
Overall cost (US **$** /250 g)		4.33

From the results, it can be seen that the overall production cost for 250 g of CCAC was much lower than that of commercial AC. This suggests that the AC prepared from *Croton caudatus* could be considered as cost-effective adsorbent for the removal studies of water pollutants.

Table 3.8. Comparative cost of *Croton caudatus* activated carbon with some commercially available activated carbon.

Brand	**Cost/250 g** (US **$)**
Activated charcoal (Merck)	119.42
Activated charcoal, NORIT(R) A SUPRA, Thermo Scientific™	141.45
Charcoal activated (Merck)	139.38
Activated carbon (Merck)	86.37
Activated charcoal, DARCO® (Merck)	64.94
Activated charcoal, Norit® (Sigma-Aldrich)	47.89
CCAC (Present study)	4.33

3.5 Conclusion

This work showed that CCAC adsorbent served as a promising sustainable adsorbent for the 2CP adsorption from aqueous medium. The synthesized activated carbon was produced at 2:1 impregnation ratio and 700 ^{o}C activation temperature for 2 hours using

a muffle furnace under self-generated atmosphere. Studies of the produced activated carbon showed a surface area of 846.29 m^2/ g, a total pore volume of 0.019 cm^3/g, and an average pore diameter of 3.82 nm. FT-IR spectrum analysis showed several peaks that represents the presence of different functional groups. XRD analysis and SEM micrograph of *Croton caudatus* activated carbon demonstrated the presence of graphite like micro-crystallite nature and porous network. Under the optimum conditions, the maximum removal efficiency (R %) and adsorption capacity for 2-chlorophenol were found to be 98.56 % and 26.33 mg/g. The equilibrium isotherm study for 2CP adsorption was fitted well to the Langmuir model with the maximum adsorption capacity (Q_{max}) of 53.619 mg/g. The behavior of 2CP adsorption on CCAC was best described by pseudo-second order where the calculated q_e values ($q_{e,\ cal}$= 26.653 mg/g) was close similar to the experimental data ($q_{e,\ exp}$ = 26.333 mg/g). Thermodynamic studies confirmed that the adsorption process was spontaneous and exothermic. Regeneration studies of the adsorbent was determined to be satisfactory throughout the fifth regeneration cycle, indicating that the adsorbent may be regenerated and recycled for multiple times. DFT investigations further revealed that the adsorption of 2CP onto AC is favorable with the –COOH functionalized AC appeared to have the strongest interaction with 2-chlorophenol. Moreover, the presence of numerous functional groups OH+CHO+COOH(AC) enhances the adsorption capacities of AC towards 2CP, relative to a single functional group. Thus, the results obtained from experimental and theoretical studies showed that the activated carbon prepared from *Croton caudatus* biomass was efficient in removing 2CP from the wastewater.

References

[1] J. Huff, Sawmill chemicals and carcinogenesis, Environ. Health Perspect., 109 (2001) 209–212.

[2] P. Lampi, T. Hakulinen, V. Luostarinen, E. Pukkala, L. Teppo, Cancer incidence following chlorophenol exposure in southern Finland, Arch. Environ. Health, 47 (1992) 167–175.

[3] P. E. Spector, S. Fox, L. M. Penney, K. Bruursema, A. Goh, S. Kessler, The dimensionality of counterproductivity, J. Vocat. Behav., 3 (2006) 446–460.

[4] A. Adewuyi, A. Göpfert, O. A. Adewuyi, T. Wolff, Adsorption of 2-chlorophenol onto Adenopus breviflorus seed, J. Environ. Chem. Eng., 4 (2016) 664–672.

[5] A. Ghaffari, M. S. Tehrani, S. W. Husain, M. Anbia, P. A. Azar, Adsorption of chlorophenols on amino-modified silica, J. Nanostruct. Chem., 4 (2014) 1–10.

[6] H. Fiege, H. Voges, T. Hamamoto, S. Umemura, T. Iwata, H. Miki, Y. Fujita, H. Buysch, D. Garbe, W. Paulus, Phenol derivatives, in: Ullmann's Encycl. Ind. Chem., 10 (2000) 9–297.

[7] A. Sundaram, Journal of Environmental Science and Health Part B overview, J. Environ. Sci. Health B, 25 (1990) 309.

[8] M. Czaplicka, Sources and transformations of chlorophenols, Sci. Total Environ., 322 (2004) 21–39.

[9] M. Radhika, K. Palanivelu, Adsorptive removal of chlorophenols by low-cost adsorbent, J. Hazard. Mater., 138 (2006) 116–124.

[10] B. H. Hameed, I. A. W. Tan, A. L. Ahmad, Activated carbon for 2,4,6-trichlorophenol removal, J. Hazard. Mater., 164 (2009) 1316–1324.

[11] A. Denizli, N. Cihangir, N. Tüzmen, G. Alsancak, Removal of chlorophenols using Pleurotus sajor caju, Bioresour. Technol., 96 (2005) 59–62.

[12] M. B. Tahir, T. Nawaz, G. Nabi, M. Sagir, M. I. Khan, N. Malik, Nanophotocatalysts for wastewater treatment, Int. J. Environ. Anal. Chem., 102 (2022) 491–515.

[13] K. Verschueren, Handbook of environmental data on organic chemicals, Wiley (2001) 1–86.

[14] M. Pera-Titus, V. García-Molina, M. A. Baños, J. Giménez, S. Esplugas, Degradation of chlorophenols by AOPs, Appl. Catal. B, 47 (2004) 219–256.

[15] S. R. Wild, S. J. Harrad, K. C. Jones, Chlorophenols in UK sewage sludges, Water Res., 27 (1993) 1527–1534.

[16] T. A. Saleh, Synthesis protocols for nanomaterial adsorbents, Environ. Technol. Innov., 24 (2021) 101821.

[17] N. A. S. Mohammed, R. A. Abu-Zurayk, I. Hamadneh, A. H. Al-Dujaili, Phenol adsorption on pine fruit shell biochar, J. Environ. Manag., 226 (2018) 377–385.

[18] P. Cañizares, J. Lobato, R. Paz, M. A. Rodrigo, C. Sáez, Electrochemical oxidation of phenolic wastes, Water Res., 39 (2005) 2687–2703.

[19] M. L. Satuf, R. J. Brandi, A. E. Cassano, O. M. Alfano, Scaling-up slurry reactors for 4-chlorophenol degradation, Catal. Today, 129 (2007) 110–117.

[20] R. A. K. Rao, M. A. Khan, B. H. Hameed, Sorption studies for toxic pollutants, Chem. Eng. J., 152 (2009) 421–427.

[21] M. F. F. Sze, G. McKay, Adsorption diffusion model for para-chlorophenol removal, Environ. Pollut., 158 (2010) 1669–1674.

[22] J. W. Lim, P. E. Lim, C. E. Seng, R. Adnan, Simultaneous 4-chlorophenol and nitrogen removal in reactors, Bioresour. Technol., 129 (2013) 485–494.

[23] A. Kuleyin, Removal of phenol and 4-chlorophenol by modified zeolite, J. Hazard. Mater., 144 (2007) 307–315.

[24] A. Alkenani, T. A. Saleh, Amine-modified graphene membrane for pollutant rejection, J. Mol. Liq., 367 (2022) 120291.

[25] G. Crini, P. M. Badot, Sorption processes and pollution, Presses Univ. Franche-Comté (2010).

[26] V. K. Gupta, T. A. Saleh, Sorption of pollutants by porous carbon materials, Environ. Sci. Pollut. Res., 20 (2013) 2828–2843.

[27] H. Han, M. K. Rafiq, T. Zhou, R. Xu, O. Mašek, X. Li, Clay-based composites for pollutant adsorption, J. Hazard. Mater., 369 (2019) 780–796.

[28] Z. Du, S. Deng, Y. Bei, Q. Huang, B. Wang, J. Huang, G. Yu, Adsorption of perfluorinated compounds, J. Hazard. Mater., 274 (2014) 443–454.

[29] M. Salari, M. H. Dehghani, A. Azari, M. D. Motevalli, A. Shabanloo, I. Ali, Magnetic chitosan for phenol removal, J. Mol. Liq., 285 (2019) 146–157.

[30] S. M. Alshehri, M. Naushad, T. Ahamad, Z. A. Alothman, A. Aldalbahi, Curcumin-based bio-adsorbent for phenol removal, Chem. Eng. J., 254 (2014) 181–189.

[31] A. Supong, P. C. Bhomick, M. Baruah, C. Pongener, U. B. Sinha, D. Sinha, Adsorptive removal of Bisphenol A and DFT insights, Sustain. Chem. Pharm., 13 (2019) 100159.

[32] Ç. Cengiz, Ü. Geçgel, H. Koraqi, O. Üner, D. Nuha, B. Durmishi, R. Daci, D. Elshani, H. Palüzar, Production of activated carbons from Quercus cerris acorn shell under various experiment conditions, and their characterizations, Adsorption, 30 (2024) 1467–1478.

[33] R. Gusain, N. Kumar, S. S. Ray, Carbon nanomaterial-based adsorbents, Coord. Chem. Rev., 405 (2020) 213111.

[34] C. Li, J. Yang, L. Zhang, S. Li, Y. Yuan, X. Xiao, X. Fan, C. Song, Carbon-based membrane materials and applications in water and wastewater treatment: a review, Environ. Chem. Lett., 19 (2021) 1457–1475.

[35] A. Demirbas, Agricultural activated carbons for dye removal, J. Hazard. Mater., 167 (2009) 1–9.

[36] C. Namasivayam, D. Sangeetha, R. Gunasekaran, Adsorption using Jatropha husk carbon, Process Saf. Environ. Prot., 85 (2007) 181–184.

[37] M. S. Reza, C. S. Yun, S. Afroze, N. Radenahmad, M. S. Abu Bakar, R. Saidur, J. Taweekun, A. K. Azad, Preparation of activated carbon from biomass and its' applications in water and gas purification, a review, Arab J. Basic Appl. Sci., 27 (2020) 208–238.

[38] M. Gayathiri, T. Pulingam, K. T. Lee, K. Sudesh, Activated carbon from biomass waste precursors: Factors affecting production and adsorption mechanism, Chemosphere, 294 (2022) 133764.

[39] S. L. Ezung, M. Baruah, A. Supong, S. Sharma, D. Sinha, Adsorption of 2,4-dichlorophenol and DFT insight, Sustain. Chem. Pharm., 26 (2022) 100643.

[40] M. Ahmaruzzaman, S. L. Gayatri, Activated neem leaf for phenol removal, J. Chem. Eng. Data, 56 (2011) 3004–3016.

[41] E. Altıntıg, H. Altundag, M. Tuzen, A. Sarı, Magnetic activated carbon for methylene blue removal, Chem. Eng. Res. Des., 122 (2017) 151–163.

[42] Altintig, Esra, Muge Onaran, Ahmet Sarı, Huseyin Altundag, and Mustafa Tuzen. Preparation, characterization and evaluation of bio-based magnetic

activated carbon for effective adsorption of malachite green from aqueous solution. Mater. Chem. Phys., 220 (2018): 313-321.

[43] M. Tuzen, A. Sarı, T. A. Saleh, Magnetic AC/CeO_2 nanocomposite for rhodamine B removal, J. Environ. Manag., 206 (2018) 170–177.

[44] A. Supong, P. C. Bhomick, R. Karmaker, S. L. Ezung, L. Jamir, U. B. Sinha, D. Sinha, Experimental and theoretical insight into the adsorption of phenol and 2,4-dinitrophenol onto Tithonia diversifolia activated carbon, Appl. Surf. Sci., 529 (2020) 147046.

[45] A. Supong, U. B. Sinha, D. Sinha, DFT study of oxygenated functionals on activated carbon, Surfaces, 5 (2022) 280–289.

[46] J. Liu, W. Qu, S.W. Joo, C. Zheng, Effect of SO_2 on mercury binding, Chem. Eng. J., 184 (2012) 163–167.

[47] S. U. Jan, A. Ahmad, A. A. Khan, S. Melhi, I. Ahmad, G. Sun, C.-M. Chen, R. Ahmad, Removal of azo dye from aqueous solution by a low-cost activated carbon prepared from coal: adsorption kinetics, isotherms study, and DFT simulation, Environ. Sci. Pollut. Res., 28 (2021) 10234–10247.

[48] F. Shen, J. Liu, Z. Zhang, Y. Dong, C. Gu, Density functional study of hydrogen sulfide adsorption mechanism on activated carbon, Fuel Process. Technol., 171 (2018) 258–264.

[49] A. M. Youssef, N. R. E. Radwan, I. Abdel-Gawad, G. A. A. Singer, Textural properties of activated carbons from apricot stones, Colloids Surf. A: Physicochem. Eng. Asp., 252 (2005) 143–151.

[50] A. Mukherjee, A. R. Zimmerman, W. Harris, Surface chemistry of biochars, Geoderma, 163 (2011) 247–255.

[51] B. M. Babić, S. K. Milonjić, M. J. Polovina, B. V. Kaludierović, Point of zero charge and intrinsic equilibrium constants of activated carbon cloth, Carbon, 37 (1999) 477–481.

[52] A. Jumasiah, T. G. Chuah, J. Gimbon, T. S. Y. Choong, I. Azni, Adsorption of basic dye onto palm kernel shell activated carbon: sorption equilibrium and kinetics studies, Desalination, 186 (2005) 57–64

[53] K. T. V. N. Vijayaraghavan, T. V. N. Padmesh, K. Palanivelu, M. Velan, Biosorption of nickel (II) ions onto Sargassum wightii: application of two-parameter and three-parameter isotherm models, J. Hazard. Mater., 133 (2006) 304–308.

[54] K. Zhou, W. Ma, Z. Zeng, X. Ma, X. Xu, Y. Guo, H. Li, L. Li, Experimental and DFT study on the adsorption of VOCs on activated carbon/metal oxides composites, Chem. Eng. J., 372 (2019) 1122–1133.

[55] S. T. Perry, E. M. Hambly, T. H. Fletcher, M. S. Solum, R. J. Pugmire, Solid-state ^{13}C NMR characterization of matched tars and chars from rapid coal devolatilization, Proc. Combust. Inst., 28 (2000) 2313–2319.

[56] S. Rengaraj, S. H. Moon, R. Sivabalan, B. Arabindoo, V. Murugesan, Agricultural solid waste for the removal of organics: adsorption of phenol from water and wastewater by palm seed coat activated carbon, Waste Manage., 22 (2002) 543–548.

[57] S. Rengaraj, S. H. Moon, R. Sivabalan, B. Arabindoo, V. Murugesan, Agricultural solid waste for the removal of organics: adsorption of phenol from water and wastewater by palm seed coat activated carbon, Waste Manage., 22 (2002) 543–548.

[58] T. Yang, A.C. Lua, Pistachio shell activated carbon, J. Colloid Interface Sci., 267 (2003) 408–417.

[59] A. I. C. da Silva, G. Paranha, L. S. Maia, D. R. Mulinari, Development of activated carbon from pineapple crown wastes and its potential use for removal of methylene blue, J. Nat. Fibers, 19 (2022) 5211–5226.

[60] M. Şirazi, S. Aslan, Comprehensive characterization of high surface area activated carbon prepared from olive pomace by KOH activation, Chem. Eng. Commun., 208 (2021) 1479–1493

[61] N. A. Rashidi, S. Yusup, M. M. Ahmad, N. M. Mohamed, B. H. Hameed, Activated carbon from the renewable agricultural residues using single step physical activation: a preliminary analysis, APCBEE Procedia, 3 (2012) 84–92

[62] D. Egirani, M. T. Latif, N. Wessey, N. R. Poyi, N. Shehata, Preparation and characterization of powdered and granular activated carbon from Palmae biomass for mercury removal, Appl. Water Sci., 11 (2021) 10.

[63] P. Paluri, K. S. Durbha, Equilibrium, kinetic, and thermodynamic study for the adsorption of methylene blue onto activated carbons prepared from the banana root through chemical activation with phosphoric acid, Biomass Convers. Biorefin., 13 (2023) 10575–10594

[64] E. Altıntıg, H. Altundag, M. Tuzen, A. Sarı, Effective removal of methylene blue from aqueous solutions using magnetic loaded activated carbon as novel adsorbent, Chem. Eng. Res. Des., 122 (2017) 151–163

[65] M. L. Martinez, M. M. Torres, C. A. Guzman, D. M. Maestri, Preparation and characteristics of activated carbon from olive stones and walnut shells, Ind. Crops Prod., 23 (2006) 23–28.

[66] N. L. Owen, D. W. Thomas, Infrared studies of woods, Appl. Spectrosc., 43 (1989) 451–455.

[67] E. Fuente, J. A. Menéndez, M. A. Díez, D. Suárez, M. A. Montes-Morán, Infrared spectroscopy of carbon materials: a quantum chemical study of model compounds, J. Phys. Chem. B, 107 (2003) 6350–6359.

[68] M. Asadullah, M. Asaduzzaman, M. S. Kabir, M. G. Mostofa, T. Miyazawa, Chemical and structural evaluation of activated carbon prepared from jute sticks for Brilliant Green dye removal from aqueous solution, J. Hazard. Mater., 174 (2010) 437–443

[69] A. E. Ogungbenro, D. V. Quang, K. A. Al-Ali, L. F. Vega, M. R. Abu-Zahra, Synthesis and characterization of activated carbon from biomass date seeds for carbon dioxide adsorption, J. Environ. Chem. Eng., 8 (2020) 104257.

[70] S. M. Yakout, G. S. El-Deen, Activated carbon from olive stones, Arab. J. Chem., 9 (2016) 1155–1162.

[71] T. C. Chandra, M. M. Mirna, J. Sunarso, Y. Sudaryanto, S. Ismadji, Activated carbon from durian shell: preparation and characterization, J. Taiwan Inst. Chem. Eng., 40 (2009) 457–462.

[72] L. Ren, J. Zhang, Y. Li, C. Zhang, Preparation and evaluation of cattail fiber-based activated carbon for 2,4-dichlorophenol and 2,4,6-trichlorophenol removal, Chem. Eng. J., 168 (2011) 553–561.

[73] K. L. Chiu, D. H. Ng, Cotton-based activated carbon fiber, Biomass Bioenergy, 46 (2012) 102–110.

[74] P. Sudhakar, I. D. Mall, V. C. Srivastava, Adsorptive removal of bisphenol-A by rice husk ash and granular activated carbon—A comparative study, Desalin. Water Treat., 57 (2016) 12375–12384.

[75] A. A. M. Daifullah, B. S. Girgis, H. M. H. Gad, A study of the factors affecting the removal of humic acid by activated carbon prepared from biomass material, Colloids Surf. A: Physicochem. Eng. Asp., 235 (2004) 1–10.

[76] E. A. Babushkina, L. V. Belokopytova, A. M. Grachev, D. M. Meko, E. A. Vaganov, Variation of the hydrological regime of Bele-Shira closed basin in Southern Siberia and its reflection in the radial growth of Larix sibirica, Reg. Environ. Change, 17 (2017) 1725–1737.

[77] M. Shirzad-Siboni, S. J. Jafari, M. Farrokhi, J. K. Yang, Removal of phenol from aqueous solutions by activated red mud: equilibrium and kinetics studies, Environ. Eng. Res., 18 (2013) 247–252.

[78] A. Spaltro, M. N. Pila, D. D. Colasurdo, E. N. Grau, G. Román, S. Simonetti, D. L. Ruiz, Removal of paracetamol from aqueous solution by activated carbon and silica: experimental and computational study, J. Contam. Hydrol., 236 (2021) 103739.

[79] O. Hamdaoui, E. Naffrechoux, Modeling adsorption isotherms of chlorophenols, J. Hazard. Mater., 147 (2007) 401–411.

[80] C. Moreno-Castilla, Adsorption of organic molecules on carbon materials, Carbon, 42 (2004) 83–94.

[81] N. U. Yamaguchi, A. J. Rubio, R. Bergamasco, Activated carbon loaded with manganese and iron for glyphosate adsorption: kinetics, isotherms and thermodynamic studies, Rev. Ambient. Água, 14 (2019) e2414

[82] K. R. Hall, L. C. Eagleton, A. Acrivos, T. Vermeulen, Pore- and solid-diffusion kinetics in fixed-bed adsorption under constant-pattern conditions, Ind. Eng. Chem. Fundam., 5 (1966) 212–223.

[83] X. Ma, H. Peng, X. Zhang, Regeneration of nitrophenol loaded granular activated carbon and its effect on the surface properties of adsorbent, Desalin. Water Treat., 57 (2016) 25494–25502

[84] A. Kumar, H.M. Jena, Removal of methylene blue and phenol using Fox nutshell carbon, J. Clean. Prod., 137 (2016) 1246–1259.

[85] S. Lagergren, Theory of adsorption of dissolved substances, Kungliga Svenska Vetenskapsakademiens Handlingar, 24 (1898) 1–39.

[86] Y. S. Ho, G. McKay, Kinetics of sorption of metal ions, Water Res., 34 (2000) 735–742.

[87] W. J. Weber Jr., J. C. Morris, Kinetics of adsorption on carbon, J. Sanit. Eng. Div., 89 (1963) 31–59.

[88] L. A. de Sousa Ribeiro, G. P. Thim, M. O. Alvarez-Mendez, A. dos Reis Coutinho, N. P. de Moraes, L. A. Rodrigues, Preparation, characterization, and application of low-cost açaí seed-based activated carbon for phenol adsorption, Int. J. Environ. Res., 12 (2018) 755–764.

[89] H. B. Senturk, D. Ozdes, A. Gundogdu, C. Duran, M. Soylak, Removal of phenol from aqueous solutions by adsorption onto organomodified Tirebolu

bentonite: equilibrium, kinetic and thermodynamic study, J. Hazard. Mater., 172 (2009) 353–362.

[90] P. Q. Thang, K. Jitae, B. L. Giang, N. M. Viet, P. T. Huong, Potential application of chicken manure biochar towards toxic phenol and 2,4-dinitrophenol in wastewaters, J. Environ. Manage., 251 (2019) 109556

[91] D. Cortés-Arriagada, L. Sanhueza, M. Santander-Nelli, Modeling the physisorption of bisphenol A on graphene and graphene oxide, J. Mol. Model., 19 (2013) 3569–3580.

[92] A. Allwar, Removal of phenol and 2-chlorophenol by banana bunch carbon, Rasayan J. Chem., 12 (2019) 598–607.

[93] N. S. Kumar, K. Min, Phenolic compound biosorption by fungus, Chem. Eng. J., 168 (2011) 562–571.

[94] E. Rubín, P. Rodríguez, R. Herrero, M. E. Sastre de Vicente, Biosorption of phenolic compounds by the brown alga Sargassum muticum, J. Chem. Technol. Biotechnol., 81 (2006) 1093–1099.

[95] N. Calace, E. Nardi, B. M. Petronio, M. Pietroletti, Adsorption of phenols by papermill sludges, Environ. Pollut., 118 (2002) 315–319.

[96] I. Senturk, H. Buyukgungor, Biosorption of chlorophenols by Aspergillus niger, Ekoloji, 22 (2013) 1–12.

[97] A. Gholizadeh, M. Kermani, M. Gholami, M. Farzadkia, Kinetic and isotherm studies of adsorption and biosorption processes in the removal of phenolic compounds from aqueous solutions: comparative study, J. Environ. Health Sci. Eng., 11 (2013) 29.

[98] M. K. Mahapatra, A. Kumar, Adsorption of 2-chlorophenol on rice straw carbon, Chem. Biochem. Eng. Q., 36 (2022) 51–65.

[99] O. A. Ekpete, M. J. N. R. Horsfall, Preparation and characterization of activated carbon derived from fluted pumpkin stem waste (Telfairia occidentalis Hook F), Res. J. Chem. Sci., 1 (2011) 10–17.

[100] W. Xiao, X. Jiang, X. Liu, W. Zhou, Z. N. Garba, I. Lawan, L. Wang, Z. Yuan, Adsorption of organic dyes from wastewater by metal-doped porous carbon materials, J. Clean. Prod., 284 (2021) 124773.

CHAPTER 4

EXPLORING THE ADSORPTION OF CATECHOL AND RESORCINOL ONTO CROTON CAUDATUS ACTIVATED CARBON: AN INTEGRATED EXPERIMENTAL AND THEORETICAL APPROACH

This chapter aimed to examine the process for adsorption of Catechol (CT) and Resorcinol (RS) onto activated carbon that was obtained from *Croton caudatus* biomass (CAB). Using a batch method, the maximum removal efficiencies of 99.23 % for CT and 98.68 % for RS was achieved at adsorbent dosage-0.2 g L^{-1}, reaction time-60 min; concentration-100 mgL^{-1} CT and 80 mgL^{-1} RS; and pH 6.0 CT and pH 4.0 RS, respectively. A maximum equilibrium adsorption of 56.05 mgg^{-1} and 61.85 mgg^{-1} was achieved at pH 6.0 and pH 4.0 for CT and RS. The adsorption behavior of both adsorbates on activated carbon were best described by the Langmuir model (correlation coefficients (R^2) = 0.996 for CT and 0.995 for RS) and the pseudo-second order kinetic model. The values of ΔG, ΔS, and ΔH suggest that the adsorption process is spontaneous and endothermic. Additionally, the adsorption process is easily reversible, enabling the reuse of the adsorbate even after fifth cycle. Further, density functional theory (DFT) simulations demonstrated that the CT and RS adsorption onto the AC adsorbent is favorable. Among the oxygen functional groups analysed, the carboxyl group showed the greatest effect on the adsorption process, exhibiting the most negative adsorption energy at -44.869 (CT) and -45.082 $kJmol^{-1}$ (RS), respectively. Therefore, the activated carbon derived from CAB has significant potential for effectively removing phenolic contaminants from wastewater.

The text of this chapter has been published as:

S. Sharma, R. S. Umdor, I. T. Longchar, S. L. Ezung, D. Sinha, Exploring the adsorption of catechol and resorcinol onto Croton caudatus activated carbon: an integrated experimental and theoretical approach, Ground water Sustain. Dev., 27 (2024) 101325.

4.1 Introduction

In recent times, there has been a growing public awareness and concern regarding issues related to the improper disposal of hazardous waste and the pollution of both surface and groundwater [1]. Phenol and substituted phenols are essential organic intermediates in the synthesis of a wide range of agricultural and industrial products. For example, Catechol (CT) and Resorcinol (RS) are di-hydroxybenzene isomers that are extensively used as industrial solvents [2]. CT (1,2-di-hydroxybenzene) is used to develop photographic and fur dyes, polymerization inhibitors, an antioxidant and food additives [3]. It is also employed for the detection and measurement of many ions in chemical laboratories [4,5]. Whilst, RS (1,3- dihydroxybenzene) is widely used in the production of synthetic fibers, resins, plastics and dyes, respectively [6]. As a result, they are present in the effluents produced by industrial manufacturing units such as petroleum refineries, cosmetics, textile and pharmaceutical effluents [7]. Due to their release into the environment, these substances are often detected in soil, as well as surface and underground water sources, resulting in harmful effects on both human well-being and the natural ecosystem [8-10]. Furthermore, they are categorized as pollutants due to their low biodegradability, significant toxicity, high oxygen demand and carcinogenicity, even at lower concentrations [11]. Catechol is highly toxic to living organisms, even at extremely low concentrations. It can cause severe health issues, including DNA damage, vascular collapse, coma, and even death. Resorcinol, similarly, is toxic and can lead to serious health problems. Inhalation of resorcinol can result in abdominal pain, nausea, and loss of consciousness. In animals, resorcinol has been shown to affect the nervous system, thyroid function, and immune system [12,13]. Moreover, exposure to such a pollutant produces chronic health problems, including eye and skin irritation, diarrhea, abdominal pain, pulmonary edema, nausea and vomiting [14-16]. Additionally, the toxicity of CT is even greater than RS and both are deemed more toxic than phenol because of their ability to disrupt erythrocyte function at low levels [17,18]. Consequently, they are placed on the priority list of pollutants by both the Ministry of Environment and Forests (MoEF) of India and the Environmental Protection Agency (EPA) of the United States (i.e., below the threshold of 1 ppm in wastewater) [19]. Therefore, monitoring and removing these chemicals from the environment is necessary by developing simple and cost-effective methods.

Multiple strategies involving membrane filtration, photocatalysis, anaerobic biodegradation, ion exchange, adsorption, and chemical oxidation have been utilized to remove these chemicals from wastewater [20-26]. Among these techniques, activated carbon (AC) adsorption has been extensively used due to its cost-effectiveness, simple design, regenerability, and eco-friendliness [27]. AC adsorbent possesses perfect adsorption ability for relatively low-molecular-weight organic compounds such as phenols and benzene derivatives owing to its impressive surface area, ample functional groups, surface reactivity and extensive porosity [28-30]. Numerous studies have demonstrated that AC effectively adsorbs organic molecules, particularly phenolic chemicals. However, its high initial cost and the need for a costly regeneration system make it less economically viable as an adsorbent [31,32]. In this regard, biomass-derived activated carbon has emerged as an affordable, renewable and abundant alternative to commercial activated carbon since these materials are cost-effective, renewable, abundant and environmentally friendly [33,34]. Moreover, numerous studies have been reported on the treatment of phenolic derivates using activated carbon derived from biomass material. For example, Vunain et al. [35], reported that CT and RS can be removed efficiently from aqueous solution using sunflower seed hull activated carbon. Effective removal of 4-nitrophenol, 4-chlorophenol, and phenol from wastewater was achieved using AC produced from Neem leaf biomass [36]. Our previous studies have also used *Croton caudatus* AC for 2-chlorophenol adsorption [37]. As a result, in this work, AC synthesized from *Croton caudatus* biomass (CAB) is employed for the adsorption of CT and RS from aquatic media.

Several studies have been carried out in recent years to understand a deeper insight onto the adsorption mechanism between AC and phenolic substituents using density functional theory. For example, a study by Kabir et al. [38] examined the impact of different functional groups attached to activated carbon (AC) surfaces on the adsorption of oxytetracycline. The results demonstrated that the functional groups significantly enhanced the adsorption capacity, showing a strong correlation with experimental findings. In another study, Abdelbassit et al. investigated the specific interactions between functionalized activated carbon and different chlorinated methane compounds such as CH_2Cl_2, $CHCl_3$, and CCl_4 [39]. Their research findings

suggested that among these functional groups, the COOH functional group on AC exhibited the most potent and stronger interactions with 2,4-dinitrophenol and cresol. Also, Bhomick and co-workers [40] used DFT method to study the influence of various oxygen-containing functional groups on carbon surface for Methylene Blue adsorption. Moreover, Jan et al. [41] also reported that the adsorption of azo dye onto AC and functionalized AC was found to be more effective. Nevertheless, the understanding of the specific adsorptive interactions between the surface of AC and the molecules of the dye remains unclear. Therefore, DFT simulations were conducted to study the effect of OFGs such as hydroxyl (OH), carbonyl (CHO) and carboxyl (COOH) on carbon surface for the removal of CT and RS. Consequently, this study will provide valuable insights and guidance supporting experimental work for tailoring carbon-based materials with an optimal affinity for specific target pollutants to save overall cost and increase efficiency.

The present study focuses in the use of waste biomass to address the demand for sustainable and cost-effective solutions for the removal of phenolic compounds from water. Consequently, this work aims to investigate the adsorption of catechol and resorcinol on activated carbon derived from *Croton caudatus*, employing both computational and experimental methods. Furthermore, batch adsorption studies were conducted and other factors such as thermodynamics, kinetics, equilibrium adsorption isotherms, the influence of co-ions, and regeneration processes for the adsorption of CT and RS onto the activated carbon adsorbent were also investigated. Density Functional Theory (DFT) simulations were conducted to investigate the interactions between the adsorbate and activated carbon (AC) adsorbent, both in its unmodified form and in functionalized forms, including OH(AC), CHO(AC), and COOH(AC) activated carbon. The findings of this study could offer new insights into enhancing the performance of activated carbon in removing phenolic compounds from aqueous solution.

4.2 Materials and methods

4.2.1 Materials

Catechol and resorcinol of purity 99.9 % were used as adsorbates and purchased from SRL (SRL Pvt. Ltd., Maharashtra, India). The molecular structure of CT and RS are

displayed in Figure 1. Working solutions were freshly prepared by diluting stock solution (1000 mgL^{-1}) of CT and RS. Milli-Q water was employed for the entire duration of the experiment. The chemicals utilized were all of analytical grade without further purification.

Catechol (CT) **Resorcinol (RS)**

Figure 4.1. Molecular structure of CT and RS.

4.2.2 Preparation of activated carbon

This study utilized *Croton caudatus* biomass derived from the vicinity of Lumami, Nagaland University, India (26° 13′ 29.60″ N | 94° 28′ 35.0″ E). The complete plant's resources were taken in the production of activated carbon and is labelled as *Croton caudatus* activated carbon (CCAC). Our previous research has provided a detailed description of the preparation methods and characterization of the activated carbon [37].

4.2.3 Adsorption experiments

Adsorptive removal of CT and RS onto activated carbon was carried out using the batch method. To investigate the influence of various factors, including temperature, pH, adsorbate concentration, dose, and contact time, a series of batch equilibrium tests were conducted. All experiments have been conducted in 250 mL Erlenmeyer flasks, and the adsorbate concentration was determined on a UV-Vis spectrophotometer (Lambda 35, Perkin Elmer) at 276 nm for CT and 273 nm for RS of maximum absorbance. All adsorbate determinations were made in triplicates and the average values were considered. The expressions for the sorption capacity, q_e (mgg^{-1}) and the percentage of adsorbate removed were computed using Equations (4.1) and (4.2), respectively:

$$q_e = V \times \frac{C_i - C_e}{X} \quad (4.1)$$

$$\text{Removal \%} = 100 \times \frac{C_i - C_e}{C_i} \quad (4.2)$$

where C_i and C_e correspond to the initial and final adsorbate concentrations (mgL^{-1}), solution volume is represented by V(L) and X is the adsorbent weight (g).

4.2.4 Error analysis

A Chi-squared (χ^2) analysis was utilized to evaluate the experimental data and determine the most suitable isotherm and kinetics models for CT and RS adsorption by CCAC adsorbent. Using the mathematical formula described by Jumasiah et al. [42], the values of χ^2 were calculated.

$$\chi^2 = \sum_{i=1}^{m} \frac{(q_e - q_c)^2}{q_c} \quad (4.3)$$

where, q_c and q_e are the calculated and estimated values. The parameter 'm' represents the required number of observations. When there is a close correspondence between calculated and experimental data of the kinetic and isotherm model data, the resultant $\chi 2$ value will be comparatively low.

4.3 Computational models and methodology

DFT-based simulations were conducted with the Gaussian 16 W software to investigate potential interactions between AC and the adsorbate (CT and RS). Molecular structures were initially generated using Gauss View 06 and subsequently optimized to achieve their ground state. The process of optimizing their geometry and performing energy calculations was conducted in a medium with a dielectric constant (ε) at 80, simulating the conditions of water.

These calculations were conducted using the B3LYP/6-31G level of theory, and the E_{ads} of adsorbate onto AC's surface was determined using Equation (4.4).

$$E_{ads} = E_{x+y} - (E_x + E_y) \quad (4.4)$$

where, E_{x+y}= Combined energy of CT and RS and AC, E_x= Overall energy of CT and RS molecule, and E_y= Overall energy of the AC adsorbent. Also, E_{ads} negative values

signifies a more favorable adsorption process with stronger interactions.

Models that simulate activated carbon surface characteristics are essential for understanding the molecular and theoretical aspects of CT and RS adsorption on AC. In a study carried out by Perry and co-workers, it revealed that the AC's surface was structured with a combination of 3 to 7-fused benzene rings [43]. Previous theoretical investigations employed cluster models consisting of 4 to 7-interconnected benzene rings to simulate the structure of the AC surface. These models provided valuable insights into comprehending the adsorptive interactions of diverse species with the surface of activated carbon. Therefore, in the current work, a model was employed that encompasses 6-fused benzene rings exhibiting armchair edge configuration and thereby providing a balance between computational cost and precision [44]. The top C atoms in the armchair model were unsaturated to create an active site, while others were covered by H-atoms. Three OFGs, namely OH, CHO, and COOH, were introduced to the active sites of the AC model to understand its impact on adsorption characteristics. Figure 4.2, illustrates the optimized models of CT, RS, unmodified and functionalized AC models utilized in this study. These variants have been labeled as follows: unmodified activated carbon (AC), activated carbon modified with COOH functionalization (COOH—AC), activated carbon with CHO functionalization (CHO—AC), activated carbon with OH functionalization (OH—AC), respectively.

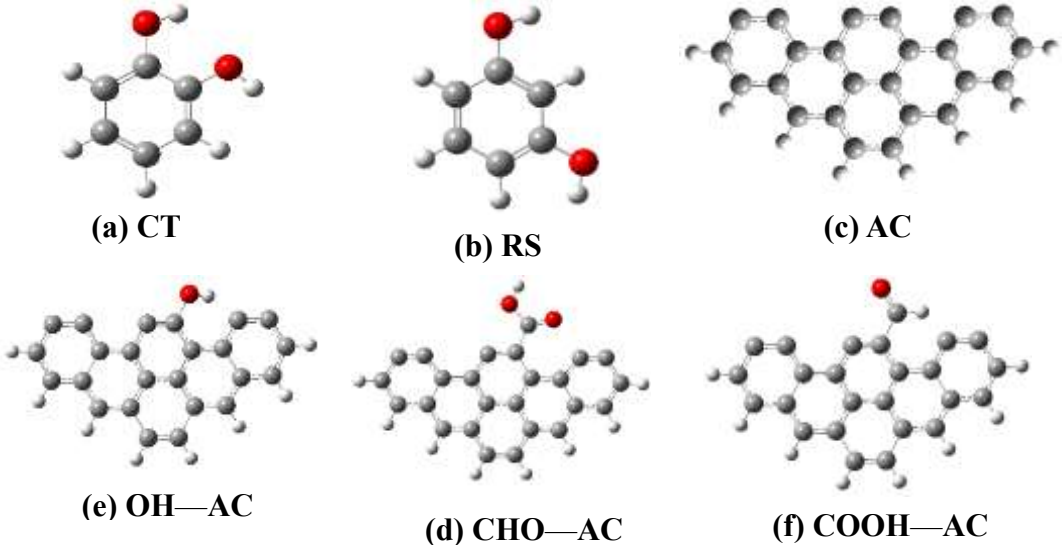

Figure 4.2. Optimized structure of adsorbates, unmodified and functionalized activated carbon.

4.4 Results and discussion

4.4.1 Batch adsorption studies

(i) Effect of adsorbent dosage

The quantity of adsorbent employed is of utmost significance in ascertaining the efficacy of removal for a given initial concentration of adsorbate molecules in an aqueous solution. Figure 4.3a illustrates the impact of varying the quantity of adsorbent (ranging from 0.05 to 0.35 gL^{-1}) on the removal of CT and RS. Under optimum operational conditions, CT and RS were significantly removed to a maximum of 99.2 % and 98.9 % at a dose of 0.2 gL^{-1} of activated carbon, respectively, thereafter continued to remain almost constant. The initial rise is ascribed to the greater adsorption site and higher surface area (BET surface area- 846.29 m^2/g) at increasing concentrations of the adsorbents [45]. However, as the carbon dosage was further increased, there was a slight decrease in adsorption. This decline was ascribed to the accumulation of mass on the active sites at higher dosages, leading to a reduction in the effective active surface area available for the adsorption process [46]. Thus, 0.2 g L^{-1} was chosen as the ideal adsorbent value for the remaining tests.

(ii) Effect of reaction time and concentration

Figure 4.3b and c presents the influence of reaction time and starting concentration on adsorbate removal efficiency. At the point of equilibrium, the ideal concentration for CT and RS were observed to be 100 mgL^{-1} and 80 mgL^{-1} (60- 180 mgL^{-1}) at the same reaction time of 60 min (5-100 min).

(iii) Effect of solution pH

The pH of the solution plays a vital role in influencing the adsorbate adsorption process. It significantly alters the surface charge of the adsorbent and the ionic strength of the adsorbate, thereby exerting the overall mechanism of adsorption. The influence of pH on CT and RS adsorption was studied under specific conditions (initial concentration- 100 mgL^{-1} for CT and 80 mgL^{-1} for RS; adsorbent dosage of 0.2 gL^{-1}; reaction time of 60 min). The pH range for CT and RS was carefully altered from 2 to 12, and the obtained results are illustrated in Figure 4.3d. From Figure 4.3d, it can be examined that the highest adsorption efficacy was 99.23 % for CT and 98.68 % for RS, respectively at pH solution 6 and 4. As a result, the adsorption process is

particularly favorable for pH values less than the pH_{zpc} (pH <pK_{zpc}). The pK_a values of CT and RS were determined to be 9.4 and 9.25, respectively, while the pH_{zpc} of the CCAC adsorbent was determined to be 7.1 in our prior studies [37]. At a pH level below the pK_{zpc}, the CCAC surface experiences positively charged. This leads to a strong interaction with the non-ionized molecular adsorbate and protonated CCAC adsorbent, thereby confirming a greater adsorption efficiency. However, the removal efficacy declines for CT and RS at higher pH values (pH>pK_{zpc}). The main reason could be due to the competition between the negatively charged phenoxy ions and the excessive presence of OH^-. Thus, the maximum adsorption percentage was 99.23 % (CT) and 98.67 (RS) at pH 6.0 and 4.0.

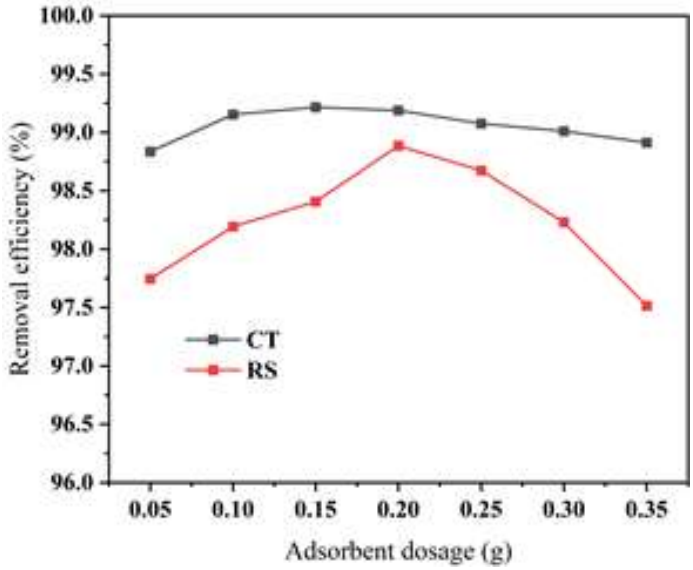

(a) Adsorbent dosage

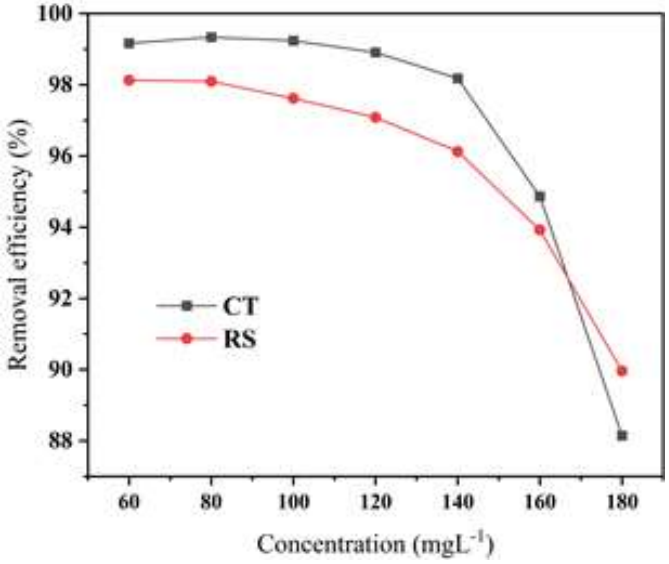

(b) Reaction time

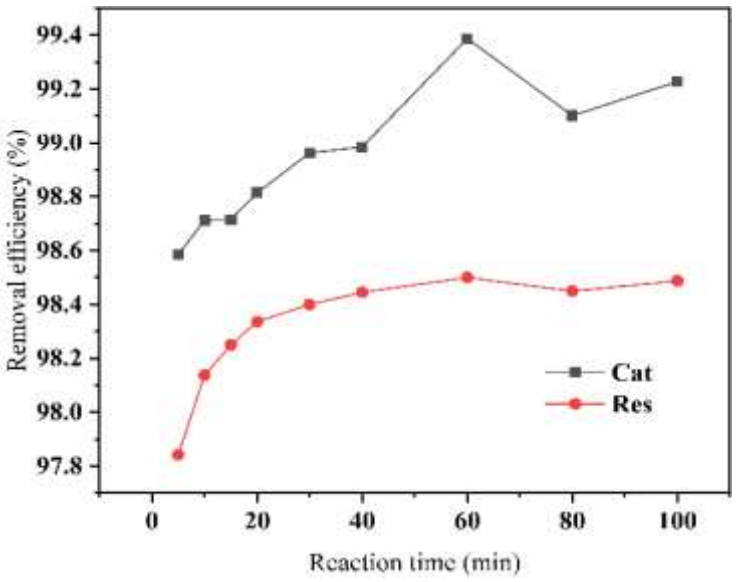

(c) Concentration

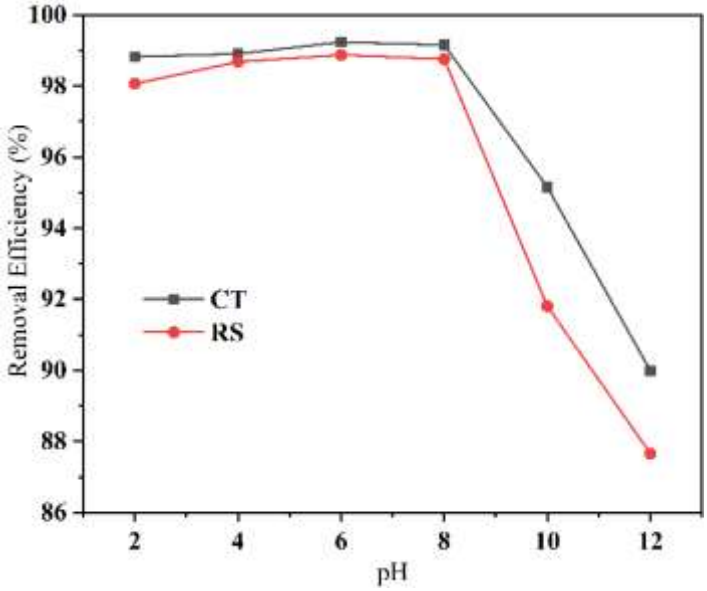

(d) pH

Figure 4.3. Influence of various batch adsorption parameters for CT and RS adsorption by CCAC adsorbent (adsorbent dosage-0.2 g L^{-1}; reaction time-60 min; concentration-100 mgL^{-1} for CT and 80 mgL^{-1} for RS; pH 6.0 for CT and pH 4.0 for RS).

(iv) Effect of temperature

The influence of temperature on the adsorptive removal of CT and RS adsorption by CCAC was explored across a range of temperatures from 298-328 K by keeping other parameters (adsorbent dosage-0.2 g L^{-1}; reaction time-60 min; concentration-100 mgL^{-1} for CT and 80 mgL^{-1} for RS; pH 6.0 for CT and pH 4.0 for RS) at constant. As depicted in the plot (Figure 4.4), the efficiency of CT and RS adsorbed by carbon

adsorbent increases as the initial temperature ascends from 298 K to 338 K. Furthermore, the improved adsorption performance at higher temperatures can be ascribed to the interaction between the adsorbent material and adsorbate molecules, leading to the generation of new adsorption sites into the pores of CCAC at higher temperatures. Similar observations for the adsorption of CT and RS by SSHAC adsorbent were reported by Vunain et al. [35].

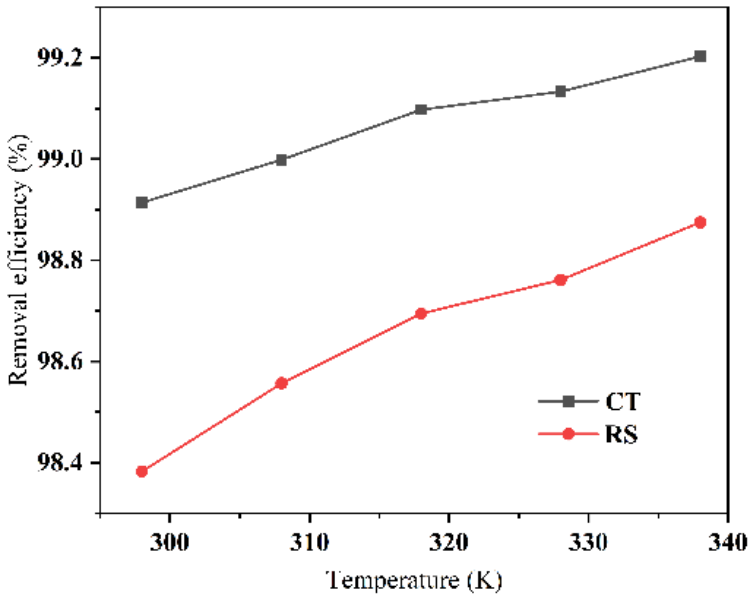

Figure 4.4 Influence of temperature (K) on CT and RS adsorption by CCAC adsorbent.

4.4.2 Adsorption's thermodynamics

Thermodynamic calculations were utilized for evaluating vital parameters such as the standard Gibbs free energy change (ΔG), standard enthalpy change (ΔH), and standard entropy change (ΔS) for adsorption of CT and RS. These important values were computed using the Equations (4.5) and (4.6), respectively.

$$\Delta G = -RT \ln K_d \tag{4.5}$$

$$\ln K_d = \frac{\Delta S}{R} - \frac{\Delta H}{RT} \tag{4.6}$$

where, $K_d = \frac{q_e}{C_e}$ is the distribution coefficient, T (K) = solution temperature, R = gas constant (8.314 $Jmol^{-1}K^{-1}$).

The values of entropy and enthalpy were determined from the intercept and slope of

linear variation of $\ln K_d$ with reciprocal temperature (1/T). Table 4.1 describes the obtained results of various thermodynamic parameters.

Table 4.1. Thermodynamic parameters of CT and RS adsorption onto CCAC adsorbent at different temperatures.

Adsorbate	ΔH (kJ/mol)	ΔS (kJ /mol/K)	ΔG (kJ/mol)				
			298K	308K	318K	328K	338K
CT	5.219	0.046	-8.598	-8.948	-9.516	-9.927	-10.465
RS	7.644	0.051	-7.456	-8.002	-8.531	-8.944	-9.491

From the Table, it can be observed that the sorption of both adsorbates on CCAC was an endothermic process, as indicated by the positive value of ΔH. The increase in randomization at the adsorbate/adsorbent interfaces during the adsorption phase was suggested by the positive ΔS value. The degree of spontaneity and feasibility in the adsorption process was evaluated through the measurement of ΔG. A more negative value of the Gibbs free energy signifies a greater degree of favourability and tendency for the adsorption to occur at higher temperatures.

4.4.3 Adsorption isotherm

The adsorption isotherm is an efficient means for describing the distribution of adsorbed molecules at equilibrium between the liquid and solid phases.

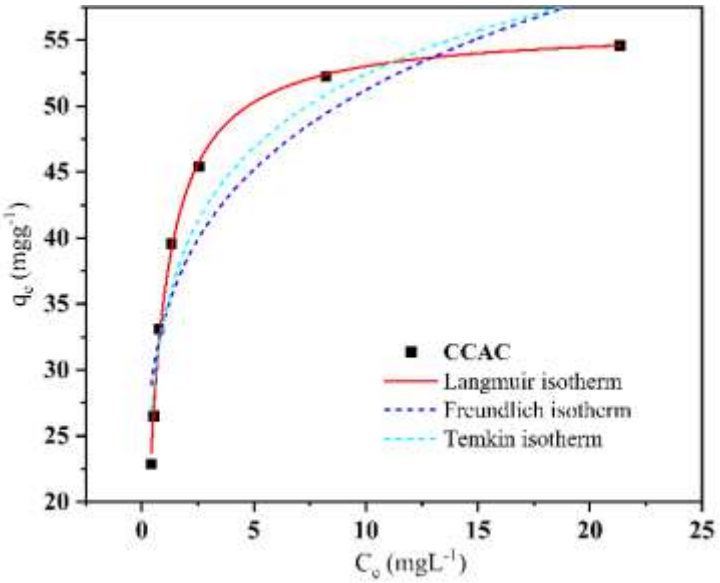

(a) Catechol (CT)

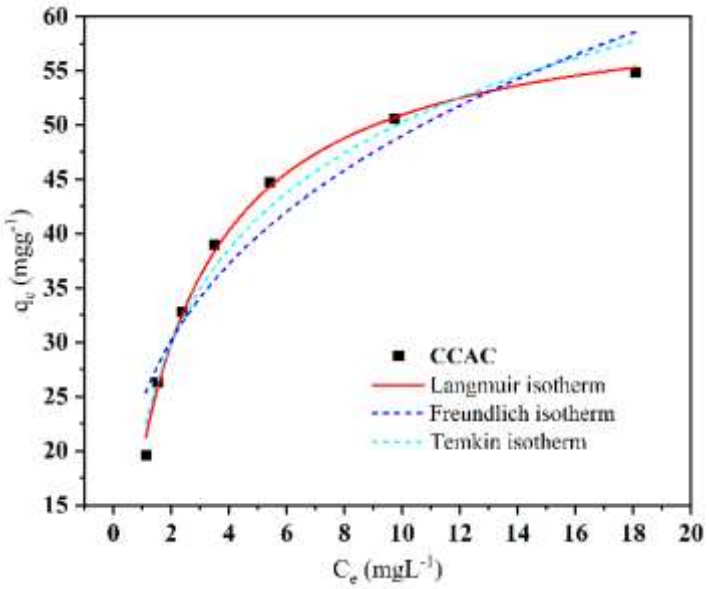

(b) Resorcinol (RS)

Figure 4.5. Non-linear adsorption isotherm fitting for adsorption of CT and RS onto CCAC adsorbent.

In this study, three isotherm models—Langmuir, Freundlich, and Temkin were used to understand the adsorption phenomena of CT and RS onto CCAC adsorbent at equilibrium (Figure 4.5). Table 4.4.2 displays the plot parameters obtained for the isotherm models and χ^2 value. In this table, the Langmuir model adequately describes CT and RS adsorption on the CCAC surface with the high correlation coefficients, R^2 (0.996 for CT) and (0.995 for RS). The maximal monolayer adsorption capacity (Q_m) of CT and RS onto CCAC was determined to be 56.056 mg g^{-1} and 61.851 mg g^{-1}, respectively.

The calculated R_L value was less than 1 while the value of n was greater than 1; hence the adsorption process was favorable. The computed R_L value ranging from (0.003 ~ 0.009 for CT) and (0.011 ~ 0.034 for RS) demonstrates an extremely favorable adsorption on CCAC adsorbent. In terms of Freundlich model, the n value of the Freundlich constant was above unity, thereby indicating an adsorption process with favorable conditions [47,48]. It was evident from the correlation coefficient values (ranging from 0.839 to 0.902) for both pollutants that the Freundlich isotherm model was not adequate to explain the experimental results. From Temkin model, the coefficient of determination of regression R^2 value was found to be 0.908 (CT) and 0.967 (RS), respectively.

Among the various isotherm models, the best-fit model was determined based on the chi-square value (χ^2) and correlation coefficient (R^2). Langmuir's isotherm model emerges as the most appropriate choice, exhibiting the smallest χ^2 value and the highest R^2 value. This result confirms Langmuir's isotherm model that effectively describes the equilibrium adsorption of CT and RS on CCAC and follows the order: Langmuir > Freundlich > Temkin.

Table 4.2. Adsorption isotherm models, its parameters and correlation coefficients of CT and RS adsorption onto CCAC adsorbent.

Isotherms Models	**Adsorbates**	
	CT	**RS**
Langmuir,	Q_m= 56.056	Q_m= 61.851
$q_e = \frac{Q_m K_L C_e}{1 + K_L C_e}$	K_L=1.744	K_L=0.466
	R_L= 0.003 ~ 0.009	R_L= 0.011 ~ 0.034
$R_L = \frac{1}{1 + K_L C_O}$	R^2 = 0.996	R^2 = 0.995
	χ^2 = 0.559	χ^2 = 0.770
Freundlich,	n = 5.537	n = 3.319
$q_e = K_F C_e^{\frac{1}{n}}$	K_F = 33.799	K_F = 34.49
	R^2 = 0.839	R^2 = 0.902
	χ^2 = 24.401	χ^2 = 16.066
Temkin,	K_T = 66.812	K_T = 5.242
$q_e = \frac{RT}{b_T} ln(K_T C_e)$	b_T = 0.307	b_T = 0.195
	R^2 = 0.908	R^2 = 0.967
	χ^2 = 13.953	χ^2 = 5.399

4.4.4 Adsorption kinetics

The study of kinetics plays a pivotal role in comprehending the dynamics of adsorption reactions and mechanism. To understand the adsorption behavior of CT and RS on CCAC adsorbent, three distinct kinetic models were applied: pseudo-first order (PFO), pseudo-second order (PSO), and intraparticle diffusion (ID) models [49-51]. Figure 4.6 demonstrate the kinetic analyses of the adsorption of CT and RS onto the CCAC adsorbent. Table 4.4.3 lists the parameters used for fitting these models using a non-linear regression process. As observed from the table, R^2 values for the PSO were notably higher (0.995 for CT and 0.985 for RS) compared to those associated with the PFO (0.696 for CT and 0.638 for RS). Also, the q_e (exp) values (33.077 mgg^{-1} for CT; 26.314 mgg^{-1} for RS) closely matched the q_e (calc) values (33.019 mgg^{-1} for CT; 26.273 mgg^{-1} for RS) predicted by the PSO model.

Table 4.3. Kinetic parameters for the adsorption of CT and RS by CCAC adsorbent.

Adsorbates	Pseudo-first order (PFO) $q_t = q_e(1 - e^{-k_1 t})$	Pseudo-second order (PSO) $q_t = \frac{q_e^2 k_2 t}{1 + q_e k_2 t}$	Intraparticle diffusion (ID) $q_t = k_{id} t^{0.5} + c$	
			Initial stage	**Final stage**
CT	k_1 = 1.11 $q_{e,cal}$ = 32.98 $q_{e,exp}$ = 33.077 R^2 = 0.696 χ^2 = 7.3 x 10^{-4}	k_2 = 1.238 $q_{e,cal}$ = 33.019 $q_{e,exp}$ = 33.077 R^2 = 0.995 χ^2 = 1.1 x 10^{-5}	$k_{id}1$ = 7.8 x 10^{-3} c = 32.8374 R^2 = 0.851 χ^2 = 4.2 x 10^{-4}	$k_{id}2$ = 3.2 x 10^{-4} c = 32.98255 R^2 = 0.68959 χ^2 =2 x 10^{-5}
RS	k_1 = 1.039 $q_{e,cal}$ = 26.235 $q_{e,exp}$ = 26.314 R^2 = 0.638 χ^2 = 1.2 x 10^{-3}	k_2 = 1.047 $q_{e,cal}$ = 26.273 $q_{e,exp}$ = 26.314 R^2 = 0.985 χ^2 = 4.9 x 10^{-5}	$k_{id}1$ = 8.6 x 10^{-4} c = 26.0646 R^2 = 0.86873 χ^2 = 4.3 x 10^{-4}	$k_{id}2$ = 4.7 x 10^{-4} c = 26.22576 R^2 = 0.62367 χ^2 = 1.1 x 10^{-4}

The calculated PSO rate constants (k_2) for CT and RS were determined to be 1.238 and 1.047, respectively. The larger value of k_2 for CT indicates that CT removal reaches equilibrium faster than RS. The intraparticle diffusion model was employed to elucidate the mass transfer mechanism of CT and RS at the interface between the solid and liquid phases. The plot derived from the intraparticle diffusion model exhibited two distinct adsorption stages: initial surface adsorption and subsequent gradual intra-particle diffusion (Figure 4.7).

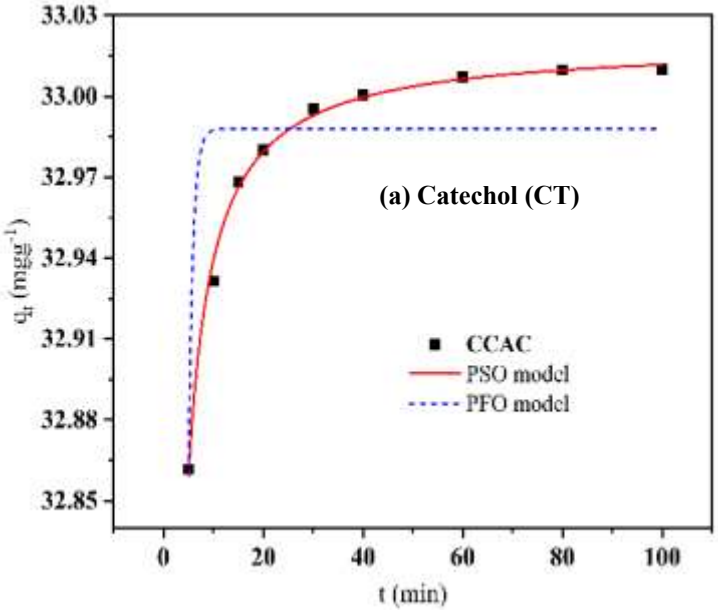

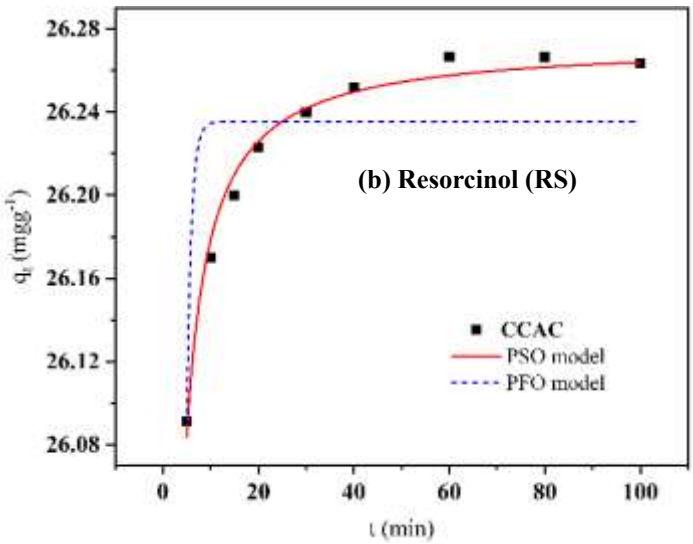

Figure 4.6. Non-linear adsorption kinetics fitting for adsorption of CT and RS by CCAC adsorbent.

Notably, the intraparticle diffusion rate constant $K_{id}1$ surpassed $K_{id}2$, signifying that the pace of intraparticle diffusion decelerated during the final adsorption stage. This reduction in diffusion rate could be attributed to pore blockage and steric repulsion arising from adsorbed CT/RS molecules on the activated carbon surface. Moreover, in employing the intra-particle diffusion model for analysis, the observed linear plot did not originate from the zero point. This indicates that the intra-particle diffusion did not singularly govern the adsorption progression as other factors played a role in the controlling the overall process [52,53].

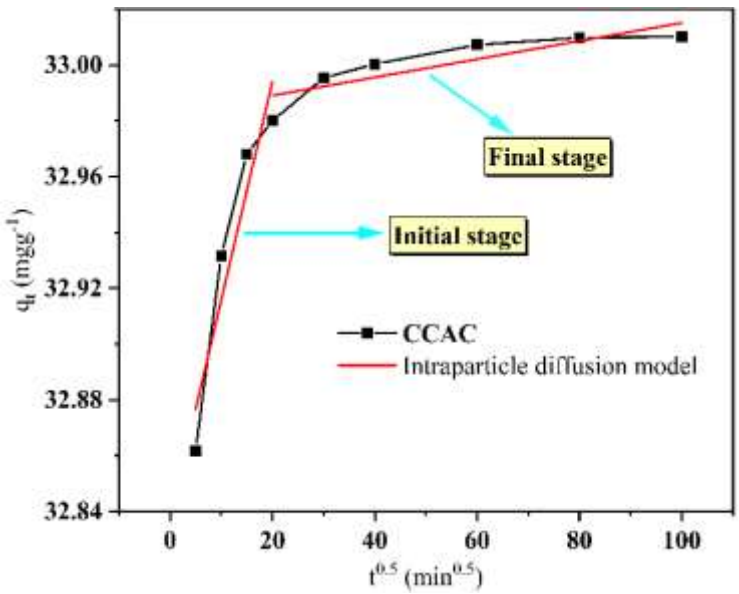

(a) Catechol (CT)

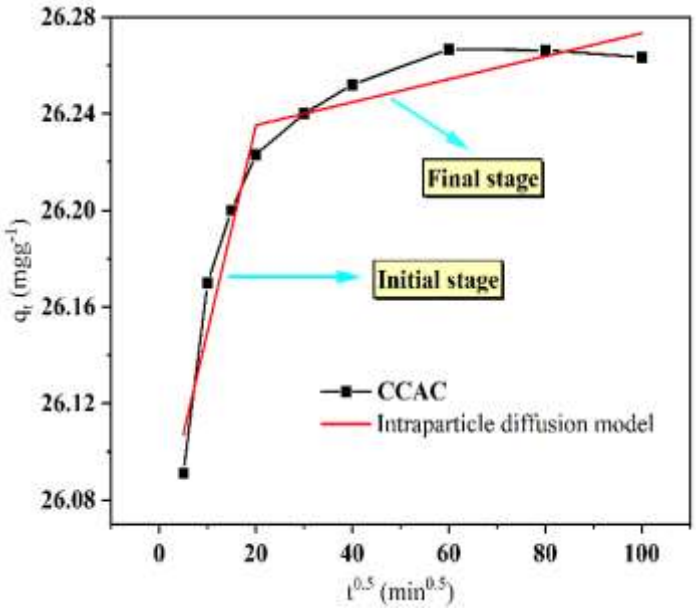

(b) Resorcinol (RS)

Figure 4.7. Intraparticle diffusion (ID) model for adsorption of CT and RS by CCAC adsorbent.

This reduction in diffusion rate could be attributed to pore blockage and steric repulsion arising from adsorbed CT/RS molecules on the activated carbon surface. Moreover, in employing the intra-particle diffusion model for analysis, the observed linear plot did not originate from the zero point. This indicates that the intra-particle diffusion did not singularly govern the adsorption progression as other factors played a role in the controlling the overall process [52,53].

Furthermore, chi-squared value (χ^2) was employed to validate the kinetic studies. The low χ^2 and highest correlation coefficients obtained for both CT (χ^2) and RS (χ^2) providing strong evidence that the PSO model is the best fit among the other kinetic models.

4.4.5 Effect of co-interfering ions

Wastewater commonly contains a variety of inorganic ions, and thus it is important to study the presence of these coexisting ions on the efficient removal of CT and RS from aqueous solutions. The adsorption behavior of CT and RS was carried out in the presence of four inorganic co-ions (NO_3^-, Cl^-, SO_4^{2-} and CO_3^{2-}). The graphical representation in Figure 4.8, demonstrates a discernible drop in the removal effectiveness of CT and RS when these co-ions are present.

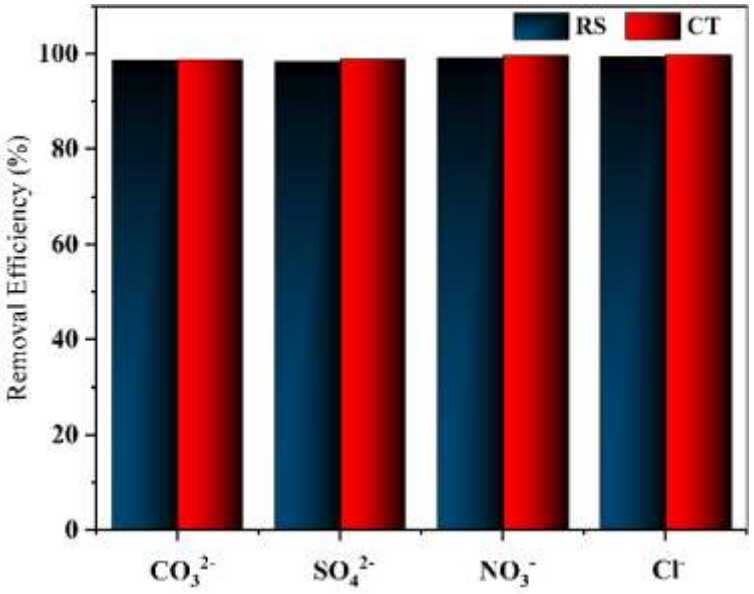

Figure 4.8. Effect of co-existing ions on CT and RS adsorption onto CCAC adsorbent (Concentration - 100 mgL^{-1} for CT and 80 mgL^{-1} for RS; activated carbon dose- 0.2 gL^{-1} for CT and RS; reaction time- 60 min for CT and RS).

Carbonate and sulfate ions showed a decline in efficiency among the various co-ions due to their higher negative charges than nitrate and chloride ions. The reason may be due to the formation of outer-sphere surface complexes by chloride and nitrate ions [54]. Thus, the sequence of these ions follows the ascending order: CO_3^{2-}>SO_4^{2-}> NO_3^- > Cl^- with the removal efficiencies from 98.64 % to 99.29 % for CT and 98.75 % to 99.65 %, respectively [55]. Similar results were also observed by Liu et al. [56] for the adsorption of Bisphenol A and Tetrabromobisphenol A.

4.4.6 Regeneration studies

Regeneration investigations are vital in any adsorption procedure as they can significantly reduce disposal costs, resulting in a more sustainable approach. In this work, 1 g L^{-1} of CCAC was consistently mixed with 50 mL of 1000 mg L^{-1} CT and RS solution for a period of 24 hours until overall saturation was attained. Desorption of fully saturated CCAC was performed using 95% ethanol for two hours with constant stirring. Afterward, the resulting solutions were filtered, rinsed, and dried using an oven set at 110 °C. This regenerated material was then employed for further CT and RS adsorption to confirm its viability for reuse. Figure 4.9 depicts the desorption efficiency of adsorbate from regenerated CCAC. The bar graph shows that after the

first cycle, the desorption efficiency of regenerated CCAC decreased from 91.10 % to 78.75 % for CT and 93.50 % to 82.10 % for RS by the fifth cycle, thus confirming the possibility of reusing regenerated CCAC for numerous cycles.

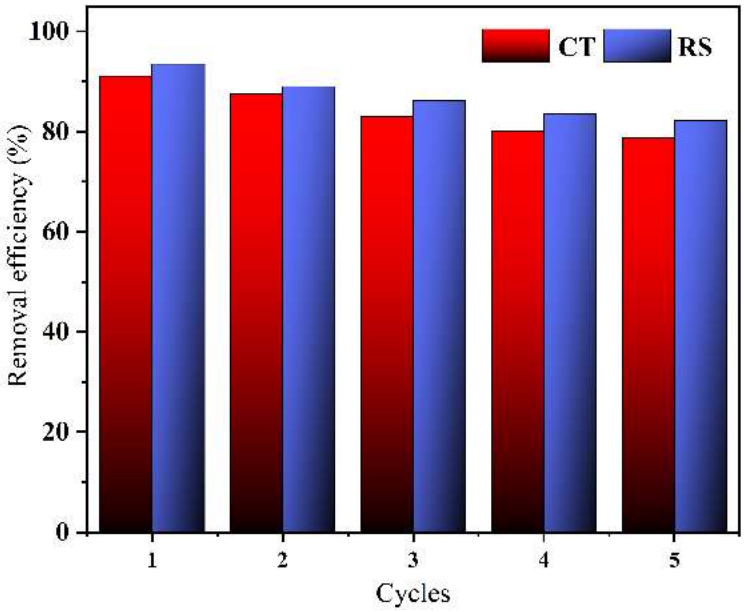

Figure 4.9. Desorption efficiencies of regenerated CCAC adsorbent for the removal of CT and RS.

4.4.7 Theoretical studies

The adsorption process of CT and RS onto activated carbon ought to involve various interactions such as π–π interactions, electrostatic forces, and hydrogen bonding between the adsorbate and unmodified AC as well as oxygen-containing functional groups present in the AC [57-59]. Furthermore, it is widely acknowledged that π-π interactions and hydrogen bonding are the key driving forces behind the interactions between contaminants and AC [60].

In this regard, a schematic representation of the possible adsorption mechanism is shown in Figure 4.8. Elucidating a potential mechanism for the adsorption of catechol and resorcinol onto activated carbon would enhance our comprehension of the interactions between the adsorbate and the adsorbent.

(i) π-π interaction

The adsorption of aromatic compounds on activated carbon surfaces is driven by π-π interactions, which involve charge transfer between the π-electrons of the adsorbate's aromatic rings and the carbon material [61]. In resorcinol, the meta-positioning of -

OH groups enhance π-electron delocalization, facilitating stronger π-π interactions compared to catechol's ortho arrangement, which can lead to steric hindrances [62]. Therefore, resorcinol shows stronger π-π interaction as compared to catechol.

(ii) hydrogen bonding

Hydrogen bonding between resorcinol and catechol and the oxygen containing functional groups on activated carbon plays a crucial role in their adsorption behavior [63]. Both compounds feature -OH groups that can form hydrogen bonds with functional groups on the activated carbon surface. This interaction increases the stability of the adsorbates on the carbon surface, facilitating effective adsorption [64]. The meta-positioning of the -OH groups provide optimal spatial orientation in resorcinol, resulting in stronger hydrogen bonding compared to catechol, which has its -OH groups in the ortho position. Consequently, resorcinol exhibits greater adsorption efficiency due to these favorable hydrogen bonding interactions, as supported by DFT results.

However, among the numerous interactions contributing to the adsorption process, this study aimed to elucidate the possible formation of hydrogen bonds between AC and the adsorbate by employing DFT calculations [65-67]. The arm-chair model was employed to replicate the processes involving both unmodified activated carbon (AC) and OFGs were introduced on the surface of AC to study the influence on the adsorption of CT and RS. Figure 4.10 depicts the best possible configurations of the interactions involving AC, functionalized AC and adsorbate. The adsorption energies (E_{ads}), mode of interaction and bond distance for various interactions have been displayed in Table 4.4.

(a) Adsorption on unmodified AC

To probe the possibility of a contact of CT and RS with AC surface, an interaction was formed between the OH group of adsorbates and the C-atom of the unmodified AC structure (Figure 4.11a and b). During the adsorption process, the distance between C—C bonds within the unmodified AC experienced minor elongation from 0.124-0.125 nm and 0.140-0.142 nm for CT and RS, respectively, thereby resulting in migration of electron density towards the adsorptive site. Moreover, the total energy obtained from the simulation was found to be highest for CT adsorption compared to

RS. This implies that CT exhibited a stronger attachment to the activated carbon surface than RS. These outcomes are in concordance with experimental findings, reinforcing their validity.

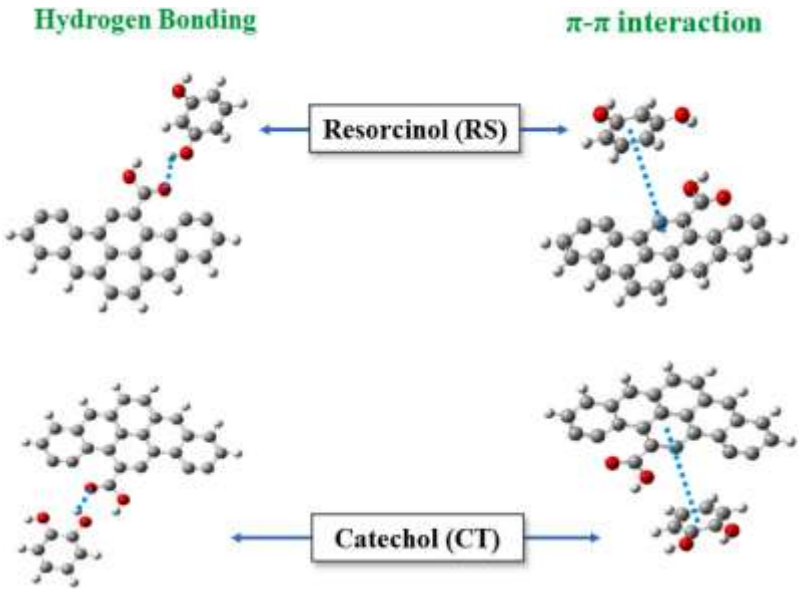

Figure 4.10. Schematic representation of the possible mechanism for CT and RS adsorption onto activated carbon.

(b) Adsorption on OH functionalized AC

In the study of CT and RS adsorption onto OH-functionalized AC, an interaction mechanism that involved the formation of hydrogen bonds between the hydrogen or oxygen atoms of OH-AC and the O or H-atoms of CT and RS was considered. As shown in Figure 4.11c-f, the interaction between OH-functionalized AC and adsorbate was investigated using two distinct attachment strategies: (CT)OH—OH(AC) and (CT)HO—HO(AC) of CT and (RS)OH—OH(AC) and (RS)HO—HO(AC) of RS. From the table, it can be seen that (CT)OH—OH(AC) and (RS)OH—OH(AC) designates the highest adsorption energy with shorter bond length as compared to (CT)HO—HO(AC) and (RS)HO—HO(AC). Furthermore, the adsorption energy of (RS)OH—OH(AC) configuration was greater than that of (CT)OH—OH(AC) configuration. Hence, the adsorption of RS was found to be strongest with AC functionalized with OH groups.

(c) Adsorption on CHO functionalized AC

In order to gain insight into the adsorption mechanism of adsorbate onto activated car-

bon modified with aldehyde (CHO) functional groups, the study primarily examined the occurrence of a H-bonding interaction between the H-atom of the OH group of the adsorbate with O-atom of the AC functionalized aldehyde group (Figure 4.11g and h). The adsorption energy (E_{ads}) for (CT)OH—OHC(AC) and (RS)OH—OHC(AC) has been determined to be -25.391 kJ/mol and -36.344 kJ/mol, indicating preferential adsorption of CT and RS onto activated carbon functionalized with CHO groups.

(d) Adsorption on COOH functionalized AC

The adsorption interaction of adsorbate on the surface of activated carbon, which has been functionalized with carboxyl (COOH) groups, is facilitated through the formation of two different kinds of hydrogen bonds (Figure 4.11i-l). The two modes of interaction between the adsorbate and AC(COOH) are depicted in Table 4.4. After adsorption, it can be seen that the adsorption energies for CT and RS correspond to -44.869 kJ/mol and -45.082 kJ/mol, respectively. These findings indicate that the interaction labeled AC(COOH)—OH(CT) and AC(COOH)—OH(RS) were determined to be more suitable for the adsorption of CT and RS.

Table 4.4. E_{ads} and bond length between adsorbates (CT and RS) and AC systems.

Adsorbate + Adsorbent System		**Mode of interaction**	**Adsorption energy (kJ/mol)**	**Bond distance(nm)**
Catechol + AC	CT + AC	(CT)OH—C(AC)	-18.231	0.282
	CT + (AC)OH	(CT)OH—OH(AC)	-29.773	0.167
		(CT)HO—HO(AC)	-24.561	0.186
	CT + (AC)CHO	(CT)OH—OHC(AC)	-25.391	0.178
	CT + (AC)COOH	(CT)OH—OCOH(AC)	-44.869	0.178
		(CT)HO—HOOC(AC)		0.162
Resorcinol + AC	RS + AC	(RS)OH—C(AC)	-16.587	3.032
	RS + (AC)OH	(RS)OH—OH(AC)	-31.650	1.669
		(RS)HO—HO(AC)	-24.369	1.734
	RS + (AC)CHO	(RS)OH—OHC(AC)	-36.344	1.780
	RS + (AC)COOH	(RS)HO—HOOC(AC)	-45.082	1.642
		(RS)OH—OCOH(AC)		2.005

Catechol (CT)	Resorcinol (RS)
	
(a)(CT)OH—C(AC)	**(b)(RS)OH—C(AC)**
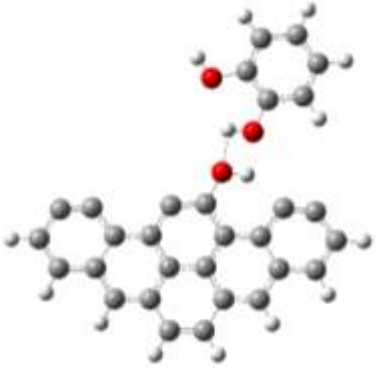	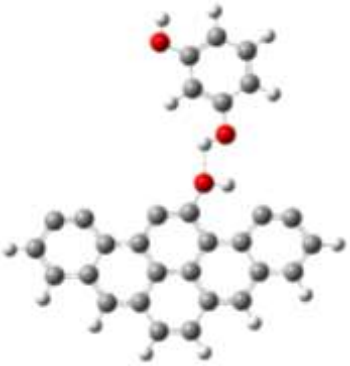
(c)(CT)OH—OH(AC)	**(d) (RS)OH—OH(AC)**
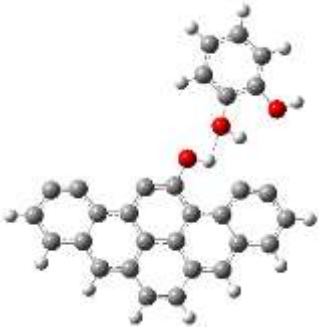	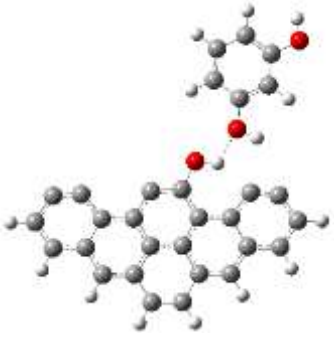
(e)(CT)HO—HO(AC)	**(f)(RS)HO—HO(AC)**
	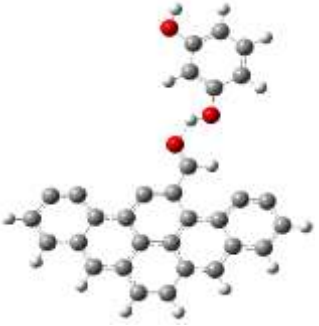
(g) (CT)OH—OHC(AC)	**(h) (RS)OH—OHC(AC)**

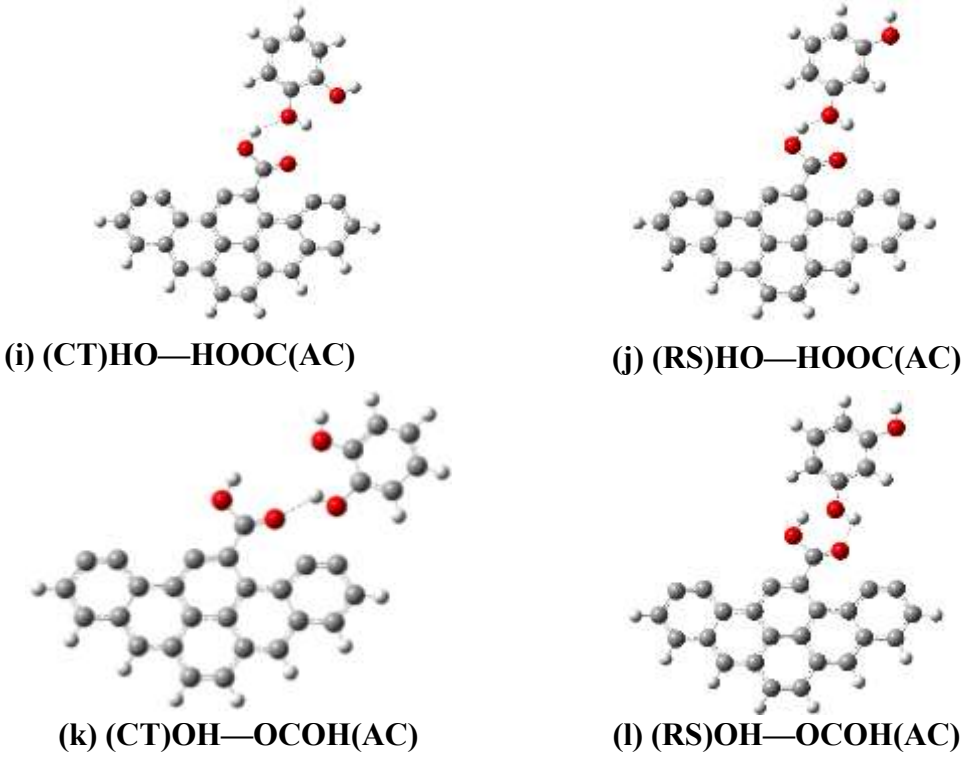

(i) (CT)HO—HOOC(AC) **(j) (RS)HO—HOOC(AC)**

(k) (CT)OH—OCOH(AC) **(l) (RS)OH—OCOH(AC)**

Figure 4.11. Optimised structures of adsorbate interactions with unmodified and functionalized AC.

Furthermore, the results of FT-IR spectra of activated carbon after catechol and resorcinol adsorption were analysed and a comparison were made with DFT studies to strengthen and support the explanation of the adsorption mechanism (Figure 4.12). The IR results show a clear shift of -OH stretching vibration toward the higher frequen-

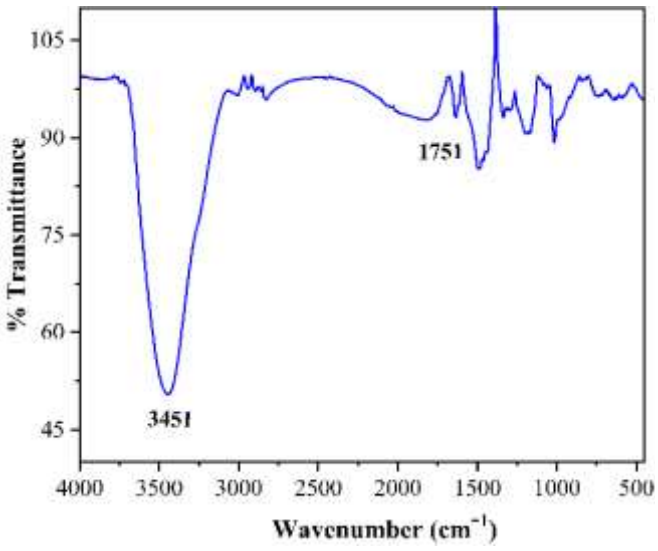

(a)

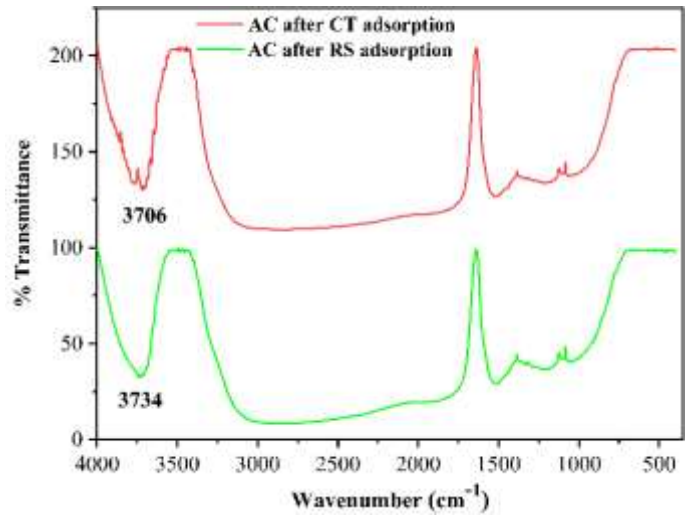

(b)

Figure 4.12. FTIR spectra of (a) AC (b) AC after CT and RS adsorption.

cy after adsorption. The IR results show a clear shift of -OH stretching vibration toward the higher frequency after adsorption. This shift could be attributed to strong interactions between the adsorbate and oxygen-containing functional groups of AC, as indicated by the DFT studies. Additionally, the carbonyl adsorption frequencies for the adsorbate-loaded activated carbon were observed to shift to a lower frequency region which could be due to favorable hydrogen bonding of CT and RS with AC, as collaborated by DFT studies [68-70].

4.4.8 Comparison of adsorption capacity of CCAC adsorbent with other adsorbents

A comparison assessment was made between the present CCAC adsorbent with other adsorbents in regard to its ability for maximum adsorption capacity (Q_m) of CT and RS from aqueous medium. Table 4.5 summarizes the findings, which reveal that the present adsorbent has significantly higher adsorption capacity for CT and RS than other reported materials.

Table 4.5. Comparative assessment of adsorption of CT and RS on CCAC adsorbent and other adsorbents.

Adsorbate	Adsorbent	Adsorption capacity (mg g^{-1})	Ref.
CT	CCAC	56.05	**This Study**
	Hypercross-linked polymers	55.00	[71]
	MWCNT	14.20	[72]

	TiO_2 Degussa P-25 surface	11.17	[73]
	Waste Fe (III)/Cr (III) hydroxide	4.00	[74]
	CSI	2.86	[75]
	AC	0.07	[76]
RS	CCAC	61.85	**This Study**
	Hypercross-linked polymers	55.00	[71]
	AC	43.09	[77]
	Modified OMC	39.2	[78]
	Granular activated carbon	8.43	[79]
	TiO_2 Degussa P-25 surface	7.87	[73]
	CSI	3.63	[75]

4.5 Conclusion and proposed future research

(i) Summary

The major findings derived from these investigations can be succinctly summarized in the following manner:

- The experimental batch adsorption yielded high removal efficiencies of 99.23 % for CT and 98.68 % for RS, respectively, under ideal process conditions.
- Adsorption of CT and RS on AC followed the Langmuir adsorption isotherm, implying a single-layer coverage and adsorptive capacities of 56.05 mgg^{-1} at pH 6 for CT and 61.85 mgg^{-1} at pH 4 for RS.
- The kinetics of adsorption process on CCAC closely followed pseudo-second order model based on the highest R^2 (0.995 for CT and 0.985 for RS) value, low χ^2 and the close agreement between calculated and theoretical q_e values.
- Thermodynamic analysis confirmed that the adsorption process was endothermic and spontaneous.
- The adsorption behavior of catechol (CT) and resorcinol (RS) was examined in the presence of four inorganic co-ions: NO_3^-, Cl^-, SO_4^{2-} and CO_3^{2-}). The removal efficiencies for these ions followed the ascending order: CO_3^{2-}>SO_4^{2-}> NO_3^-> Cl^-, with removal rates ranging from 98.64-99.29 % for catechol and from 98.75-99.65% for resorcinol.
- Regeneration studies indicated that the CCAC adsorbent remained effective up to the fifth cycle (78.75 % for CT and 82.10 % for RS), suggesting that the adsorbent

can be reused and recycled multiple times.

- DFT analyses suggests the favorable nature of the adsorption of CT and RS on AC based solely on the assumption of hydrogen bond interactions. Notably, the AC containing COOH groups demonstrated the strongest interaction with phenolic compounds, indicating its superior potential for adsorption.

The outcomes of the study underscored the suitability of *Croton caudatus* AC could serve as a potentially effective and recyclable adsorbent for the removal of CT and RS from water. Additionally, the insights from the theoretical investigations might be valuable in developing and producing activated carbon materials with enhanced binding capabilities for phenolic compounds.

(ii) Proposed future requirements

Although significant progress has been made in developing potential sorbents, further research should focus on:

(i) Forecasting the efficacy of adsorption processes for removing phenolic compounds from real wastewater under various operating conditions.

(ii) Enhancing the precision of the adsorption mechanism by extending it to more than one kind of activated carbon model.

(iii) Molecular dynamics simulations or hybrid approaches that integrate DFT with classical force fields can effectively capture the dynamic aspects of adsorption processes and the complexities associated with multi-component systems.

(iv) Comprehensive understanding of the adsorption mechanism involved between the oxygen containing functional groups of activated carbon and phenolic compounds.

References

[1] B. K. Korbahti, A. Tanyolac, Continuous electrochemical treatment of phenolic wastewater in a tubular reactor, Water Res., 37 (2003) 1505–1514.

[2] M. Khodari, A. Abd El-Rady, E. Rabee, N. Nabil, Electro analytical determination of dihydroxybenzene isomers using glassy carbon electrode, J. Chem. Eng., 8 (2014) 654–661.

[3] F. Behboodi-Sadabad, H. Zhang, V. Trouillet, A. Welle, N. Plumere, P. A. Levkin, Bioinspired strategy for controlled polymerization and photopatterning of plant polyphenols, Chem. Mater., 30 (2018) 1937–1946.

[4] B. Dellinger, W. A. Pryor, R. Cueto, G. L. Squadrito, V. Hegde, W. A. Deutsch, Role of free radicals in the toxicity of airborne fine particulate matter, Chem. Res. Toxicol., 14 (2001) 1371–1377.

[5] P. W. Milligan, M. M. Haggblom, Biodegradation of resorcinol and catechol by denitrifying enrichment cultures, Environ. Toxicol. Chem., 17 (1998) 1456–1461.

[6] M. D. Hays, P. M. Fine, C. D. Geron, M. J. Kleeman, B. K. Gullett, Open burning of agricultural biomass: physical and chemical properties of particle-phase emissions, Atmos. Environ., 39 (2005) 6747–6764.

[7] M. F. Hanafi, N. Sapawe, A review on the water problem associate with organic pollutants derived from phenol, methyl orange, and remazol brilliant blue dyes, Mater. Today Proc., 31 (2020) 141–150.

[8] A. Kumar, S. Kumar, S. Kumar, Adsorption of resorcinol and catechol on activated carbon: equilibrium and kinetics, Carbon, 41 (2003) 3015–3025.

[9] N. Schweigert, A. J. B. Zehnder, R. I. L. Eggen, Chemical properties of catechols and their molecular modes of toxic action in cells, from microorganisms to mammals, Environ. Microbiol., 3 (2001) 81–91.

[10] H. Freeman, E. Harris, Hazardous waste remediation: innovative treatment technologies, CRC Press (1995).

[11] E. Bayram, N. Hoda, E. Ayranci, Adsorption/electrosorption of catechol and resorcinol onto high area activated carbon cloth, J. Hazard. Mater., 168 (2009) 1459–1466.

[12] S. Cohen, P. A. Belinky, Y. Hadar, C. G. Dosoretz, Characterization of catechol derivative removal by lignin peroxidase in aqueous mixture, Bioresour. Technol., 100 (2009) 2247–2253.

[13] S. M. Abu Nayem, S. S. Shaheen Shah, N. Sultana, M. A. Aziz, A. J. Saleh Ahammad, Electrochemical sensing platforms of dihydroxybenzene: part 1—carbon nanotubes, graphene, and their derivatives, Chem. Rec., 21 (2021) 1039–1072.

[14] J. Huang, K. Huang, C. Yan, Application of an easily water-compatible hypercrosslinked polymeric adsorbent for efficient removal of catechol and resorcinol in aqueous solution, J. Hazard. Mater., 167 (2009) 69–74.

[15] S. Agarwal, A. Rani, Adsorption of resorcinol from aqueous solution onto CTAB/NaOH/fly ash composites: equilibrium, kinetics and thermodynamics, J. Environ. Chem. Eng., 5 (2017) 526–538.

[16] K. Othmer, Hydroquinone, resorcinol, and catechol, in: Kirk Othmer Encyclopedia of Chemical Technology, John Wiley & Sons, New York (1981) 1–21.

[17] R. Subramanyam, I. M. Mishra, Critical review of anaerobic biodegradation of benzenediols: catechol, resorcinol, and hydroquinone, J. Hazard. Toxic Radioact. Waste, 17 (2013) 218–229.

[18] R. Raff, B. V. Etlling, In: Kirk-Othmer Encyclopedia of Chemical Technology, Wiley-Interscience, New York (1966) 462.

[19] S. Suresh, V. C. Srivastava, I. M. Mishra, Adsorption of catechol, resorcinol, hydroquinone, and their derivatives: a review, Int. J. Energy Environ. Eng., 3 (2012) 1–19.

[20] N. A. S. Mohammed, R. A. Abu-Zurayk, I. Hamadneh, A. H. Al-Dujaili, Phenol adsorption on biochar prepared from pine fruit shells: equilibrium, kinetic and thermodynamics studies, J. Environ. Manage., 226 (2018) 377–385.

[21] P. Canizares, J. Lobato, R. Paz, M. A. Rodrigo, C. Sáez, Electrochemical oxidation of phenolic wastes with boron-doped diamond anodes, Water Res., 39 (2005) 2687–2703.

[22] M. L. Satuf, R. J. Brandi, A. E. Cassano, O. M. Alfano, Scaling-up of slurry reactors for photocatalytic degradation of 4-chlorophenol, Catal. Today, 129 (2007) 110–117.

[23] R. A. K. Rao, M. A. Khan, B. H. Hameed, Sorption/desorption studies on natural minerals for removal of toxic organic pollutants from aqueous solution, J. Chem. Eng., 152 (2009) 421–427.

[24] M. F. F. Sze, G. McKay, Adsorption diffusion model for removal of para-chlorophenol by activated carbon derived from bituminous coal, Environ. Pollut., 158 (2010) 1669–1674.

[25] J. W. Lim, P. E. Lim, C. E. Seng, R. Adnan, Simultaneous 4-chlorophenol and nitrogen removal in moving bed sequencing batch reactors, Bioresour. Technol., 129 (2013) 485–494.

[26] A. Kuleyin, Removal of phenol and 4-chlorophenol by surfactant-modified natural zeolite, J. Hazard. Mater., 144 (2007) 307–315.

[27] A. T. Adeleye, A. A. Akande, C. K. Odoh, M. Philip, T. T. Fidelis, P. I. Amos, O. O. Banjoko, Efficient synthesis of bio-based activated carbon for catalytic systems: a green approach, J. Ind. Eng. Chem., 96 (2021) 59–75.

[28] X. Wang, H. Cheng, G. Ye, J. Fan, F. Yao, Y. Wang, Y. Jiao, W. Zhu, H. Huang, D. Ye, Key factors and modification methods of activated carbon for adsorption of carbon-based gases: a review, Chemosphere, 287 (2002) 131995.

[29] R. Gusain, N. Kumar, S. S. Ray, Recent advances in carbon nanomaterial-based adsorbents for water purification, Coord. Chem. Rev., 405 (2020) 213111.

[30] C. Li, J. Yang, L. Zhang, S. Li, Y. Yuan, X. Xiao, X. Fan, C. Song, Carbon-based membrane materials and applications in water and wastewater treatment: a review, Environ. Chem. Lett., 19 (2021) 1457–1475.

[31] A. Demirbas, Agricultural based activated carbons for removal of dyes from aqueous solutions: a review, J. Hazard. Mater., 167 (2009) 1–9.

[32] C. Namasivayam, D. Sangeetha, R. Gunasekaran, Removal of anions, heavy metals, organics and dyes using activated carbon from Jatropha husk, Process Saf. Environ. Prot., 85 (2007) 181–184.

[33] M. S. Reza, C. S. Yun, S. Afroze, N. Radenahmad, M. S. A. Bakar, R. Saidur, J. Taweekun, A.K. Azad, Preparation of activated carbon from biomass and its applications in water and gas purification: a review, Arab. J. Basic Appl. Sci., 27 (2020) 208–238.

[34] M. Gayathiri, T. Pulingam, K. T. Lee, K. Sudesh, Activated carbon from biomass waste precursors: production and adsorption mechanism, Chemosphere, 294 (2022) 133764.

[35] E. Vunain, D. Houndedjihou, M. Monjerezi, A. A. Muleja, B. Kodom, Adsorption and equilibrium studies on catechol and resorcinol removal using sunflower seed hull activated carbon, Water Air Soil Pollut., 229 (2018) 1–23.

[36] M. Ahmaruzzaman, S. L. Gayatri, Activated neem leaf as adsorbent for phenol and chlorophenol removal, J. Chem. Eng. Data, 56 (2011) 3004–3016.

[37] S. Sharma, S. L. Ezung, A. Supong, M. Baruah, S. Kumar, R. S. Umdor, D. Sinha, Activated carbon derived from Croton caudatus for 2-chlorophenol removal: kinetics, isotherm and DFT simulation, Chem. Eng. Res. Des., 190 (2023) 777–792.

[38] M. Kebir, R. Bourzami, N. Nasrallah, S. E. I. Lebouachera, F. Dergal, R. Ladji, L. Khezami, Pharmaceutical pollutant adsorption onto activated carbon: isotherm and DFT modeling, C. R. Chim., 25 (2022) 9–25.

[39] M. S. Abdelbassit, S. A. Popoola, T. A. Saleh, H. H. Abdallah, A. A. Al-Saadi, K. R. Alhooshani, DFT and kinetic evaluation of chloromethane removal using activated carbon, Arab. J. Sci. Eng., 45 (2020) 4705–4716.

[40] P. C. Bhomick, A. Supong, S. Kumar, A. I. Sema, T. Merry, D. Sinha, Biomass-derived activated carbon for methylene blue removal: adsorption and mechanistic insights, Water Conserv. Sci. Eng., 8 (2023) 1–15.

[41] S. U. Jan, A. Ahmad, A. A. Khan, S. Melhi, I. Ahmad, G. Sun, C. M. Chen, R. Ahmad, Removal of azo dye using coal-derived activated carbon: kinetics and DFT simulation, Environ. Sci. Pollut. Res., 28 (2021) 10234–10247.

[42] A. Jumasiah, T. G. Chuah, J. Gimbon, T. S. Y. Choong, I. Azni, Adsorption of basic dye onto palm kernel shell activated carbon, Desalination, 186 (2005) 57–64.

[43] S. T. Perry, E. M. Hambly, T. H. Fletcher, M. S. Solum, R. J. Pugmire, Solid-state ^{13}C NMR characterization of tars and chars from coal devolatilization, Proc. Combust. Inst., 28 (2000) 2313–2319.

[44] J. S. Smith, O. Isayev, A.E. Roitberg, ANI-1: neural network potential with DFT accuracy, Chem. Sci., 8 (2017) 3192–3203.

[45] A. Adewuyi, A. Göpfert, O.A. Adewuyi, T. Wolff, Adsorption of 2-chlorophenol onto Adenopus breviflorus seed surface, J. Environ. Chem. Eng., 4 (2016) 664–672.

[46] G. Özsin, M. Kılıç, E. Apaydın-Varol, A.E. Pütün, Activated carbon from chickpea waste for heavy metal adsorption, Appl. Water Sci., 9 (2019) 1–14.

[47] K. R. Hall, L. C. Eagleton, A. Acrivos, T. Vermeulen, Pore and solid diffusion kinetics in fixed-bed adsorption, Ind. Eng. Chem., 5 (1966) 212–223.

[48] X. Ma, H. Peng, X. Zhang, Regeneration of nitrophenol-loaded granular activated carbon, Desalin. Water Treat., 57 (2016) 25494–25502.

[49] A. Kumar, H. M. Jena, Removal of methylene blue and phenol using nutshell activated carbon, J. Clean. Prod., 137 (2016) 1246–1259.

[50] S. Lagergren, Zur theorie der sogenannten adsorption geloster stoffe, Kungliga Svenska Vetenskapsakademiens Handlingar, 24 (1898) 1–39.

[51] Y. S. Ho, G. McKay, Kinetics of sorption of divalent metal ions onto sphagnum moss peat, Water Res., 34 (2000) 735–742.

[52] W. J. Weber Jr., J. C. Morris, Kinetics of adsorption on carbon from solution, J. Sanit. Eng. Div., 89 (1963) 31–59.

[53] L. A. de Sousa Ribeiro, G. P. Thim, M. O. Alvarez-Mendez, A. dos Reis Coutinho, N. P. de Moraes, L. A. Rodrigues, Açaí seed-based activated carbon for phenol adsorption, Int. J. Environ. Res., 12 (2018) 755–764.

[54] P. C. Bhomick, A. Supong, R. Karmaker, M. Baruah, C. Pongener, D. Sinha, Biomass-derived activated carbon for fluoride adsorption: experimental and theoretical investigation, Korean J. Chem. Eng., 36 (2019) 551–562.

[55] Y. Xue, Z. Zhang, W. Xu, Y. Yan, F. Ma, M. Yang, Transformation of organic sulfur in cation exchange resins in molten salt system, New J. Chem., 47 (2023) 7527–7537.

[56] S. Liu, P. Wu, M. Chen, L. Yu, C. Kang, N. Zhu, Z. Dang, Modified vermiculites for removal of organic pollutants, Environ. Pollut., 228 (2017) 277–286.

[57] W. Zheng, M. Guo, T. Chow, D. N. Bennett, N. Rajagopalan, Sorption properties of greenwaste biochar for triazine pesticides, J. Hazard. Mater., 181 (2010) 121–126.

[58] A. U. Rajapaksha, M. Vithanage, M. Ahmad, D. Seo, J. Cho, S. Lee, S. S. Lee, Y.S. Ok, Enhanced sulfamethazine removal by steam-activated biochar, J. Hazard. Mater., 290 (2015) 43–50.

[59] K. Zhang, B. Chen, J. Mao, L. Zhu, B. Xing, Water clusters contribution to pollutant interaction with biochar via π-PAHB, Environ. Pollut., 240 (2018) 342–352.

[60] F. Xiao, J. J. Pignatello, Effects of post-pyrolysis air oxidation of biomass chars on adsorption, Environ. Sci. Technol., 50 (2016) 6276–6283.

[61] R. W. Coughlin, F. S. Ezra, Role of surface acidity in adsorption of organic pollutants on carbon, Environ. Sci. Technol., 2 (1968) 291–297.

[62] S. Suresh, V. C. Srivastava, I. M. Mishra, Adsorption of catechol and resorcinol: a review, Int. J. Energy Environ. Eng., 3 (2012) 1–19.

[63] P. Q. Thang, J. Kim, B. L. Giang, N. M. Viet, P. T. Huong, Chicken manure biochar for phenol removal, J. Environ. Manage., 251 (2019) 109556.

[64] N. F. Cimirro, E. C. Lima, M. R. Cunha, P. S. Thue, A. Grimm, G. S. dos Reis, N. Rabiee, M. R. Saeb, F. Keivanimehr, S. Habibzadeh, Removal of diphenols using pine biochar, J. Mol. Liq., 364 (2022) 119979.

[65] X. F. Tan, S. S. Zhu, R. P. Wang, Y. D. Chen, P. L. Show, F. F. Zhang, S. H. Ho, Role of biochar surface characteristics in adsorption of aromatic compounds, Chin. Chem. Lett., 32 (2021) 2939–2946.

[66] B. Pan, H. Zhang, Reconstruction of adsorption potential in Polanyi-based models, Environ. Sci. Technol., 48 (2014) 6772–6779.

[67] F. Guo, D. Li, J. B. Fein, J. Xu, Y. Wang, Q. Huang, X. Rong, Roles of hydrogen bond and ion bridge in bisphenol adsorption, Appl. Clay Sci., 217 (2022) 106406.

[68] Q. Zhou, R. L. Frost, H. He, Y. Xi, H. Liu, Adsorbed para-nitrophenol on HDTMAB organoclay, J. Colloid Interface Sci., 307 (2007) 357–363.

[69] A. P. Terzyk, Influence of activated carbon surface chemistry on acetaminophen adsorption, Colloids Surf. A, 177 (2001) 23–45.

[70] S. Suresh, V. C. Srivastava, I. M. Mishra, Catechol and resorcinol adsorption mechanism study, Sep. Sci. Technol., 46 (2011) 1750–1766.

[71] Y. Sun, J. Chen, A. Li, F. Liu, Q. Zhang, Adsorption of resorcinol and catechol by aminated hypercrosslinked polymers, React. Funct. Polym., 64 (2005) 63–73.

[72] Q. Liao, J. Sun, L. Gao, Adsorption of resorcinol using multi-walled carbon nanotubes, Colloids Surf. A, 312 (2008) 160–165.

[73] J. Arana, E. P. Melián, V. R. López, A. P. Alonso, J. D. Rodríguez, O. G. Díaz, J. P. Pena, Photocatalytic degradation of phenolic compounds: adsorption and FTIR study, J. Hazard. Mater., 146 (2007) 520–528.

[74] C. Namasivayam, S. Sumithra, Adsorptive removal of catechol on Fe(III)/Cr(III) hydroxide, Ind. Eng. Chem. Res., 43 (2004) 7581–7587.

[75] F. S. Mohamed, W. A. Khater, M. R. Mostafa, Phenol sorptive properties of sulfuric acid activated carbons, J. Chem. Eng., 116 (2006) 47–52.

[76] A. Kumar, A. Jash, R. Priyadarshinee, B. Sengupta, D. Dasguptamandal, G. N. Halder, T. Mandal, Removal of catechol using Eichhornia crassipes activated carbon, Desalin. Water Treat., 73 (2017) 389–398.

[77] L. A. Amola, T. Kamgaing, R. F. TiegamTagne, C. D. Atemkeng, I. H. T. Kuete, S. G. Anagho, Removal of hydroquinone and resorcinol using shea residue activated carbon, J. Chem., 2022 (2022) 1–15.

[78] R. Guo, J. Guo, F. Yu, D. D. Gang, Mesoporous carbons for resorcinol removal, Microporous Mesoporous Mater., 175 (2013) 141–146.

[79] S. Kumar, M. Zafar, J. K. Prajapati, S. Kumar, S. Kannepalli, Simultaneous adsorption of phenol and resorcinol on granular activated carbon, J. Hazard. Mater., 185 (2011) 287–294.

CHAPTER 5

HIGHLY EFFICIENT PHOTOCATALYTIC DEGRADATION OF ORGANIC POLLUTANTS USING NOVEL CARBON INTEGRATED ZrO_2-ZnO NANOCOMPOSITES: KINETICS, MOLECULAR DOCKING, DFT SIMULATION AND REAL WASTEWATER APPLICATION

This chapter described the synthesis of a CCAC/ZrO_2-ZnO nanocomposite via a hydrothermal method by anchoring ZrO_2-ZnO onto activated carbon derived from Croton caudatus biomass for 4-nitrophenol (4-NP) degradation. The nanocomposite was thoroughly characterized using advanced analytical techniques, including XRD, FT-IR, SEM/TEM with SAED and EDS, PL spectroscopy, BET surface area analysis, and XPS. Photocatalytic activity was evaluated through the 4-NP degradation under UV light, achieving an impressive 98.2 % degradation with a catalyst dosage of 0.07 g/L, initial concentration of 40 ppm, irradiation time of 80 min and pH 6. The degradation intermediates and pathway were identified using LC-MS analysis. The nanocomposite exhibited good recyclability, retaining 78.5 % efficiency after multiple cycles and achieved a notable 87.86 % degradation efficiency in real wastewater. Density Functional Theory (DFT) calculations were performed to investigate the chemical reactivity and formation mechanism of the prepared nanocomposite. The results indicated a significant enhancement in its reactivity, which contributed to improve the efficacy in the degradation of 4-NP. Subsequently, the molecular docking studies targeting DNA gyrase and DHFR revealed favorable binding energies (MolDock), providing a valuable theoretical framework for future *in vitro* and *in vivo* experimental validation. These findings may significantly aid in the rational design and development of next-generation antibacterial agents designed at combating the growing threat of antibiotic-resistant pathogens such as *Escherichia coli (E. coli)* and *Staphylococcus aureus (S. aureus)*.

The text of this chapter has been published and patented as:

S. Sharma, R.S. Umdor, I.T. Longchar, B. Singha, S.L. Ezung, P.C. Bhomick, D. Sinha, Highly efficient photocatalytic degradation of organic pollutants using novel carbon integrated ZrO_2–ZnO nanocomposites: kinetics, molecular docking, DFT simulation and real wastewater application, J. Mol. Liq., (2025) 128260.

S. Sharma, R.S. Umdor, I.T. Longchar, B. Singha, D. Sinha, Carbon based ZrO_2–ZnO nanocomposite for 4-nitrophenol degradation, Indian Patent Appl. 202531037955 A, Published on 25 April 2025.

5.1 Introduction

Nitrophenols are anthropogenic, inhibitory, and biorefractory organic molecules. They have been extensively applied in chemical industry for insecticides, medicines, and dyes [1,2]. 4- nitrophenol (4-NP) is a phenolic molecule that contains two functional groups on its benzene ring; nitro (NO_2) and hydroxyl (OH). European Economic Union and US Environmental Protection Agency consider 4-NP among priority contaminants due to its potential to negatively impact aquatic life, animals, and human beings at low amounts with the maximum allowable limit of 1ppm [3]. The exposure of 4-NP also leads to a spectrum of acute and chronic health effects including gastrointestinal complication, respiratory tract problems, injury to organs like kidneys and liver, skin and eye irritant, and cardiovascular system problem. It may also lead to hypersalivation, suppression of hunger, breakdown of protein, and interference with the central nervous and circulatory systems [4,5]. In view of the adverse health implications, the presence of 4-NP in wastewater requires an effective treatment before being discharged into the aquatic environment.

Various treatment techniques have been explored for the removal of 4-NP contamination in wastewater such as electrochemical degradation, biodegradation, membrane separation, photocatalytic degradation, precipitation, and ozonation process [6-8]. However, these technologies often face challenges such as operational complexity, pre-treatment requirements, reliability issues, secondary waste generation, harmful by-product formation as well as environmental impacts [9]. Among these, photocatalysis, an advanced oxidation process (AOP), employs specific wavelengths of light to degrade organic and toxic pollutants by generating highly reactive hydroxyl radicals (•OH). These radicals engage in redox reactions with the electron-hole pairs of the photocatalyst, which lead to the degradation of the pollutants into carbon dioxide (CO_2) and water (H_2O) [10].

Photocatalytic degradation offers several notable advantages over conventional treatment methods: it facilitates the complete breakdown of contaminants into less harmful substances; effectively degrades highly stable compounds that may resist other treatment methods; performs efficiently at room temperature and pressure, thereby reducing energy consumption; and eliminates the need of oxygen injection which simplifies the treatment process. Moreover, the end product of photocatalysis is

free from pollution, making it environmentally benign. Owing to its economic feasibility and technological adaptability, photocatalysis is widely recognized as a sustainable and promising approach for environmental remediation and advanced wastewater treatment [11-13].

Some typical semiconductor photocatalysts have been studied for their ability to remove organic pollutants and other dyes in aqueous media. These include tungsten trioxide (WO_3), titanium dioxide (TiO_2), iron oxide (Fe_2O_3), silicon dioxide (SiO_2), zinc oxide (ZnO), molybdenum disulfide (MoS_2) and zirconium dioxide (ZrO_2) [14-16]. These metal oxides are assisting in multi-step photolysis of organic compounds to harmless byproducts in the presence of ultraviolet irradiation [17,19]. Among them, ZnO has gained particular attention due to its wide bandgap (3.37 eV), substantial electron mobility (~300 cm^2/Vs) and high exciton binding energy (60 meV), chemical stability, non-toxicity and cost-effectiveness [18,19]. Nevertheless, ZnO as an individual photocatalyst faced significant drawbacks, including susceptibility to photocorrosion, instability under continuous light exposure and high recombination rates of photogenerated electron-hole pairs. These factors collectively result to a substantial reduction in its overall photocatalytic efficiency and limit its practical usage in environmental remediation processes [20-22]. To overcome these challenges, recent research has focused on coupling or doping ZnO with other metals or metal oxides [23,24]. ZrO_2 with its wide bandgap (~5.0 eV), excellent thermal stability, outstanding corrosion resistance and high dielectric constant, has emerged as a suitable candidate for forming heterojunctions with ZnO [25,26]. The incorporation of ZrO_2 in ZnO-ZrO_2 systems enables separation of photogenerated charge carriers and suppresses recombination rate, leading to enhanced production of hydroxyl radicals (•OH), which play a vital role in photocatalytic degradation. ZrO_2 also significantly improves the thermo-mechanical and chemical stability of ZnO. Notably, ZnO is susceptible to dissolution at lower pH levels; however, coupling with ZrO_2 enhances its resistance to degradation in acidic environments [27]. Conversely, the presence of ZnO may slightly narrow the band gap of ZrO_2, potentially improving its light absorption capabilities.

Several studies have demonstrated that the integration of an adsorbent with a photocatalytic system significantly enhances the removal efficiency of organic

contaminants. In this context, biomass-derived activated carbon (AC) has gained considerable attention as a co-adsorbent material. Activated carbon (AC), owing to its high specific surface area, well-developed porosity and abundant surface function groups, is considered an ideal support material for photocatalysts as it can effectively absorb organic pollutant near the active catalytic sites during the adsorption-degradation process [28,29]. The integration of metal oxide nanoparticles with AC further increases the overall adsorptive performance by offering numerous active sites capable of forming strong chemical interactions with pollutant molecules. Moreover, AC promotes uniform dispersion of the photocatalyst particles, thereby improving light absorption and catalytic performance. However, previous studies have primarily focused on single or binary photocatalyst systems, which inherently lack the synergistic effects associated with multiple heterojunctions [30-32]. To address this, the present study introduces a novel nanocomposite comprising activated carbon (AC) integrated with a ZrO_2-ZnO photocatalyst. The inclusion of AC into ZrO_2-ZnO matrix enables heterojunction formation, improve charge separation, minimize electron-hole recombination and broaden light absorption. These synergistic effects are expected to significantly improve the photocatalytic efficiency of the composite material, offering a more efficient and sustainable approach for water treatment.

Quantum chemical approaches, specifically Density functional theory (DFT), offer a valuable tool for understanding the relationship between the structure and reactivity of materials, enabling efficient selection of highly effective materials. DFT allows researchers to study the electronic structure, properties, reactivity, and stability of atoms and molecules [33]. These methods have successfully predicted the reactivity and interaction features of nanomaterials [34]. Several theoretical studies have been reported in the literature to better understand the reactivity and interaction mechanisms of photocatalytic materials. For instance, Blantocas et al. [35] utilised Gaussian 09W software to assess the reactivity of pure chitosan and chitosan-TiO_2 composites based on various molecular properties. Similarly, the chemical reactivity of basic dyes interacting with activated carbon was also investigated using DFT-based descriptors by de Souza et al. [36]. In another study, Ullah et al. [37] observed the optical and electrical structures, surface interactions, electronegativity, and charge transfer mechanisms in polypyrrole-TiO_2 nanocomposites. Thus, this research aims to develop

a theoretical understanding explaining the reactivity of nanocomposites in degrading 4-NP using DFT simulation.

Antibacterial resistance is a critical global health threat, diminishing the efficacy of existing therapies and elevating morbidity and mortality. Resistant strains such as *S. aureus* and *E. coli*, driven by genetic mutations and horizontal gene transfer, have compromised the effectiveness of many antibiotics, thereby obstructing medical progress and limiting treatment options [38]. Consequently, there is an urgent need to develop novel therapeutics with innovative mechanisms of action, including new antibiotic classes. Nanocomposites offer a promising strategy against antibiotic resistance through their unique physicochemical properties, enabling targeted drug delivery, enhanced efficacy, and reduced toxicity. In this context, several studies have utilized computational molecular docking to evaluate the binding modes and interaction profiles of nanocomposites against bacterial pathogens, aiming to assess their potential efficacy and mechanism of action. Notably, Arularasu et al. [39] and Iram et al. [40] reported significant *in silico* findings, highlighting key molecular interactions that may contribute to the antibacterial activity of these nanomaterials. Accordingly, the present work aims to investigate the antibacterial potential of nanocomposite-based compounds using structure-based molecular docking. The findings seek to bridge the gap between *in silico* predictions and biological relevance, offering deeper insights into the promise of nanocomposites as effective antibacterial agents.

Therefore, in this study, ZnO-ZrO_2 nanocomposite incorporated with activated carbon derived from *croton caudatus* biomass (CCAC) was successfully synthesized via a hydrothermal method. The synthesized nanocomposite was characterized using various analytical techniques to elucidate its structural formation, functional groups, morphology, surface area and topographical properties. The photocatalytic activity of CCAC/ZrO_2-ZnO was subsequently evaluated for the degradation of 4-NP under UV-light irradiation. Reusability and stability assessments were conducted through multiple degradation cycles. Catalytic efficiency tests were conducted using pristine ZnO, ZrO_2 and the synthesized composite material for comparative evaluation. The predominant reactive species involved in the catalytic process were identified through scavenging experiments and a degradation mechanism was alsoproposed. The

synthesized nanocomposite was further validated under real wastewater conditions, highlighting its practical applicability for environmental remediation. Furthermore, theoretical investigations utilizing the DFT method were conducted to supplement the experimental findings in the degradation of 4-NP. Chemical descriptors such as HOMO-LUMO gap, chemical hardness and softness, chemical potential, electronegativity, electrophilicity index and maximum charge transfer were also investigated. Molecular docking simulations were also performed to assess the potential antibacterial activity of the CCAC/ZrO_2-ZnO and ZrO_2-ZnO nanocomposite by targeting the proteins such as dihydrofolate reductase (DHFR) and DNA gyrase B enzymes in *S. aureus* and *E. coli*.

5.2 Experimental

5.2.1 Chemicals

Zinc acetate (Zn $(CH_3COO)_2 \cdot H_2O$; ≥ 99 % purity), Zirconium dioxide (ZrO_2, ≥ 99 % purity) and 4-NP ($C_6H_5NO_3$; ≥ 99 % purity) were procured from Sigma Aldrich, India. The chemical structure and properties of 4-NP is detailed in Table 5.1.

Table 5.1. Physicochemical properties of 4-NP.

Chemical structure	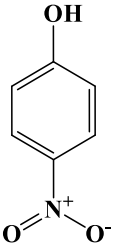
Chemical formula	$C_6H_5NO_3$
Molecular weight (g/mol)	139.11
Solubility in water (mg/mL @ 25 °C)	15,600
Density at 68 F	1.48
pK_a (@25°C)	7.15
λ_{max} (nm)	317

All the chemicals utilized in the present work are of analytical grade and used without further purification. Ultrapure Milli-Q water (MQW: 18.2 MΩ cm) was utilized throughout all experiments.

5.2.2 Preparation of activated carbon

Croton caudatus biomass collected from the vicinity of Lumami, Nagaland University, India (26° 13′ 29.60″ N | 94° 28′ 35.0″ E), was used as the primary raw material. The

entire plant was processed to produce AC, which was subsequently labeled as Croton caudatus activated carbon (CCAC). The preparation and characterization of CCAC have been previously reported in Chapter 3 (see under Subsection **3.2.2)** [41].

5.2.3 Preparation of ZrO_2-ZnO nanocomposite

For the synthesis of ZrO_2-ZnO nanocomposite, a mixture of 2.2 g Zn $(CH_3COO)_2 \cdot H_2O$ and 0.5 g ZrO_2 was dispersed in 100 mL of MQW under vigorous stirring for 35 min at ambient temperature. The solution's pH was adjusted to 9 using 2M NH_4OH. Subsequently, the mixture underwent sonication for 35 min to ensure homogeneity [42]. The resulting solution was transferred to a Teflon-lined stainless-steel autoclave and subjected to hydrothermal treatment at 170 °C for approximately 12 h. The mixture was then separated by centrifugation, filtered, and thoroughly washed with MQW. The final ZrO_2-ZnO nanocomposite was obtained after overnight drying in an oven at 50 °C.

5.2.4 Synthesis of CCAC/ZrO_2-ZnO nanocomposite

The CCAC/ZrO_2-ZnO nanocomposite was produced by mixing 0.5 g of ZrO_2-ZnO and 1 g of prepared CCAC in 100 mL of MQW, shaking for 35 min at room temperature, and finally sonicating for another 35 min to achieve homogenous conditions. The resulting precursor mixture was subjected to hydrothermal treatment in a Teflon-lined autoclave at 160 °C for about 12 h.

Scheme 5.1. Schematic illustration of the synthesis procedure for CCAC/ZrO_2-ZnO nanocomposite.

After cooling, the solution was centrifuged and washed several times with MQW. The nanocomposite was dried in an oven at 50 °C for 24 h. The synthesized CCAC/ZrO_2-ZnO nanocomposite was further characterized for evaluation of its 4-NP degradation (Scheme 5.1).

5.2.5 Characterization techniques

The CCAC/ZrO_2-ZnO nanocomposite was characterized using several analytical techniques. X-ray diffraction (XRD) (PANalytical, Empyrean, CuKα radiation) was used to determine its crystal structure and catalyst phase. Functional groups were identified using Fourier transform infrared (FTIR) spectroscopy (Perkin Elmer, Spectrum Two, USA) in the range 400-4000 cm^{-1}. Surface morphology and elemental composition were analyzed using scanning electron microscopy (SEM) (JSM-6360, JEOL) with energy dispersive X-ray analysis (PHI 5000 Versa Probe III, USA). Transmission electron microscopy (TEM) provided insights into morphology and surface texture (2100F, JOEL). Photoluminescence (PL) analysis was carried out to analyze the emission spectra (Horiba Fluoromax4CP spectrofluorometer, 150 W xenon lamp). Surface area and porosity were determined (Quantachrome AutosorbiQ Station 1 at 77 K), with pore volume and radii calculated using the Barrett-Joyner-Halenda method. The surface composition and chemical states of the synthesized nanocomposite was evaluated using X-ray photoelectron spectroscopy (XPS). The zero-point charge (pH_{zpc}) was determined via the batch equilibration method [43]. To assess the extent of mineralization in the residual solution following photocatalytic reactions, the total organic carbon (TOC) content was measured using a total organic carbon system (Shimazu Model 5000A).

5.2.6 Photocatalytic degradation experiments

A photocatalytic degradation experiment of 4-NP was carried out in a reactor (dimension of 63 x 44 x 44 cm) enclosed in a black box. 50 mL of 4-NP solution with a specific amount of CCAC/ZrO_2-ZnO photocatalyst was placed in a 250 mL Pyrex jar on a magnetic stirrer. A 450 W ultraviolet light (mercury lamp) emitting at a peak wavelength of 325 nm was positioned 10 cm away from the reaction mixture. To ensure thorough mixing of the reaction system, a magnetic stirrer was placed directly beneath the double-jacketed glass vessel. To maintain the reactor temperature at 25 °C,

a continuous flow of water was utilized throughout the reaction process. Additionally, an exhaust fan was installed to facilitate constant air circulation within the reactor. The experimental setup for the UV light photocatalytic device is schematically illustrated in Chapter 2 (see Figure 2.2.).

A 1000 mg/L stock solution was prepared by adding 1g of 4-NP in 1L of MQW. Serial dilutions were then performed to obtain working solutions with concentrations ranging from 40 to 100 ppm. For the experimental study, the synthesized nanocomposite was incorporated into the 4- NP solutions at varying concentrations (40, 60, 80 and 100 ppm) and subjected to vigorous stirring for 30 min under dark condition. This process facilitated the establishment of adsorption-desorption equilibrium within the reaction system. The pH of the solutions was adjusted by the addition of HCl and NaOH (0.1M). After achieving equilibrium, UV light was passed through the reaction media. At 10 min intervals, 3.5 mL of the 4-NP solution was collected, and the concentration of 4-NP was measured using a UV-Vis spectrophotometer (Lambda-365) at the 316 nm absorbance wavelength. All tests were conducted in triplicate to ensure data quality. The percentage degradation of 4-NP was calculated using the Equation (5.1):

$$\text{Degradation (\%)} = \frac{C_o - C}{C_o} \times 100 \quad (5.1)$$

where C_o and C are the concentrations of 4-NP before and after the photocatalytic treatment at different time intervals.

5.2.7 Computational studies

Theoretical calculations based on DFT method was employed to investigate the chemical reactivity of a nanocomposite material composed of CCAC, ZrO_2, and ZnO. The structure of the CCAC surfaces, assumed to consist of graphite clusters with 12-25 C-atoms (3-7 fused benzene carbon rings), was modeled and optimization were done using Gauss View 05 and Gaussian 09W software program [44]. Calculations were performed using the B3LYP functional and the 6-31G/LanL2DZ basis set in water to obtain a stable conformation [45]. Quantum chemical descriptors, including HOMO-LUMO energy gap, chemical potential, chemical softness and hardness, chemical potential, electronegativity, electrophilicity index and maximum charge transfer were calculated to understand potential interactions and reactivity between the

surfaces of CCAC/ZrO_2-ZnO and the ZrO_2-ZnO catalyst using the following equations:

(i) HOMO-LUMO energy gap

The reactivity of a molecule is determined by the HOMO-LUMO energy gap (H); thus, the larger the value of the HOMO-LUMO energy gap, the less reactive and stable is the molecule [46]. Equation (5.2) provides an expression for the HOMO-LUMO energy gap (s).

$$H = E_{LUMO} - E_{HOMO} \tag{5.2}$$

where E_{HOMO} refers to the energy of the highest occupied molecular orbital, while E_{LUMO} denotes the energy of the lowest unoccupied molecular orbital.

(ii) Chemical softness and chemical hardness

Chemical softness (S) and hardness (η) are key concepts in understanding chemical reactivity. Molecular stability is directly proportional to hardness and inversely proportional to softness. Therefore, as hardness increases, stability increases, and reactivity decreases. Conversely, as softness increases, stability decreases, and reactivity increases [47]. Chemical hardness and softness are calculated using Equations (5.3) and (5.4):

$$S = \frac{1}{2\eta} \tag{5.3}$$

$$\eta = \frac{(E_{LUMO} + E_{HOMO})}{2} \tag{5.4}$$

(iii) Chemical potential and electronegativity

A molecule's reactivity depends on its chemical potential (μ) and electronegativity (χ) [48], which can be calculated using Equations (5.5) and (5.6):

$$\mu = \frac{(E_{HOMO} + E_{LUMO})}{2} \tag{5.5}$$

$$\chi = -\mu \tag{5.6}$$

(iv) Electrophilicity index

The electrophilicity index (ω) quantifies the energy stabilization when the maximum number of electrons are transferred between an electron donor and acceptor. Higher electrophilicity values correspond to increased molecular reactivity [49] and is calculated according to Equation (5.7):

$$\omega = \frac{\mu^2}{2\eta} \tag{5.7}$$

where electrophilicity (ω) is categorized as high (ω > 1.5 eV), moderate (0.8 eV < ω < 1.5 eV), and marginal (ω < 0.8 eV), respectively.

(v) Maximum charge transfer

The maximum amount of electronic charge that can be transferred during a charge transfer interaction is represented by the value of ΔN_{max} [50] and is defined as

$$\Delta N_{max} = -\frac{\mu}{\eta} \tag{5.8}$$

5.2.8 Molecular docking analysis

Molecular docking is a computational technique used to predict the interaction between a drug candidate and its biological target. It facilitates the identification of compounds that can effectively bind to and inhibit disease-associated targets. By revealing binding interactions at the molecular level, docking supports the rational design of more potent and selective drugs with fewer side effects. Overall, it serves as an essential tool in modern medicinal chemistry and pharmaceutical research for developing novel, target-specific therapies [51]. To evaluate the antibacterial potential of the synthesized nanocomposite, it was subjected to molecular docking simulations against two pivotal bacterial targets: *S. aureus* DHFR, a key enzyme in the folate biosynthesis pathway essential for bacterial proliferation [52] and *E. coli* DNA gyrase B, a crucial component of the bacterial type II topoisomerase system responsible for maintaining DNA supercoiling and integrity [53]. These targets were selected based on their indispensable roles in bacterial survival and their established relevance in antimicrobial drug design. Molecular docking simulations were conducted using Molegro Virtual Docker 6.0 (MVD) [54]. MVD exhibits a superior docking success

rate of 87.0%, outperforming other established docking algorithms, including Glide (81.8 %), Gold (78.2 %), Surflex (75.3 %), and FlexX2 (57.9 %). This high accuracy underscores MVD's reliability in ligand binding predictions, thereby underscoring its pre-eminence in ligand-binding accuracy [55]. In this work, a semi-flexible docking strategy was employed, where the protein receptor was treated as rigid while allowing the ligand to adopt multiple conformations. This approach enables the exploration of various ligand shapes within the static binding site of the protein. Compared to fully rigid docking, semi-flexible docking generally provides more reliable predictions by accounting for ligand flexibility without compromising computational efficiency [56]. Furthermore, Molegro Virtual Docker (MVD) enhances docking accuracy by offering protein structure refinement tools such as “Repair and Optimize Residues” and “Optimize Neighborhood” during the preparation phase.

MVD employs a sophisticated cavity-detection algorithm to systematically identify potential ligand- binding sites within the three-dimensional protein architecture. This algorithm ranks the top five predicted binding cavities based on surface area, assigning higher priority to larger cavities due to their increased ligand accommodation potential. For all docking studies, the binding site was defined using the position of the co-crystallized ligand, following established protocols in structure-based drug design [57]. This approach ensures that docking simulations are conducted within a biologically relevant pocket that accurately represents the spatial and chemical characteristics of the authentic binding site. The use of co-crystallized ligands provides additional validation of the binding site identification, underscoring its structural and functional importance.

PDB ID: 5MMN (Chain A): Cavity 1 with a volume of 51.712, centre X: -46.73, Y: 4.13, Z: 3.76, within a constraint of a radius of 12 Å. PDB ID: 3FY8 (Chain A): Cavity 1 with a volume of 201.216, centre designated as X: 27.58, Y: 14.91, Z: 43.98, within a constraint of radius 16 Å.

For this study, a grid resolution of 0.30 Å was employed and simulations were refined with a maximum iteration threshold of 1,500 and a population size of 50 across all designated PDB IDs. Each ligand underwent 30 independent docking runs to enhance computational predictive reliability. Binding energy assessments were conducted

using the MolDock score followed by an interaction analysis between ligands and receptor active sites [57].

Scoring functions

The MolDock scoring function in MVD utilizes the Piecewise Linear Potential (PLP) method [58]. Binding interactions are evaluated using two primary metrics: the MolDock Score and the Re-rank Score, which vary in precision when calculating interaction energies.

- **MolDock score**

The docking score, known as the E_{score}, integrates various energetic contributions [59]. It consists primarily of two components: the interaction energy between the ligand and the protein (E_{inter}) and the ligand's internal energy (E_{intra}), as expressed in Equation (5.9).

$$E_{score} = E_{inter} + E_{intra} \tag{5.9}$$

As illustrated in Equation (5.10), the interaction energy term (E_{inter}) represents the total sum of interactions between the ligand and the protein, ligand and water molecules, as well as ligand and cofactors.

$$E_{inter} = \sum_{i=ligand} \sum_{j=protein} \left[E_{PLP}(r_{ij}) + 332.0 \frac{q_i q_j}{4 {r_{ij}}^2} \right] \tag{5.10}$$

The EPLP scoring function employs a piecewise linear potential that incorporates two primary parameters: one to model van der Waals (steric) interactions and another, with a steeper gradient, to represent hydrogen bonding. Electrostatic interactions between charged atoms are described by a Coulomb potential, where the dielectric constant varies with interatomic distance according to D(r) = 4r. A conversion factor of 332.0 is used to convert electrostatic energy values into kcal/mol. To avoid the electrostatic attraction overpowering the repulsive core-core forces, interactions between atom pairs closer than 2.0 Å are excluded from the calculation. As depicted in Equation (5.11), the internal energy (E_{intra}) is determined by summing the interaction energies of all non-bonded atomic pairs within the ligand, excluding those separated by two or fewer bonds. This energy term accounts for multiple factors, including electronic

interactions, hydrogen bonds, steric repulsion, sp^2–sp^2 clashes, torsional strain (both general and ligand-specific), van der Waals forces, penalties from soft constraints and solvation effects.

$$E_{intra} = \sum_{i=ligand} \sum_{j=protein} E_{PLP}(r_{ij}) + \sum_{flexible\ bonds} A[1 - \cos(m.\theta - \theta_0)] + E_{clash} \quad (5.11)$$

The torsional energy term is calculated based on the hybridization states of the atoms involved, with the average contribution considered when multiple torsional modes exist; here, θ represents the torsion angle of the bond. Additionally, the clash energy (E_{clash}) penalizes steric clashes between heavy atoms by imposing a significant penalty 1000 units if the interatomic distance falls below 2.0 Å and 10,000 units if a heavy atom is located outside the interaction zone defined by the spherical grid boundary.

- **Re-rank score**

In MVD, the re-rank score serves as an estimate of interaction strength but is not expressed in standard chemical units nor does it involve complex energy calculations. After generating one or more candidate poses, additional energy components are calculated and combined to produce the re-rank score. This score integrates contributions from the docking function, such as sp^2-sp^2 torsion and Lennard-Jones 12-6 potentials [60]. Although it requires more computational resources than the primary scoring methods (MolDock and PLANTS), the re-rank score is generally considered more reliable for selecting the best binding pose and assessing ligand affinity.

5.3 Results and discussion

5.3.1 Characteristics of CCAC/ZrO_2-ZnO

(i) XRD analysis

X-ray diffraction was used to analyze the crystalline structure and phase composition of synthesized CCAC/ZrO_2-ZnO nanocomposites as illustrated in Figure 5.1. The characteristic peaks of hexagonal graphitized carbon at 2θ = 26.55° and 44.57° are associated with (002) and (101) crystallographic planes (ref. JCPDS 01-089-8487). Additionally, the intense diffraction peaks at 2θ values of 31.73°, 34.36°, 36.21°, 47.47° and 56.53° correspond to the (110), (002), (101), (102) and (110) planes,

confirming the hexagonal wurtzite phase of ZnO (ref. JCPDS 01-080- 0074). The diffraction peaks correspond to the monoclinic (ref. JCPDS 00-037-1484) and tetragonal (ref. JCPDS 01-080-2155) phases of ZrO_2 were observed at 2θ = 28.17°, 30.27°, 31.47°, 35.16°, 50.17° and 62.85°, respectively. These peaks are indexed to the (−111), (101), (111), (110), (022) and (202) crystallographic planes indicating the coexistence of both phases. The average crystallite size (D) of the prepared sample was determined using the Scherrer formula [61], expressed as:

$$D = \frac{0.9\,\lambda}{\beta\,\mathrm{Cos}\,\theta} \tag{5.12}$$

where λ denotes the X-ray radiation wavelength, θ is the Bragg's angle, and β is the full width at half-maximum (FWHM). Notably, the D value for CCAC/ZrO_2-ZnO was calculated to be 30.46 nm based on the FWHM of its most intense diffraction peaks.

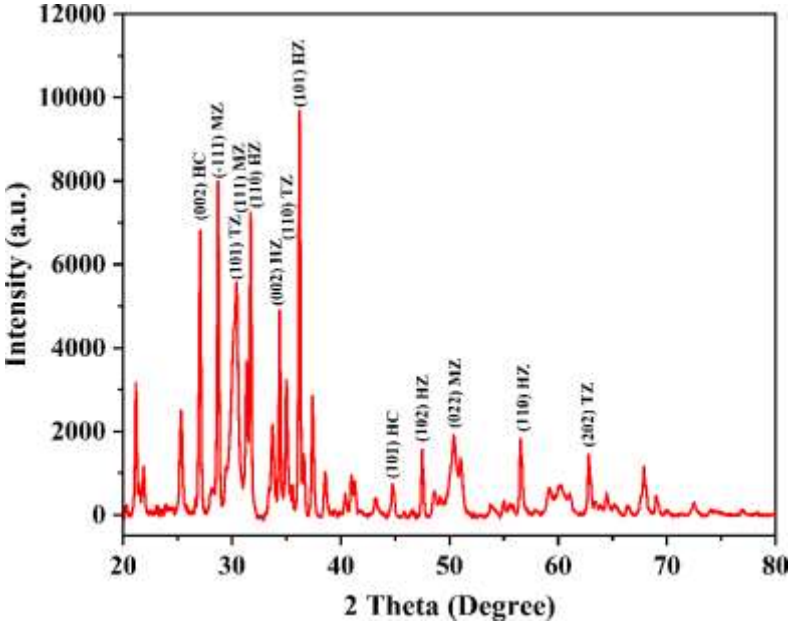

Figure 5.1. XRD pattern of CCAC/ZrO_2-ZnO (HC- Hexagonal phase of CCAC, HZ- Hexagonal phase of ZnO, TM/TZ- Monoclinic/Tetragonal phase of ZrO_2).

(ii) FTIR analysis

FTIR analysis of the CCAC/ZrO_2-ZnO nanocomposite revealed several functional groups on its surface as shown in Figure 5.2. The broad bands observed are consistent with those of AC from various biomass sources, indicating similar functional groups. The band within the 3440 to 2470 cm^{-1} range is attributed to O-H stretching vibrations

from water, alcohol, or carboxylic acid [62]. Peaks around 3006, 2946 and 2837 cm^{-1} were attributed to aromatic and aliphatic C- H stretching vibrations, respectively, also matching earlier reports [63,64]. A peak at 1630 cm^{-1} signified carbonyl group (C=O) bending vibrations. C-O stretching in alcohol, carboxylic acid, phenol, ester, or ester group derivatives was indicated by transmittance at 1204 cm^{-1} and 1015 cm^{-1} [65,66]. Zn-O and Zn-O-Zr stretching vibrations were evident at 931 cm^{-1} and 672 cm^{-1} [67,68], while Zr-O stretching in the ZrO_2 phase was observed at 866 cm^{-1} [69]. These results confirm the surface activation of the carbon in the nanocomposite.

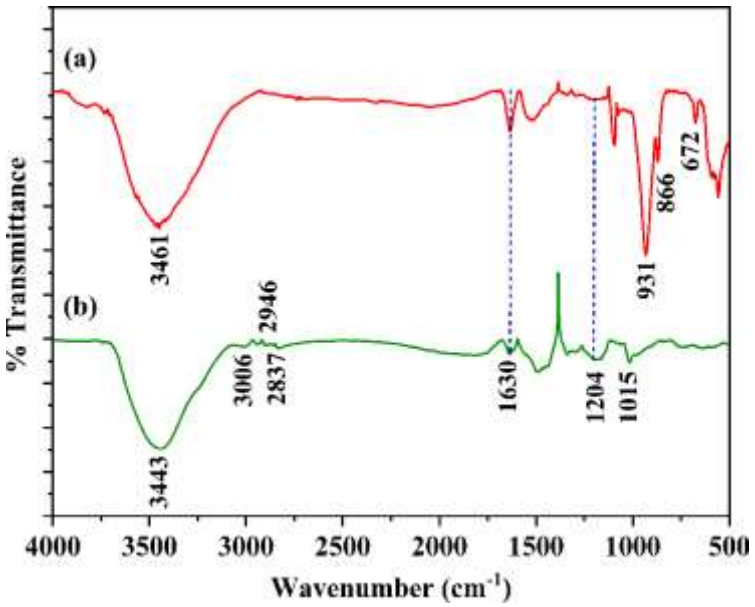

Figure 5.2. FT-IR spectrum of (a) CCAC/ZrO_2-ZnO and (b) CCAC.

(iii) SEM, TEM with EDS analysis

The surface and structural characteristics of CCAC/ZrO_2-ZnO were examined using SEM and TEM analysis. Additionally, the selected area diffraction pattern (SAED) was analyzed to verify the crystallinity of the synthesized nanocomposite. SEM analysis as depicted in Figure 5.3(a) revealed that the pores of the CCAC were occupied by ZnO-ZrO_2 nanocatalysts. The particles exhibited irregular shapes and non-uniform sizes, ranging from larger structures to smaller aggregates [70].

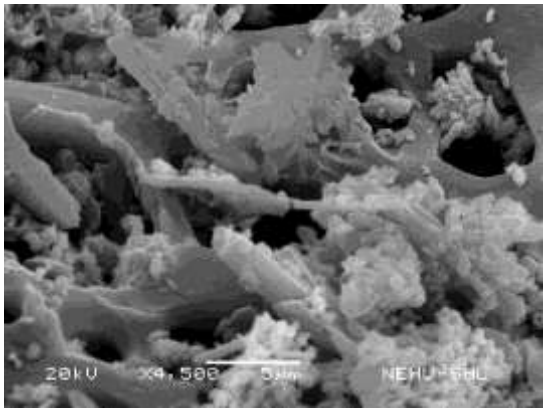
20kV X4,500 5μm NEHU-SHU

(a)

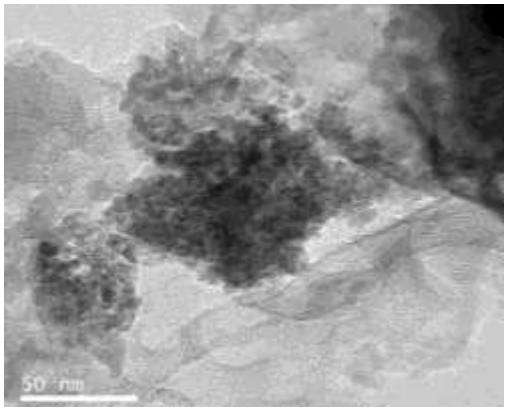
50 nm

(b)

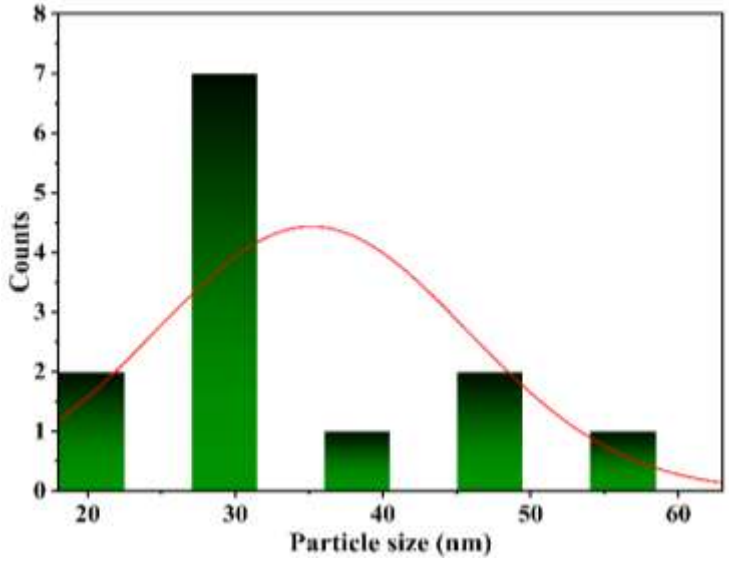
Counts
Particle size (nm)
0
1
2
3
4
5
6
7
8
20
30
40
50
60

(c)

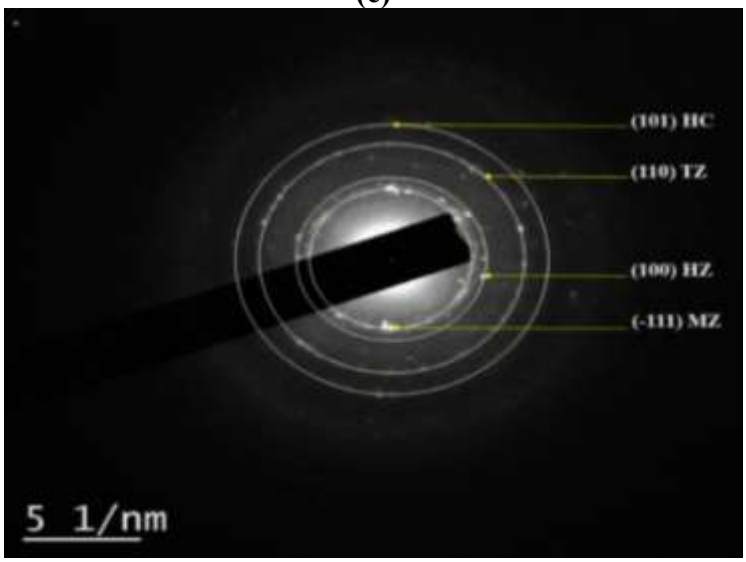
(101) HC
(110) TZ
(100) HZ
(-111) MZ
5 1/nm

(d)

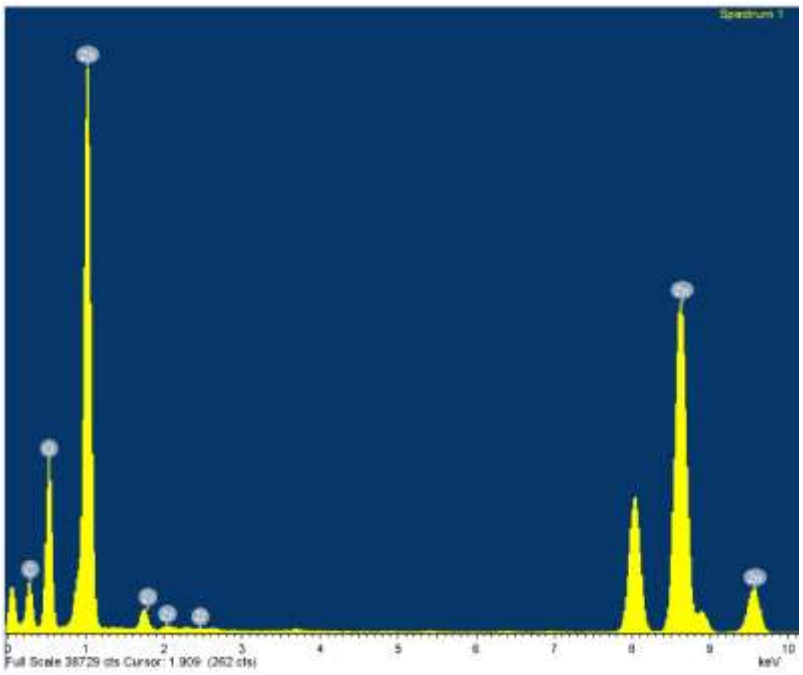

(e)

Figure 5.3. (a) SEM image, (b) TEM image, (c) size distribution (d) SAED pattern and (e) EDS spectrum of synthesised nanocomposite.

TEM analysis indicated that the particles were partially spherical, with a size range of 10-36 nm and an average diameter of 35.16 nm (Figure 5.3(b,c)). Moreover, the SAED pattern in Figure 5.3(d) indicated a polycrystalline material with reduced crystallinity, likely due to the incorporation of ZrO_2-ZnO nanocomposite particles within the CCAC matrix. The concentric electron diffraction rings in the SAED patterns corresponded well with the XRD analysis results. The chemical composition of CCAC/ZrO_2-ZnO was further investigated using Energy Dispersive X-ray Spectroscopy (EDS) coupled with TEM, which confirmed the presence of the expected elements such as Zn, O, C and Zr with the elemental weight percentages of 71.91 % for Zn, 20.71 % for O, 6.78 % for C and 0.6 % for Zr, respectively (Figure 5.3(e)).

(iv) Photoluminescence analysis

Photoluminescence (PL) spectra were measured at an excitation wavelength of 77 nm to investigate charge separation efficiency and movement of photo-generated e^-/h^+ pairs in the composite materials. The resulting spectra is presented in Figure 5.4. Photoluminescence involves photon emission resulting from electron-hole recombination. Increased photocatalytic efficiency corresponds to reduced

photoluminescence intensity and lower electron-hole recombination rates [71]. The figure clearly shows a strong emission peak at 495 nm for ZnO, which is attributed to the intense photon emission resulting from electron-hole recombination. The reduction in PL intensity after the formation of the CCAC/ZrO_2-ZnO nanocomposite indicates a decreased electron-hole recombination rate of excitons (e^- and h^+), indicating enhanced photocatalytic efficiency of the composite material.

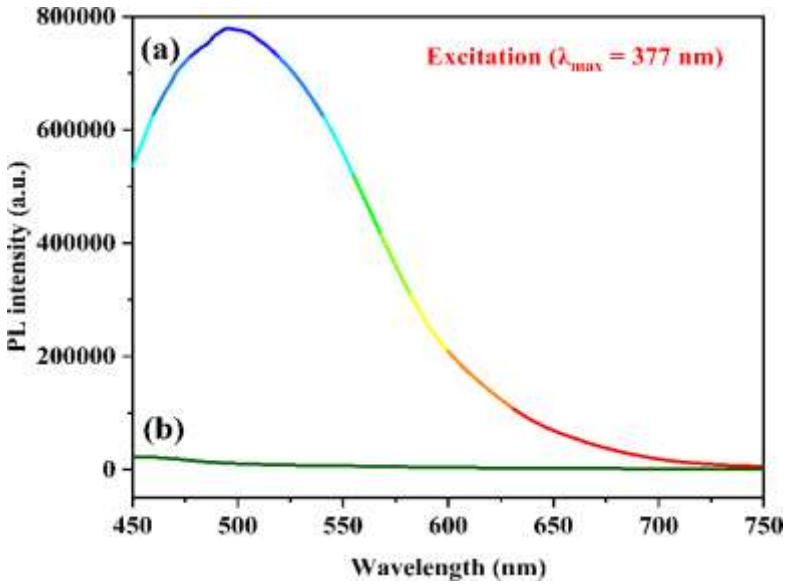

Figure 5.4. PL spectra of (a) ZnO and (b) CCAC/ZrO_2-ZnO.

(v) BET surface area

The analysis of the surface textural properties of synthesized CCAC/ZrO_2-ZnO nanocomposites reveals significant insights into their structural characteristics. The results indicates that the CCAC nanocomposite possesses a higher surface area (846.29 m^2/g) than the CCAC/ZrO_2-ZnO measured at 588.454 m^2/g. This decrease in surface area is likely attributed to the incorporation of ZnO and ZrO_2 nanoparticles, which may partially occlude the pores of CCAC, suggesting that a substantial fraction of the CCAC surface is occupied by these nanoparticles. Furthermore, the CCAC/ZrO_2-ZnO demonstrates a total pore volume of 0.085 cm^3/g and an average pore diameter of 3.627 nm, categorizing a type IV isotherm which corresponds to porous material according to IUPAC standards. Consequently, the enhanced surface area of the mesoporous CCAC/ZrO_2-ZnO nanocomposite is expected to facilitate improved photocatalytic

performance. The N2-adsorption-desorption isotherm for the synthesized nanocomposite is illustrated in Figure 5.5.

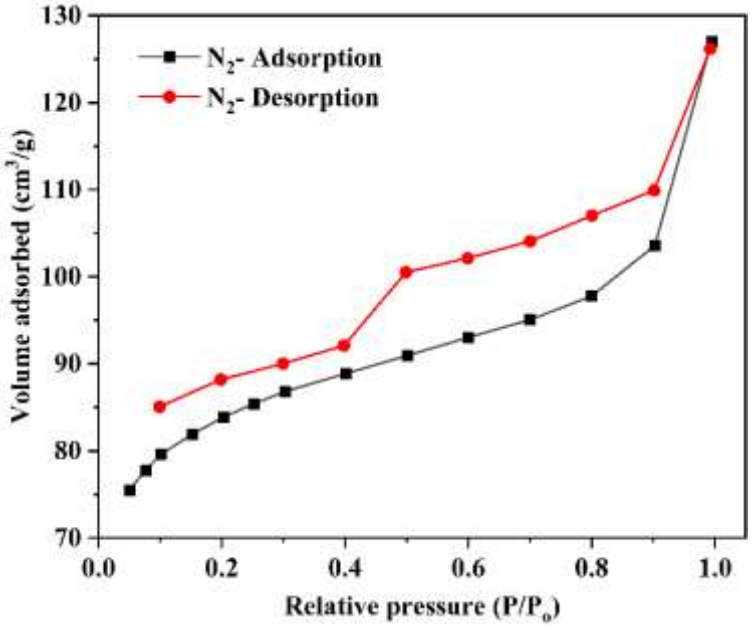

Figure 5.5. N_2 adsorption-desorption isotherm of CCAC/ZrO_2-ZnO nanocomposite.

(vi) XPS analysis

X-ray photoelectron spectroscopy (XPS) was employed to investigate the surface composition and chemical states of the synthesized CCAC/ZrO_2-ZnO composite as presented in Figure 5.6(a-e). The survey spectrum indicated the presence of key elements, namely carbon (C), oxygen (O), zinc (Zn), and zirconium (Zr), with binding energies observed at 284, 532.5, 1022.5, 1045 and 182 eV, confirming the successful formation of the nanocomposite [72,73]. The deconvoluted C 1s spectrum shows peaks at 284.7, 286.6 and 288.7 eV correspond to C–C/C–H (graphitic carbon from CCAC), C–O (hydroxyl or epoxy groups), and COO^- (carboxylate groups), indicating the presence of oxygen-containing functional groups in CCAC/ZrO_2-ZnO [74]. The O 1s spectrum revealed peaks at 531.9, 532.4 and 532.9 eV attributed to metal-oxygen (M–O) bonds, metal-hydroxyl (M–OH) groups, and adsorbed water or oxygenated groups from CCAC, respectively [75-77]. The high resolution XPS spectrum for Zn 2p shows two peaks: one centered at 1022.7 eV, corresponding to Zn $2p_{3/2}$, and other centered at 1045.8 eV assigned to Zn $2p_{1/2}$, indicating the presence of Zn^{2+} in ZnO [78,79]. Moreover, the Zr 3d spectrum exhibits peaks at 182.2 eV (Zr $3d_{5/2}$) and 184.4 eV (Zr $3d_{3/2}$), corresponding to Zr^{4+} in ZrO_2 structure [80].

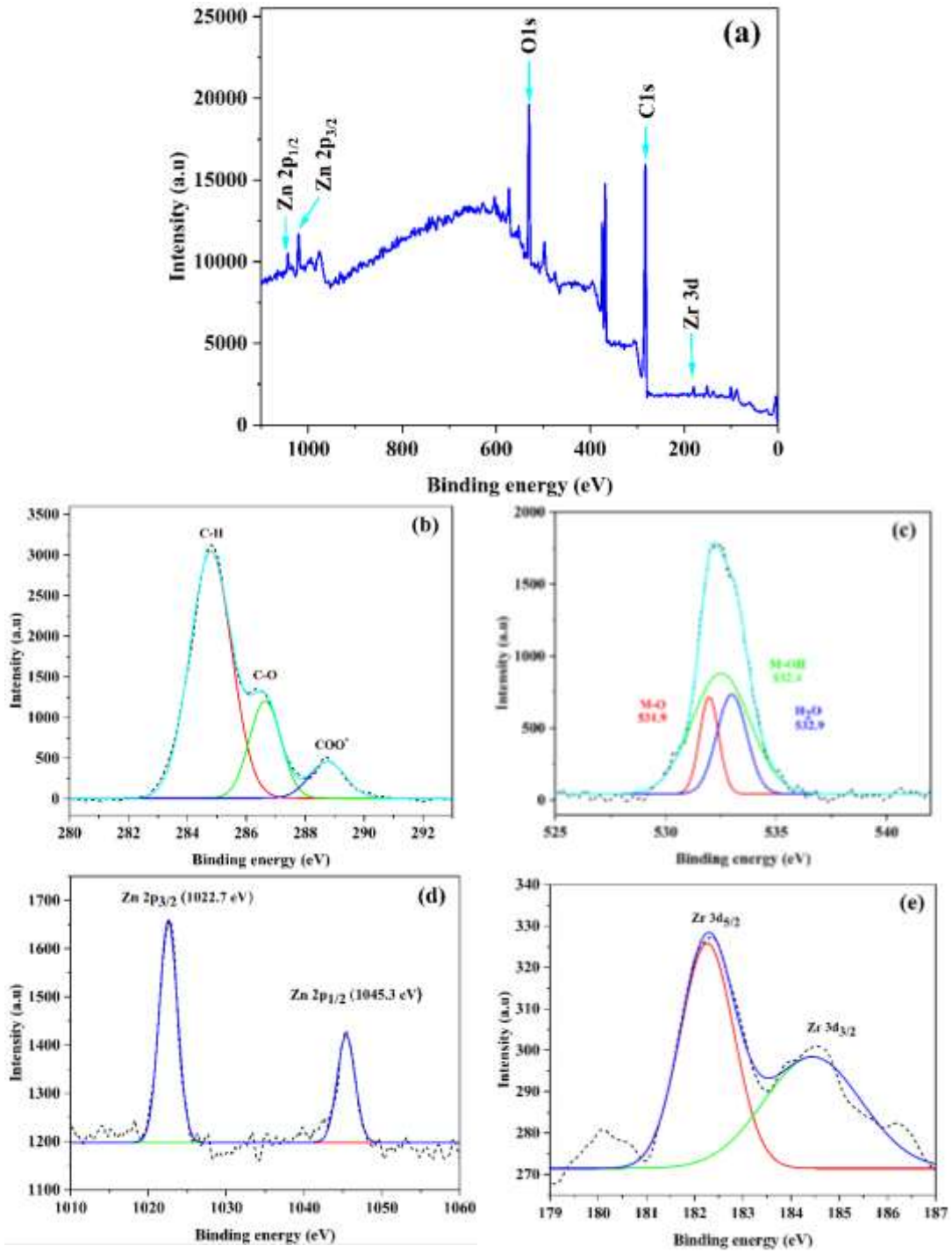

Figure 5.6. (a) Survey scan, (b) C1s spectra, (c) O1s spectra, (d) Zn 2p and (e) Zr 3d. XPS spectra of CCAC/ZrO_2-ZnO.

5.3.2 Photocatalytic degradation studies

(i) Effect of catalyst dosage

The study of the photocatalytic activity of the CCAC/ZrO_2-ZnO nanocomposite re-

vealed that the degradation of 4-NP solutions is significantly influenced by the dosage (0.05-0.14 g/L) of the nanocomposite (Figure 5.7(a)). An optimal dosage of 0.07 g/L was identified, achieving a degradation rate of 98.19 % for a 40 ppm concentration under UV light for 80 min. This suggests that while increasing the dosage enhances active site availability, excessive amounts can lead to particle aggregation, reducing the effective interfacial area and hindering UV light penetration. Thus, the balance between active site availability and light penetration is crucial for maximizing photocatalytic activity. Similar findings have been reported in literature, indicating a consistent trend across various photocatalysts [81,82].

(ii) Effect of pH

The pH of the reaction medium significantly influences the degradation of 4-NP using CCAC/ZrO_2-ZnO, playing a crucial role in the efficiency of the catalytic process. This effect is primarily due to the pH impact on the catalyst surface charge, the ionization state of the pollutant, and the overall reaction kinetics. The study examined pH ranges from 6.0 to 10.0, maintaining constant conditions of 40 ppm initial 4-NP concentration, 0.07 g/L nanocomposite dose and 80 min UV light irradiation time. As illustrated in Figure 5.7(b), photodegradation of 4-NP increases as pH rises from 2.0 to 6.0, followed by a decrease in degradation efficiency in basic conditions. The pH range between the composite's zero-point charge (6.57) and pK_a value of 4-NP (7.15) is particularly significant. At pH levels below 6.6, the catalyst surface acquires a positive charge, which enhances the adsorption of negatively charged 4-NP molecules, potentially improving degradation rates. In contrast, at pH levels exceeding 7.15, both the catalyst surface and 4-NP molecules carry negative charges, possibly leading to electrostatic repulsion and reduced degradation efficiency. Additionally, pH can affect the formation and stability of reactive oxygen species, which are key intermediates in the photocatalytic degradation process. Optimal pH conditions can promote the generation of hydroxyl radicals and other oxidative species, thereby accelerating the degradation of 4-NP [83]. Thus, pH 6.0 was considered for the subsequent experiments with the maximum degradation efficiency of 98.2 %.

(iii) Effect of initial 4-NP concentration and light irradiation time

The influence of 4-NP concentration and light irradiation time on degradation efficiency was investigated using 0.07 g/L of the nanocomposite at the optimized pH of 6.0, with 4-NP concentrations ranging from 40 to 100 ppm (Figure 5.7(c)). The degradation efficiency initially increased with irradiation time, peaking at 80 min for all concentrations. At this duration, the 40 mg/L 4-NP solution achieved near-complete degradation (~98.8 %), while higher concentrations (60-100 ppm) exhibited reduced efficiencies.

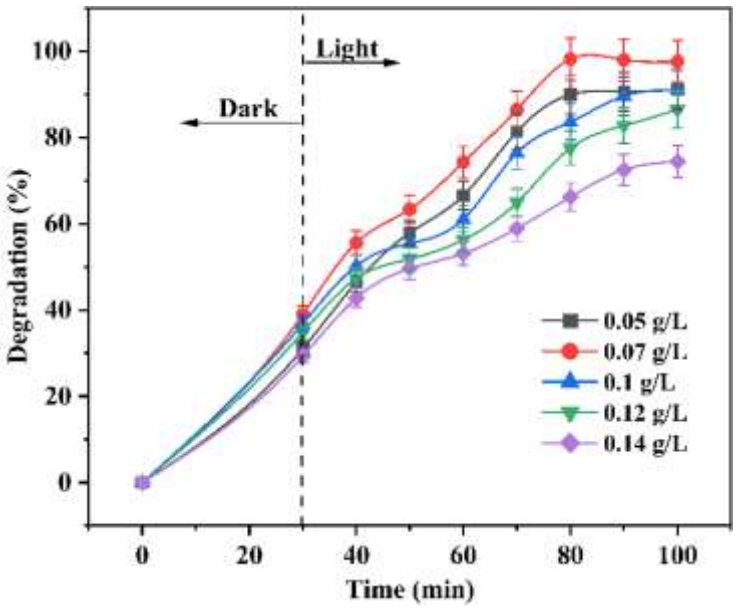

(a)

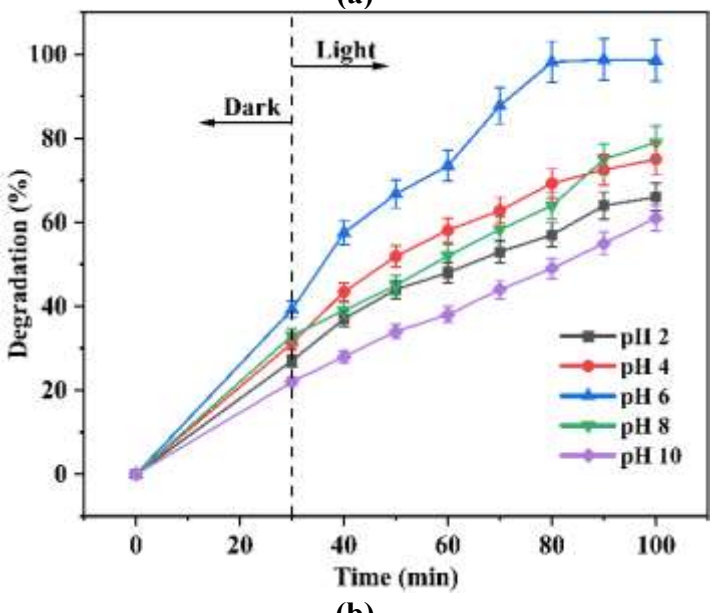

(b)

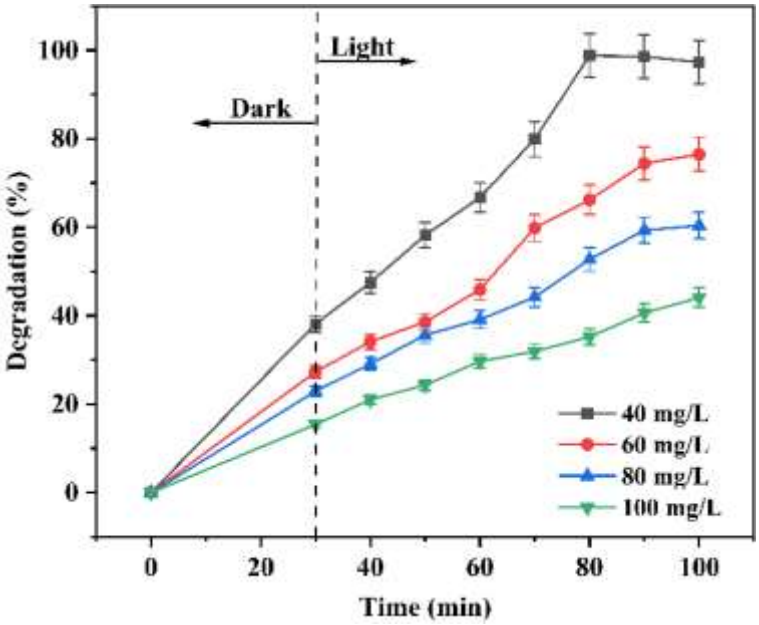

(c)

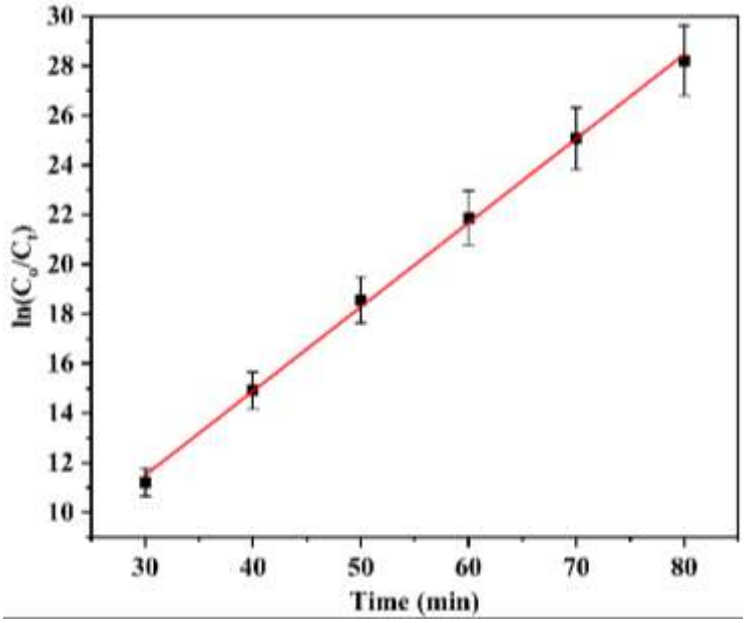

(d)

Figure 5.7. Effect of (a) catalyst dosage, (b) pH, (c) Initial 4-NP concentration and light irradiation time and (d) Kinetic studies of CCAC/ZrO_2-ZnO.

This decline in performance at elevated concentrations is likely due to competitive interactions: as 4-NP concentration rises, the abundance of negatively charged phenol ions increases, occupying the positively charged active sites on the nanocomposite surface and limiting hydroxyl group availability for photoreactions. At higher 4-NP concentrations, more molecules are available for adsorption, leading to light trapping

between phenolic particles and hindering light penetration to the nanocomposite surface. Consequently, the generation of reactive hydroxyl radicals diminishes, reducing overall phenol degradation. Beyond 80 min of irradiation, the degradation process plateaued as the elevated substrate concentrations promote the formation of reaction intermediates, which tend to adsorb onto the catalyst surface. The limited diffusion of these surface-bound intermediates can cause progressive deactivation of the photocatalyst's active sites, ultimately leading to a decline in degradation kinetics [84,85].

5.3.3 Reaction kinetics

Kinetic studies were conducted under optimal conditions (40 ppm 4-NP, pH 6.0, 80 min irradiation time, and 0.07 g/L nanocomposite). The effectiveness of the 4-NP concentration was evaluated using the Langmuir-Hinshelwood (LH) model [86]. The kinetic analysis employed pseudo first-order (PFO) kinetics and half-life period ($t_{1/2}$), as described by Equations (5.13) and (5.14), respectively.

$$ln(C_O/C_t) = k_{ap}t \tag{5.13}$$

$$t_{1/2} = \frac{ln\,2}{k_{ap}} \tag{5.14}$$

where K_{ap} is the apparent reaction rate constant, calculated from the slope of the graph of $\ln(C_o/C_t)$ vs time, C_o = initial 4-NP concentration, C_t = concentration at time t and $t_{1/2}$ = the half-life period, respectively.

The strong linear relationship between time and $\ln(C_o/C_t)$ for the CCAC/ZrO_2-ZnO nanocomposite, evidenced by a high correlation coefficient ($R^2 = 0.998$), indicates that the degradation of 4-NP follows PFO rate kinetics as presented in Figure 5.7(d). The analysis of curve's slope yields a photocatalytic rate constant (K_{ap}) of 0.339 min^{-1}, with a corresponding half-life ($t_{1/2}$) of 2.044 min.

5.3.4 Catalyst efficiency test for 4-NP degradation

The photocatalytic efficiency of pristine ZrO_2, pristine ZnO, and the synthesized CCAC/ZrO_2- ZnO nanocomposite was assessed under optimized conditions. The

experiments were conducted using a catalyst dosage of 0.07 g/L, an initial 4-NP concentration of 40 ppm, a pH level of 6.0, and 80 min of UV light exposure.

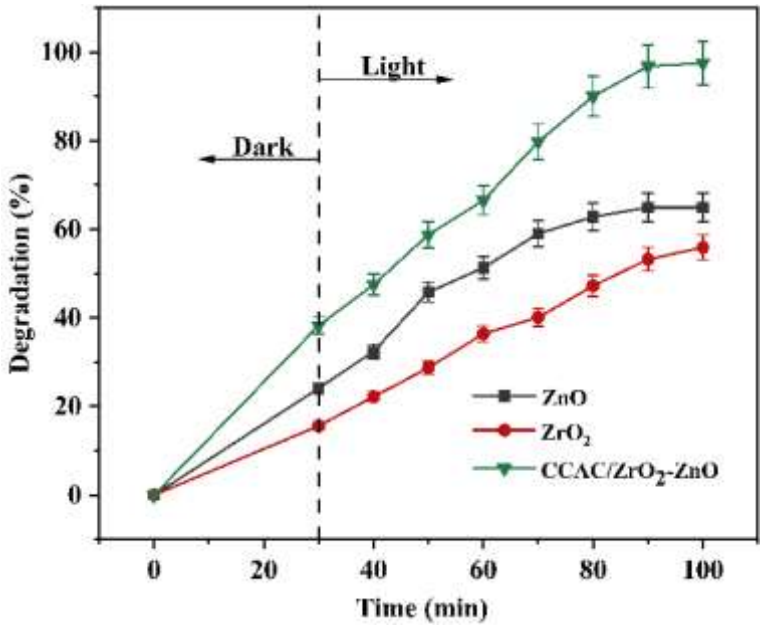

Figure 5.8. Catalytic activity test of 4-NP degradation using ZnO, ZrO_2 and CCAC/ZrO_2-ZnO nanocomposite (Catalyst dose = 0.07 g/L; Initial 4-NP concentration = 40 ppm; pH = 6.0; Reaction time = 80 min).

As shown in Figure 5.8, the CCAC/ZrO_2-ZnO nanocomposite exhibited significantly higher photocatalytic performance compared to the pristine catalysts. The degradation efficiency followed the order: pristine ZrO_2 (53.2 %) < pristine ZnO (64.9 %) < CCAC/ZrO_2-ZnO (98.2 %). These findings suggest that integrating ZrO_2 into ZnO with the support of CCAC substantially enhances photocatalytic performance, likely due to improved charge separation, increased light absorption, and a greater surface area for pollutant adsorption.

5.3.5 Reusability and photostability of the catalyst

The reusability of a photocatalyst is a critical factor for its long-term application in large-scale processes. To assess the reusability of the CCAC/ZrO_2-ZnO photocatalyst, its degradation efficiency for 4-NP was examined over multiple recycling cycles. Following each photocatalytic reaction, the nanocomposite residue was collected through centrifugation, washed with MQW, and dried in an oven. The dried catalyst was then reused for 4-NP degradation in subsequent cycles (Figure 5.9(a)).

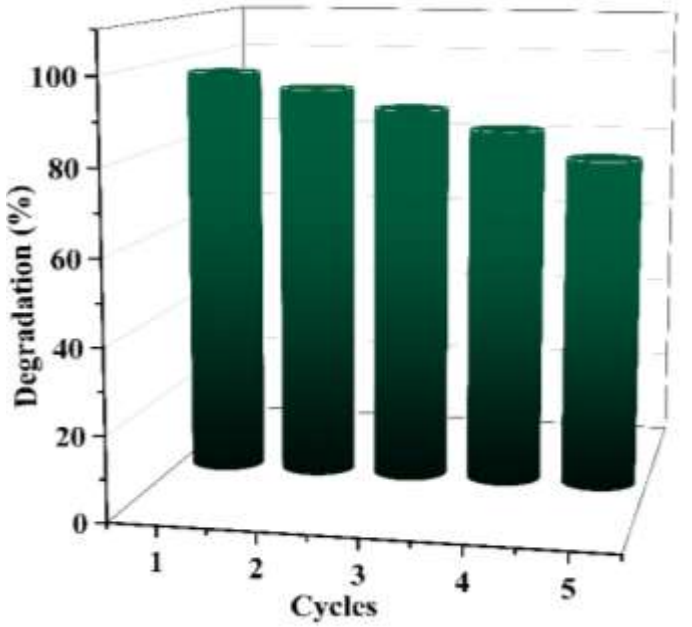

(a)

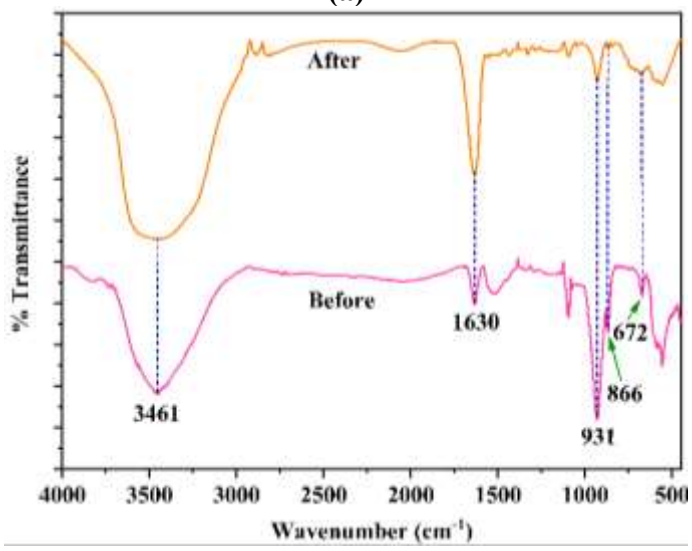

(b)

Figure 5.9. Reusability and photostability studies: (a) Degradation % during five cycles (b) FTIR analysis of the photocatalyst before and after 4-NP degradation.

In the first cycle, the degradation efficiency of 4- NP was 97.25 %, which decreased progressively to 93.75 % in the second cycle, 89.37 % in the third, 84.87 % in the fourth cycle, respectively. The slight decline in degradation efficiency observed over repeated cycles can be attributed to the accumulation of 4-NP intermediates on the CCAC/ZrO_2-ZnO nanocomposite surface, which partially block active sites, as well as the gradual loss of nanocomposite material during the recovery and reuse processes

[87,88]. Remarkably, even after several cycles, the nanocomposite demonstrated a degradation efficiency of approximately 78.5 % in the fifth cycle, highlighting its retained catalytic activity. These findings confirm that the regenerated CCAC/ZrO_2-ZnO catalyst maintains significant usability after multiple cycles. Moreover, the photostability of the CCAC/ZrO_2-ZnO nanocomposite was evaluated using FTIR analysis on the material recovered after five reuse cycles. The resultant spectrum was compared with that of the unmodified CCAC/ZrO_2-ZnO nanocomposite (Figure 5.9(b)). The analysis of FT-IR peaks before and post 4-NP degradation revealed no substantial alterations in the functional groups. This finding demonstrates that the CCAC/ZrO_2-ZnO nanocomposite maintains its structural integrity during the photocatalytic process, exhibiting proper stability. The absence of significant structural changes indicates that the nanocomposite retains its efficacy and stability during multiple 4-NP degradation reactions.

5.3.6 Real wastewater applications

The photocatalytic performance of pristine ZrO_2, pristine ZnO, and the synthesized CCAC/ZrO_2-ZnO nanocomposite was systematically evaluated for the degradation of 4-NP in real wastewater. Sample were collected from wastewater source in Mokokchung district, Nagaland, India and preserved in glass container. Due to the undetectable native concentration of 4-NP, a controlled spiking method was employed,

Figure 5.10. Real wastewater collection site.

introducing 40 ppm of 4-NP to the wastewater to facilitate degradation studies. The wastewater sampling site is depicted in Figure 5.10 and the procedures used for water quality analysis are summarized in Table 5.2. The physicochemical properties of the wastewater were characterized by a pH of 6.52, total dissolved solids (TDS) of 19 ppm, electrical conductivity (EC) of 39 μS/cm, total hardness (TH) of 84 ppm, and biological oxygen demand (BOD) of 3.3 ppm. Inorganic analysis revealed the presence of sulfate (SO42-, 20 ppm), phosphate (PO43-, 0.2 ppm), calcium (Ca2+, 4 ppm), magnesium (Mg^{2+}, 48.79 ppm), chloride (Cl^-, 4.26 ppm), and an alkalinity of 4 ppm.

Table 5.2. Method of determination of water quality parameters.

Parameters	**Method of determination**
pH	pH meter (EZ-9908)
TDS	TDS meter (EZ-9908)
EC	Conductivity meter (EZ-9908)
TH	EDTA - Titrimetry
BOD	Benchtop meter (HI5421)
Sulfate	Test kit (HI38001A-0)
Phosphate	Multiparameter Photometer (HI83300)
Calcium	EDTA – Titrimetry
Magnesium	EDTA – Titrimetry
Chloride	AgNO3 – Titrimetry
Alkalinity	HCl – Titrimetry

Photocatalytic experiments conducted under optimized conditions (catalyst dose: 0.07 g/L; pH: 6.0; reaction time: 80 min) showed that the CCAC/ZrO_2-ZnO nanocomposite exhibit superior photocatalytic performance, achieving an 87.86 % degradation efficiency of 4-NP, compared to 55.38 % and 45 % achieved with pristine ZnO and ZrO_2, respectively (Figure 5.11). The reduced photocatalytic efficiencies in real wastewater compared to laboratory conditions were attributed to the complex matrix of coexisting inorganic species. The elevated concentrations of Mg^{2+} likely promoted catalyst aggregation and surface passivation, reducing the availability of active sites, while moderate levels of SO_4^{2-} and Cl^- ions potentially contributed to hydroxyl radicals (•OH) scavenging, impeding oxidative degradation pathways.

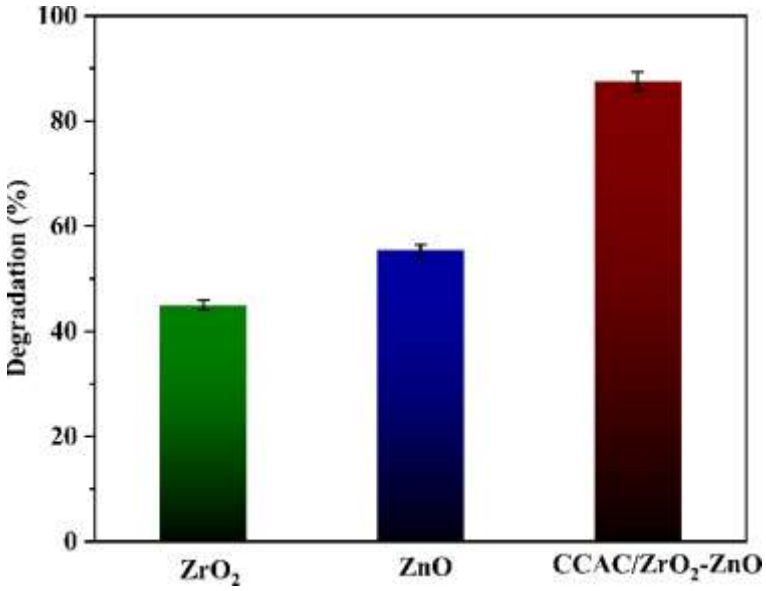

Figure 5.11. Degradation efficiency of 4-NP in the real water environment.

As a result, the CCAC/ZrO_2-ZnO nanocomposite demonstrated significant photocatalytic activity, highlighting its potential as a robust material for the remediation of organic pollutants in complex, real-world wastewater systems.

5.3.7 Mineralization

Total organic carbon analysis was carried out at varying concentrations (40-100 mg/L) to confirm the complete mineralization of 4-NP using a photocatalyst, while keeping other parameters constant.

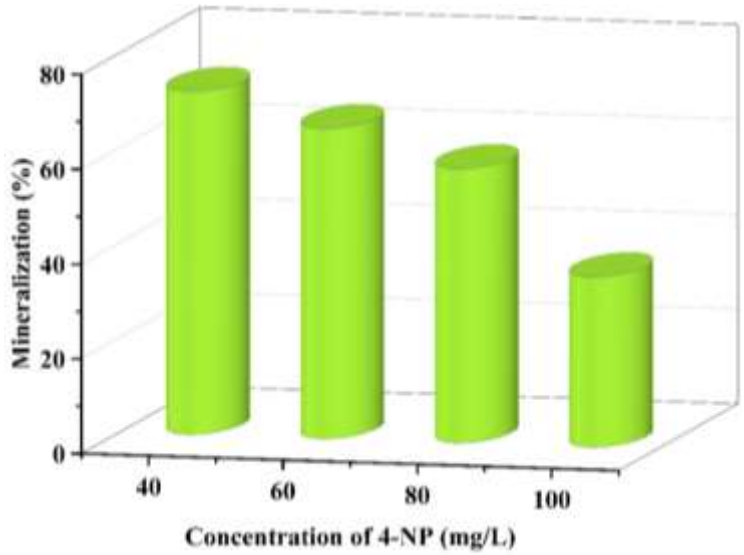

Figure 5.12. Mineralization (%) at various concentration of 4-NP (Catalyst dose = 0.07 g/L; pH = 6.0; Reaction time = 80 min).

As depicted in Figure 5.12, the results showed that 72.35 % of the 4-NP underwent successful mineralization after 80 min reaction period. The decrease in TOC indicates the oxidation and breakdown of the organic pollutant into smaller molecules, primarily CO_2 and H_2O. However, the mineralization efficiency dropped to 35.9 % when the initial 4-NP concentration was increased to 100 mg/L, indicating that higher pollutant concentrations can hinder the process, potentially due to insufficient reactive oxidative species [89]. This observation is further supported by LC-MS method, discussed in subsequent sections.

5.3.8 Degradation pathways and products from 4-NP

LC-MS analysis was utilized to identify the degradation products, revealing the formation of smaller fragments. The spectral fragmentation peaks and its intermediates for 4-NP observed after 80 min of UV light exposure are detailed in Figure 5.13 and Table 5.3. Based on the findings, a reaction mechanism was proposed for the formation of important intermediates observed during the photocatalytic breakdown of 4-NP (Scheme 5.2). Initially, 4-NP (m/z 138.02) is reduced to 4-nitrosophenol (m/z 123.09), along with other intermediates. Further reduction leads to the formation of 4-aminophenol (4-AP) (m/z 109.05). The presence of oxidizing species results in the oxidation of 4-AP molecules to hydroquinone (m/z 110.08), which then reaches equilibrium with p-benzoquinone (m/z 108.02). Moreover, oxidation by •OH radicals generate short-chain carboxylic acids such as malonic acid (m/z 102.08), succinic acid (m/z 118.05) and sorbic acid (m/z 144.05). These results corroborate prior research, suggesting that the generated small molecules can undergo further mineralization into final products such as CO_2 and H_2O.

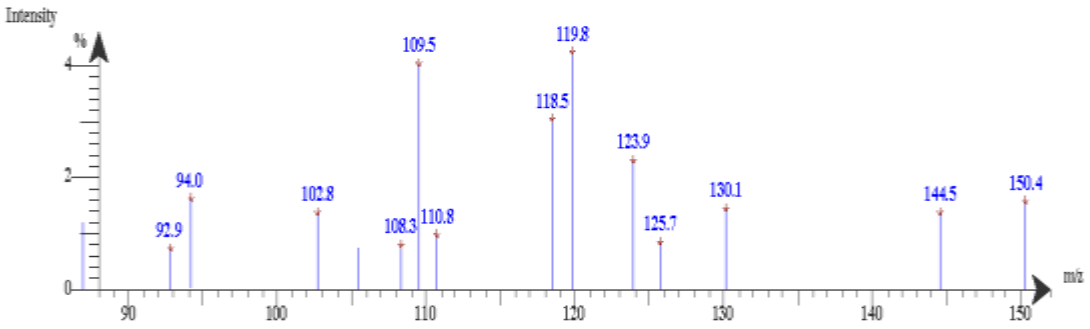

Figure 5.13. LC-MS profile of 4-NP after photocatalytic degradation.

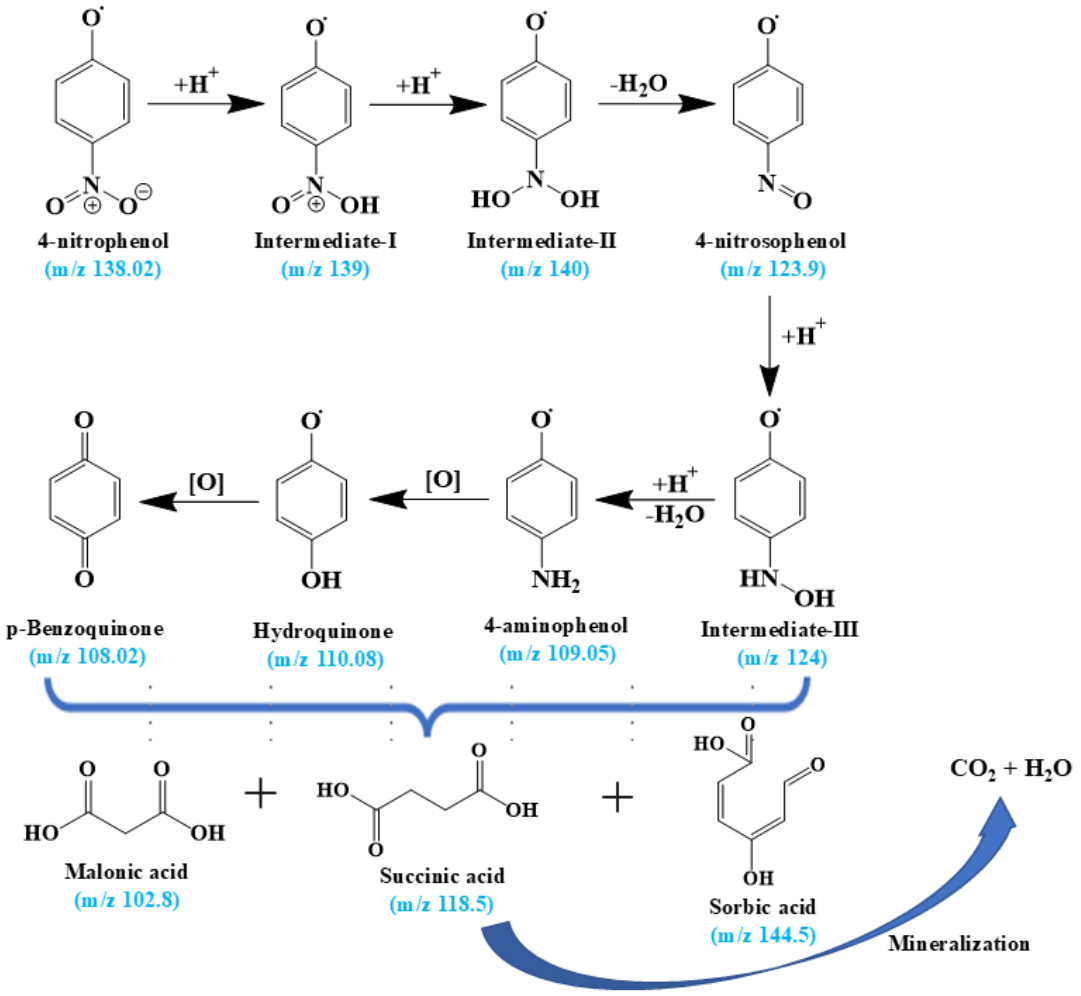

Scheme 5.2. Proposed 4-NP degradation pathway.

5.3.9 Degradation mechanism

The mechanism of degradation of 4-NP can be explained based on the band structures of ZnO and ZrO_2 which were used based on previous studies [90]. Scheme 5.3 illustrate the energy diagram for the proposed photodegradation mechanism.

Table 5.3. Possible intermediate products of 4-NP observed from the photocatalytic degradation.

Sl. No.	Degradation Products	m/z ratio	Proposed structure
1.	Phenyl propanoic acid	150.4	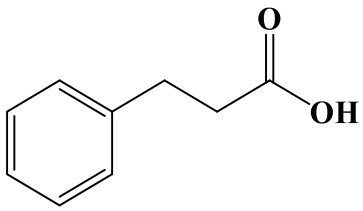

2.	Sorbic acid	144.5	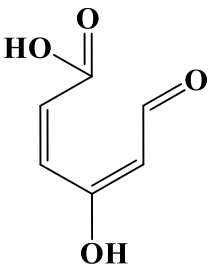
3.	p- Benzoquinone	108.02	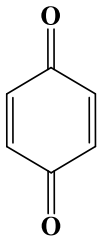
4.	4-Nitrosophenol	123.09	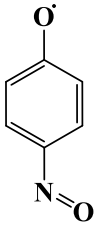
5.	Succinic acid	118.5	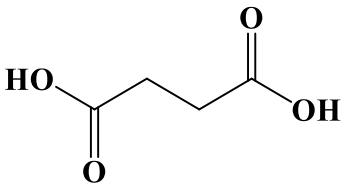
6.	Hydroquinone	110.08	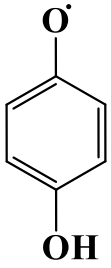
7.	4-aminophenol	109.5	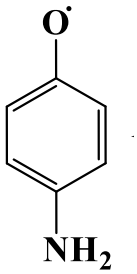
8.	Malonic acid	102.8	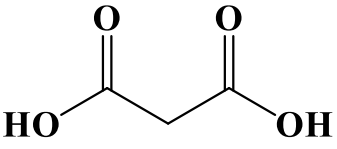

9.	Phenol	94.0	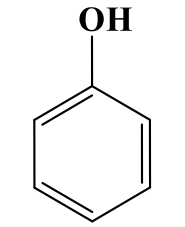
10.	Methyl benzene	92.9	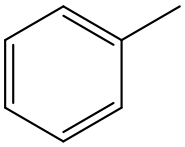

Similarly, the hole in the valence band of ZnO transfers to the valence band of ZrO_2 [91].

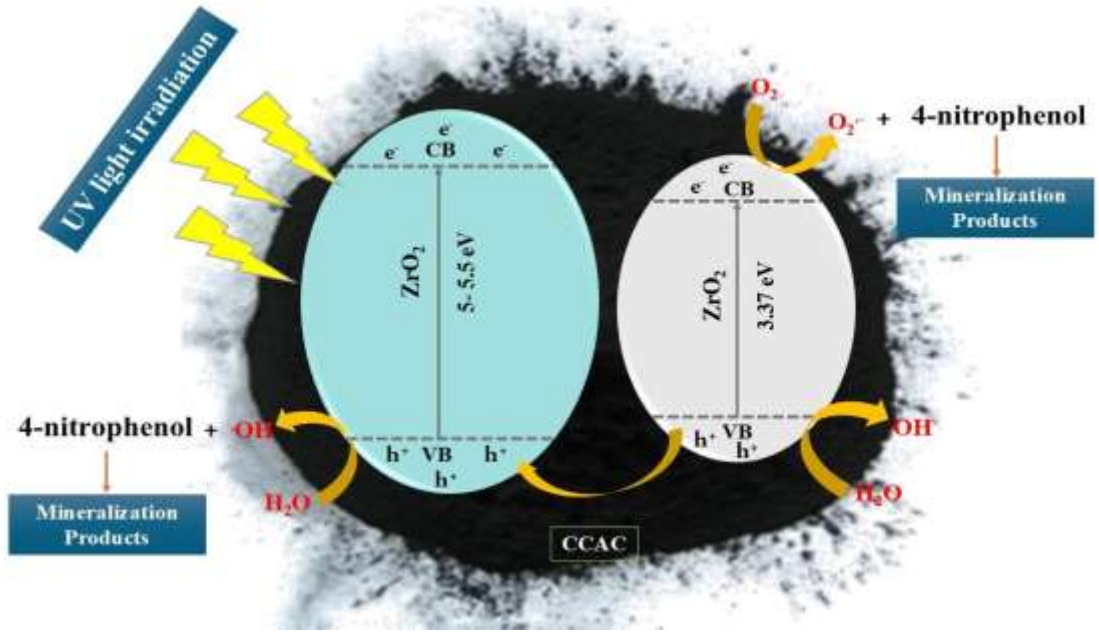

Scheme 5.3. Energy diagram illustrating the degradation pathway of 4-NP.

When exposed to UV light, both ZnO and ZrO_2 absorb energy, exciting electrons and creating electron-hole pairs. Since ZrO_2 has a more negative conduction band than ZnO, the electrons in the conduction band of ZrO_2 transfers to conduction band of ZnO. AC is utilized to extend the lifetime of electron-hole pairs of the catalyst [92]. The photo generated electrons (e^-) on the surface of ZnO reacts with oxygen molecules to generate highly reactive superoxide radicals ($\bullet O_2^-$), while the holes (h^+) in the valence band react with water molecules or hydroxide ions to generate hydroxyl radicals (•OH). These reactive oxygen species then break down 4-NP step by step,

ultimately converting it into harmless by-products like CO_2 and H_2O. The following equations summarize this process:

$$ZrO_2 \xrightarrow{\text{UV light}} ZrO_2\,(h^+ + e^-) \quad (5.15)$$

$$ZnO \xrightarrow{\text{UV light}} ZnO\,(h^+ + e^-) \quad (5.16)$$

$$ZrO_2\,(h^+ + e^-)/\,ZnO\,(h^+ + e^-) \rightarrow ZrO_2\,(h^+ + h^+)/\,ZnO\,(e^- + e^-) \quad (5.17)$$

$$e + O_2 \rightarrow \bullet O_2^- \quad (5.18)$$

$$h^+ + OH^- \rightarrow \bullet OH \quad (5.19)$$

$$3\bullet O_2^- + 2H_2O + 2H^+ \rightarrow 3H_2O_2 + O_2 \quad (5.20)$$

$$h^+ + H_2O \rightarrow \bullet OH + H^+ \quad (5.21)$$

$$h^+ + e^- \rightarrow \text{heat (recombination)} \quad (5.22)$$

$$\bullet OH \text{ or } \bullet O_2^- + \text{4-NP} \rightarrow \text{Degradation products} \rightarrow CO_2 + H_2O \quad (5.23)$$

5.3.10 Scavenger experiment

To gain a deeper insight into the photocatalytic reaction mechanism for the degradation of 4- NP driven by reactive oxygen species (ROS), a scavenging experiment was conducted to investigate the roles of various active species, including superoxide anion

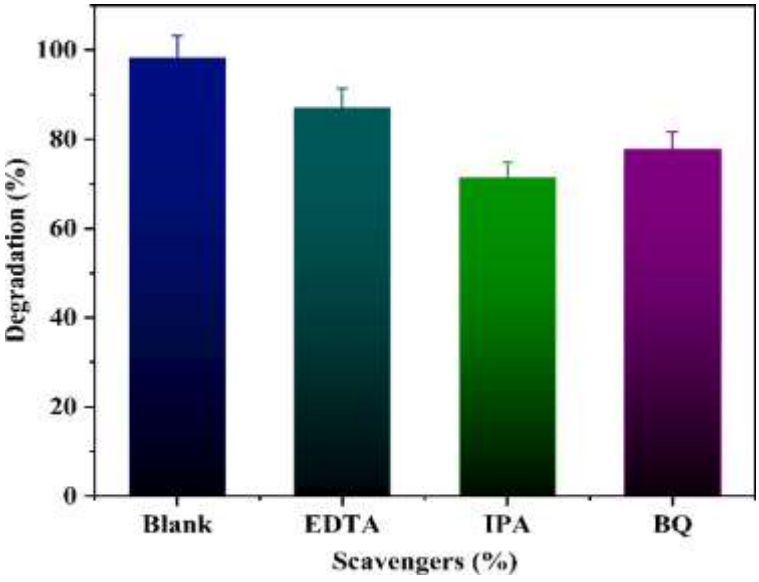

Figure 5.14. Effect of radical scavengers on 4-NP degradation.

radicals ($\bullet O_2^-$) for benzoquinone (BQ), hydroxyl radicals (•OH) for isopropanol (IPA), and holes (h^+) for EDTA, respectively. The introduction of these scavengers was found to reduce the degradation performance by deactivating the reactive species. Consequently, degradation efficiency was evaluated under optimal conditions both with and without the different scavengers.

The degradation efficiency decreased significantly when scavengers were introduced, as illustrated in Figure 5.14. The effectiveness of these scavengers followed the order: IPA > BQ > EDTA, indicating that (•OH) radicals were the primary contributors, followed by ($\bullet O_2^-$) radicals. The addition of EDTA have a minimal impact on the degradation process, suggesting that holes (h^+) played a negligible role in degradation performance. Therefore, it can be concluded that photodegradation primarily occurs through the involvement of hydroxyl radicals and superoxide processes.

5.3.11 Theoretical calculations

A theoretical analysis was conducted to explore into the chemical reactivity and formation mechanism of the prepared nanocomposite. In this study, six configurations of fused benzene rings were utilized to represent CCAC [93]. The coupling of CCAC with ZrO_2-ZnO occurred through the formation of hydrogen bonds facilitated by the O-linkage of the O-Zr-O bond within the CCAC/ZrO_2-ZnO nanocomposite. Figure 5.15 displays the optimized geometrical profile of ZrO_2-ZnO and the CCAC/ZrO_2-ZnO composite. The computed values and quantum chemical descriptors for the ZrO_2-ZnO and CCAC/ZrO_2- ZnO nanocomposite are provided in Table 5.4.

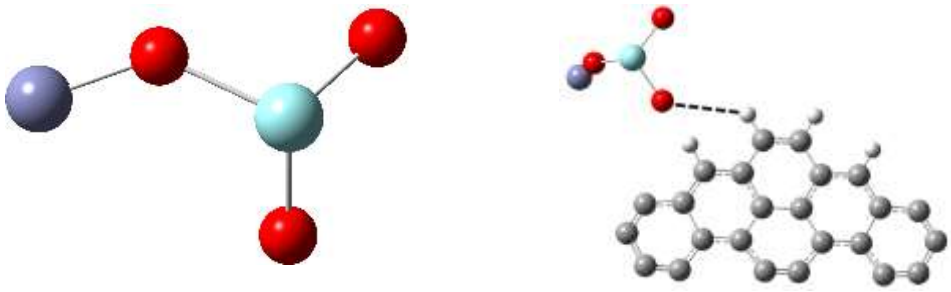

(a) **(b)**

Figure 5.15. Optimized molecular structure of (a) ZrO_2-ZnO and (b) CCAC/ZrO_2-ZnO at 6- 31G/LanL2DZ level of theory.

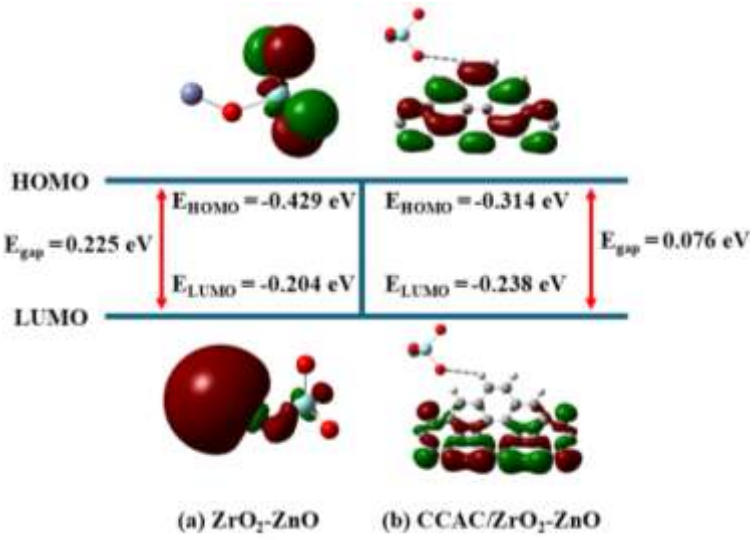

Figure 5.16. HOMO and LUMO distributions of (a) ZrO_2-ZnO and (b) CCAC/ZrO_2-ZnO nanocomposite.

Table 5.4. Chemical descriptors of ZrO_2-ZnO and CCAC/ZrO_2-ZnO nanocomposite.

System complex	η (eV)	S (eV)	μ (eV)	ω (eV)	χ (eV)	ΔN_{max}	Dipole moment (Debye)	$E_{gap} = E_{LUMO}-E_{HOMO}$ (eV)
CCAC/ZrO_2-ZnO	0.038	13.116	-0.276	0.999	0.161	7.239	26.631	0.076
ZrO_2-ZnO	0.113	4.444	-0.317	0.139	0.447	2.817	25.372	0.225

The introduction of ZrO_2-ZnO into CCAC increases its dipole moment while decreases the energy band gap (Figure 5.16). This suggests the resulting nanocomposite is highly reactive and exhibits favorable interactions.

Table 5.5 shows that the CCAC/ZrO_2-ZnO nanocomposite has a smaller HOMO-LUMO band gap energy compared to other catalysts, further supporting its enhanced reactivity and interaction potential.

Table 5.5. Energy gap (E_{gap}) of various catalysts.

System	E_{gap} (eV)	Ref.
ZnBTC	2.300	[94]
SWCNTs	1.16	[95]
$Mg(H_2BTC)_2(H_2O)_2$	3.570	[96]
CCAC/ZrO_2-ZnO	0.076	**This work**

The CCAC/ZrO_2-ZnO nanocomposite has a stronger reactivity than ZrO_2-ZnO, as evidenced by its notable lower chemical hardness (η) and increased chemical softness (S). This enhanced reactivity is ascribed to the addition of ZrO_2-ZnO nanoparticles to CCAC. Furthermore, CCAC/ZrO_2-ZnO is a more efficient electron acceptor than ZrO_2-ZnO due to its greater electronegativity and electrophilicity index. Additionally, the lower μ value of CCAC/ZrO_2- ZnO implies that it is more susceptible to electron acquisition than electron loss. Besides, the nanocomposite exhibits a greater ΔN_{max} value, suggesting the capability of charge transfer for electron transfer reactions.These indicates that the incorporation of ZrO_2-ZnO into CCAC improves its reactivity, hence increasing its efficacy in removing 4-NP. These theoretical investigations provide significant insights into material reactivity, facilitating the selection of highly efficient compounds for pollution remediation.

5.3.12 Molecular docking studies

The expanding integration of computational methodologies in biological research has propelled the rapid advancement of computational biology over the past decade [97]. The molecular docking analysis conducted against two key bacterial targets of interest revealed promising antibacterial potential.

(i) For PDB ID: 3FY8, the docking study (Table 5.6) demonstrated that the CCAC/ZrO_2-ZnO complex exhibited a MolDock score of -127.873 kcal/mol closely approximating the score of the co-crystallized ligand (-129.415 kcal/mol). However, the ZrO_2-ZnO complex exhibited the lowest docking score, indicating reduced stabilization within the target's active site. The docking score of co-crystallized ligand's serves as a reference for evaluating test compounds' binding efficiency.

Table 5.6. Docking scores of the ligands with PDB ID: 3FY8 generated *via* MVD.

Ligand	MolDock Score	[a]Rerank Score	[b]Interaction	[c]Internal	[d]H-Bond	[e]LE1	[f]LE3
Co-crystallized	-129.415	-106.566	-141.236	11.820	-3.429	-4.977	-4.098
CCAC/ZrO_2-ZnO Complex	-127.873	-102.856	-150.568	22.695	-0.167	-4.409	-3.546
ZrO_2-ZnO	-45.3552	-35.0911	-44.643	-0.711	-11.115	-9.071	-7.018

[a]*The rerank score is a linear combination of E-inter (steric, Van der Waals, hydrogen bonding, electrostatic) between the ligand and the protein, and E-intra. (torsion, sp2-sp2, hydrogen bonding, Van der Waals, electrostatic) of the ligand weighted by pre-defined coefficients.* [b]*The total interaction*

energy between the pose and the protein (kJ/mol). [c]The internal energy of the pose. [d]Hydrogen bonding energy (kJ/mol). [e]Ligand efficiency 1: MolDock score divided by heavy atoms count. [f]Ligand efficiency 3: Rerank score divided by heavy atoms count.

A comparable or close-range score suggests strong binding potential. As the co-crystallized ligand serves as a structural reference within the target of interest, its binding coordinates delineate the active site, ensuring that docking simulations accurately probe the biologically relevant binding pocket.

Table 5.7. Ligand-protein (3FY8) interaction *via* MVD.

Ligand	Interaction (P---L)	Interaction distance	Intercation energy	Hybridization protein	Hybridization ligand
Co-crystallized CCAC/ ZrO_2-ZnO Complex	Gln19 (O)----N(25)	3.20 Å	-1.97	Sp2 Acceptor	Sp2 Donor
	Asn18 (OD1)----N(0)	2.95 Å	-2.5	Sp2 Acceptor	Sp2 Donor
	Tyr98(OH)----O(23)	2.83 Å	-2.5	Sp3 Both	Sp3 Acceptor
	Ala7(N)----O(34)	3.57 Å	-0.16	Sp2 Donor	Sp3 Acceptor
	Tyr98 (OH)----O(34)	3.16 Å	-2.19	Acceptor	Sp3 Acceptor
	Arg44 (N)----O(3)	3.21 Å	-0.11	Sp2 Donor	Sp3 Both
	Thr46(OG1)----O(0)	2.61 Å	-2.5	Sp3 Both	Sp3 Acceptor
	Gly94 (N)----O(0)	3.55 Å	-0.005	Sp2 Donor	Sp3 Acceptor
	Lys45 (N)----O(3)	3.29 Å	-1.55	Sp2 Donor	Sp3 Both
	Thr96 (O)----O(4)	3.03 Å	-2.5	Sp3 Both	Sp3 Both
ZrO_2-ZnO	Leu97 (N)----O(4)	-2.99 Å	-2.5	Sp2 Donor	Sp3 Both

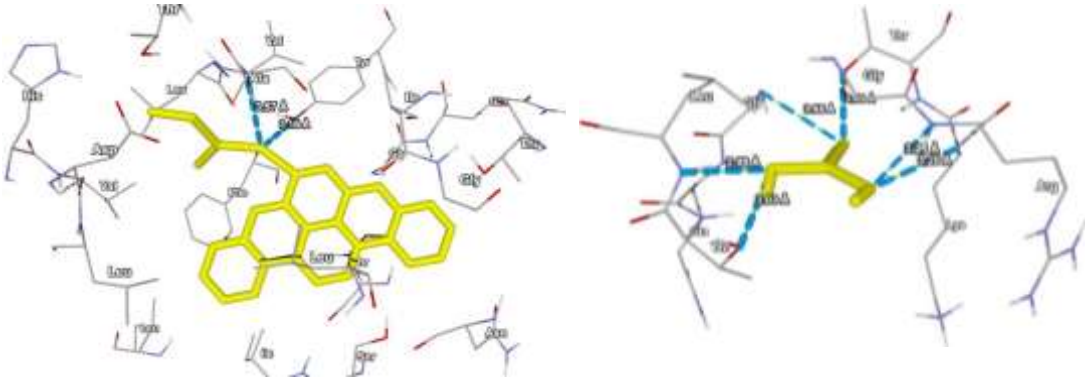

(a) **(b)**

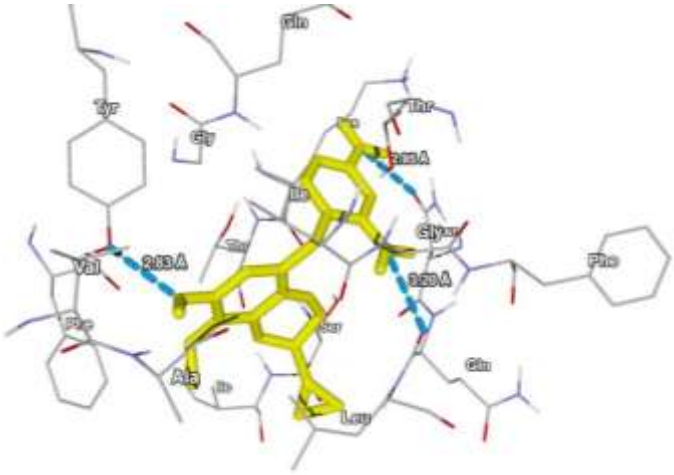

(c)

Figure 5.17. Molecular illustration of the binding interactions of (a) CCAC/ZrO_2-ZnO complex**,** (b) ZrO_2-ZnO and (c) Co-crystallized ligand within the active site of PDB ID: 3FY8 (The blue dotted line represents hydrogen bonding interactions).

These findings indicate that the CCAC/ZrO_2-ZnO complex promising binding energy to the target, comparable to the co-crystallized ligand. The interaction analysis elucidates distinct binding mechanisms, with the interaction profile summarized in Table 5.7.

The co-crystallized ligand establishes hydrogen bonding interactions with Gln19, Asn18, and Tyr98, with Tyr98 playing a pivotal role at the interaction interface.

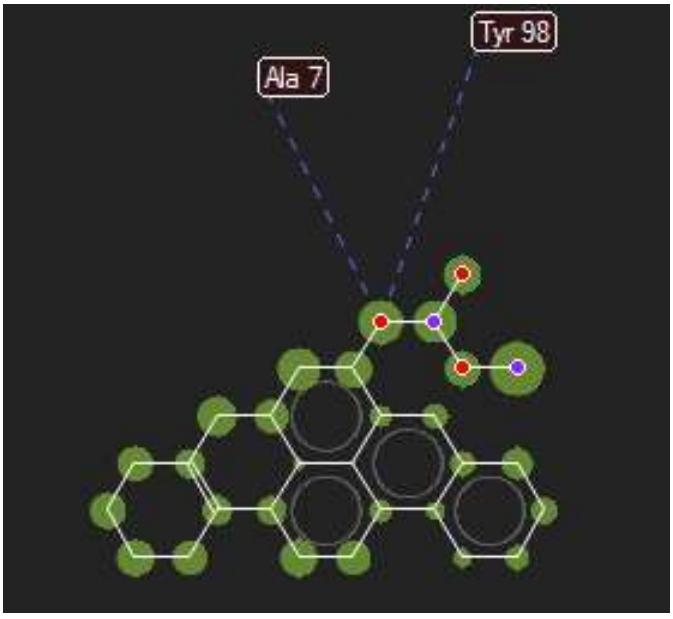

Figure 5.18. 2D Visualization and molecular illustration of the binding interactions of CCAC/ZrO_2-ZnO complex within the active site of the target protein (PDB ID: 3FY8).

In contrast, the CCAC/ZrO_2-ZnO complex preserves a common interacting residue Tyr98, indicating a binding mode analogous to that of the co- crystallized ligand. Furthermore, its additional interaction with Ala7 may contribute to binding stability and optimal ligand orientation within the active site. In contrast, the ZrO_2-ZnO complex interacts with Arg44, Thr46, Gly94, Lys45, Thr96, and Leu97, but lacks common interacting residues with the co-crystallized ligand, indicating a divergent binding pattern. This suggests that CCAC/ZrO_2-ZnO may exhibit antibacterial potential against *S. aureus*.

(ii) For PDB ID: 5MMN, docking score analysis (Table 5.8) reveals that the CCAC/ZrO_2-ZnO complex exhibits MolDock score of -116.892 kcal/mol relative to the co-crystallized ligand (- 129.711 kcal/mol), indicating its potential. In contrast, the ZrO_2-ZnO complex demonstrates significantly weaker binding affinity (-40.0651 kcal/mol), implying a markedly reduced interaction with the target and potentially lower antibacterial efficacy. The interaction profile summarized in Table 5.9, and 3-D binding conformation is illustrated in Figure 5.19, while the corresponding 2-D interaction map is presented in Figure 5.20.

Table 5.8. Docking scores of the ligands with PDB ID: 5MMN generated *via* MVD.

Ligand	MolDock Score	[a]Rerank Score	[b]Interaction	[c]Internal	[d]H-Bond	[e]LE1	[f]LE3
Co-crystallized	-129.711	-103.929	-139.505	9.79345	-3.15193	-5.40463	-4.33038
CCAC/ ZrO_2-ZnO Complex	-116.892	-69.9845	-143.931	27.0385	-2.06319	-4.03077	-2.41326
ZrO_2-ZnO	-40.0651	-30.8227	-39.3571	-0.708087	-5.13558	-8.01303	-6.16454

[a]The rerank score is a linear combination of E-inter (steric, Van der Waals, hydrogen bonding, electrostatic) between the ligand and the protein, and E-intra. (torsion, sp2-sp2, hydrogen bonding, Van der Waals, electrostatic) of the ligand weighted by pre-defined coefficients. [b]The total interaction energy between the pose and the protein (kJ/mol). [c]The internal energy of the pose. [d]Hydrogen bonding energy (kJ/mol). [e]Ligand efficiency 1: MolDock score divided by heavy atoms count. [f]Ligand efficiency 3: Rerank score divided by heavy atoms count.

Table 5.9. Ligand-protein (5MMN) interaction *via* MVD.

Ligand	Interaction (P---L)	Interaction distance	Intercation energy	Hybridization protein	Hybridization ligand
Co-crystallized	Asn46(ND2)----N(20)	2.82 Å	-2.5	Sp2 Donor	Sp2 Acceptor

	Thr165 (OG1)----N(16)	2.96 Å	-2.5	Sp3 Both	Sp2 Acceptor
	Asp73 (OD1)----N(5)	2.76 Å	-1.93	Sp3 Acceptor	Sp2 Donor
CCAC/ZrO_2-ZnO Complex	Asn46 (ND2)----O(31)	2.68 Å	-2.5	Sp2 Donor	Sp3 Acceptor
	Gly77 (N)----O(4)	2.67 Å	-2.5	Sp2 Donor	Sp3 Both
	Asp73 (OD2)----O(4)	2.70 Å	-2.5	Sp2 Acceptor	Sp3 Both
	Thr165 (OG1)----O(4)	3.00 Å	-2.5	Sp3 Both	Sp3 Both
ZrO_2-ZnO	Asp73 (OD1)----O(3)	2.95 Å	-0.92	Sp3 Acceptor	Sp3 Both

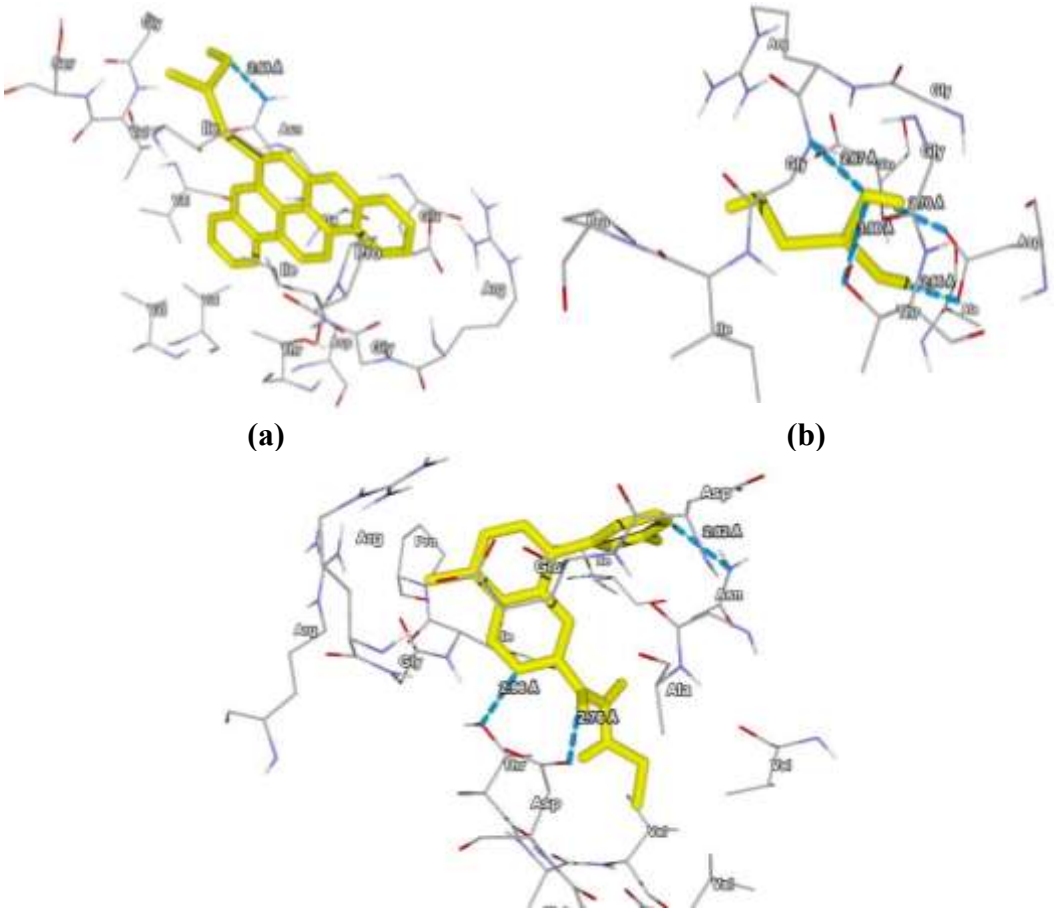

(a) **(b)**

(c)

Figure 5.19. Molecular illustration of binding interactions for (a) CCAC/ZrO_2-ZnO complex**,** (b) ZrO_2-ZnO and (c) Co-crystallized ligand within the active site of PDB ID: 5MMN (The blue dotted line represents hydrogen bonding interactions).

The co-crystallized ligand forms hydrogen bonds with Asn46, Thr165, and Asp73. The CCAC/ZrO_2-ZnO complex retains interaction with Asn46, indicating partial conservation of the co-crystallized binding mode. Conversely, the ZrO_2-ZnO complex interacts with Gly77, Asp73, and Thr165, suggesting a distinct binding mechanism. The preservation of Asn46 interaction by CCAC/ZrO_2-ZnO implies structural mimicry and may contribute to ligand stabilization, reinforcing CCAC/ZrO_2-ZnO antibacterial potential against *E. coli*.

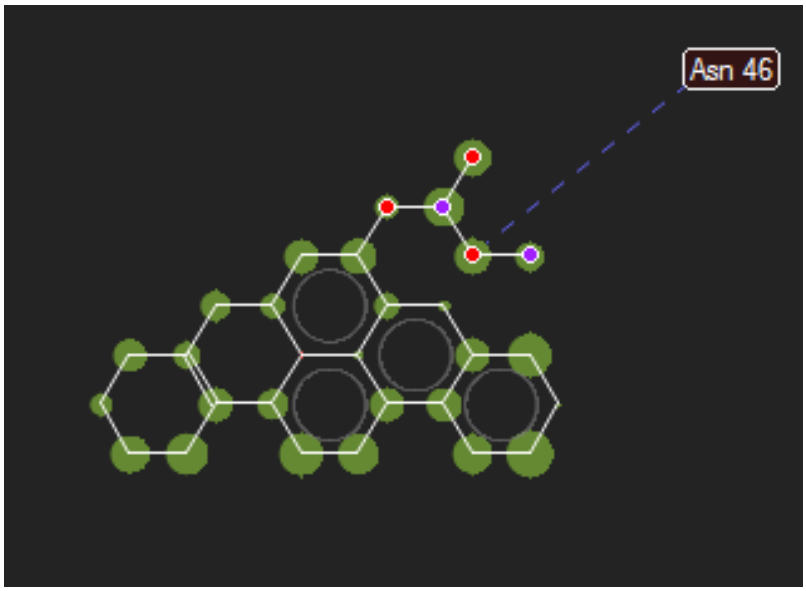

Figure 5.20. 2D Visualization and molecular illustration of the binding interactions of CCAC/ZrO_2-ZnO complex within the active site of the target protein (PDB ID: 3FY8).

The docking results and interaction profiles indicate that the CCAC/ZrO_2-ZnO nanocomposite exhibits a Moldock score comparable to that of the co-crystallized ligands, underscoring its potential as an effective bacterial inhibitor. For PDB ID 3FY8, the co-crystallized ligand AR-101 functions as a competitive inhibitor. Its binding conformation, as resolved by crystallography, reflects its potent affinity and reported antibacterial activity. In this study, AR-101 was used as a reference to evaluate the binding performance of the nanocomposite. The CCAC/ZrO_2-ZnO complex showed a similar docking score and preserved a key interaction with Tyr98, a residue critical to AR-101 binding suggesting a comparable binding orientation and inhibitory capability. Similarly, for PDB ID 5MMN, the co-crystallized ligand *1-ethyl-3-[8-methyl-5-(2-methylpyridin-4-yl)isoquinolin-3-yl]urea* served as the reference

inhibitor. While the nanocomposite exhibited a slightly lower docking score relative to this ligand, it displayed substantial binding potential. Both compounds shared a common interaction with Asn46, reinforcing the likelihood of similar target engagement. Overall, the docking scores and shared key interactions suggest that the CCAC/ZrO_2-ZnO nanocomposite effectively mimics the behavior of established inhibitors. This alignment in profiles implies that the nanocomposite may exhibit significant antibacterial activity, positioning it as a promising candidate for therapeutic development against these strains.

5.3.13 Comparison studies

This study thoroughly assessed the 4-NP degrading efficiency of the CCAC/ZrO_2-ZnO nanocomposite and compared it with other nanocomposites published in the existing literature, as outlined in Table 5.10.

Table 5.10. Evaluation of the degradation performance of synthesized catalyst compared to other reported findings.

Targeted Pollutant	**Photocatalysts**	**Irradiation time (min)**	**Performance of photocatalyst (%)**	**Ref.**
4 nitrophenol	ZnO/HZSM-5	90	91	[98]
MB	ZnO/GO	90	84	[99]
p-nitrophenol	ZrO_2-Cr_2O_3	100	92.72	[100]
Phenol	ZnO-ZrO_2	120	71	[101]
Tetracycline hydrochloride	ZrO_2/ZnO@Q	150	90.6	[102]
Crystal violet	5 %-C-doped ZnO	-	92.7	[103]
Methyl Orange		-	87.8	
4-nitropheol	V_{Zn+S}-$ZnIn_2S_4$	120	95	[104]
4-NP	CCAC/ZrO_2-ZnO	80	98.2	**This work**

The comparison investigation reveals that the CCAC/ZrO_2-ZnO nanocomposite has enhanced 4-NP degrading efficiency compared to previously reported materials. These findings highlight its potential as a highly effective catalyst for the elimination of 4-NP from aquatic environments.

5.4 Conclusion

This study presents a novel photocatalyst based on *Croton caudatus*-derived activated carbon incorporated with ZrO_2-ZnO, which has not been previously explored. The synergistic integration of these components results in enhanced charge separation, improved photostability and superior degradation efficiency compared to conventional single or binary photocatalysts for the degradation of 4-NP. The synthesized nanocomposite was thoroughly characterized using various techniques such as XRD, FTIR, SEM, TEM with EDS, PL, BET surface area, XPS analysis, respectively, providing valuable insights into its its formation, morphology, surface and functional properties. The prepared CCAC/ZrO_2-ZnO photocatalyzed exhibited a high degradation efficiency of 98.2 % for 4-NP (40 ppm) under UV light irradiation (80 min, pH 6) with a catalyst loading of 0.07 g/L. Based on LH model, the degradation process followed PFO kinetics, with a $t_{1/2}$ of 2.044 min and K_{ap} of 0.339 min^{-1}. Scavenger experiments indicated that superoxides and hydroxyl radicals played a significant role in the degradation mechanism. The catalyst maintained 78.5 % efficacy after five successive cycles, confirming its stability and reusability. Furthermore, the photocatalyst exhibited notable applicability in real wastewater treatment, supporting its feasibility for scale-up and selective removal of organic contaminants. LC-MS analysis of the 4-NP degradation suggested a potential pathway involving low molecular weight intermediates, ultimately leading to the complete mineralization of carbon dioxide and water. DFT simulations revealed hydrogen bonding via O-linkage of the O-Zr-O bond with CCAC, leading to the formation of a chemically reactive CCAC/ZrO_2–ZnO nanocomposite. Reactivity descriptors further validated its favorable electronic structure and chemical stability, correlating well with the observed enhancement in photocatalytic performance. In addition, the nanocomposite demonstrated promising antibacterial potential, attributed by its ability to inhibit DHFR and DNA gyrase, as evidenced by molecular docking simulation. However, further optimization and experimental validation through *in vitro* and *in vivo* studies are essential to confirm these findings. The next phase of this research will involve a thorough biological evaluation of the synthesized nanocomposite, assessing their antibacterial efficacy against the aforementioned strains and other clinically relevant pathogens. Promising outcomes will lead to *in vivo* testing using appropriate animal

models to assess therapeutic effectiveness, pharmacokinetics and potential toxicity under physiological conditions. Concurrently, mechanistic studies will also be undertaken to investigate the pathways by which the nanocomposite exert its antibacterial effects. This comprehensive approach aims to validate the therapeutic potential of the synthesized nanocomposite and advance their development toward clinical application. Overall, the results acquired from produced nanocatalysts indicate no hazardous behavior in wastewater treatment applications, highlighting its potential as a robust, stable and reusable material for the efficient removal of organic contaminants.

References

[1] Y. Ji, Y. Shi, Y. Yang, P. Yang, L. Wang, J. Lu, J. Li, L. Zhou, C. Ferronato, J. M. Chovelon, Rethinking sulfate radical-based oxidation of nitrophenols: Formation of toxic polynitrophenols, nitrated biphenyls and diphenyl ethers, J. Hazard. Mater. 361 (2019) 152–161.

[2] S. Naraginti, A. Sivakumar, Eco-friendly synthesis of silver and gold nanoparticles with enhanced bactericidal activity and study of silver catalyzed reduction of 4-nitrophenol, Spectroc. Acta Pt. A-Molec. Biomolec. Spectr. 128 (2014) 357–362.

[3] K. G. Pavithra, P. S. Rajan, J. Arun, K. Brindhadevi, Q. H. Le, A. Pugazhendhi, A review on recent advancements in extraction, removal and recovery of phenols from phenolic wastewater: Challenges and future outlook, Environ. Res. 237 (2023) 117005.

[4] Q. Mei, H. Cao, D. Han, M. Li, S. Yao, J. Xie, J. Zhan, Q. Zhang, W. Wang, M. He, Theoretical insight into the degradation of p-nitrophenol by OH radicals synergized with other active oxidants in aqueous solution, J. Hazard. Mater. 389 (2020) 121901.

[5] H. Zheng, Y. Guo, H. Zhu, D. Pan, L. Pan, J. Liu, p-Nitrophenol enhanced degradation in high-voltage pulsed corona discharges combined with ozone system, Plasma Chem. Plasma Process. 33 (2013) 1053–1062.

[6] R. Jayachitra, J. N. Jebaranjitham, A. Prasannan, V. Lincy, S. Sangaraju, P.-D. Hong, Multitasking needle-shaped copper oxide nanorods decorated cystine modified polymer/graphene oxide nanocomposite for 4-nitrophenol reduction, dye degradation, and textile effluent treatment, J. Environ. Chem. Eng. 12 (2024) 112346–112346.

[7] N. El Messaoudi, Y. Miyah, M. Benjelloun, J. Georgin, D. S. P. Franco, Z. M. Şenol, Z. Ciğeroğlu, M. El. Hajam, S. Knani, P. Nguyen-Tri, A comprehensive review on designing nanocomposite adsorbents for efficient removal of 4-nitrophenol from water, Nano-Struct. Nano-Objects. 40 (2024) 101326.

[8] A. A. Kassem, H. N. Abdelhamid, D. M. Fouad, S. A. Ibrahim, Catalytic reduction of 4-nitrophenol using copper terephthalate frameworks and CuO@C composite, J. Environ. Chem. Eng. 9 (2020) 104401–104401.

[9] M. A. Khan, S. Mutahir, I. Shaheen, Y. Qunhui, M. Bououdina, M. Humayun, Recent advances over the doped g-C_3N_4 in photocatalysis: A review, Coord. Chem. Rev. 522 (2024) 216227.

[10] A. Chakravorty, S. Roy, A review of photocatalysis, basic principles, processes, and materials, Sustain. Chem Environ. 8 (2024) 100155.

[11] S. Dadvar, B. Shahmoradi, S. Habibi, K. Wantala, T. Suwannaruang, A. Maleki, H.P. Shivaraju, S.-M. Lee, Photocatalytic degradation of water disinfection by-products using zirconium doped zinc oxide nanoparticles, *Desalination Water Treat.* **252** (2022) 339–347.

[12] S. F. Darmiyan, M. R. Rezaei, M. Hossein, S. Anari, Investigating photocatalytic removal of Doxycycline antibiotic using ZnO@g-C_3N_4 nanocomposite in aqueous environments, *Environment* **11** (2025) 89–96.

[13] S. Kohzadi, A. Maleki, M. Bundschuh, Z. Vahabzadeh, S. A. Johari, R. Rezaee, B. Shahmoradi, N. Marzban, N. Amini, Doping zinc oxide (ZnO) nanoparticles with molybdenum boosts photocatalytic degradation of Rhodamine B (RhB): Particle characterization, degradation kinetics and aquatic toxicity testing, J. Mol. Liq. 385 (2023) 122412.

[14] R. Ameta, S. C. Ameta, Photocatalysis: Principles and Applications, CRC Press, 2016.

[15] M. R. Rajeshwari, M. K. Okla, S. Kokilavani, M. A. A. Maksoud, I. A. Saleh, H. A. A. Harirah, T. N. AlRamadneh, S. Sudheer Khan, Synergistic visible light assisted photocatalytic degradation of p-chlorophenol and rifampicin from aqueous solution using a novel g-C_3N_4 quantum dots incorporated α-MoO_3 nanohybrid – Mechanism, pathway and toxicity studies, Chemosphere. 339 (2023) 139529–139529.

[16] V. Subhiksha, M. K. Okla, P. R. Sivaranjani, M. A. A. Maksoud, I. A. Saleh, H. A. A. Harirah, S. S. Khan, Congregating Ag into γ-Bi_2O_3 coupled with $CoFe_2O_4$ for enhanced visible light photocatalytic degradation of ciprofloxacin, Cr(VI) reduction and genotoxicity studies, Chemosphere. 342 (2023) 140181–140181.

[17] M. S. S. Danish, L. L. Estrella, I. M. A. Alemaida, A. Lisin, N. Moiseev, M. Ahmadi, M. Nazari, M. Wali, H. Zaheb, T. Senjyu, Photocatalytic applications of metal oxides for sustainable environmental remediation, Metals. 11 (2021) 80.

[18] M. Ikram, H. Shahid, J. Haider, A. Haider, S. Naz, A. Ul-Hamid, I. Shahzadi, M. Naz, W. Nabgan, S. Ali, Nb/Starch-doped ZnO nanostructures for polluted water treatment and antimicrobial applications: molecular docking analysis, ACS Omega. 7 (2022) 39347–39361.

[19] A. R. Bhapkar, S. Bhame, A review on ZnO and its modifications for photocatalytic degradation of prominent textile effluents: Synthesis, mechanisms, and future directions, J. Environ. Chem. Eng. 12 (2024) 112553–112553.

[20] B. Weng, M. Y. Qi, C. Han, Z. R. Tang, Y. J. Xu, Photocorrosion inhibition of semiconductor-based photocatalysts: basic principle, current development, and future perspective, ACS Catal. 9 (2019) 4642–4687.

[21] S. Kumar, A. Kumar, A. Kumar, V. Krishnan, Nanoscale zinc oxide based heterojunctions as visible light active photocatalysts for hydrogen energy and environmental remediation, Rev. Catal. 62 (2019) 346–405.

[22] S. Maiti, S. Pal, K. K. Chattopadhyay, Recent advances in low temperature, solution processed morphology tailored ZnO nanoarchitectures for electron emission and photocatalysis applications, Cryst. Eng. Comm. 17 (2015) 9264–9295.

[23] D. S. P. Sivakuma, Review on the photocatalytic activity of various composite catalysts, Chem. Eng. Process 97 (2015) 112–133.

[24] K. Lee, H. Yoon, C. Ahn, J. Park, S. Jeon, Strategies to improve the photocatalytic activity of TiO_2: 3D nanostructuring and heterostructuring with graphitic carbon nanomaterials, Nanoscale 11 (2019) 7025–7040.

[25] H. Anwer, J. W. Park, Synthesis and characterization of a heterojunction rGO/ZrO_2/Ag_3PO_4 nanocomposite for degradation of organic contaminants, J. Hazard. Mater. 358 (2018) 416–426.

[26] S. N. Basahel, T. T. Ali, M. Mokhtar, K. Narasimharao, Influence of crystal structure of nanosized ZrO_2 on photocatalytic degradation of methyl orange, Nanoscale Res. Lett. 10 (2015) 73.

[27] M. Lee, S. I. Han, C. Kim, S. Velumani, A. Han, A. H. Kassiba, H. Castaneda, ZrO_2/ZnO/TiO_2 nanocomposite coatings on stainless steel for improved corrosion resistance, biocompatibility, and antimicrobial activity, ACS Appl. Mater. Interfaces. 14 (2022) 13801–13811.

[28] M. Iwanow, T. Gärtner, V. Sieber, B. König, Activated carbon as catalyst support: precursors, preparation, modification and characterization, Beilstein J. Org. Chem. 16 (2020) 1188–1202.

[29] F. Zhou, C. Lu, Y. Yao, L. Sun, F. Gong, D. Li, K. Pei, W. Lü, W. Chen, Activated carbon fibers as an effective metal-free catalyst for peracetic acid activation: Implications for the removal of organic pollutants, J. Chem. Eng. 281 (2015) 953–960.

[30] S. Thakur, V. Mutreja, A. Tomar, S. Nainwal, K. Kaur, R. Kaur, Q. Li, F. S. Ataya, Phytochemical-assisted fabrication of ZrO_2/ZnO nanocomposites: A sustainable approach for efficient photodegradation of tetracycline hydrochloride, J. Mol. Struct. 1330 (2025) 141350.

[31] M. Nazim, A. A. P. Khan, A. M. Asiri, J. H. Kim, Exploring rapid photocatalytic degradation of organic pollutants with porous CuO nanosheets: Synthesis, dye removal, and kinetic studies at room temperature, ACS Omega 6 (2021) 2601–2612.

[32] K. A. Sultana, M. T. Islam, J. A. Silva, R. S. Turley, J. A. Hernandez-Viezcas, J. L. Gardea-Torresdey, J. C. Noveron, Sustainable synthesis of zinc oxide nanoparticles for photocatalytic degradation of organic pollutant and generation of hydroxyl radical, J. Mol. Liq. 307 (2020) 112931.

[33] M. Baruah, A. Supong, P. C. Bhomick, R. Karmaker, C. Pongener, D. Sinha, Batch sorption–photodegradation of Alizarin Red S using synthesized TiO_2/activated carbon nanocomposite: an experimental study and computer modelling, Nanotechnol. Environ. Eng. 5 (2020) 1-13.

[34] N. Vieira, S. Maria, M. Gurgel, Carlos, S. Barros, Adsorption of basic dyes onto activated carbon: Experimental and theoretical investigation of chemical reactivity of basic dyes using DFT-based descriptors, Appl. Surf. Sci. 448 (2018) 662–670.

[35] G. Q. Blantocas, A. S. Alaboodi, A. B. H. Mekky, Synthesis of chitosan–TiO_2 antimicrobial composites via a 2-step process of electrospinning and plasma sputtering, *Arab. J. Sci. Eng.* **43** (2018) 389–398.

[36] T. N. V. de Souza, S. M. L. de Carvalho, M. G. A. Vieira, M. G. C. da Silva, D. D. S. B. Brasil, Adsorption of basic dyes onto activated carbon: Experimental and theoretical investigation of chemical reactivity of basic dyes using DFT-based descriptors, *Appl. Surf. Sci.* **448** (2018) 662–670.

[37] H. Ullah, A. A. Tahir, T. K. Mallick, Polypyrrole/TiO_2 composites for the application of photocatalysis, *Sens. Actuators B Chem.* **241** (2017) 1161–1169.

[38] W. Y. Belay, M. Getachew, B. A. Tegegne, Z. H. Teffera, A. Dagne, T. K. Zeleke, R. B. Abebe, A. A. Gedif, A. Fenta, G. Yirdaw, A. Tilahun, Mechanism of antibacterial resistance, strategies and next-generation antimicrobials to contain antimicrobial resistance: A review, Front. Pharmacol. 15 (2024) 1444781.

[39] M. V. Arularasu, M. Harb, R. Sundaram, Synthesis and characterization of cellulose/TiO_2 nanocomposite: Evaluation of *in vitro* antibacterial and *in silico* molecular docking studies, *Carbohydr. Polym.* **249** (2020) 116868.

[40] N. Iram, M. S. Khan, R. Jolly, M. Arshad, M. Alam, P. Alam, F. Firdaus, Interaction mode of polycarbazole–titanium dioxide nanocomposite with DNA: Molecular docking simulation and *in vitro* antimicrobial study, *J. Photochem. Photobiol. B* **153** (2015) 20–32.

[41] S. Sharma, S. L. Ezung, A. Supong, M. Baruah, S. Kumar, R. S. Umdor, D. Sinha, Activated carbon adsorbent derived from waste biomass, "*croton caudatus*" for efficient removal of 2-chlorophenol from aqueous solution: Kinetics, isotherm, thermodynamics and DFT simulation, Chem. Eng. Res. Des. 190 (2023) 777–792.

[42] A. Shokufeh, Structural and antibacterial properties of ZrO_2@ZnO core-shell by sonosynthesis methods, Res. J. Chem. Environ. 19 (2015) 28–32.

[43] M. Feizi, M. Jalali, Sorption of aquatic phosphorus onto native and chemically-modified plant residues: modeling the isotherm and kinetics of sorption process, Desalin. Water Treat. 57 (2014) 3085–3097.

[44] M. Frisch, Gaussian 09, Revision d. 01, Gaussian, Inc, Wallingford CT. 201 (2024).

[45] S. L. Ezung, M. Baruah, S. Kumar, S. Sharma, D. Sinha, Photocatalytic degradation of the organophosphorus insecticide chlorpyrifos in aqueous suspensions using a novel activated carbon ZrO_2-ZnO nanocomposite under UV light, Korean J. Chem. Eng. 40 (2023) 1360–1372.

[46] G. Q. Blantocas, A. S. Alaboodi, A. H. Mekky, Synthesis of chitosan–antimicrobial composites via a 2-step process of electrospinning and plasma sputtering, Arab. J. Sci. Eng. 43 (2017) 389–398.

[47] A. Bendjeddou, T. Abbaz, A. K. Gouasmia, D. Villemin, Molecular Structure, HOMO-LUMO, MEP and Fukui Function Analysis of Some TTF-donor Substituted Molecules Using DFT (B3LYP) Calculations, Int. Res. J. Pure Appl. Chem. 12 (2016) 1–9.

[48] E. O. Akintemi, K. Govender, T. Singh, A DFT study of the chemical reactivity properties, spectroscopy and bioactivity scores of bioactive flavonols, Comput. Theor. Chem. 1210 (2022) 113658–113658.

[49] S. Pratihar, S. Roy, Nucleophilicity and Site Selectivity of Commonly Used Arenes and Heteroarenes, J. Org. Chem. 75 (2010) 4957–4963.

[50] F. B. Shittu, A. Iqbal, M. N. Ahmad, M. R. Yusop, M. N. M. Ibrahim, S. Sabar, L. D. Wilson, D. H. Y. Yanto, Insight into the photodegradation mechanism of bisphenol-A by oxygen doped mesoporous carbon nitride under visible light irradiation and DFT calculations, RSC Adv. 12 (2022) 10409–10423.

[51] J. M. Paggi, A. Pandit, R. O. Dror, The art and science of molecular docking, *Annu. Rev. Biochem.* 93 (2024).

[52] L. H. Al-Wahaibi, M. A. Mahmoud, H. A. Alzahrani, H. A. A. Zied, A. Abdelmoez, B. G. M. Youssif, S. Bräse, S. M. Rabea, Synthesis, enzyme inhibition, and docking studies of new schiff bases of disalicylic acid methylene-based derivatives as dual-target antibacterial agents, Front. Chem. 12 (2024) 1–18.

[53] K. Rajakumari, K. Aravind, M. Balamugundhan, M. Jagadeesan, A. Somasundaram, P. Brindha Devi, P. Ramasamy, Comprehensive review of DNA

gyrase as enzymatic target for drug discovery and development, Eur. J. Med. Chem. 12 (2024) 100233.

[54] M. ApS, Molegro Virtual Docker, ApS, Aarhus, Denmark, 2.4 (2008).

[55] R. Thomsen, M. H. Christensen, MolDock: a new technique for high-accuracy molecular docking, J. Med. Chem. 49 (2006) 3315–3321.

[56] B. Singha, P. P. Gogoi, P. Longkumer, B. Ahmed, N. Boruah, B. Bezbaruah, U.B. Sinha, A holistic computational exploration of AZD7762 as a potent selective modulator of LXRα, LXRβ and FXR: An underexplored pathway in cancer therapeutics, Comput. Biol. Med. 194 (2025) 110433.

[57] B. Singha, B. Arora, R. Karmaker, K. Richa, N. Longkumer, H. T. Abdulhameed, M. Abid, U. B. Sinha, Evaluating Terrestrol A as an inhibitor against SARS-CoV-2 and invasive fungal pathogens: A comprehensive computational analysis, *Chem. Select* **9** (2024) e202304761.

[58] R. Thomsen, M. H. Christensen, MolDock: A new technique for high-accuracy molecular docking, J. Med. Chem. 49 (2006) 3315–3321.

[59] W. L. M. Alencar, T. da Silva Arouche, A. F. G. Neto, T. de Castro Ramalho, R. N. de Carvalho Júnior, A. M. de Jesus Chaves Neto, Interactions of Co, Cu, and non-metal phthalocyanines with external structures of SARS-CoV-2 using docking and molecular dynamics, Sci. Rep. 12 (2022) 3316.

[60] F. P. Moraes, W. F. de Azevedo, Targeting imidazoline site on monoamine oxidase B through molecular docking simulations, J. Mol. Model. 18 (2012) 3877–3886.

[61] W. Ahmed, J. Iqbal, S. O. Aisida, A. Badshah, I. Ahmad, K. Alamgir, I. H. Gul, Structural, magnetic and dielectric characteristics of optically tuned Fe doped ZrO_2 nanoparticles with visible light driven photocatalytic activity, Mater. Chem. Phys. 251 (2020) 122999.

[62] S. Khalili, H. M. Chenari, The influence of ZrO_2 addition on the morphological, structural, vibrational, and optical characteristics of composite fibers based on ZnO, Thin Solid Films. 741 (2022) 139031.

[63] X. Liu, C. He, X. Yu, Y. Bai, L. Ye, B. Wang, L. Zhang, Net-like porous activated carbon materials from shrimp shell by solution-processed carbonization and H_3PO_4 activation for methylene blue adsorption, Powder Technol. 326 (2018) 181–189.

[64] Y. Sahu, R. Patel, A.K. Singh, S. Singh, V. Sahu, Md. A. B. H. Susan, Highly fluorescent ZnO composite of N-doped carbon dots from dregea volubilis for

fluorometric determination of glucose in biological samples, J. Fluoresc. 35 (2024) 805–818.

[65] T. Kalak, High efficiency of the bioremoval process of Cu(II) ions with blackberry (*Rubus L.)* residues generated in the food industry, Desalin. Water Treat. 238 (2024) 174–197.

[66] W. Gao, J. Liu, P. Zhang, X. Zeng, Z. Han, Y. Teng, Physicochemical, structural and functional properties of pomelo peel pectin extracted by combination of pulsed electric field and cellulase hydrolysis, Int. J. Biol. Macromol. 278 (2024) 134469.

[67] S. Aghabeygi, M. K. Shamami, ZnO/ZrO_2 nanocomposite: Sonosynthesis, characterization and its application for wastewater treatment, Ultrasound. Sonochem. 41 (2018) 458–465.

[68] W. Wang, X. Zhang, S. Weng, C. Peng, Tuning catalytic activity of CO_2 hydrogenation to C1 product via metal support interaction over metal/metal oxide supported catalysts, ChemSusChem. 17 (2024) 1–24.

[69] D. Soni, J. Singh, N. Kaurav, J. Tripathi, A. Sharma, Synthesis and characterization of zirconia nanocrystalline powder by thermal treatment method, Mater. Today: Proc. 54 (2022) 908–911.

[70] C. Du, E. Hondo, L. G. Chizema, D. Shen, Q. Ma, X. Yan, S. Mo, P. Lu, N. Tsubaki, LPG direct synthesis from syngas over a $Cu/ZnO/ZrO_2/Al_2O_3$@H-β zeolite capsule catalyst prepared by a facile physical method, ChemistrySelect. 5 (2020) 1932–1937.

[71] K. Mishra, S. H. Kim, Y. R. Lee, Bandgap narrowing of highly stable heterogeneous ZrO_2–ZnO nanocomposites for the reductive amination of carbonyl compounds with formic acid and triethylamine, ChemSusChem. 12 (2018) 881–889.

[72] M. Yadav, A. Yadav, R. Fernandes, Y. Popat, M. Orlandi, A. Dashora, D. C. Kothari, A. Miotello, B. L. Ahuja, N. Patel, Tungsten-doped TiO_2/reduced graphene oxide nano-composite photocatalyst for degradation of phenol: A system to reduce surface and bulk electron-hole recombination, J. Environ. Manag. 203 (2017) 364–374.

[73] S. B. Khan, K. A. Alamry, H. M. Marwani, A. M. Asiri, M. M. Rahman, Synthesis and environmental applications of cellulose/ZrO_2 nanohybrid as a selective adsorbent for nickel ion, Compos. B: Eng. 50 (2013) 253–258.

[74] V. D. Dao, N. T. Q. Hoa, L. L. Larina, J. K. Lee, H. S. Choi, Graphene–platinum nanohybrid as a robust and low-cost counter electrode for dye-sensitized solar cells, Nanoscale. 5 (2013) 12237.

[75] C. H. Kim, B. H. Kim, Zinc oxide/activated carbon nanofiber composites for high-performance supercapacitor electrodes, J. Power Sourc. 274 (2015) 512–520.

[76] R. Wang, C. V. Reddy, A. Nagar, S. Basu, N. P. Shetti, B. Cheolho, J. Shim, R.R. Kakarla, 2D g-C_3N_4 nanosheets functionalized with nickel-doped ZrO_2 nanoparticles for synergistic photodegradation of toxic chemical pollutants, Chemosphere. 341 (2023) 139955.

[77] L. Feng, Q. Zhang, F. Ji, L. Jiang, C. Liu, Q. Shen, Q. Liu, Phosphate removal performances of layered double hydroxides (LDH) embedded polyvinyl alcohol/ lanthanum alginate hydrogels, J. Chem. Eng. 430 (2022) 132754–132754.

[78] M. Samadi, H. A. Shivaee, M. Zanetti, A. Pourjavadi, A. Moshfegh, Visible light photocatalytic activity of novel MWCNT-doped ZnO electrospun nanofibers, J. Mol. Catal. A Chem. 359 (2012) 42–48.

[79] Y. Haldorai, W. Voit, J. J. Shim, Nano ZnO@reduced graphene oxide composite for high performance supercapacitor: Green synthesis in supercritical fluid, Electrochimica Acta. 120 (2014) 65–72.

[80] C. V. Reddy, I. N. Reddy, B. Akkinepally, V. V. N. Harish, K. R. Reddy, S. Jaesool, Mn-doped ZrO_2 nanoparticles prepared by a template-free method for electrochemical energy storage and abatement of dye degradation, Ceram. Int. 45 (2019) 15298–15306.

[81] D. Pathania, A. Sharma, S. Kumar, A. K. Srivastava, A. Kumar, L. Singh, Bio-synthesized Cu–ZnO hetro-nanostructure for catalytic degradation of organophosphate chlorpyrifos under solar illumination, Chemosphere. 277 (2021) 130315.

[82] R. Nekooie, T. Shamspur, A. Mostafavi, Novel CuO/TiO_2/PANI nanocomposite: Preparation and photocatalytic investigation for chlorpyrifos degradation in water under visible light irradiation, J. Photochem. Photobiol. A: Chem. 407 (2021) 113038.

[83] C. Zhao, L. Xue, Y. Zhou, Y. Zhang, K. Huang, A microwave atmospheric plasma strategy for fast and efficient degradation of aqueous p-nitrophenol, J. Hazard. Mater. 409 (2020) 124473.

[84] K. Shang, W. Li, X. Wang, N. Lu, N. Jiang, J. Li, Y. Wu, Degradation of p-nitrophenol by DBD plasma/Fe^{2+}/persulfate oxidation process, Sep. Purif. Technol. 218 (2019) 106–112.

[85] Y. Gao, N. Gao, Y. Deng, J. Gu, Y. Gu, D. H. Zhang, Factors affecting sonolytic degradation of sulfamethazine in water, Ultrasound. Sonochem. 20 (2013) 1401–1407.

[86] A. Saljooqi, T. Shamspur, A. Mostafavi, Synthesis and photocatalytic activity of porous ZnO stabilized by TiO_2 and Fe_3O_4 nanoparticles: investigation of pesticide degradation reaction in water treatment, Environ. Sci. Pollut. Res. 28 (2020) 9146–9156.

[87] G. Shukla, M. Rani, U. Shanker, Enhanced solar-light driven photocatalytic potential of green synthesized Ag-doped cobalt oxide incorporated rGO nanocomposite: Mechanism insight and agricultural application, Inorg. Chem. Commun. 179 (2025) 114733.

[88] S. Sudan, J. Kaushal, Visible light promoted photocatalytic degradation of benzidine-based anionic diazo dye and its mechanistic studies using copper carbon dots incorporated biochar, J. Mol. Liq. 430 (2025) 127828.

[89] H. Dihingia, D. Tiwari, Green and facile synthesis of heterojunction nanocatalyst: Insights and mechanism of antibiotics removal, Sep. Purif. Technol. 306 (2022) 122641.

[90] A. S. Landge, A. S. Pathan, S. V. Bhosale, Y. V. Hase, T. R. Gaje, V. B. Autade, S. R. Jadkar, S.A. Arote, Studies on combustion synthesized ZnO and ZnO@ZrO_2 nanocomposites for dye contaminated wastewater treatment, Next Sustainability. 4 (2024) 100053.

[91] M. A. Wahba, S. M. Yakout, W. A. A. Mohamed, H. R. Galal, Remarkable photocatalytic activity of Zr doped ZnO and ZrO_2/ZnO nanocomposites: Structural, morphological and photoluminescence properties, Mater. Chem. Phys. 256 (2020) 123754.

[92] P. T. Lendeh, A. H. M. Sarrafi, A. Alihosseini, N. B. Laleh, Synthesis and characterisation ZnO/TiO_2 incorporated activated carbon as photocatalyst for gas refinery effluent treatment, Polyhedron. 247 (2023) 116715.

[93] P. He, J. Wu, X. Jiang, W. Pan, J. Ren, Effect of SO_3 on elemental mercury adsorption on a carbonaceous surface, Appl. Surf. Sci. 258 (2012) 8853–8860.

[94] C. A. Anyama, B. I. Ita, A. A. Ayi, H. Louis, E. E. D. Okon, J. O. Ogar, C. O. Oseghale, Experimental and density functional theory studies on a Zinc(II) coordination polymer constructed with 1,3,5-benzenetricarboxylic acid and the derived nanocomposites from activated carbon, ACS Omega. 6 (2021) 28967–28982.

[95] M. A. Daiem, A. A. Alotaibi, E. M. Alosime, B. Zaidi, N. Said, Structural-property relationship in activated carbon synthesized from rice straw for electronic application, Pol. J. Environ. Stud. 29 (2020) 3535–3547.

[96] E. E. Ekpenyong, H. Louis, C. A. Anyama, J. O. Ogar, P. M. Utsu, A. A. Ayi, Experimental and density functional theory studies on the adsorption behavior of

selected gas molecules on Mg(II) coordination polymer constructed with 1,3,5-benzenetricarboxylates, J. Mol. Struct. 1220 (2020) 128641–128641.

[97] M. Shah, M. Patel, M. Shah, M. Patel, M. Prajapati, Computational transformation in drug discovery: A comprehensive study on molecular docking and quantitative structure activity relationship (QSAR), Intelligent Pharmacy. 2 (2024) 589–595.

[98] M. Khatamian, Z. Alaji, Efficient adsorption-photodegradation of 4-nitrophenol in aqueous solution by using ZnO/HZSM-5 nanocomposites, Desalination. 286 (2011) 248–253.

[99] N. A. F. Al-Rawashdeh, O. Allabadi, M. T. Aljarrah, Photocatalytic activity of graphene oxide/zinc oxide nanocomposites with embedded metal nanoparticles for the degradation of organic dyes, ACS Omega. 5 (2020) 28046–28055.

[100] Z. Noroozi, H. Ali Rasekh, M. Jaafar Soltanianfard, Preparation and characterization of ZrO_2-Cr_2O_3 nanocomposite as a p-n heterojunction by a facile sol-gel method: A kinetic investigation on the removal of p-nitrophenol dye from aqueous media, Polyhedron. 168 (2019) 11–20.

[101] M. C. U. López, M.A.A. Lemus, M. C. Hidalgo, R.L. González, P.Q. Owen, S. O. Ruiz, S. A. U. López, J. Acosta, Synthesis and Characterization of ZnO-ZrO_2 Nanocomposites for Photocatalytic Degradation and Mineralization of Phenol, J. Nanomater. 2019 (2019) 1015876.

[102] S. Thakur, V. Mutreja, A. Tomar, S. Nainwal, K. Kaur, R. Kaur, Q. Li, F. S. Ataya, Phytochemical-assisted fabrication of ZrO_2/ZnO nanocomposites: A sustainable approach for efficient photodegradation of tetracycline hydrochloride, J. Mol. Struct. 1330 (2025) 141350.

[103] M. Farag, S. M. El-Dafrawy, S. M. Hassan, ZnO and C/ZnO catalysts synthesized via plant mediated extracts for photodegradation of crystal violet and methyl orange dyes, J. Inorg. Organomet. Polym. Mater. 34 (2023) 930–943.

[104] G. Zhang, J. Yang, Z. Huang, G. Pan, B. Xie, Z. Ni, S. Xia, Construction dual vacancies to regulate the energy band structure of $ZnIn_2S_4$ for enhanced visible light-driven photodegradation of 4-NP, J. Hazard. Mater. 441 (2022) 129916–129916.

CHAPTER 6

HARNESSING SYNERGISTIC EFFECTS IN POROUS CARBON/Co–ZnO HETEROJUNCTION FOR ENHANCED VISIBLE-LIGHT PHOTOCATALYTIC REMOVAL OF BISPHENOL A

This chapter deals with the hydrothermal synthesis of a CCAC/Co-ZnO nanocomposite, achieved by anchoring cobalt doped ZnO nanoparticles onto activated carbon obtained from Croton caudatus biomass. Characterization studies (XRD, SEM, EDS, HR-TEM, XPS, BET surface area, PL and UV-Vis DRS) validated the optimized nanostructure, and photocatalytic evaluations showed 99.67 % BPA breakdown within 60 min under visible light irradiation at optimal conditions. The reaction obeyed pseudo-first-order kinetics ($t_{1/2}$ of 12.6 min and k_{ap} of 0.055 min^{-1}), dominated by hydroxyl radicals (•OH), and photogenerated holes (h^+) as primary reactive oxygen species (ROS). LC-MS identified intermediates enabled proposal of a plausible BPA degradation pathway, while reusability studies showed 77.63 % efficiency over five cycles, confirming excellent photostability and reusability. Moreover, DFT calculations elucidated improved ROS generation mechanisms, providing mechanistic insights into the degradation processes. These findings provide a viable strategy for designing biomass-derived, visible-light-responsive photocatalysts for sustainable environmental remediation applications.

The text of this chapter has been published as:

S. Sharma, R. S. Umdor, I. T. Longchar, P. P. Gogoi, S. L. Ezung, D. Sinha, Harnessing synergistic effects in porous carbon/Co-ZnO heterojunction for enhanced visible-light photocatalytic removal of bisphenol A, RSC Adv., 16 (2026) 14107–14122.

6.1 Introduction

In recent times, the widespread occurrence of endocrine-disrupting chemicals (EDCs) in the aquatic environment has become a global concern. Bisphenol A (BPA) is one of the commonly detected EDCs in groundwater, surface water, industrial effluents, and landfill leachate. Its presence is primarily attributed to its wide-ranging application as a precursor in the production of epoxy resins, polycarbonate plastics and other polymers (e.g., rubber antioxidants, food packaging containers, dental sealants, PCV pipes, and other fine chemical materials) [1-3]. BPA is constituted of two phenolic rings joined by an acetone-derived bridge, from which its nomenclature is derived ('A' denotes acetone) [4]. According to reports, 27 million tonnes of polymers containing BPA are produced globally each year, with 60 % (approx.) of the world's BPA consumption comes from Asian countries [5,6]. Owing to its extensive use, BPA is ubiquitously released in the environment, posing adverse effects on both human health and the ecosystem. BPA also poses other health concerns, due to its potential carcinogenic and genotoxic implications [7,8]. Studies have indicated that exposure to BPA may promote the growth of cancer cells, especially in the tissues of the breast and prostate. Beyond this, BPA has been associated with various other health issues, including infertility, obesity, and developmental abnormalities [9-11]. The substantial toxicity of BPA is largely due to its unique physicochemical properties. These include high solubility in water (about 200 mg/L @ 25 °C), chemical stability, and resistance to biodegradation, allow to persist in aquatic environments even at very low concentrations (pM or nM) [12,13]. Consequently, several nations and regions, including the European Union, Sweden, Canada, United States, Norway, India and China, have banned the usage of BPA [14]. Similarly, the USEPA has also labelled this compound on the Drinking Water Contaminant Candidate List 5 [15]. As a result, there is an urgent need to develop highly efficient strategies for the BPA removal from aqueous media.

To address the growing concern pertaining emerging organic substances (e.g., BPA) in wastewater, several methods of treatment have been investigated, including chemical oxidation, biological treatment, adsorption, membrane separation, electro-Fenton processes and photocatalysis [16-18]. Among these, heterogeneous photocatalysis has emerged as a promising approach in advanced oxidation processes (AOPs) over other

conventional methods due to its mild operating conditions, eco-friendliness, reusability, long-term stability, high degradation efficiency, no secondary pollutants and wide applications [19,20]. In AOPs, the absorption of UV or visible radiation by a semiconductor material promotes an electron from the valence band (VB) to the conduction band (CB), leading to the generation of an electron-hole (e^-/h^+) pair. The photogenerated holes in the VB exhibit significant oxidative potential, enabling them to combine with water molecules or surface-bound hydroxyl groups to produce hydroxyl radicals (•OH), whilst the conduction band electrons can convert molecular oxygen to superoxide radicals ($•O_2^-$) [21-23]. These reactive oxygen species (ROS) initiate a series of redox reactions that lead to the degradation of organic pollutants, converting them into complete mineralized of byproducts such as carbon dioxide (CO_2) and water [24,25]. For instance, Rajeshwari et al. [26] developed a g-C_3N_4 quantum dot-modified α-MoO_3 nanohybrid and demonstrated its effectiveness in the visible-light irradiation for photocatalytic degradation of *p*-chlorophenol and rifampicin.

Numerous studies have reported the use of semiconductor photocatalysts such as ZnO, TiO_2, CdO, Fe_3O_4, CuO, and CdS for the effective degradation of organic pollutants [27-29]. Among them, ZnO has attracted considerable interest due to its excellent photochemical stability, high electron mobility (300 $cm^2/V·s$), non- toxicity, strong exciton binding energy (60 meV), favorable optical properties and cost-effectiveness [30]. Nevertheless, ZnO suffers from intrinsic limitations: a wide band gap (3.37 eV), low photon absorption, poor separation, rapid recombination of photogenerated electron-hole pairs, that restrict their catalytic activity under visible-light irradiation [31]. To overcome these challenges, extensive efforts have been focused on tuning the electronic and optical properties of ZnO through doping with transition metals (e.g., Co, Ni, Mn, Fe, Cu, etc.) [32,33]. The incorporation of these dopants introduces intermediate energy levels within the ZnO band structure, effectively narrowing the band gap and extending its light absorption into the visible range [34]. For example, Lu et al. (2011) synthesized Co-doped ZnO nanorods via a hydrothermal method and reported a 93 % degradation efficiency of 58 μM alizarin red dye within 60 min under visible-light irradiation [35]. Similarly, Ullah and coauthors observed enhanced discolouration of methylene blue using Mn-doped ZnO nanoparticles [36]. The

photocatalytic degradation of rhodamine B under visible light was significantly improved by Ni-doped ZnO nanorods, as studied by Zhao et al. [37]. Cobalt (Co) is widely recognized as a highly compatible dopant for ZnO, supported by the Lattice Compatibility Theory [38]. Its high electron-donating ability, resistance to photo-corrosion, strong surface adsorption, visible surface plasmon resonance, and excellent solubility within the ZnO lattice contribute to its efficacy as a dopant [39,40].

Another problem faced with ZnO nanoparticles is their vulnerability to photo-induced deterioration in aqueous conditions, as well as their tendency to aggregate, especially at higher concentrations, which complicates post-reaction separation and restricts their reusability [41,42]. One practical and innovative technique to overcome the limitations of conventional photocatalyst involves the use of biomass-derived carbonaceous materials to form heterojunction composites [43]. Carbon-based nanostructures offer numerous benefits, such as high porosity, tunable surface functions, large BET surface area, high stability and good recycling characteristics, making them appropriate as support material for photocatalysts. In addition, transforming biomass waste into activated carbon (AC) is considered an environmentally beneficial solution because it not only tackles solid waste management issues yet also lowers the cost of raw material procurement [44,45]. In this context, ZnO nanoparticle is immobilized on high-surface-area carbonaceous supports, which promote uniform dispersion of the photocatalyst, inhibit nanoparticle agglomeration, and enhance overall photocatalytic activity during adsorption-degradation pathways [46,47]. The superior performance of these heterogeneous photocatalyst is primarily attributed to the synergistic interactions formed between the porous carbon matrix and semiconductor interface. For instance, Faisal et al. [48] developed a novel biomass-derived activated carbon (AC)@ZnO/SnO_2 composite, which demonstrated outstanding visible-light-driven activity, achieving 94.6 % degradation of the antibiotic linezolid. In another study, Shanmugam et al. [49] successfully synthesised carbon aerogel-supported CA/ZnS-Ag composites using low-cost biomass precursors via hydrothermal process and reported 98.64 % degradation within 150 min. This integrated approach represents a promising and sustainable strategy for the removal of BPA from wastewater.

Despite these developments, there is still a significant gap in the development of visible-light-active photocatalysts that are designed to degrade BPA. Although ZnO-

based photocatalysts have been rigorously investigated for the degradation of organic contaminants, the integration of Co-doped ZnO with biomass derived AC for degradation of BPA under visible light illumination remains unexplored. Moreover, to the best of our knowledge, there has been no report of using *croton caudatus* biomass as a carbon precursor in photocatalytic applications.

Therefore, the present work aims to synthesize Co-doped ZnO photocatalyst immobilized on biomass derived AC (porous carbon) via hydrothermal synthesis route. The resultant heterojunction photocatalyst were systematically characterized and studied. The performance of CCAC/Co-ZnO nanocomposite was assessed under visible light irradiation for the degradation of BPA. Furthermore, multiple-cycle experiments were conducted to evaluate the stability and reusability of the photocatalyst. Radical scavenging assays were used to determine the primary reactive species involved in the degradation mechanism. Additionally, a plausible degradation pathway was postulated based on the identification of intermediate products obtained through liquid chromatography–mass spectrometry (LC-MS) analysis.

6.2 Experimental section

6.2.1 Materials

Cobalt nitrate hexahydrate ($Co(NO_3)_2 \cdot 6H_2O$, MW: 291.03 g/mol, ≥ 99.90 %), zinc oxide (ZnO, MW: 81.38 g/mol, ≥ 99 %), bisphenol A (BPA, MW: 228.29 g/mol, ≥ 99 %) were purchased from the Sigma Aldrich, India. Ethanol, HCL and NaOH were procured from SRL, India. The chemical structure and properties of BPA are shown in Table 6.1. The chemicals obtained were of analytical grade and used without further treatment. Double distilled water (DDW) from Milli-Q system (18.2 MΩ cm) was utilized throughout all testing experiments.

Table 6.1. Physicochemical properties of BPA.

Chemical structure	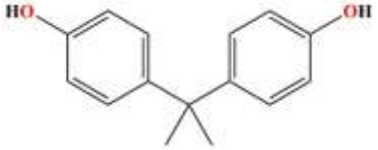
Chemical formula	$C_{15}H_{16}O_2$
Molecular weight (g/mol)	228.29 g/mol
Solubility in water (mg/L @ 25 °C)	300
Density at 25 °C	1.195
pK_a (@25°C)	9.6
λ_{max} (nm)	276

6.2.2 Preparation of porous carbon

The croton caudatus biomass collected from the University Campus (26°13′29.60″ N | 94°28′35.0″ E), was used as the primary raw material. The entire plant was employed to produce activated carbon. The collected biomass was cut into small fragments and thoroughly rinsed with DDW to eliminate surface contaminants and residual materials. The biomass was then oven-dried at 105 °C for 24 h to remove the moisture content. The processed biomass was subsequently used for the preparation of *Croton caudatus* activated carbon (CCAC). The overall yield of porous carbon obtained from the raw biomass was around 32.5 %. Details on the synthesis and characterisation of CCAC have been described in our previous paper [50].

6.2.3 Synthesis of CCAC/Co-ZnO nanocomposite

The CCAC/Co-ZnO nanocomposite was created via a hydrothermal approach. Initially, 0.15 g of ZnO nanoparticles were gradually added to 100 mL of cobalt nitrate solution (1 g) while continuously stirring for 30 min.

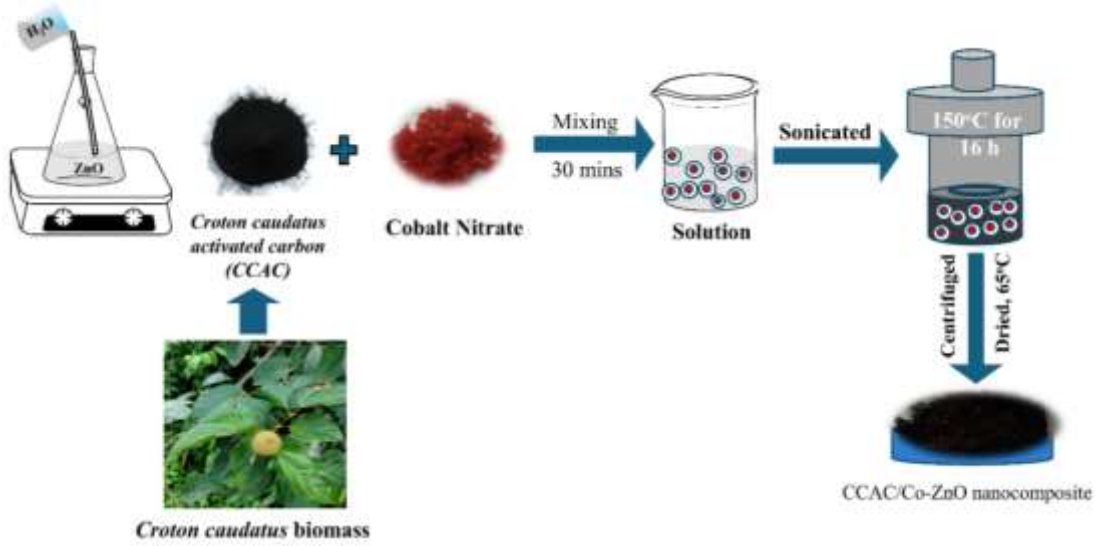

Figure 6.1. Scheme for preparation of the *Croton caudatus* activated carbon (CCAC)/Co-ZnO photocatalyst.

Subsequently, 0.3 g of synthesised CCAC was gently added to the resultant mixture, which was then ultrasonically dispersed for 1 hour to achieve uniform distribution. The resulting suspension was then transferred into a Teflon-lined autoclave and subjected to hydrothermal treatment at 150 °C for 16 hours. After completion, the product was thoroughly washed using centrifugation until a neutral pH was achieved

and then dried at 65 °C for 12 hours. The synthesised nanocomposite was further explored to assess BPA degradation. Figure 6.1 depicts a schematic illustration of the preparation procedure for the synthesized nanocomposite.

6.2.4 Characterization techniques

Several advanced characterisation techniques were used to analyse the CCAC/Co-ZnO nanocomposite. These include X-ray diffraction (XRD, PANalytical, Empyrean, CuKα radiation), Transmission electron microscopy (TEM, 2100F, JOEL), Scanning electron microscopy (SEM, JSM-6360, JEOL), accompanied by energy dispersive X-ray spectroscopy (EDX), X-ray photoelectron spectroscopy (XPS, M/s Physical Electronics, PHI 5000 versa probe III) Photoluminescence analysis (PL, Horiba Fluoromax4CP spectrofluorometer, 150 W Xenon Lamp), Diffuse reflection spectrophotometer (DRS, Shimadzu, and wavelength), BET surface area analyzer (Quantachrome AutosorbiQ Station 1 at 77 K), LC-MS spectrophotometer (INKAR, Expression-S), Total organic carbon, (TOC, Shimazu Model 5000A). The batch equilibration method was employed to determine the zero-point charge (pH_{zpc}) of the photocatalyst [43].

6.2.5 Photocatalytic degradation experiments

The photocatalytic degradation of BPA was carried out inside a photocatalytic reactor enclosed within a light-shielded black box with dimensions of 63 × 44 × 44 cm. In this experiment, the catalytic degradation of BPA was performed over a period of 60 min under visible light emitted from a 350 W high-pressure Hg lamp (wavelength 520 nm) positioned 10 cm above the reactor to illuminate the reaction mixture. Typically, 50 mL of BPA solution (20 mg/L) and required load of the photocatalyst were introduced and agitated for 30 min in the absence of light to attain adsorption-desorption equilibrium inside the reaction system. During the reaction, 3.5 mL of the solution was extracted every 10 min, and the concentration of the solution was determined at 276 nm using a UV-Vis spectroscopy analysis (Lambda-365). All tests were repeated three times and averages were reported to assure data quality. Equation (6.1) was used to calculate the degradation rate of BPA.

$$\text{Degradation rate (\%)} = (1 - C_t/C_0) \times 100 \quad (6.1)$$

where C_o and C_t are the concentrations (mg/L or ppm) of BPA before and after the photocatalytic process at varying irradiation intervals, respectively.

The schematic representation of the experimental setup used for the visible light-driven photocatalytic process is presented in in Chapter 2 (see Figure 2.2.).

6.3 Results and discussion

6.3.1 Characteristics of CCAC/Co-ZnO

X-ray diffraction (XRD) analysis was performed to examine the crystal lattice structure of the synthesized nanocomposite as shown in Figure 6.2a. The intensity peak at 2θ = 26.5° represents the (1 0 0) planes of hexagonal graphitised carbon (ICDD 08-0415) [51]. The diffraction peaks at 2θ values of 31.73° (100), 34.36° (002), 36.21° (101), 47.47° (102), 56.53° (110), 62.75° (103), 67.85° (112) and 68.99° (201) attribute to the hexagonal wurtzite crystal structure of ZnO (ICDD 80-0074) [52]. The observed diffraction peaks are in good agreement with previously reported literature [53,54]. Despite the incorporation of Co^{2+} ions into the Zn^{2+} sites within the ZnO lattice, no alteration in the crystalline structure of the ZnO was observed [55]. The Scherrer equation was used to calculate the average crystallite size (D) of the synthesised sample and is represented in Equation (6.2).

$$D = \frac{0.9\,\lambda}{\beta\,\mathrm{Cos}\,\theta} \tag{6.2}$$

where λ indicate the wavelength of X-ray radiation, θ is the glancing angle, and β is the full width at half-maximum (FWHM). Evidently, the D value for CCAC/Co-ZnO was determined to be 18.24 nm using the FWHM of its most strong diffraction peaks. The XRD pattern of pristine CCAC is provided in Fig. S2, suggesting the amorphous nature of CCAC.

FT-IR analysis indicated the existence of various surface functional groups on the CCAC/Co–ZnO nanocomposite as depicted in Figure 6.2b. The extensive absorption band centered at 3440–3444 cm^{-1} is indicative of O–H stretching vibrations from surface hydroxyl groups, physisorbed water, and oxygen-containing functional groups present in CCAC. The inclusion of Co–ZnO results in the further broadening and intensification of the O–H band, signifying stronger hydrogen bonding and improved surface hydroxylation in the composite. The peak at around 1632 cm^{-1} is attributed to

the H–O–H bending vibration of adsorbed water molecule [56]. The intensity variations within the 1500–1600 cm^{-1} range validate the interactions between the carbon matrix and metal oxides. Notably, the formation of new absorption bands in the 500–700 cm^{-1} range corresponds to Zn–O and Co–O stretching vibrations, offering the successful integration of Co–ZnO nanoparticles onto the CCAC surface [57,58].

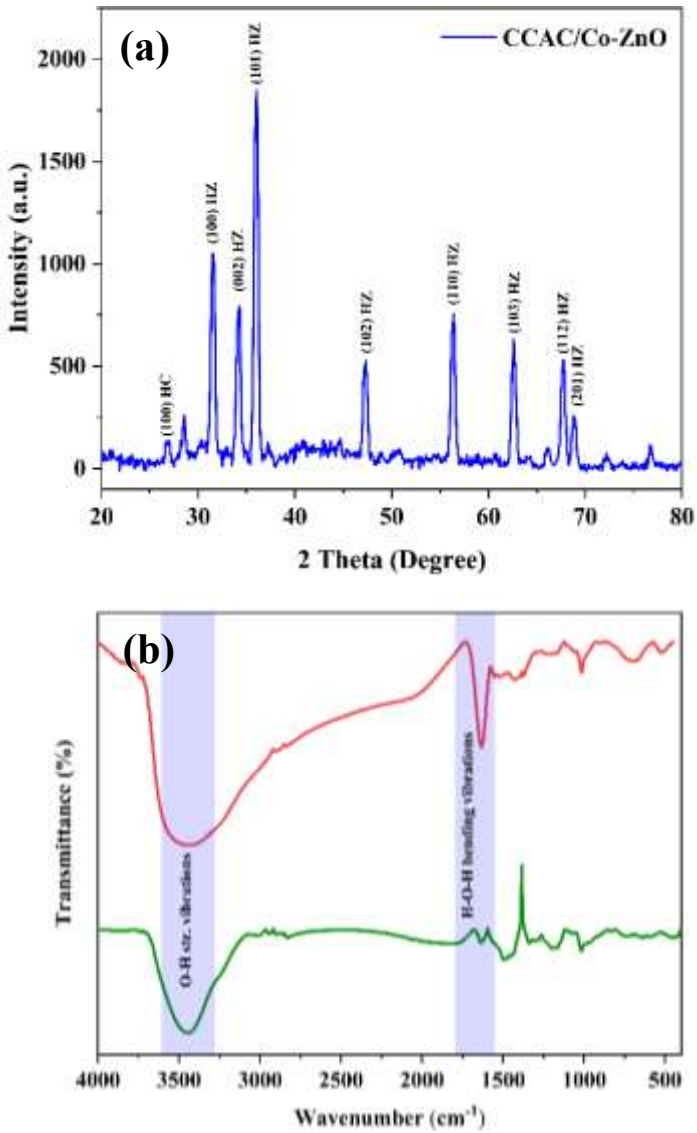

Figure 6.2. (a) XRD pattern, and (b) FT-IR spectra of synthesized nanomaterial.

The surface morphology, elemental distribution, and compositional properties of the synthesised CCAC/Co-ZnO composite were investigated using field emission scanning electron microscopy (FE-SEM) coupled with energy-dispersive X-ray spectroscopy (EDAX), as depicted in Figure 6.3a. The micrograph demonstrates that

Co-doped ZnO nanoparticles, exhibiting irregular morphologies, are uniformly dispersed across the carbon surface and form heterojunctions in close contact with the carbon material. In specific regions, particle agglomeration was observed, probably contribute to improved photocatalytic activity by increasing reactive surface sites and facilitating charge carrier transport [59]. The EDAX spectrum of the nanocomposite is displayed in Figure 6.3b.

The spectrum validates the presence of Zn, O, C, and Co, indicating that cobalt was successfully incorporated into the ZnO lattice and disseminated across the carbon surface. The spectrum shows no evidence of elemental impurities, further confirming the purity of the synthesized composite.

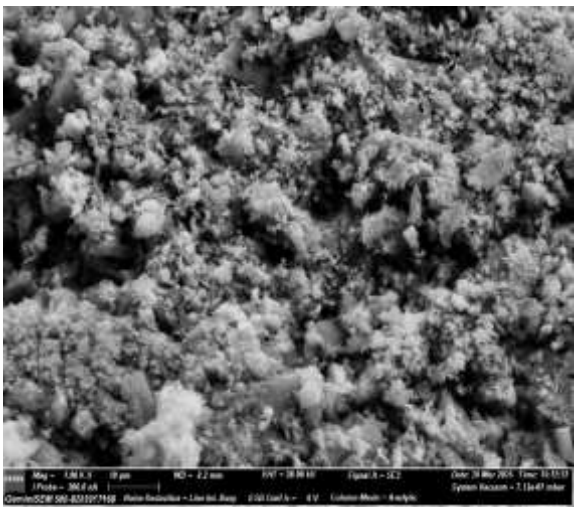

(a)

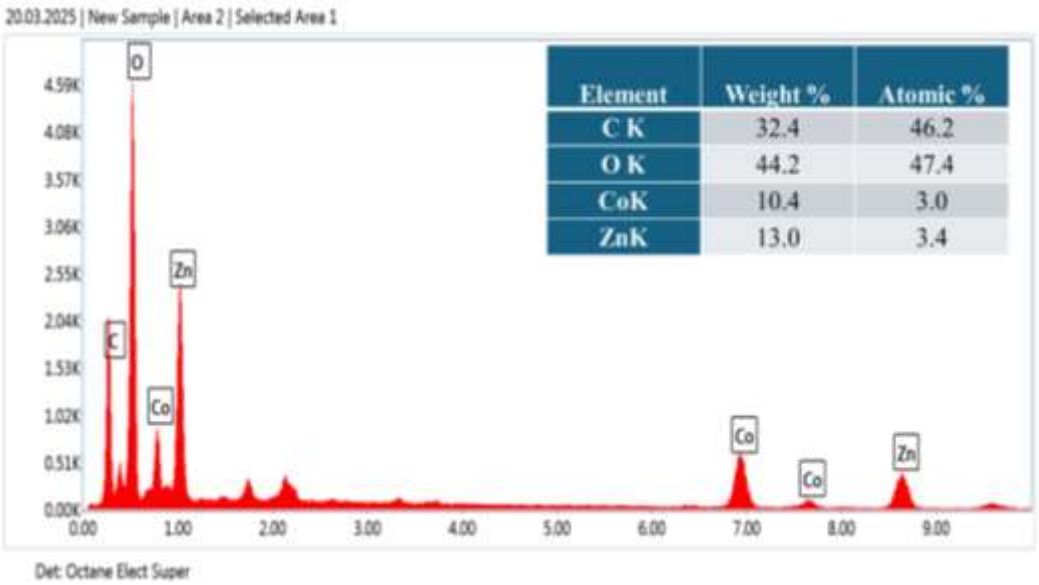

Element	Weight %	Atomic %
C K	32.4	46.2
O K	44.2	47.4
CoK	10.4	3.0
ZnK	13.0	3.4

(b)

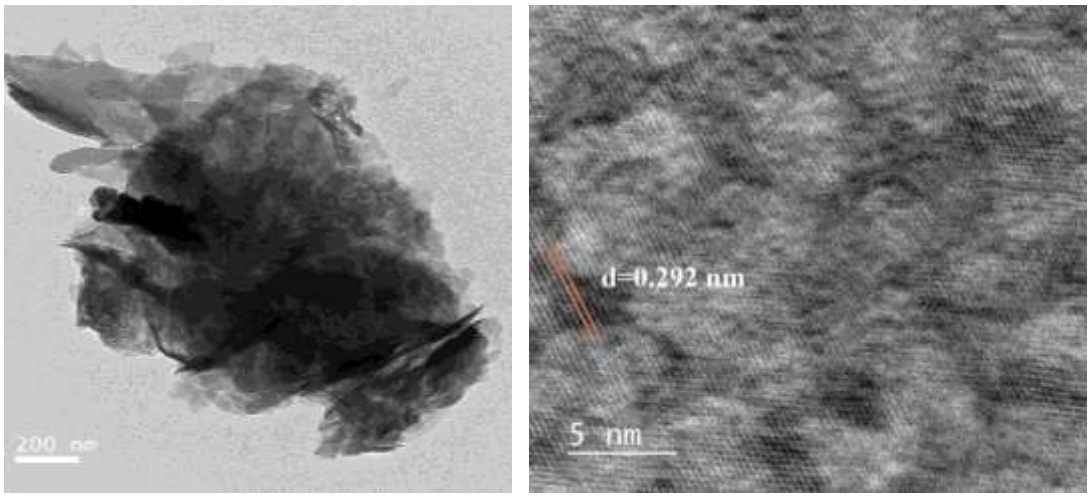

(c) **(d)**

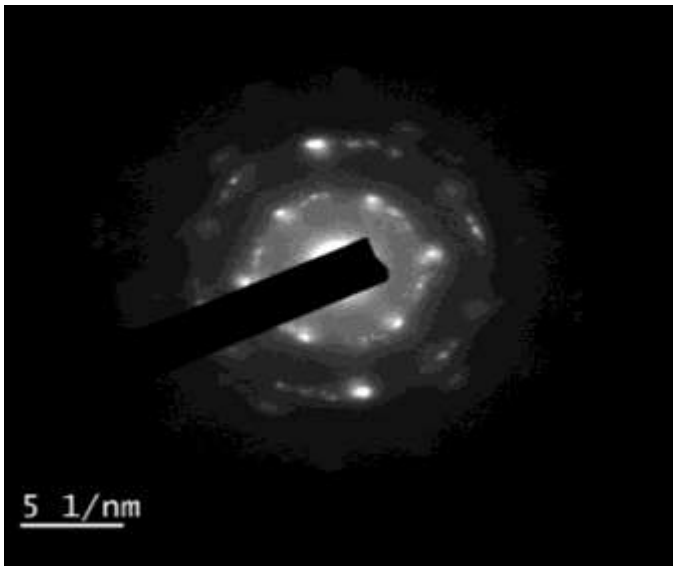

(e)

Figure 6.3. (a) SEM image, (b) EDX spectrum, (c) TEM image, (d) HRTEM image, and (e) SAED image of carbon/Co-ZnO.

The morphological features and average particle size of the CCAC/Co-doped ZnO nanoparticles were studied *via* transmission electron microscopy (TEM), as illustrated in Figure 6.3c. TEM analysis revealed that the produced nanoparticles were partly spherical, with an average diameter of 5.67 ± 2.5 nm. Notably, the particles demonstrated a tendency to agglomerate, a characteristic further substantiated by the SEM result, which reveal aggregated nanoparticle regions throughout the sample

surface. The interplanar spacing of the lattice fringes in the HR-TEM image (Figure 6.3d) is 0.292 nm, corresponding to the (100) crystal plane of ZnO. Furthermore, the selected area electron diffraction (SAED) pattern as shown in Figure 6.3e, revealed a polycrystalline material characterized by discrete diffraction spots, which may be attributed to the presence of ZnO particles embedded within the CCAC matrix [60]. The concentric rings of various crystallographic planes in the SAED patterns corresponded to the (002), (110), and (201) planes of ZnO, in good agreement with the XRD spectrum.

The optical band gap energy (E_g) of ZnO and CCAC/Co-ZnO nanoparticles are vital for selecting the appropriate light energy to eliminate organic contaminants from aquatic tributaries via photocatalysis [61]. UV-Vis diffuse reflectance spectroscopy (DRS) was applied to explore the light-harvesting properties of the synthesized photocatalysts as shown in Figure 6.4a. As can be observed from the figure that the absorption edge of CCAC/Co-ZnO is shifted into the visible spectrum in comparison to pure ZnO, signifying improved light-harvesting capacity. The red shift is ascribed to the inclusion of Co^{2+} ions, which introduce new energy levels within the band gap of ZnO and promote charge transfer processes, thereby improving photocatalytic activity.

The E_g values were determined using the Kubelka-Munk function and calculated from Tauc's plot, which is represented by the following expression:

$$(\alpha h\nu)^n = A\,(h\nu - E_g) \tag{6.3}$$

where α = optical absorption coefficient, $h\nu$ = photon energy, K = the proportionality constant, and n = the type of transition.

The E_g values of the synthesized materials were determined from the Tauc plots $(\alpha h\nu)^2$ vs $h\nu$ (Figure 6.4b). The pristine ZnO exhibited an E_g of 3.3 eV, while the Co–ZnO/carbon composite showed a substantial reduction in band gap energy of 2.1 eV. The introduction of Co ions effectively reduces the band gap, resulting in a red shift in light absorption from the ultraviolet to the visible spectrum. The presence of mesoporous carbon not only increases the specific surface area but also improves light absorption efficiency, expedites the generation of active sites and charge carriers. These synergistic effects significantly develop the photocatalytic breakdown of BPA

driven by visible light. In addition, the valence band (E_{VB}) and conduction band (E_{CB}) potentials of the ZnO nanoparticles were theoretically determined using the Mulliken electronegativity approach in combination with the calculated band gap energy [62,63].

A photoluminescence (PL) spectral analysis was performed at an excitation wavelength of 377 nm to obtain a more profound understanding of the behaviour of charge carriers [64]. Generally, a decline in PL intensity suggests a reduced recombination rate of photogenerated electron–hole pairs.

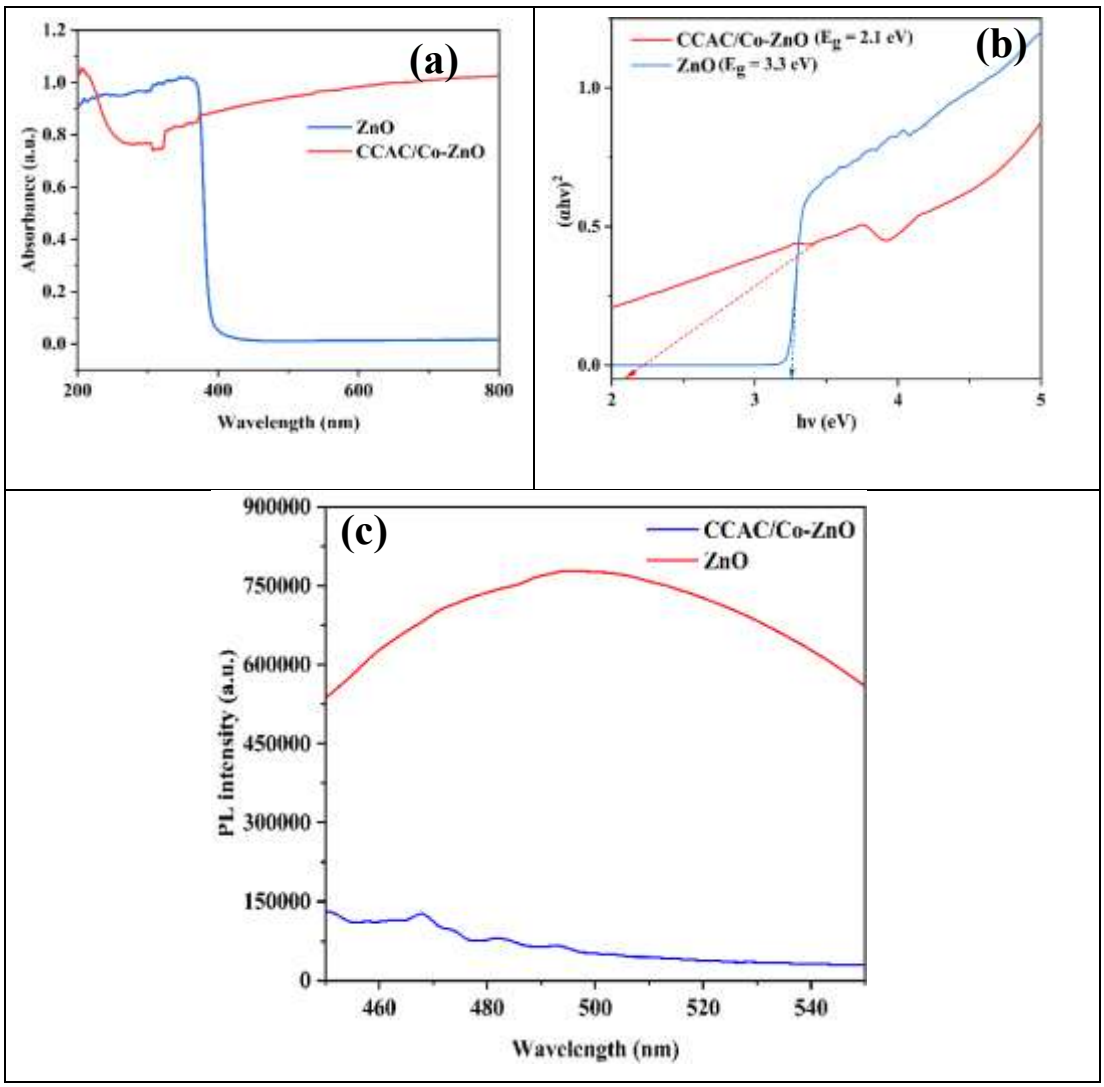

Figure 6.4. (a) UV-DRS spectra, (b) Tauc's plot, and (c) PL spectra of ZnO and CCAC/Co-ZnO photocatalyst.

The PL spectra (Figure 6.4c) exhibit a significant drop in intensity for the CCAC/Co-ZnO composite in comparison to pure ZnO, suggesting a substantial decrease in the

recombination rate of photoexcited e^-/h^+ pairs. This implies that the composite structure significantly improves the separation of charge carriers, thereby increasing the availability of reactive species for photocatalytic processes. The construction of a heterojunction between the porous carbon and Co-ZnO is responsible for the improved performance, as it facilitates efficient charge transfer and prevents recombination [65]. This outcome demonstrates that the synthesised nanocomposite possesses enhanced photocatalytic efficiency relative to pure ZnO.

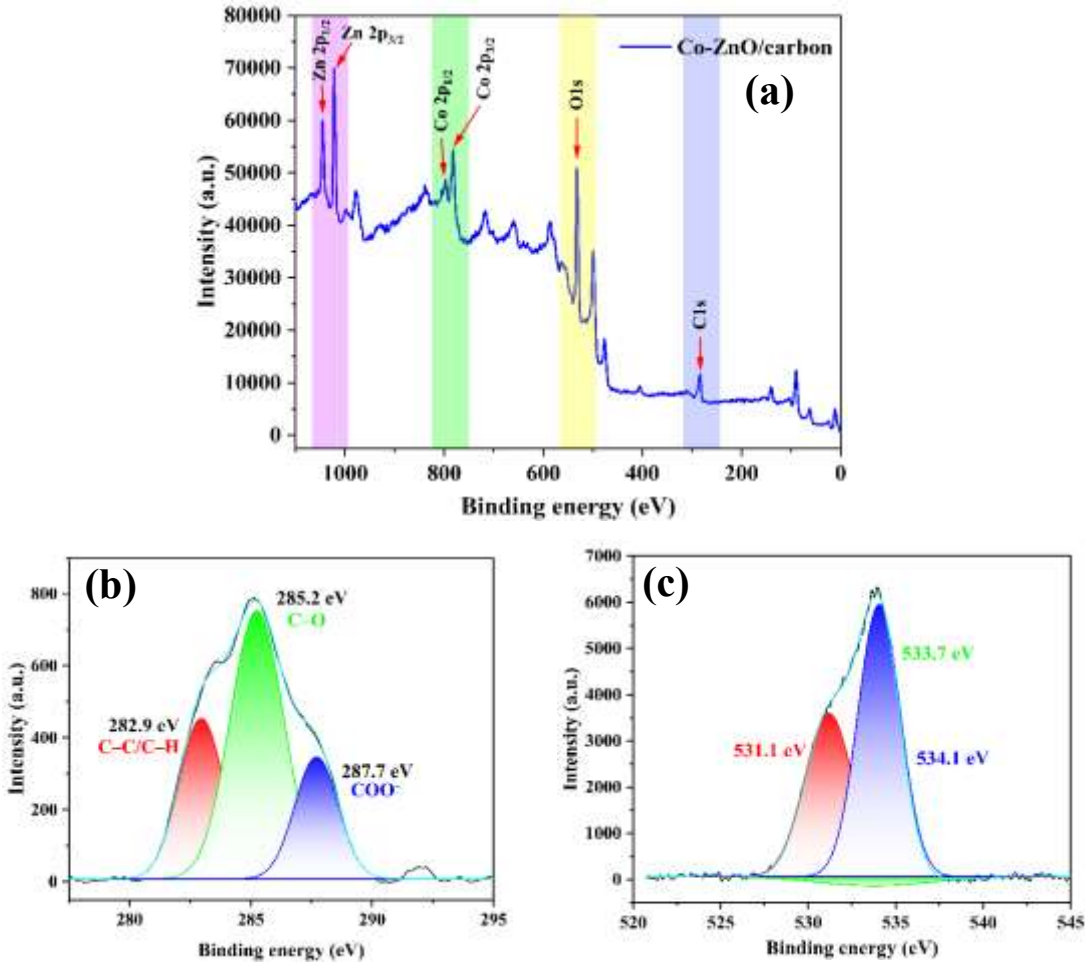

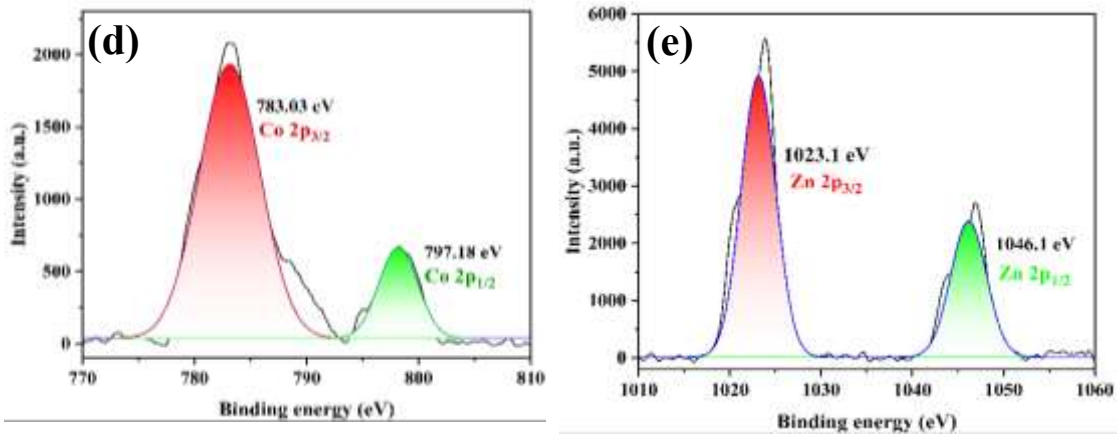

Figure 6.5. XPS spectra of CCAC/Co-ZnO nanocomposite: (a) Survey scan, (b) C1s (c) O1s, (d) Co 2p, and (e) Zn 2p.

X-ray photoelectron spectroscopy (XPS) investigation was conducted to examine the composition and elemental state of the CCAC/Co-ZnO nanocomposite. The resulting spectra are shown in Figure 6.5a-e. The wide spectrum indicated the coexistence of Zn, Co, O and C elements in the nanoparticles. The deconvoluted C 1s XPS spectrum reveals three distinct peaks at 282.9, 285.2 and 287.7 eV, corresponding to C–C/C–H bonds (graphitic carbon from CCAC), C–O groups (hydroxyl or epoxy), and COO^- species (carboxylate groups), respectively. The peaks corroborate the existence of several oxygen-containing functional groups on the surface of the nanocomposite. The O 1s spectrum showed binding energies at 529.9 eV, 531.4 eV, and 532.9 eV, indicating oxygen vacancies, oxygen atomic orientations, and chemisorbed O_2^- species, respectively in the ZnO lattice. The two peaks observed at binding energies of 797.2 eV and 783 eV, representing Co $2p_{1/2}$ and Co $2p_{3/2}$, respectively, confirming the presence of Co^{2+} ions [66]. The high-resolution XPS spectrum of Zn 2p indicates two distinct peaks: one at 1022.7 eV for Zn $2p_{3/2}$ and another at 1045.8 eV for Zn $2p_{1/2}$, signifying the presence of Zn^{2+} oxidation state in ZnO particles [67].

The surface area and pore structure of the synthesized photocatalyst were performed using the Brunauer–Emmett–Teller (BET) method. According to the findings, the porous carbon (CCAC) demonstrates a greater specific surface area of 846.29 m^2/g [50], whereas the Co-ZnO/carbon nanocomposite has a reduced surface area of 367.755 m^2/g. This reduction is most likely owing to the integration of Co and ZnO

nanoparticles, which may partially block the pores of the carbon surface, implying that these particles occupy a large percentage of the porous material.

The CCAC/Co-ZnO composite has a total pore volume of 0.085 cm^3/g and an average pore diameter of 3.627 nm, indicating a type IV isotherm, which corresponds to mesoporous materials as classified by IUPAC. The existence of such mesoporosity, along with a relatively large surface area, is expected to improve photocatalytic efficiency by increasing active sites and aiding reactant diffusion.

6.3.2 Photocatalytic degradation of BPA

The photocatalytic activity of pure ZnO, Co-ZnO and CCAC/Co-ZnO under visible light was evaluated using BPA (20 mg/L) as the target pollutant. Figure 6.6 illustrates that the degradation efficiency of BPA increased with irradiation time, which is due to improved charge separation on the catalyst surface [68].

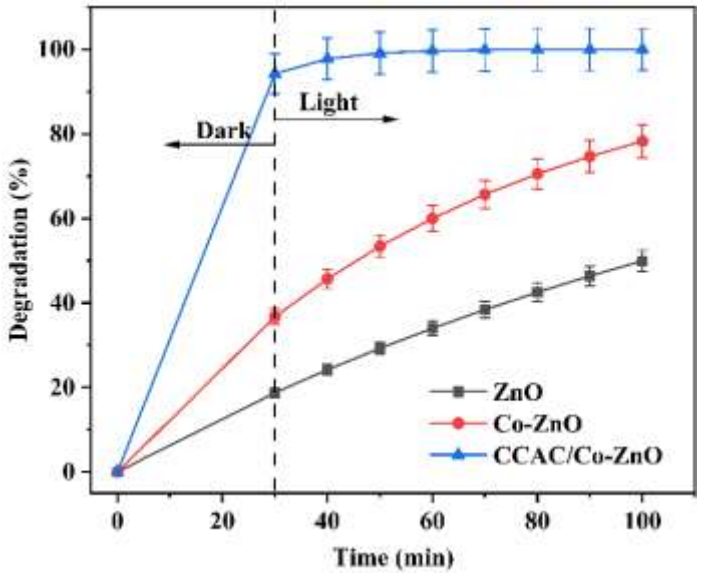

Figure 6.6. Degradation of bisphenol A (BPA) using different catalyst.

The CCAC/Co-ZnO photocatalyst showed the best photocatalytic performance, removing 99.67 % of BPA after 60 min. In comparison, the Co-ZnO composite exhibited a degrading efficiency of 60 %, but pristine ZnO attained just 34 % under identical conditions.

To further elucidate the individual contributions of adsorption and photocatalysis to BPA removal, control experiments were conducted using pure CCAC and a photocatalytic blank (without catalyst) under identical experimental conditions. The

blank experiment showed negligible BPA degradation, indicating that direct photolysis under visible light was insignificant. In contrast, pure CCAC exhibited moderate BPA removal due to its adsorption capacity, which can be attributed to the porous structure and abundant surface functional groups of the AC (Fig. S3). However, the removal efficiency obtained with CCAC alone was significantly lower than that of the CCAC/Co-ZnO nanocomposite, confirming that adsorption alone cannot account for the high BPA degradation efficiency observed.

The enhanced photocatalytic performance of the CCAC/Co-ZnO nanocomposite can be attributed to the effective suppression of charge carrier recombination and the strong light absorption capability of the material in the visible region [69]. These results demonstrate that the prepared material has the highest photocatalytic activity of BPA.

6.3.3 Influence of reaction conditions

To prevent using photocatalysts excessively in photocatalytic experiments, the required amount of catalyst needs to be adjusted. The effect of CCAC/Co-ZnO dosage on the photocatalytic degradation of BPA under visible light exposure was performed by varying the catalyst concentration from 0.05 g/L to 0.25 g/L as shown in Figure 6.7a. At an optimal catalyst loading of 0.1 g/L, the degradation efficacy of BPA was observed to increase as the catalyst dosage was increased, resulting in a maximum of 99.7 % degradation within 60 min. This implies that the used catalyst was effectively activated by visible light irradiation, resulting in the indirect formation of reactive species and the increased generation of photoinduced electron–hole (e^-/h^+) pairs. However, increasing the catalyst amount beyond 0.1 g/L range resulted in a decrease in degradation performance. The decrease in removal effectiveness seen with increasing catalyst dosages could be explained by the fact that the photocatalyst is not effectively activated due to the increased light dispersion as well as reduced light penetration [70]. Additionally, an increase in catalyst dosage leads to an increase in particle–particle interactions (agglomeration), which subsequently diminishes the effective surface area available for pollutant adsorption and light absorption. As a result, the photodegradation rate drops as the catalyst concentration rises. Similar observations have been reported in previous studies [71,72].

The effect of initial BPA concentration on photocatalytic degradation was investigated by increasing BPA levels from 10 to 50 ppm while holding other parameters constant (solution pH at 6, catalyst amount at 0.1 g/L). As shown in Figure 6.7b, increasing the initial BPA concentration led to a decrease in degradation efficiency from 98 % to 72.4 %. This reduction could be ascribed to the increased amount of pollutant molecules adsorbed onto the catalyst surface at high concentrations, resulting in surface saturation. As a result, photon penetration is limited, preventing effective light-catalyst interaction. These factors combine to reduce the generation of excitons and hydroxyl radicals, resulting in a decrease in photocatalytic activity at higher concentrations. Prior studies have revealed comparable findings found that increasing the initial concentration of BPA considerably lowers its degradation efficiency, corroborating the observed pattern [73].

The pH significantly influences photocatalytic processes by affecting the surface charge characteristics of the semiconductor material. To evaluate the effect of pH on BPA degradation, experiments were conducted by varying the solution pH from 2 to 12, while maintaining a constant catalyst dosage of 0.1 g/L and an initial BPA concentration of 20 ppm. The pH of the reaction mixture was adjusted using 0.1 M NaOH and HCl solutions. As shown in Figure 6.7c, the photodegradation efficiency of BPA increases with increasing pH from 2.0 to 6.0, however decreases under alkaline circumstances after 60 min of visible light exposure. The pH range between the composite's point of zero charge (6.7) (Figure 6.7d) and the pK_a of BPA (9.6) is crucial in determining photocatalytic behaviour, as it significantly affects the catalyst's surface charge and the ionic state of the pollutant, thereby influencing adsorption and degradation efficiency. Under weak acidic conditions (pH < 6.7), the catalyst surface becomes positively charged, enhancing the adsorption of negatively charged BPA species and potentially increasing photocatalytic efficiency. Conversely, at pH levels exceeding 10, both the catalyst surface and the BPA molecules are negatively charged, which may cause electrostatic repulsion, limiting adsorption and consequently lowering degrading performance. Moreover, pH can influence the generation and stability of ROS, which serve as vital intermediates in the degradation pathway.

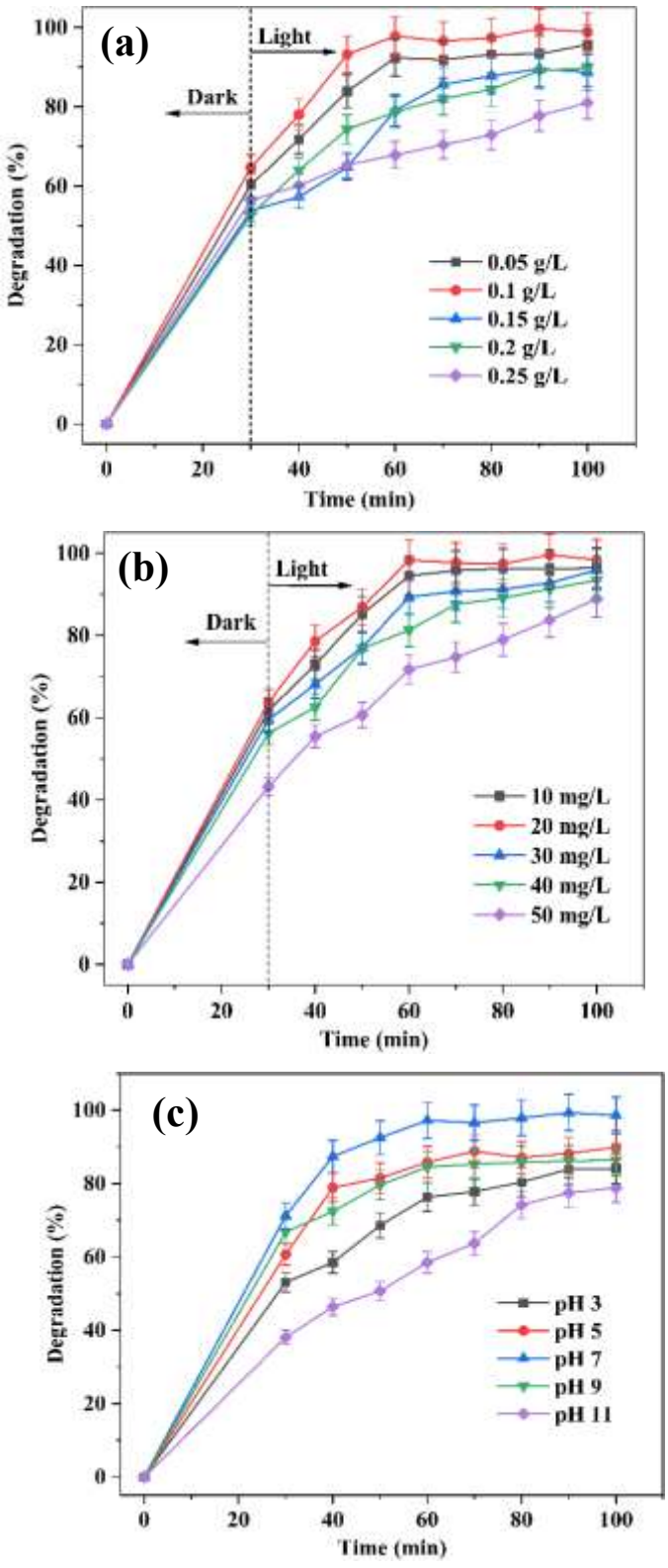
(a)
Light
Dark
Degradation (%)
Time (min)
0.05 g/L
0.1 g/L
0.15 g/L
0.2 g/L
0.25 g/L
(b)
Light
Dark
Degradation (%)
Time (min)
10 mg/L
20 mg/L
30 mg/L
40 mg/L
50 mg/L
(c)
Degradation (%)
Time (min)
pH 3
pH 5
pH 7
pH 9
pH 11

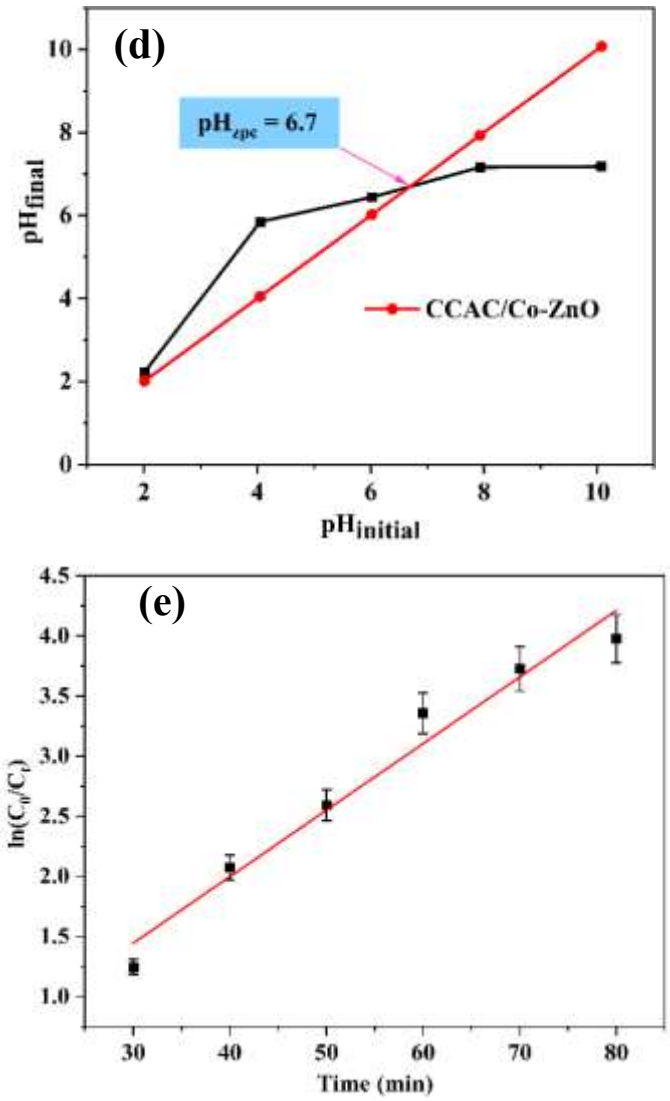

Figure 6.7. Effect of (a) Catalyst amount, (b) BPA concentration, (c) pH, (d) Zero-point charge, and (e) Kinetic studies.

Optimal pH conditions promote the production of hydroxyl radicals and other oxidative species, facilitating the breakdown of BPA [74].

The degradation kinetics of BPA can be explained using a pseudo-first order (PFO) reaction model based on the Langmuir-Hinshelwood (L-H) kinetic framework [75]. This model is mathematically represented as follows:

$$\ln\left(\frac{C_0}{C_t}\right) = k_{ap}t \tag{6.4}$$

$$t_{1/2} = \frac{ln\,2}{k_{ap}} \tag{6.5}$$

where C_0 = initial BPA concentration, C_t = concentration at time t, $t_{1/2}$ = the half-life period, and K_{ap} is the apparent reaction rate constant, respectively.

Figure 6.7e presents the graph of $\ln(C_0/C_t)$ against reaction time, indicating the kinetic characteristics of BPA photodegradation. The experimental findings provide a strong linear correlation ($R^2 > 0.969$), validating that the reaction adheres to PFO kinetics. The slope of the fitted line yielded an apparent rate constant (k_{ap}) of 0.055 min^{-1}, which corresponds to a half-life ($t_{1/2}$) of 12.6 min. These kinetic parameters demonstrate that the synthesised catalyst promotes a reasonably fast degradation rate under visible-light irradiation.

6.3.4 Recyclability and photostability of nanocomposite

The reusability of a photocatalyst is a vital consideration for its sustained implementation in large-scale processes. To evaluate the reusability of the CCAC/Co-ZnO photocatalyst, its degradation efficacy for BPA was tested across five successive cycles (Figure 6.8a). The synthesized catalyst demonstrated excellent performance, attaining 97.4 % degradation of BPA during the initial cycle.

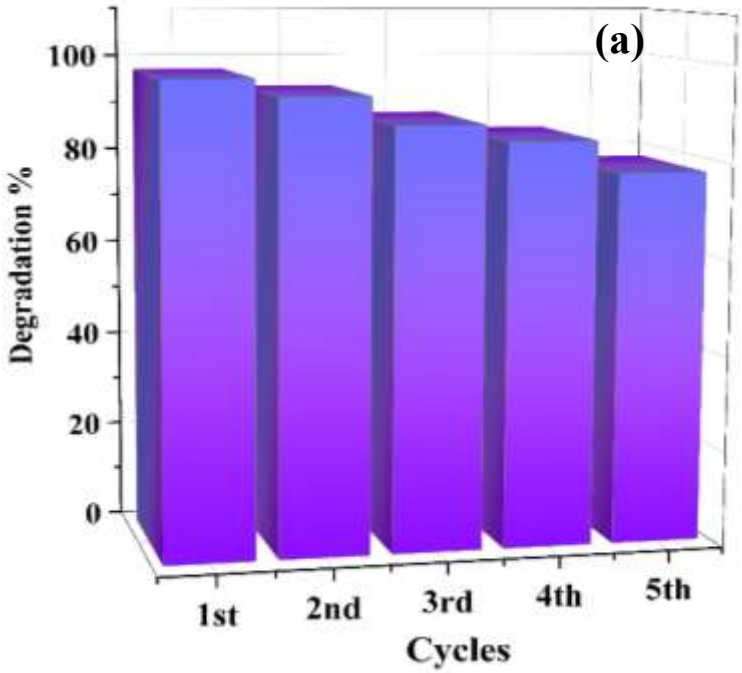

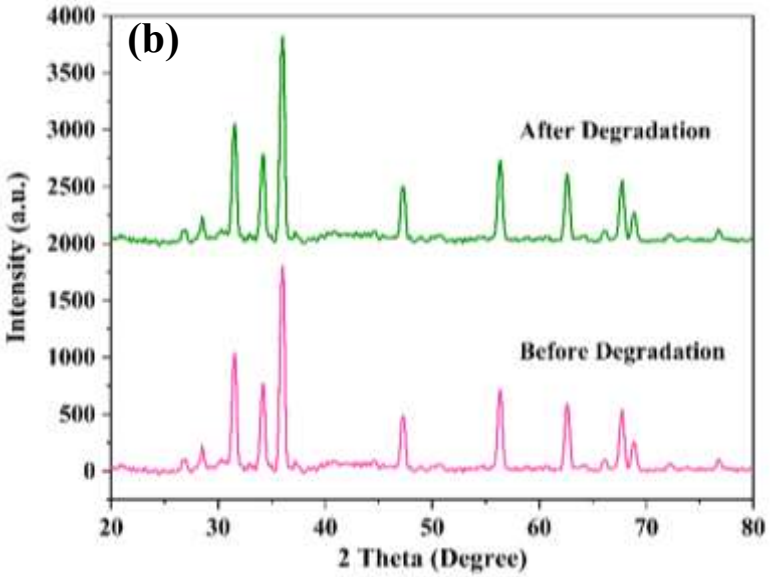

Figure 6.8. (a) Degradation % of nanocomposite upto five cycles, and (b) XRD spectra of nanocomposite (before and after degradation).

Subsequently, the catalytic efficiency exhibited a gradual decrease, attaining 84.38 % by the fourth cycle. Although the reduction is slight, it highlights the necessity for further research to elucidate the underlying mechanisms responsible for the loss of activity. The slight decline in photocatalytic efficiency observed over successive cycles may be attributed to various factors: (a) accumulation of BPA degradation intermediates on the catalyst surface and the agglomeration of nanoparticles, and (b) the continual loss of nanocomposite material during the recovery and reuse procedures [76]. These factors collectively impede visible-light irradiation and diminish the quantity of active sites available for photocatalysis. Notably, after multiple cycles, the nanocomposite exhibited a degradation efficiency of around 77.63 % in the fifth cycle, underscoring its sustained catalytic activity. Furthermore, the photostability of the CCAC/Co-ZnO nanocomposite was assessed using XRD analysis of the material collected after five reuse cycles. The resulting spectrum was compared to that of the unmodified nanocomposite (Figure 6.8b).

The resulting spectrum was compared to that of the unmodified nanocomposite (Figure 6.8b). The examination of XRD peaks prior to and following BPA degradation indicated no significant changes in the characteristic peaks. This finding indicates that the CCAC/Co-ZnO nanocomposite preserves its structural integrity throughout the

photocatalytic process, demonstrating adequate stability. The lack of substantial structural alterations suggests that the nanocomposite maintains its effectiveness and stability after numerous breakdown processes.

6.3.5. Real wastewater applications

To evaluate the practical applicability of the catalyst (CCAC/Co-ZnO)) in real water systems, two representative water matrices, including DDW and real wastewater source, were employed for the degradation experiments. Wastewater samples were collected from Mokokchung district, Nagaland, India and stored in glass containers. Since the native concentration of BPA was undetectable, the samples were spiked with 20 ppm of BPA to conduct degradation experiments. The sampling location and water quality analysis procedures are provided in Chapter 5 (Figure 5.10 and Table 5.2). The physicochemical characteristics of the wastewater included a pH of 6.52, total dissolved solids (TDS) of 19 ppm, electrical conductivity (EC) of 39 µS/cm, total hardness (TH) of 84 ppm, and biological oxygen demand (BOD) of 3.3 ppm. Inorganic analysis indicated the presence of sulfate (SO_4^{2-}, 20 ppm), phosphate (PO_4^{3-}, 0.2 ppm), calcium (Ca^{2+}, 4 ppm), magnesium (Mg^{2+}, 48.79 ppm), chloride (Cl^-, 4.26 ppm), and alkalinity of 4 ppm.

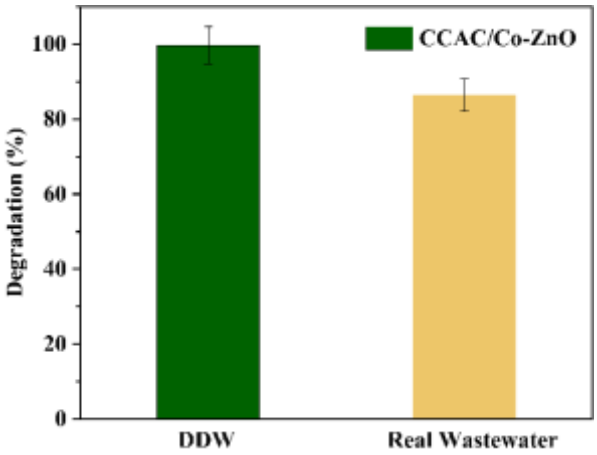

Figure 6.9. Degradation of BPA in the real wastewater environment.

Photocatalytic experiments performed under optimized conditions (catalyst dose: 0.1 g/L, pH: 7.0, reaction time: 60 min) demonstrated that the CCAC/Co-ZnO nanocomposite exhibited significant photocatalytic activity, achieving 86.42 % degradation of BPA in real wastewater, compared to 99.67 % in DDW (Figure 6.9).

The comparatively lower efficiency observed in real wastewater can be attributed to the complex water matrix containing coexisting inorganic ions. In particular, the relatively high concentration of Mg^{2+} may promote catalyst aggregation and surface passivation, thereby reducing the number of available active sites. Additionally, the presence of SO_4^{2-} and Cl^- ions may act as scavengers of hydroxyl radicals (•OH), which can hinder the oxidative degradation process.

6.3.6 Role of scavengers

To understand the mechanism of BPA photodegradation, it is imperative to explore the role of ROS and identify the specific reactive radicals involved in the process. The reactive species responsible for BPA degradation were identified through a series of diagnostic analyses using the Co-ZnO/carbon composite.

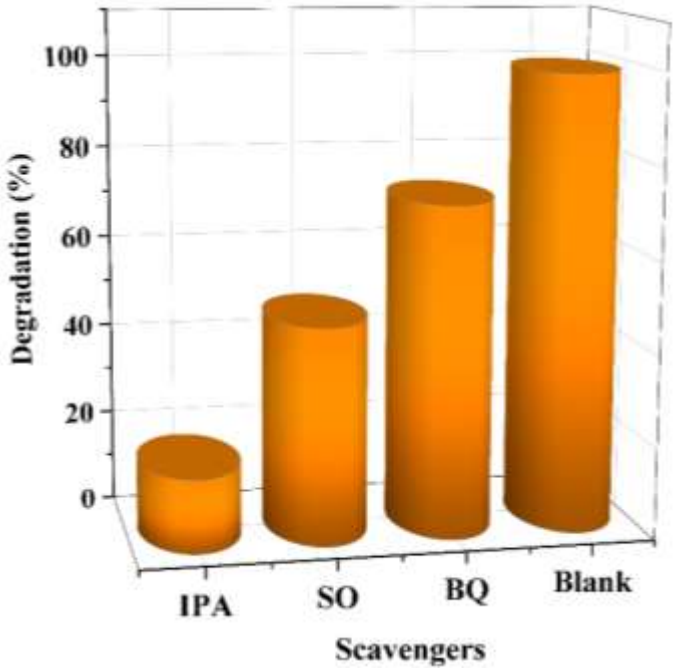

Figure 6.10. Effect of different radical scavengers for BPA degradation.

The experiments were conducted in the presence of isopropanol (IPA, •OH scavenger), benzoquinone (BQ, $•O_2^-$ inhibitor) and sodium oxalate (SO, h^+ scavenger) respectively. The degradation efficiency of BPA was substantially reduced by the addition of these scavengers compared to the blank photocatalyst. The photodegradation efficiency of BPA declined from 99.7 % to 72 %, 47 %, and 16 % upon the addition of BQ, SO and IPA respectively (Figure 6.10). Scavengers were

effective in the following order: IPA >SO > BQ. This investigation found that all major reactive species, including hydroxyl radicals (•OH), photogenerated holes (h^+) and superoxide radicals ($•O_2^-$) contributed to the photocatalytic destruction of BPA.

6.3.7 Mineralization

Total organic carbon analysis was conducted at different concentrations (20–50 mg/L) to ascertain the complete mineralization of BPA using a photocatalyst, while maintaining other parameters constant. Figure 6.11 illustrates that 81.02 % of the BPA achieved effective mineralization following a 60 min reaction period for 20 mg/L concentration. The reduction in TOC signifies the oxidation and destruction of the organic contaminant into less harmful substances. Nevertheless, the mineralization efficiency diminished to 54.4 % upon elevating the initial BPA concentration to 50 mg/L, suggesting that increased contaminant levels may impede the process, possibly as a result of inadequate ROS [77]. The above observation is supported by the LC-MS approach, as explained in the following sections.

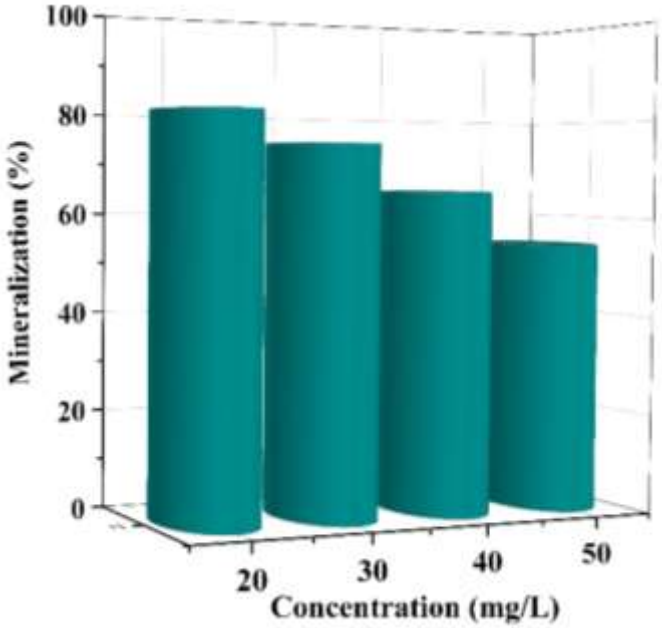

Figure 6.11. Mineralization (%) of BPA at various concentration.

6.3.8 LC-MS analysis

LC-MS analysis was conducted to investigate the intermediate compounds produced during the photocatalytic breakdown of BPA. Figure 6.12 and Table 6.2 outline the spectrum fragmentation peaks, and the corresponding intermediates of BPA identified

after 60 min of visible light exposure. A comprehensive photocatalytic degradation pathway was proposed based on these insights, as illustrated in Scheme 6.1.

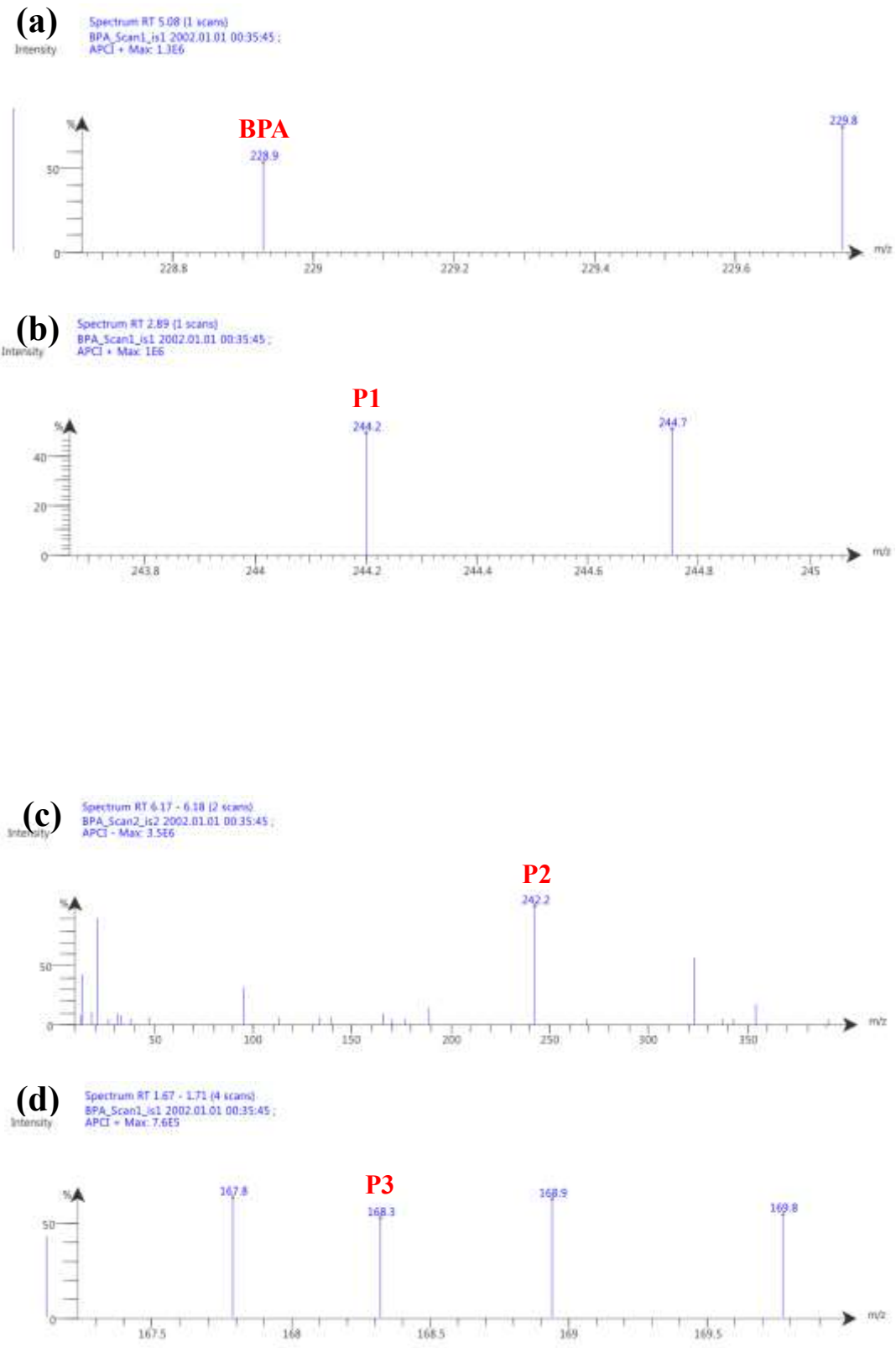

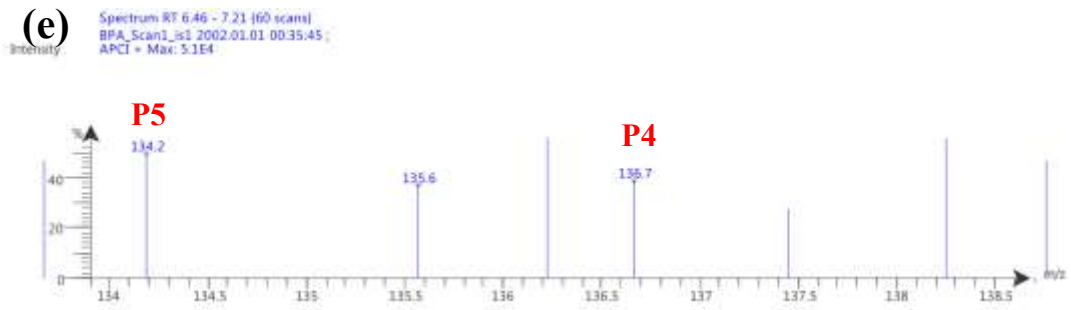
(e)
Spectrum RT 6.46 - 7.21 (60 scans)
BPA_Scan1_is1 2002.01.01 00:35:45 ;
APCI + Max: 5.1E4
P5
134.2
135.6
P4
136.7
m/z

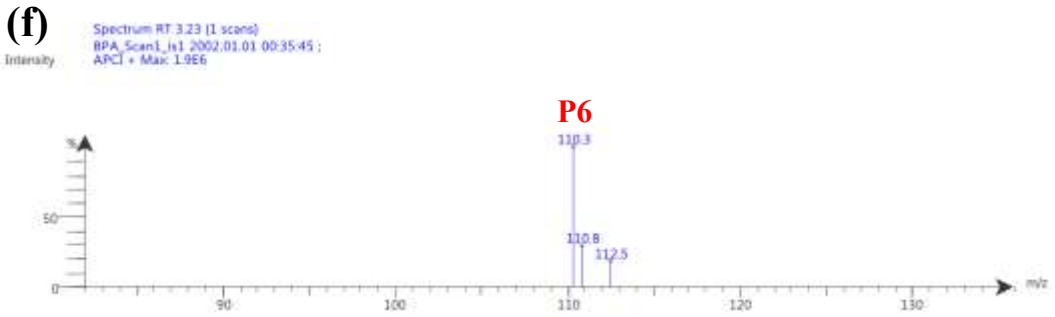
(f)
Spectrum RT 3.23 (1 scans)
BPA_Scan1_is1 2002.01.01 00:35:45 ;
APCI + Max: 1.9E6
P6
110.3
110.8
112.5
m/z

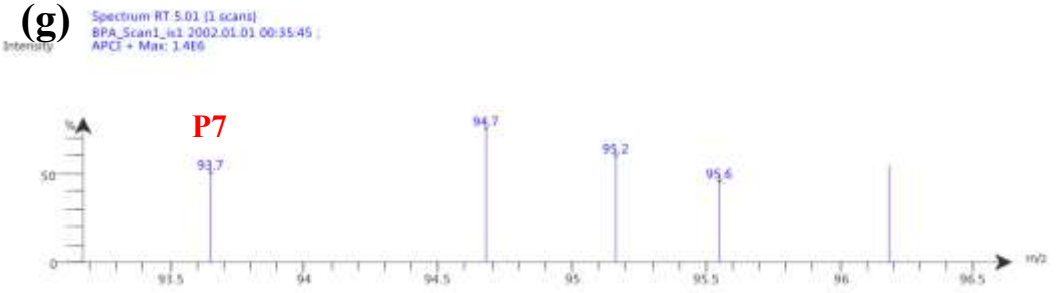
(g)
Spectrum RT 5.01 (1 scans)
BPA_Scan1_is1 2002.01.01 00:35:45 ;
APCI + Max: 1.4E6
P7
93.7
94.7
95.2
95.6
m/z

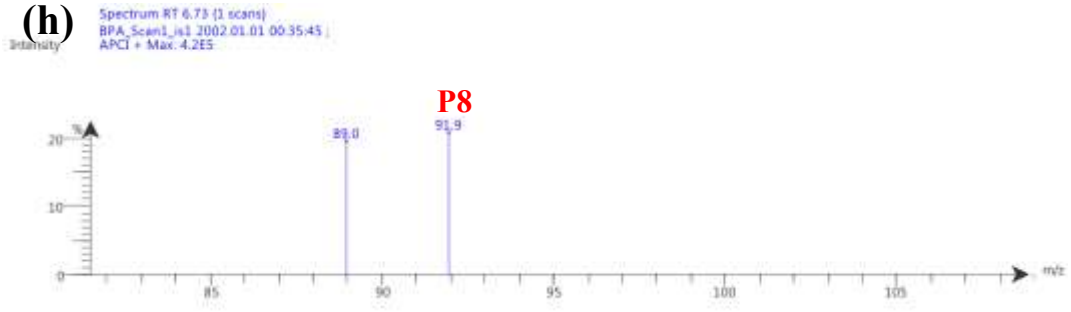
(h)
Spectrum RT 6.73 (1 scans)
BPA_Scan1_is1 2002.01.01 00:35:45 ;
APCI + Max: 4.2E5
P8
89.0
91.9
m/z

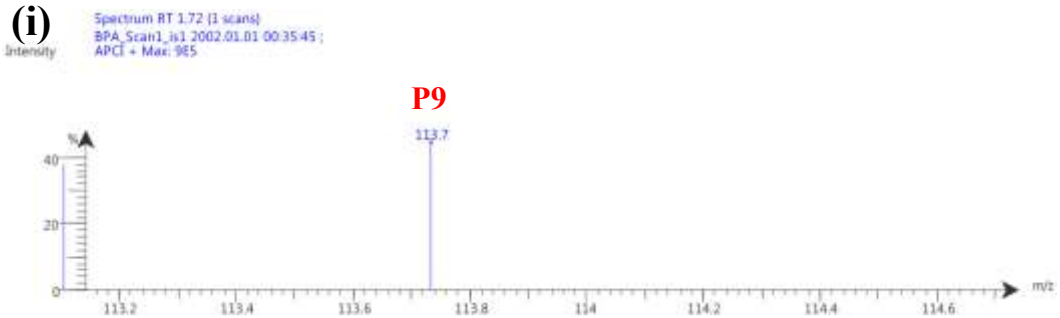
(i)
Spectrum RT 1.72 (1 scans)
BPA_Scan1_is1 2002.01.01 00:35:45 ;
APCI + Max: 9E5
P9
113.7
m/z

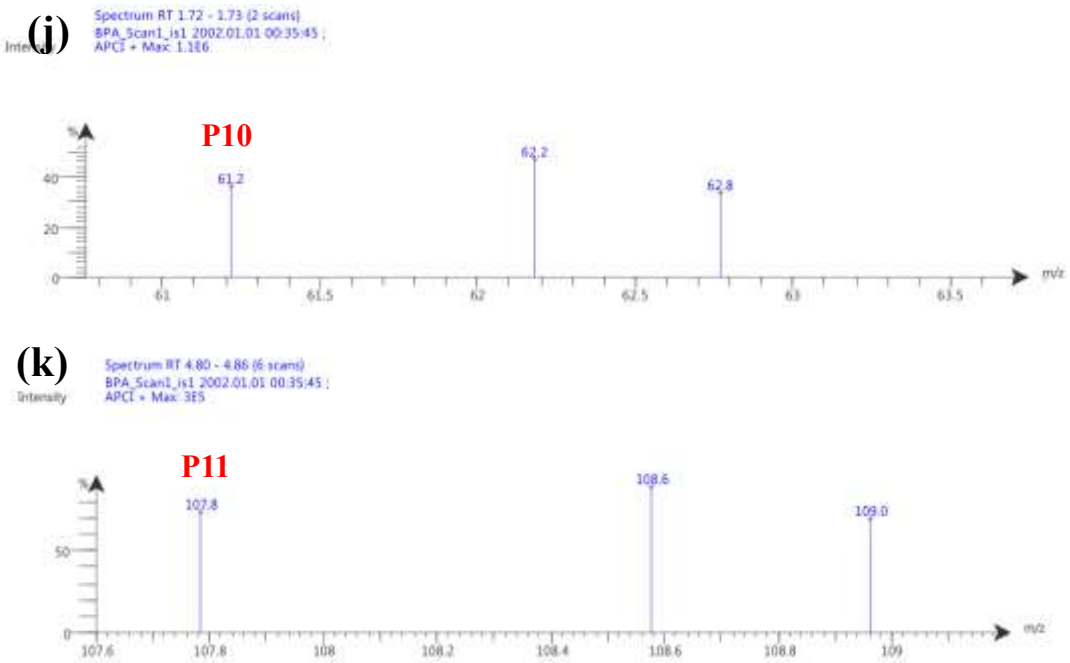

Figure 6.12. LC-MS profile of BPA after photocatalytic degradation.

Table 6.2. Possible intermediate products of BPA degradation determined by LC-MS.

Product	m/z	Chemical structure
BPA	228	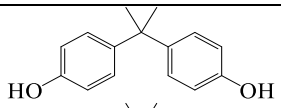
P1	244	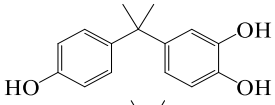
P2	242	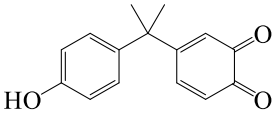
P3	168	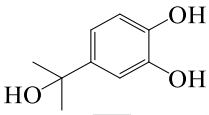
P4	136	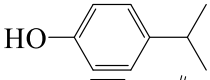
P5	134	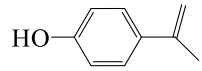
P6	110	
P7	94	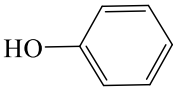

P8	91	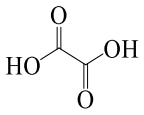
P9	113	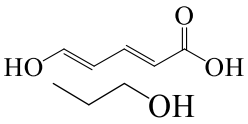
P10	61	
P11	107	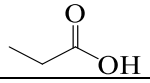

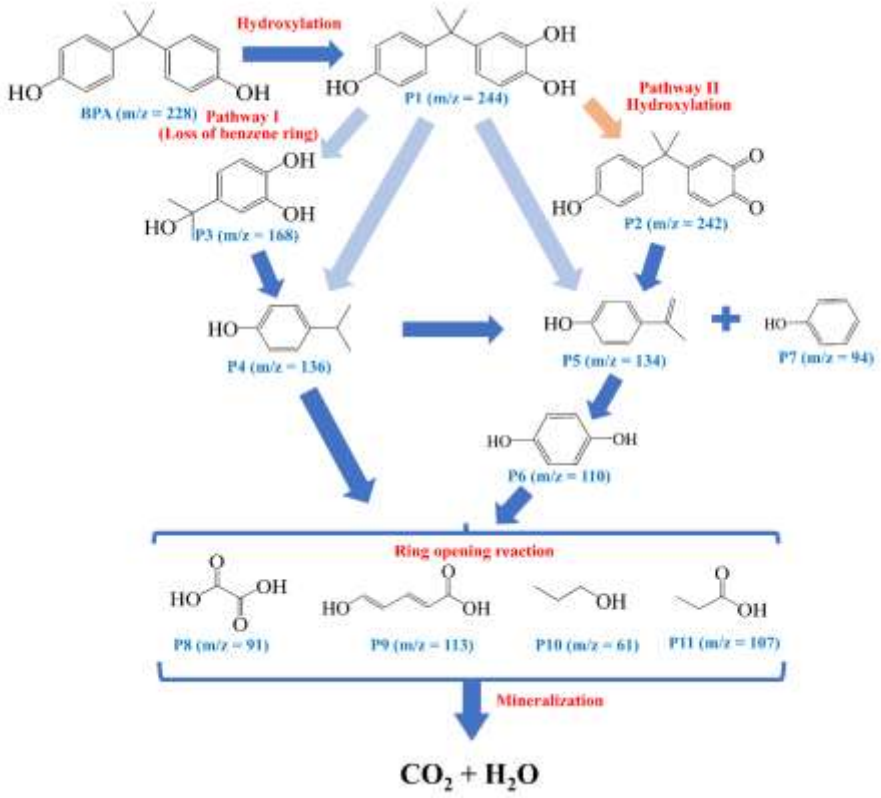

Scheme 6.1. Possible degradation pathways of BPA using CCAC/Co-ZnO photocatalyst.

Initially, the hydroxyl radical (•OH) attacked the C-H bond of the benzene ring, forming a hydroxylated intermediate, P1 (m/z = 243). Previous research using density functional theory (DFT) has shown that the carbon atoms closest to the benzene ring's hydroxyl group are the most susceptible to radical and electrophilic attacks [78]. The hydroxylation process would therefore be preferentially initiated, which is in accordance with the results that have been identified. Subsequently, the degradation proceeded along two possible reaction pathways. For pathway I, further hydroxylation

produced intermediate P2 (m/z = 241) from P1. For pathway II, P1 was responsive to phenyl ring cleavage, resulting in fragment products with a single benzene ring, including P3 (m/z = 167), P4 (m/z = 135), P5 (m/z = 133), P6 (m/z = 110) and P7 (m/z = 94). Researchers have identified intermediates with similar structures in the degradation of serial bisphenols [79,80]. These intermediates may reach relatively high abundance and the main degrading mechanism identified was due to loss of benzene fragments [81]. Under continuous oxidation, the ring structure would be entirely opened, leading to the formation of smaller molecular products such as P8 (m/z = 90), P9 (m/z = 112), P10 (m/z = 60), and P11 (m/z = 106). Finally, they could breakdown into CO_2 and H_2O, resulting in mineralisation of BPA.

6.3.9 Proposed degradation mechanism of BPA pollutant

The probable degradation mechanism of BPA under simulated visible light irradiation on the CCAC/Co-ZnO photocatalyst is illustrated in Figure 6.13.

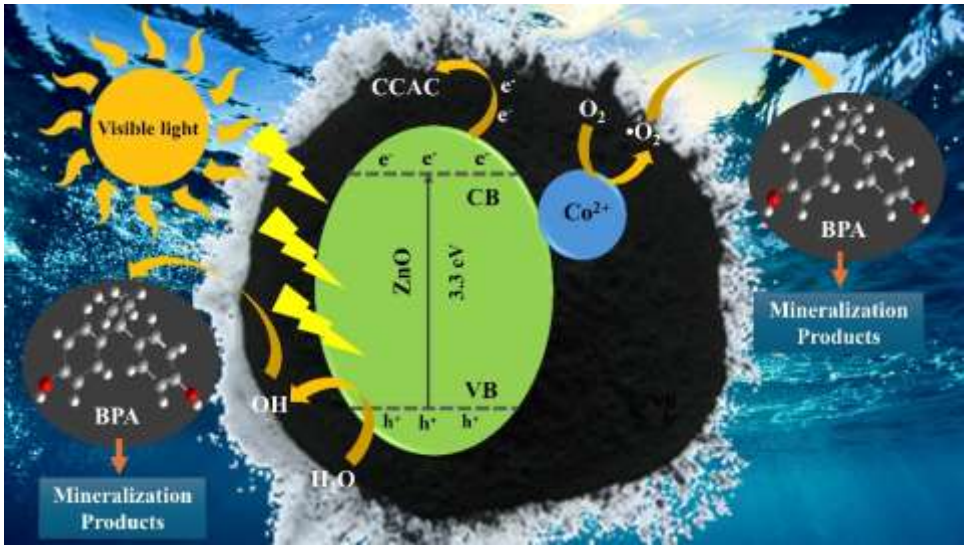

Figure 6.13. Illustration of the plausible BPA photocatalytic degradation mechanism over CCAC/Co-ZnO nanocomposite.

Consequently, when the energy of the irradiation light exceeds the band gap energy of ZnO, the excited electrons (e^-) from the VB of ZnO are transferred to its CB, concurrently generating an equivalent number of holes (h^+) in the VB. Besides, the incorporation of Co-ions into the ZnO framework introduces new energy levels between the CB and VB of ZnO, serving as charge-trapping centres that impede the recombination rate of electron-hole pairs and extend the lifetime of photogenerated

carriers. Consequently, given that porous carbon serves as an appropriate electron acceptor and transfer medium, the excited electrons can rapidly migrate from the conduction band of ZnO to the CCAC, thereby inhibiting charge recombination. The following reactions represent the electron transfer process:

$$\text{Co-ZnO/CCAC} \xrightarrow{hv} \text{Co- ZnO}(e^- + h^+)\text{/CCAC} \quad (6.6)$$

$$\text{Co- ZnO}(e^- + h^+)\text{/CCAC} \rightarrow \text{Co- ZnO}(h^+)\text{/CCAC}(e^-) \quad (6.7)$$

Subsequently, the photoexcited electrons interact with oxygen molecules, resulting in the formation of reductive superoxide radicals ($\bullet O_2^-$). On the other hand, oxidative hydroxyl radicals (•OH) can be produced when holes react with water molecules (H_2O) or hydroxyl ions (OH^-). ROS, specifically superoxide and hydroxyl radicals, engage in the photodegradation of BPA molecules, facilitating their decomposition into CO_2, H_2O, and various mineralization products, as seen in the reactions below:

$$\text{CCAC}(e^-) + O_2 \rightarrow \text{CCAC} + \bullet O_2^- \quad (6.8)$$

$$\text{Co- ZnO}(e^-) + O_2 \rightarrow \text{Co-ZnO} + \bullet O_2^- \quad (6.9)$$

$$2(\bullet O_2^-) + 2H_2O \rightarrow H_2O_2 + 2OH^- + O_2 \quad (6.10)$$

$$H_2O_2 + 2(\bullet O_2^-) \rightarrow \bullet OH + OH^- + O_2 \quad (6.11)$$

$$\text{Co- ZnO}(h^+) + H_2O \text{ or } OH^- \rightarrow \text{Co-ZnO} + \bullet OH \quad (6.12)$$

$$h^+ + OH^- \rightarrow \bullet OH \quad (6.13)$$

$$h^+ + H_2O \rightarrow H^+ + \bullet OH \quad (6.14)$$

$$\bullet OH/\ \bullet O_2^-/h^+ \text{ (ROS)} + \text{BPA} \rightarrow \text{intermediate products} \rightarrow CO_2 + H_2O \quad (6.15)$$

6.3.10 Theoretical insights of BPA toxicity and its intermediates

The toxicity of BPA and its degradation intermediates was studied with two toxicity evaluation servers Protox-3 and ADMETlab 2.0 [82,83]. Herein, the median lethal concentration for *Fathead minnow* (LC_{50}-96 h), median lethal concentration for

Daphnia magna (LC_{50}-48 h), bioaccumulation factors, LD_{50}, IGC_{50} and mutagenicity were chosen as main toxicity indicators [84,85]. BPA and its degradation intermediates (P1 to P11) have LD_{50} values greater than 100, which can be classified as harmless, while P9 with the highest LD_{50} value making it even less toxic relatively than BPA. As shown in Figure 6.13a, only the LC_{50}-96 h of P1 and P2 were slightly higher than that of BPA while P3, P4, P5, P6, P7 and P9 with lower LC_{50}-96 h were be classified as not harmful substance.

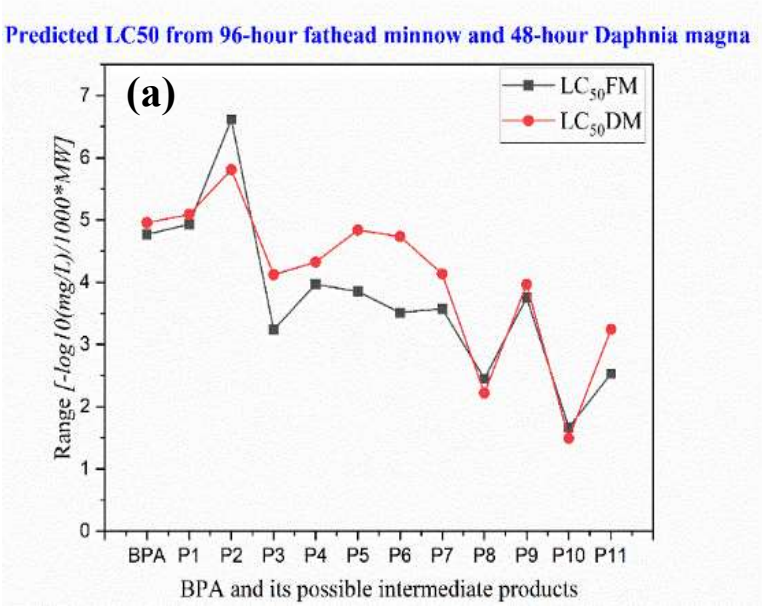

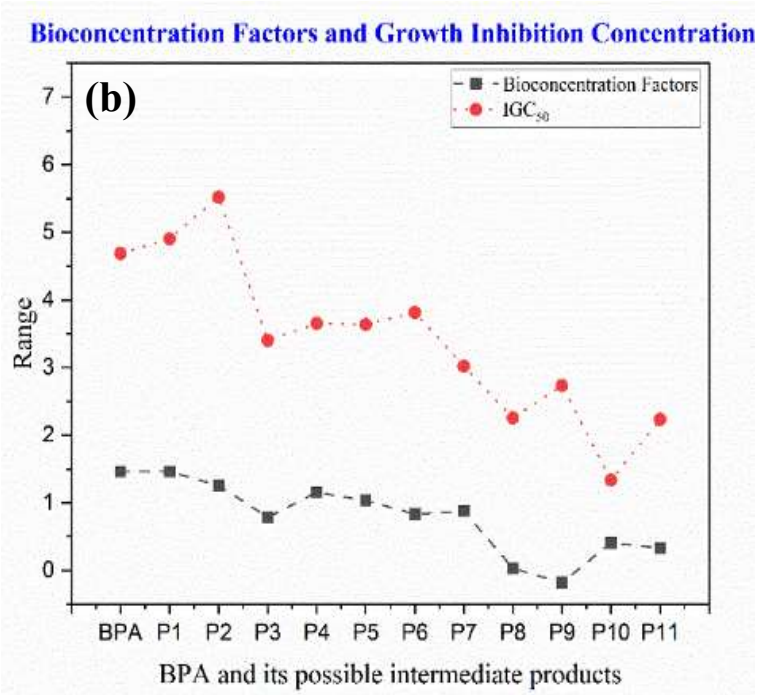

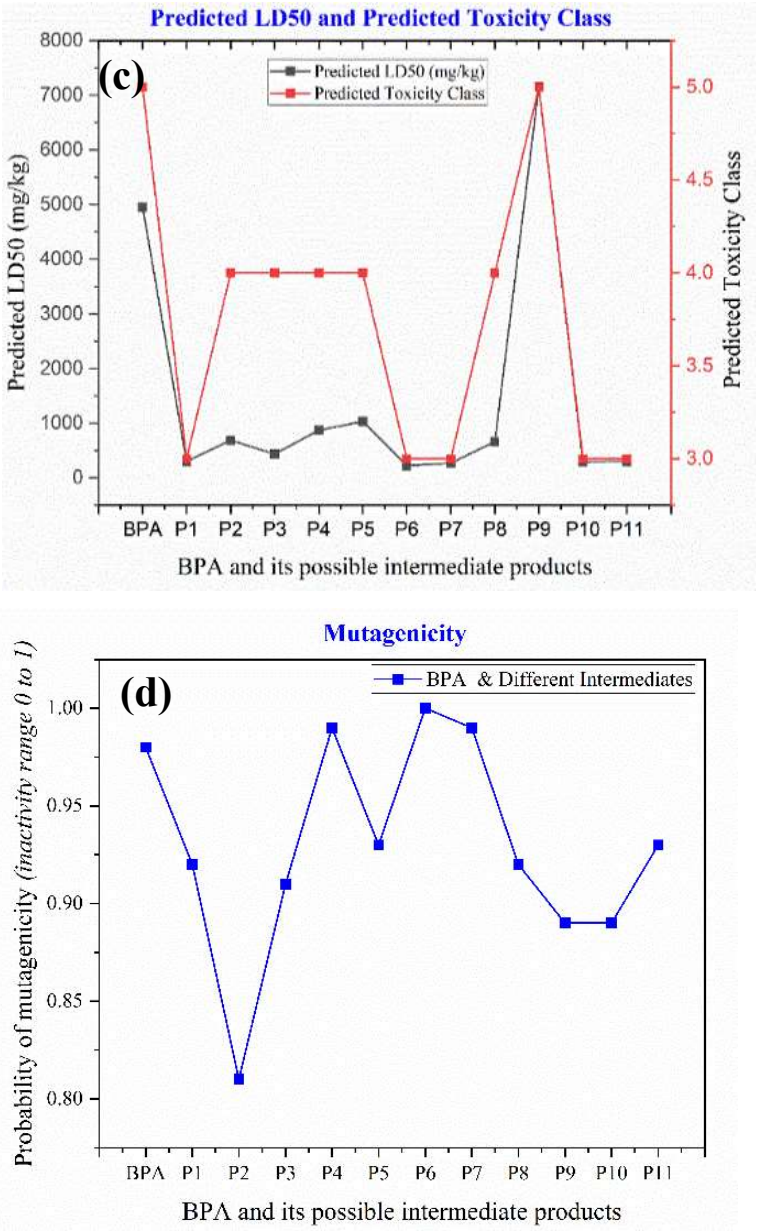

Figure 6.14. Toxicity study conducted via theoretical insights (a) LC50 FM and DM, (b) bioaccumulation factor and GIC, (c) Predicted LD50 and toxicity class, and (d) Mutagenicity for BPA and its intermediates.

Also, P8, P10 and P11 with the least LC_{50}-96 values can be considered slightly toxic. Similar results were obtained from LC_{50}-48 h where P1 and P2 exhibited higher values than BPA (Figure 6.14a) itself and P3, P4, P5, P6, P7, P9 and P11 with lower LC_{50}-48 h can be classified as not harmful substance. P8 and P10 with lower LC_{50}-48 h can be considered as slightly toxic. Compared with BPA, the bioaccumulation factor of the degradation intermediates was reduced considerably (Figure 6.14b). BPA and its

degradation intermediates (P1 to P11) have LD_{50} values greater than 100, which can be classified as harmless, while P9 with the highest LD_{50} value making it even less toxic relatively than BPA (Figure 6.14c).

Similarly, for IGC_{50}, BPA was found to be moderately toxic with P1 and P2 having a higher IGC_{50} value supporting its relatively lower ecological impact in terms of growth inhibition. However, P3 to P7 demonstrated greater environmental toxicity than BPA with lower IGC_{50} values than P1 and P2. The most environmentally toxic degradation products, based on IGC_{50} were P10, P11 and P8 indicating that these compounds could exert strong growth-inhibitory effects on aquatic organisms even at relatively low concentrations (Figure 6.14b).

In addition, BPA has a high mutagenicity which can be classified as toxic. However, the mutagenicity of degradation products except P7 was significantly reduced (Figure 6.14d). The above analysis indicates that the toxic BPA molecules were successfully degraded during the reaction process and converted into less harmful intermediate species. Similar observations have also been reported in various studies [86,87]. Further verification of the environmental friendliness of the developed treatment process by performing acute toxicity test for the reaction solution containing BPA and its degradation products warrants future investigations.

6.3.11 Frontier Orbital Theory analysis of BPA using conceptual DFT in photocatalytic degradation

Conceptual DFT calculations were conducted using Gaussian 16 to investigate the reactivity of BPA during photocatalytic degradation, with visualizations generated using GaussView 6.0 (Figure 6.15). The calculations focused on frontier molecular orbitals (FMOs), electrostatic potential (ESP) surfaces, and Fukui reactivity indices to elucidate the electronic properties and identify reactive sites of BPA under photocatalytic conditions [88]. The optimised BPA structure consists of two phenyl rings connected by an isopropylidene bridge in a nearly planar arrangement, with a C-C bond length of ~ 1.54 Å. The computed HOMO and LUMO energies are −9.18 eV and −5.27 eV, respectively, resulting a HOMO–LUMO energy gap of 3.91 eV, which suggests increased electronic polarizability and favorable charge-transfer capability during photocatalytic reactions [89].

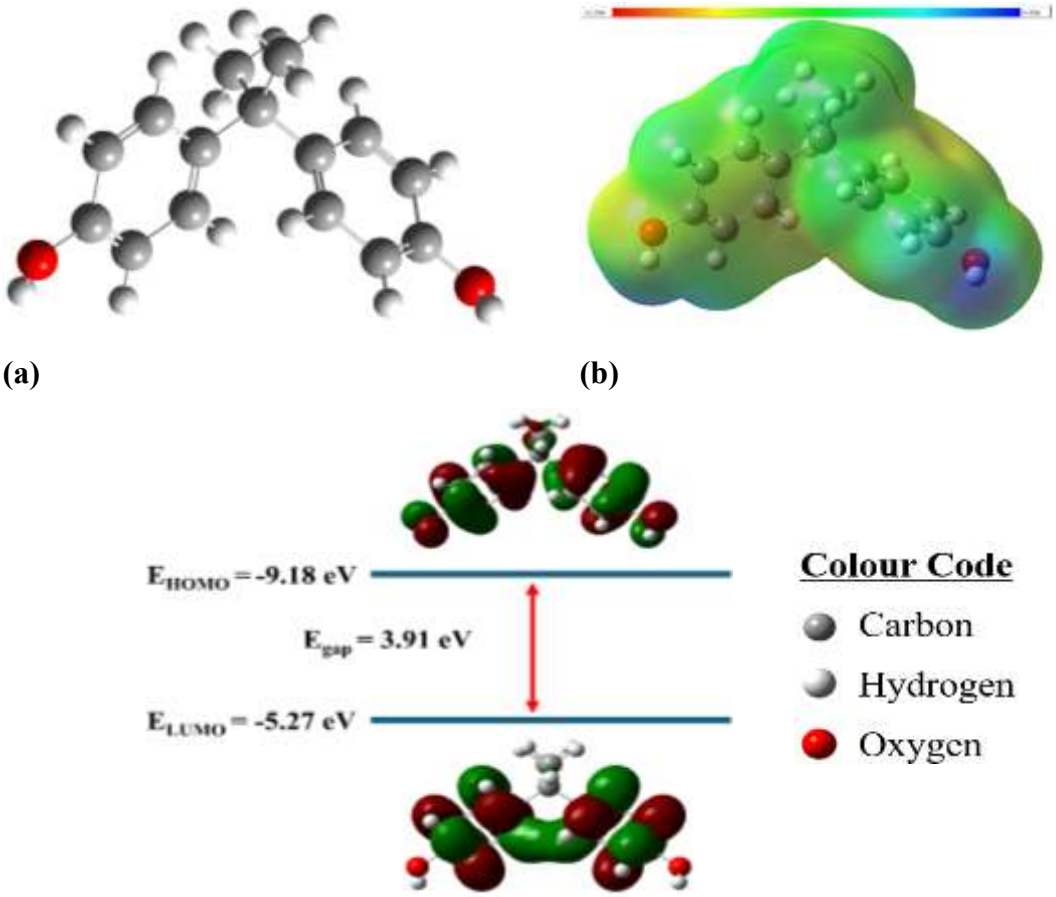

Figure 6.15. (a) Optimized structure, (b) E_{gap} and (c) ESP surfaces showing charge distribution of BPA.

The ESP surface, mapped within a potential range of −0.105 to +0.105 a.u., reveals strongly negative potential regions localized around the phenolic –OH groups, reflecting high electron density associated with oxygen lone pairs, while relatively positive regions are distributed over the aromatic hydrogen atoms and the alkyl bridge. The charge distribution indicates that the phenolic oxygen atoms serve as primary sites for electrophile attraction, whereas the aromatic rings are more prone to nucleophilic and radical-mediated interactions [90].

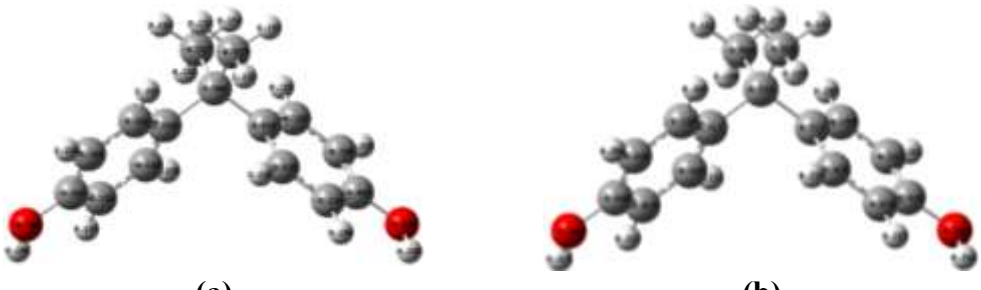

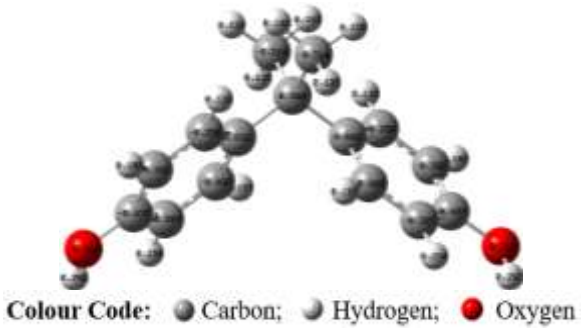

(c)

Figure 6.16. Fukui function corresponding to (a) radical (f^0), (b) electrophilic (f^-), and (c) nucleophilic (f^+), susceptibility of BPA.

Fukui function analysis further corroborates this behavior: the electrophilic Fukui function (f^-) designates the phenolic oxygen atoms and adjacent carbon atoms as the most favorable sites for oxidation by photogenerated holes and hydroxyl radicals, whereas the nucleophilic fukui function (f^+) emphasizes the aromatic π-system as a favored region for electron acceptance. The radical fukui function (f^0) substantiates aromatic rings as primary sites for radical assault (Figure 6.16) [91]. These findings suggest that BPA degradation initiates at electron-rich phenolic and aromatic sites via synergistic electron-transfer and ROS driven pathways under photocatalytic conditions.

6.3.12 Comparison studies

The photocatalytic degradation efficiency of BPA attained by the CCAC/Co-ZnO nanocomposite was compared with several nanocomposite systems reported in the literature, as outlined in Table 6.3. The findings demonstrate that the synthesized photocatalyst exhibit significantly improved BPA degradation efficiency relative to previously studied materials. The synthesized nanocomposite exhibits significant potential as an effective photocatalyst for the removal of BPA from wastewater.

Table 6.3. Photocatalytic performance comparison of the synthesized nanocomposite with reported photocatalysts for BPA degradation.

Targeted Pollutant	Photocatalysts	Irradiation time (min)	Performance of photocatalyst (%)	Ref.
	ZnO/rGO	30	93.1	[92]
	Ag_2O_x(1 wt%)/ST	180	98	[93]

BPA	MOF-Derived $Bi_{12}O_{17}Cl_2$ Nanoflakes	60	94.3	[94]
	Fe/Cu@NC-x	30	98	[95]
	ZnO/carbon xerogel	300	78	[96]
	ZnO/OCN nanocomposite	180	92.5	[97]
	CCAC/Co-ZnO	**60**	**99.6**	**Present study**

6.4 Conclusion

In this work, a novel photocatalyst based on *Croton caudatus*–derived activated carbon decorated with Co-doped ZnO nanoparticles is developed, which has not been previously investigated. The synergistic incorporation of these components improves charge separation *via* reduce band gap of 2.1 eV, photostability, and degradation efficiency relative to conventional single- or binary-component photocatalysts for BPA removal. Under ideal conditions, the photocatalyst showed great efficacy, attaining 99.67 % BPA degradation and 81 % mineralization after 60 min of visible light illumination. The L-H model showed that the degradation process followed PFO behavior, with a $t_{1/2}$ of 12.6 min and an apparent rate constant (k_{ap}) of 0.055 min^{-1}, respectively. Scavenger tests revealed that hydroxyl radicals played the significant role for the breakdown process, followed by photogenerated holes and superoxide radicals. Reusability tests showed that the catalyst maintained 77.63 % efficiency after five consecutive cycles without significant loss of its activity, confirming its good stability and reusability. LC-MS investigation of BPA degradation showed a possible pathway leading to complete mineralization of carbon dioxide and water. DFT calculations further elucidated the mechanisms underlying the enhanced generation of ROS, providing valuable insights into the photocatalytic degradation pathways. Overall, the findings of this work demonstrate the potential of cost-effective and facilely synthesized photocatalyst as promising materials for addressing organic contamination in wastewater treatment applications.

References

[1] E. Baralla, V. Pasciu, M. V. Varoni, M. Nieddu, R. Demuro, M. P. Demontis, Bisphenols' occurrence in bivalves as sentinel of environmental contamination, Sci. Total Environ. 785 (2021) 147263.

[2] P. Loganathan, S. Vigneswaran, J. Kandasamy, T. V. Nguyen, A. K. Cuprys, H. Ratnaweera, Bisphenols in water: Occurrence, effects, and mitigation strategies, Chemosphere 328 (2023) 138560.

[3] K. Czarny-Krzymińska, B. Krawczyk, D. Szczukocki, Bisphenol A and its substitutes in the aquatic environment: Occurrence and toxicity assessment, Chemosphere 315 (2023) 137763.

[4] M. H. Mahmoudian, A. Mesdaghinia, A. H. Mahvi, S. Nasseri, R. Nabizadeh, M. H. Dehghani, Photocatalytic degradation of bisphenol A using bismuth ferric magnetic nanoparticle: synthesis, characterization and response surface methodology modeling, J. Environ. Health Sci. Eng. 20 (2022) 617–628.

[5] C. Naveira, N. Rodrigues, F. S. Santos, L. N. Santos, R. A. Neves, Acute toxicity of bisphenol A to tropical marine and estuarine species, Environ. Pollut. 268 (2021) 115911.

[6] H. J. Lehmler, B. Liu, M. Gadogbe, W. Bao, Exposure to bisphenol A, F and S in US adults and children: NHANES 2013–2014, ACS Omega 3 (2018) 6523–6532.

[7] J. Chudzinska, B. Woźniak, M. Sprynskyy, I. Nowak, A. Feliczak-Guzik, Photoremoval of bisphenol A using hierarchical zeolites and diatom biosilica, Int. J. Mol. Sci. 24 (2023) 2878.

[8] Y. S. Jung, S. T. Ro, S. W. Kang, H. Lee, J. S. Lee, Y. K. Chae, Bisphenol A release from commercially available 3D printed resins and human cell apoptosis: an in-vitro study, J. Clin. Pediatr. Dent. 47 (2023) 89–95.

[9] J. Liu, K. Sun, R. Zhu, X. Wang, M. G. Waigi, S. Li, Biotransformation of bisphenol A by Trametes hirsuta La-7: kinetics, products and mechanisms, Environ. Pollut. 321 (2023) 121155.

[10] C. Oussalah, F. Kaouah, S. Boumaza, M. Trari, Highly efficient removal of bisphenol A by activated carbon derived from Sapindus mukorossi nut cores, Biomass Convers. Biorefin. (2023) 1–17.

[11] Z. Song, Y. Zhang, X. Zhang, X. Zhou, Y. Chen, X. Duan, N. Ren, Chloride-activated peracetic acid for bisphenol A purification: kinetics and radical mechanism, Water Res. (2023) 120274.

[12] D. Roy, S. Neogi, S. De, Mechanistic investigation of photocatalytic degradation of bisphenol A using MIL-88A(Fe)/MoS_2 composite, Chem. Eng. J. 428 (2022) 131028.

[13] H. T. Nguyen, J. Lee, E. Kwon, G. Lisak, B. X. Thanh, F. Ghanbari, K. Y. A. Lin, Bamboo-like N-doped carbon nanotube-confined cobalt catalyst for bisphenol A degradation, Chemosphere 279 (2021) 130569.

[14] T. T. Cao, D. D. Zhou, X. D. Wang, C. Cui, Photocatalytic degradation of bisphenol A over Co-BiOCl/biochar hybrid catalysts: properties, efficiency and mechanism, J. Mol. Liq. 362 (2022) 119622.

[15] USEPA, Contaminant candidate list (CCL5) and regulatory determination, U.S. Environmental Protection Agency (2023).

[16] N. I. Pratiwi, A. Mukimin, N. Zen, I. Septarina, Integration of electrocoagulation, adsorption and wetland technology for jewelry industry wastewater treatment, Sep. Purif. Technol. 279 (2021) 119690.

[17] Y. Zhang, Z. Chen, P. Wu, Y. Duan, L. Zhou, Y. Lai, F. Wang, S. Li, Three dimensional heterogeneous electro-Fenton system with a novel catalytic particle electrode for bisphenol A removal, J. Hazard. Mater. 393 (2020) 120448.

[18] L. C. Ferreira, J. R. Fernandes, J. A. Peres, P. B. Tavares, M. S. Lucas, Wireless UV-A LEDs-driven AOP in treatment of agro-industrial wastewaters, Environ. Res. 200 (2021) 111430.

[19] S. Dadvar, B. Shahmoradi, S. Habibi, K. Wantala, T. Suwannaruang, A. Maleki, H. P. Shivaraju, S. M. Lee, Photocatalytic degradation of water disinfection by-products using zirconium doped zinc oxide nanoparticles, Desalin. Water Treat. 252 (2022) 339–347.

[20] A. Farhan, J. Arshad, E.U. Rashid, H. Ahmad, S. Nawaz, J. Munawar, J. Zdarta, T. Jesionowski, M. Bilal, Metal ferrites-based nanocomposites and nanohybrids for photocatalytic water treatment and electrocatalytic water splitting, Chemosphere 310 (2023) 136835.

[21] Y. Quan, M. Liu, H. Wu, X. Tian, L. Dou, Z. Wang, C. Ren, S-scheme CeO_2/AgCl heterojunction with enhanced photocatalytic tetracycline degradation, Appl. Surf. Sci. 642 (2024) 158601.

[22] H. Ren, F. Qi, A. Labidi, J. Zhao, H. Wang, Y. Xin, J. Luo, C. Wang, Carbon quantum dots/Bi_2WO_6 S-scheme heterojunction for antibiotic degradation, Appl. Catal. B 330 (2023) 122587.

[23] K. Davididou, R. Nelson, J. M. Monteagudo, A. Durán, A. J. Expósito, E. Chatzisymeon, Photocatalytic degradation of bisphenol A under UV-LED, blacklight and solar irradiation, J. Clean. Prod. 203 (2018) 13–21.

[24] O. Bechambi, S. Sayadi, W. Najjar, Photocatalytic degradation of bisphenol A in presence of C-doped ZnO, J. Ind. Eng. Chem. 32 (2015) 201–210.

[25] B. Gao, T. M. Lim, D. P. Subagio, T. T. Lim, Zr-doped TiO_2 for enhanced photocatalytic degradation of bisphenol A, Appl. Catal. A 375 (2010) 107–115.

[26] M. R. Rajeshwari, M. K. Okla, S. Kokilavani, M. A. Abdel-Maksoud, I. A. Saleh, H. A. Abu-Harirah, T. N. AlRamadneh, S. S. Khan, Visible-light assisted degradation using g-C_3N_4 QDs/α-MoO_3 nanohybrid, Chemosphere 339 (2023) 139529.

[27] R. Katwal, H. Kaur, G. Sharma, M. Naushad, D. Pathania, Electrochemically synthesized CuO nanoparticles for photocatalytic activity, J. Ind. Eng. Chem. 31 (2015) 173–184.

[28] K. Mun, C. Wei, K. Sing, J. Ching, ZnO-based photocatalysts in water treatment: a review, Water Res. 88 (2016) 428–448.

[29] X. Zhou, Y. Mu, S. Zhang, L. Gao, H. Chen, J. Mu, X. Zhang, M. Zhang, W. Liu, CdS sensitized SnO_2 nanoparticles for photocatalysis, Mater. Res. Bull. 111 (2019) 118–125.

[30] M. Ikram, H. Shahid, J. Haider, A. Haider, S. Naz, A. Ul-Hamid, I. Shahzadi, M. Naz, W. Nabgan, S. Ali, Nb/starch-doped ZnO nanostructures for polluted water treatment, ACS Omega 7 (2022) 39347–39361.

[31] M. Li, P. Li, L. Zhang, M. Chen, J. Tang, C. Qin, S. L. J. Lee, S. Lin, ZnO decorated ZnFe-LDH@biochar nanocomposites for tetracycline photodegradation, Chem. Eng. J. 434 (2022) 134772.

[32] C. Zhu, G. Fang, D.D. Dionysiou, C. Liu, J. Gao, W. Qin, D. Zhou, Persulfate activation by zero-valent iron nanoparticles, J. Hazard. Mater. 316 (2016) 232–241.

[33] H. Liang, Y. Zhang, S. Huang, I. Hussain, Oxidative degradation of p-chloroaniline by copper oxidate activated persulfate, Chem. Eng. J. 218 (2013) 384–391.

[34] O. Ola, M. M. Maroto-Valer, Review of TiO_2 photocatalysis for CO_2 reduction, J. Photochem. Photobiol. C 24 (2015) 16–42.

[35] Y. Lu, Y. Lin, D. Wang, L. Wang, T. Xie, T. Jiang, Cobalt-doped ZnO visible-light photocatalyst, Nano Res. 4 (2011) 1144–1152.

[36] R. Ullah, J. Dutta, Photocatalytic degradation of dyes with Mn-doped ZnO nanoparticles, J. Hazard. Mater. 156 (2008) 194–200.

[37] J. Zhao, L. Wang, X. Yan, Y. Yang, Y. Lei, J. Zhou, Y. Huang, Y. Gu, Y. Zhang, Ni-doped ZnO nanorods: structure and photocatalytic activity, Mater. Res. Bull. 46 (2011) 1207–1210.

[38] P. Petkova, K. Boubaker, Lattice compatibility theory for Urbach tailing patterns, J. Alloys Compd. 546 (2013) 176–179.

[39] S. Kuriakose, B. Satpati, S. Mohapatra, Co-doped ZnO nanodisks for methyl orange degradation, Adv. Mater. Lett. 6 (2015) 217–223.

[40] L. H. Mohammed, F. Gulbagca, R. N. E. Tiri, A. Aygun, M. Bekmezci, F. Sen, Hydrothermal synthesis of Co-doped ZnO for pollutant degradation, Chem. Eng. J. Adv. 14 (2023) 100495.

[41] S. Mustapha, M. M. Ndamitso, A. S. Abdulkareem, J. O. Tijani, D. T. Shuaib, A. O. Ajala, A. K. Mohammed, TiO_2 and ZnO nanoparticles immobilized on clay for wastewater treatment, Appl. Water Sci. 10 (2020) 1–36.

[42] S. L. Ezung, M. Baruah, S. Sharma, R. S. Umdor, I.T. Longchar, B. Giridharan, U. B. Sinha, D. Sinha, Photocatalytic degradation of chlorpyrifos using Fe-doped ZnO/activated carbon nanocomposite, J. Mol. Struct. 1319 (2025) 139434.

[43] P. Lisowski, J. C. Colmenares, O. Mašek, D. Łomot, O. Chernyayeva, D. Lisovytskiy, Biomass-derived hybrid TiO_2/carbon material, J. Anal. Appl. Pyrolysis 131 (2018) 35–41.

[44] Q. Yao, H. Wang, C. Wang, C. Jin, Q. Sun, Nitrogen-carbon derived material for supercapacitor applications, ACS Sustain. Chem. Eng. 6 (2018) 4695–4704.

[45] B. T. Son, N.V. Long, N. T. N. Hang, Biomass-derived carbon-based photocatalysts: review, RSC Adv. 11 (2021) 30574–30596.

[46] D. Mohanta, Activated carbon@SnO_2 nanocomposites for arsenite and fluoride removal, J. Environ. Chem. Eng. 6 (2018) 356–366.

[47] W. Zhou, P. Zhang, W. Liu, Anatase TiO_2 nanospindle/activated carbon composite photocatalysts, Int. J. Photoenergy (2012) 28–30.

[48] M. Faisal, M. Alsaiari, M. A. Rashed, F. A. Harraz, Biomass-derived Carbon@ZnO/SnO_2 photocatalyst for pollutant degradation, J. Taiwan Inst. Chem. Eng. 120 (2021) 313–324.

[49] P. Shanmugam, B. Parasuraman, S. Boonyuen, P. Thangavelu, M. S. AlSalhi, A. L. T. Zheng, A. Viji, ZnS-Ag composites based on biomass-derived carbon aerogel, Environ. Geochem. Health 46 (2024) 92.

[50] S. Sharma, S. L. Ezung, A. Supong, M. Baruah, S. Kumar, R. S. Umdor, D. Sinha, Croton caudatus activated carbon for 2-chlorophenol removal, Chem. Eng. Res. Des. 190 (2023) 777–792.

[51] S. Lam, J. Sin, H. Zeng, H. Lin, H. Li, Y. Chai, M. Choong, A. R. Mohamed, Green synthesis of Fe-ZnO nanoparticles for photocatalysis, Mater. Sci. Semicond. Process. 123 (2021) 105574.

[52] A. Najafidoust, E. A. Asl, H. K. Hakki, M. Sarani, H. Bananifard, M. Sillanpaa, M. Etemadi, Fe-ZnO over silica aerogel as floating photocatalyst, Sol. Energy 225 (2021) 344–356.

[53] H. R. Mardani, M. Forouzani, M. Ziari, P. Biparva, Visible-light degradation over Fe or Cu promoted ZnO, Spectrochim. Acta A 141 (2015) 27–33.

[54] T. Srinivasulu, K. Saritha, K. T. R. Reddy, Fe-doped ZnO thin films by spray pyrolysis, Mod. Electron. Mater. 3 (2017) 76–85.

[55] R. Vinod, M. J. Bushiri, Hydrothermal growth of doped ZnO nanostructures, J. Lumin. 256 (2023) 119628.

[56] Z. Lü, Y. Cheng, L. Xue, H. Wang, H. Lin, X. Sun, Z. Miao, S. Zhuo, J. Zhou, MCr–LDHs/BiOBr heterojunction nanocomposites, J. Alloys Compd. 898 (2022) 162871.

[57] R. Naveenkumar, B. Karthikeyan, S. Senthilvelan, Green-synthesized activated carbon-supported Co-doped ZnO for dye degradation, ChemistrySelect 9 (2024) e202401448.

[58] C. K. Bandoh, B. Y. Danu, E. S. Agorku, F. K. Ampong, R. K. Nkum, Cobalt-doped ZnO-g-C_3N_4 heterostructures for eosin yellow degradation, Results Mater. 21 (2024) 100515.

[59] P. Zhang, T. Wang, X. Chang, J. Gong, Effective charge carrier utilization in photocatalysis, Acc. Chem. Res. 49 (2016) 911–921.

[60] S. L. Ezung, M. Baruah, S. Sharma, R. S. Umdor, I. T. Longchar, B. Giridharan, U. B. Sinha, D. Sinha, Photocatalytic degradation of chlorpyrifos using Fe-doped ZnO/activated carbon nanocomposite, J. Mol. Struct. 1319 (2025) 139434.

[61] D. A. Kader, A. H. Mohammed, S. J. Mohammed, D. M. Aziz, ZnO@henna nanocomposite for 4-nitrophenol degradation, RSC Adv. 15 (2025) 18245–18265.

[62] M. Mahajan, S. Kumar, J. Gaur, S. Kaushal, J. Dalal, G. Singh, M. Misra, D. S. Ahlawat, Green synthesis of ZnO nanoparticles using Justicia adhatoda, RSC Adv. 15 (2025) 2958–2980.

[63] W. B. Soltan, W. Wang, J. Sun, T. Toupance, G. Yu, F. Li, W-doped ZnO/$ZnWO_4$ photocatalysts for organic degradation, New J. Chem. 45 (2021) 11051–11067.

[64] Q. Ji, H. Yang, J. Li, R. Wang, C. Zhang, Charge carrier dynamics in perovskite films, J. Phys. Chem. C 128 (2024) 10520–10527.

[65] J. Luo, R. Li, Y. Chen, X. Zhou, X. Ning, L. Zhan, L. Ma, X. Xu, L. Xu, L. Zhang, Z-scheme $LaFeO_3$/SnS_2 hybrid for tetracycline degradation, Sep. Purif. Technol. 210 (2019) 417–430.

[66] E. Kuruvilla, A.S. Nesaraj, V. Jose, D. Padmanabhan, M. Arunkumar, Co, Mn co-doped ZnO@graphite for dye degradation, Mater. Today Commun. 41 (2024) 110227.

[67] Y. T. Chung, M. M. Ba-Abbad, A. W. Mohammad, A. Benamor, Functionalization of ZnO nanoparticles for membrane applications, Desalin. Water Treat. 57 (2016) 7801–7811.

[68] H. Zhang, J. Wu, J. Han, L. Wang, W. Zhang, H. Dong, Y. Wang, Photocatalyst/enzyme heterojunction for BPA degradation, Chem. Eng. J. 385 (2020) 123764.

[69] Y. Cao, S. Alsharif, A. S. El-Shafay, g-C_3N_4/MoS_2 pn heterojunction photocatalyst for tetracycline degradation, Mater. Sci. Semicond. Process. 144 (2022) 106569.

[70] J. Ryu, S. Kim, H. I. Kim, E. H. Jo, Y. K. Kim, M. Kim, H. D. Jang, TiO_2/reduced graphene oxide hybrid photocatalyst, Chem. Eng. J. 262 (2015) 409–416.

[71] K. Javed, M. Bilal, N. Abbas, S. Mahmood, T. Fazal, S. Iqbal, K. M. Alotaibi, MOF/$CuFe_2O_4$ composite for BPA degradation, Microsc. Res. Tech. 88 (2025) 1727–1738.

[72] A. Mantilla, E. S. Benitez, I. M. Valenzuela, G. R. Ortiz, S. C. Díaz, L. L. Rojas, F. J. T. Morales, M. N. Magaña, Cr-TiO_2 nanoparticles for BPA degradation, J. Photochem. Photobiol. A 459 (2025) 116079.

[73] Ö. Görmez, E. Yakar, B. Gözmen, B. Kayan, A. Khataee, $CoFe_2O_4$/graphene oxide/g-C_3N_4 catalyst for BPA degradation, Chemosphere 288 (2022) 132663.

[74] Q. Han, M. Wang, F. Sun, B. Yu, Z. Dong, P. Li, J. Luo, M. Li, X. Jin, Z. Dai, Degradation pathways of BPA via radicals: DFT prediction, Environ. Res. 216 (2023) 114601.

[75] A. Saljooqi, T. Shamspur, A. Mostafavi, Porous ZnO stabilized by TiO_2 and Fe_3O_4 for pesticide degradation, Environ. Sci. Pollut. Res. 28 (2021) 9146–9156.

[76] G. Shukla, M. Rani, U. Shanker, Ag-doped cobalt oxide incorporated rGO nanocomposite for solar photocatalysis, Inorg. Chem. Commun. (2025) 114733.

[77] H. Dihingia, D. Tiwari, Green synthesis of heterojunction nanocatalyst for antibiotic removal, Sep. Purif. Technol. 306 (2023) 122641.

[78] F. Liu, Q. Dong, C. Nie, Z. Li, B. Zhang, P. Han, W. Yang, M. Tong, PMS enhanced degradation of bisphenols using COFs, Chem. Eng. J. 430 (2022) 132833.

[79] J. Lai, X. Jiang, M. Zhao, S. Cui, J. Yang, Y. Li, Layered $BiOIO_3$ modified with carbon quantum dots for BPA degradation, Appl. Catal. B 298 (2021) 120622.

[80] P. Xu, P. Wang, Q. Wang, R. Wei, Y. Li, Y. Xin, T. Zheng, L. Hu, X. Wang, G. Zhang, Ag_2O/ZnO/rGO heterojunction for solar photocatalysis, J. Hazard. Mater. 403 (2021) 124011.

[81] J. Shen, A. Shi, J. Lu, X. Lu, H. Zhang, Z. Jiang, Cu-doped ZnO/CoFe-LDH composite for BPA degradation via visible-light photocatalysis and persulfate activation, Environ. Pollut. 323 (2023) 121186.

[82] P. Banerjee, E. Kemmler, M. Dunkel, R. Preissner, ProTox 3.0: toxicity prediction webserver, Nucleic Acids Res. 52 (2024) W513–W520.

[83] G. Xiong, Z. Wu, J. Yi, L. Fu, Z. Yang, C. Hsieh, M. Yin, X. Zeng, C. Wu, ADMETlab 2.0: online ADMET prediction platform, Nucleic Acids Res. 49 (2021) W5–W14.

[84] G. T. Ankley, D. L. Villeneuve, The fathead minnow in aquatic toxicology, Aquat. Toxicol. 78 (2006) 91–102.

[85] L. Guilhermino, T. Diamantino, M. C. Silva, A. M. Soares, Acute toxicity test with Daphnia magna, Ecotoxicol. Environ. Saf. 46 (2000) 357–362.

[86] J. Shen, A. Shi, J. Lu, X. Lu, H. Zhang, Z. Jiang, Optimized fabrication of Cu-doped ZnO/calcined CoFe-LDH composite for efficient degradation of bisphenol A through synergistic visible-light photocatalysis and persulfate activation: Performance and mechanisms, Environ. Pollut. 323 (2023) 121186.

[87] Y. Quan, M. Liu, H. Wu, X. Tian, L. Dou, C. Ren, Z. Wang, Construction of La_2O_3/AgCl S-scheme heterojunction with interfacial chemical bond for efficient photocatalytic degradation of bisphenol A, Appl. Surf. Sci. 664 (2024) 160212.

[88] Y. H. Azeez, R. O. Kareem, A. F. Qader, R. A. Omer, L. O. Ahmed, DFT investigation of AHPE-dop compounds, Next Mater. 3 (2024) 100184.

[89] F. B. Shittu, A. Iqbal, M. N. Ahmad, M. R. Yusop, M. N. M. Ibrahim, S. Sabar, L. D. Wilson, D. H. Y. Yanto, Photodegradation mechanism of BPA by oxygen doped carbon nitride, RSC Adv. 12 (2022) 10409–10423.

[90] Y. Hu, Y. Jin, Y. Gao, M. Li, X. Wang, H. Ma, Y. N. Zhang, 3D Co_3O_4-Ov/TiO_2 for simultaneous BPA and Cr(VI) removal, Adv. Funct. Mater. 35 (2025) 2414350.

[91] H. Yu, Y. Zhang, L. Wang, Y. Tuo, S. Yan, J. Ma, X. Zhang, Y. Shen, H. Guo, L. Han, Adsorption mechanism of methylene blue by modified biochar: DFT insights, RSC Adv. 14 (2024) 1854–1865.

[92] C. Liu, M. Yue, L. Liu, Y. Rui, W. Cui, 3D network ZnO/rGO–rGH hydrogel for adsorption enriched photocatalysis, RSC Adv. 8 (2018) 22402.

[93] R. Vaithiyanathan, K. Shanmugaraj, T. Kanagaraj, V. Manikandan, S. Singh, S. Dixit, M. S. A. J. Bosco, Y. Y. Li, P. S. M. Kumar, Ag_2O_x-infused silica-titania composites for BPA degradation, Sep. Purif. Technol. (2025) 133389.

[94] Y. Wang, S. Xue, Y. Liao, Q. Lu, H. Wang, C. Zhao, N. Tang, F. Du, MOF-derived $Bi_{12}O_{17}Cl_2$ nanoflakes for BPA degradation, ACS Appl. Nano Mater. 7 (2024) 3188–3198.

[95] F. P. Hu, P. Zhan, L. Long, J. Zhu, G. Xu, X. Peng, PMS activation by Fe/Cu encapsulated N-doped carbon for BPA degradation, Chemosphere 293 (2022) 133455.

[96] N. P. de Moraes, R. B. Valim, R. da Silva Rocha, M. L. C. P. da Silva, T. M. B. Campos, G. P. Thim, L. A. Rodrigues, ZnO/carbon xerogel composites for visible light degradation of phenols, Colloids Surf. A 584 (2020) 124034.

[97] A. Uddin, M. Bilal, J. Qian, M. Akram, Q. He, Oxygen-vacant Z-scheme ZnO/g-C_3N_4 nanocomposites for BPA degradation and CO_2 reduction, Sep. Purif. Technol. (2025) 133420.

CHAPTER 7

SUMMARY AND CONCLUSION

This chapter presents the overall summary and conclusions of the thesis. The future scope of the work is also highlighted in this chapter.

7.1 Summary of the work

Croton caudatus biomass was used as a precursor in the production of *croton caudatus* activated carbon (CCAC). The as-prepared AC was evaluated for the adsorption of phenolic pollutants, namely 2-CP, CT, and RS. Moreover, the produced AC was combined with metal/metal oxide components to form heterojunction nanocomposites, which were then used for the photocatalytic degradation of 4-NP and BPA in aqueous solutions. Furthermore, density functional theory (DFT) studies were conducted to better understand the adsorption processes and reactivity behavior of AC toward diverse phenolic pollutants. A summary of the overall thesis work is presented below:
1. CCAC adsorbent served as a promising sustainable adsorbent for the 2CP adsorption from aqueous medium. The synthesized AC was produced at 2:1 impregnation ratio and 700 ºC activation temperature for 2 hours using a muffle furnace under self-generated atmosphere. Studies of the produced AC showed a surface area of 846.29 m^2/ g, a total pore volume of 0.019 cm^3/g, and an average pore diameter of 3.82 nm. FT-IR spectrum analysis showed several peaks that represents the presence of different functional groups. XRD analysis and SEM micrograph of CCAC demonstrated the presence of graphite like micro-crystallite nature and porous network. Under the optimum conditions, the maximum removal efficiency (R %) and adsorption capacity for 2CP were found to be 98.56 % and 26.33 mg/g. The equilibrium isotherm study for 2CP adsorption was fitted well to the Langmuir model with the maximum adsorption capacity (Q_{max}) of 53.619 mg/g. The behavior of 2CP adsorption on CCAC was best described by pseudo-second order where the calculated q_e values ($q_{e,\,cal}$= 26.653 mg/g) was close similar to the experimental data ($q_{e,\,exp}$ = 26.333 mg/g). Thermodynamic studies confirmed that the adsorption process was spontaneous and exothermic. Regeneration studies of the adsorbent was determined to be satisfactory throughout the fifth regeneration cycle, indicating that the adsorbent may be regenerated and recycled for multiple times. DFT investigations further revealed that the adsorption of 2CP onto AC is favorable with the –COOH functionalized AC appeared to have the strongest interaction with 2CP. Moreover, the presence of numerous functional groups OH+CHO+COOH(AC) enhances the adsorption capacities of AC towards 2CP, relative to a single functional group. Thus, the results obtained from experimental and

theoretical studies showed that the AC prepared from *Croton caudatus* biomass was efficient in removing 2CP from the wastewater.

2. The synthesized material was then used for the removal of CT and RS from water. The experimental batch adsorption yielded high removal efficiencies of 99.23 % for CT and 98.68 % for RS, respectively, under ideal process conditions. Adsorption of CT and RS on AC followed the Langmuir adsorption isotherm, implying a single-layer coverage and adsorptive capacities of 56.05 mg/g at pH 6 for CT and 61.85 mg/g at pH 4 for RS. The kinetics of adsorption process on CCAC closely followed pseudo-second order model based on the highest R^2 (0.995 for CT and 0.985 for RS) value, low χ^2 and the close agreement between calculated and theoretical q_e values. Thermodynamic analysis confirmed that the adsorption process was endothermic and spontaneous. The adsorption behavior of CT and RS was examined in the presence of four inorganic co-ions: NO_3^-, Cl^-, SO_4^{2-} and CO_3^{2-}. The removal efficiencies for these ions followed the ascending order: CO_3^{2-}>SO_4^{2-}> NO_3^-> Cl^-, with removal rates ranging from 98.64-99.29 % for CT and from 98.75-99.65% for RS. Regeneration studies indicated that the CCAC adsorbent remained effective up to the fifth cycle (78.75 % for CT and 82.10 % for RS), suggesting that the adsorbent can be reused and recycled multiple times. DFT analyses suggests the favorable nature of the adsorption of CT and RS on AC based solely on the assumption of hydrogen bond interactions. Notably, the AC containing COOH groups demonstrated the strongest interaction with phenolic compounds, indicating its superior potential for adsorption.

3. A novel photocatalyst based on CCAC coupled with ZrO_2-ZnO, which has not been previously explored. The synergistic integration of these components results in enhanced charge separation, improved photostability and superior degradation efficiency compared to conventional single or binary photocatalysts for the degradation of 4-NP. The synthesized nanocomposite was thoroughly characterized using analytical techniques, providing valuable insights into its formation, morphology, surface and functional properties. The prepared CCAC/ZrO_2-ZnO photocatalyzed exhibited a high degradation efficiency of 98.2 % for 4-NP (40 ppm) under UV light irradiation (80 min, pH 6) with a catalyst loading of 0.07 g/L. Based on LH model, the degradation process followed PFO kinetics, with a $t_{1/2}$ of 2.044 min

and K_{ap} of 0.339 min^{-1}. Scavenger experiments indicated that superoxides and hydroxyl radicals played a significant role in the degradation mechanism. The catalyst maintained 78.5 % efficacy after five successive cycles, confirming its stability and reusability. Furthermore, the photocatalyst exhibited notable applicability in real wastewater treatment, supporting its feasibility for scale-up and selective removal of organic contaminants. LC-MS analysis of the 4-NP degradation suggested a potential pathway involving low molecular weight intermediates, ultimately leading to the complete mineralization of carbon dioxide and water. DFT simulations revealed hydrogen bonding via O-linkage of the O-Zr-O bond with CCAC, leading to the formation of a chemically reactive CCAC/ZrO_2–ZnO nanocomposite. Reactivity descriptors further validated its favorable electronic structure and chemical stability, correlating well with the observed enhancement in photocatalytic performance. In addition, the nanocomposite demonstrated promising antibacterial potential, attributed by its ability to inhibit DHFR and DNA gyrase, as evidenced by molecular docking simulation. However, further optimization and experimental validation through *in vitro* and *in vivo* studies are essential to confirm these findings. The next phase of this research will involve a thorough biological evaluation of the synthesized nanocomposite, assessing their antibacterial efficacy against the aforementioned strains and other clinically relevant pathogens. Promising outcomes will lead to *in vivo* testing using appropriate animal models to assess therapeutic effectiveness, pharmacokinetics and potential toxicity under physiological conditions. Concurrently, mechanistic studies will also be undertaken to investigate the pathways by which the nanocomposite exert its antibacterial effects. This comprehensive approach aims to validate the therapeutic potential of the synthesized nanocomposite and advance their development toward clinical application. Overall, the results acquired from produced nanocatalysts indicate no hazardous behavior in wastewater treatment applications, highlighting its potential as a robust, stable and reusable material for the efficient removal of organic contaminants.

4. A novel photocatalyst consisting of AC produced from Croton caudatus, incorporated with Co-doped ZnO nanoparticles, was successfully developed. The synergistic integration markedly increased charge separation, lowered the band gap to

2.1 eV, and boosted photostability and degrading efficiency relative to traditional single- and binary-component systems for BPA elimination. Under optimal circumstances, the photocatalyst attained 99.67 % breakdown of BPA and 81 % mineralization during 60 min of visible-light irradiation. The degradation kinetics adhered to the L–H kinetic model, demonstrating PFO characteristics, with a half-life of 12.6 min and an apparent rate constant of 0.055 min^{-1}. Radical scavenging tests found hydroxyl radicals as the most reactive species, succeeded by photogenerated holes and superoxide radicals. The catalyst maintained 77.63 % efficiency after five reuse cycles, indicating commendable stability and recyclability. LC–MS analysis indicated a probable degradation route resulting in full mineralization to CO_2 and H_2O. Moreover, DFT simulations provide mechanistic insights into the augmented formation of ROS and photocatalytic pathways.

7.2 Future scope of the work

Despite significant progress in the development of effective sorbents and photocatalysts, further investigation is necessary to overcome current limitations and enhance usage. The subsequent sections outline many prospective avenues for further research:

1. Investigation of alternative biomass precursors to tailor pore structure and surface chemistry.
2. Advancement of dual- and tri-doped semiconductor materials to improve visible-light activity.
3. Investigation into the simultaneous removal of mixed contaminants, including phenols, pesticides, and pharmaceuticals, as well as emerging pollutants such as microplastics and PFAS, should be explored.
4. Advanced characterisation techniques such as electrochemical impedance spectroscopy, transient photocurrent, and EPR can be carried out to understand an in-depth comprehension of the kinetics of charge transfer.

CURRICULUM VITAE

SHISAK SHARMA
Research Scholar
Department of Chemistry,
Nagaland University,
H.Q. Lumami-798627, Nagaland, India
Email: shisakz95@gmail.com; shisak_rs2019@nagalanduniversity.ac.in

Education

- **Ph.D. (Chemistry), 2019- Ongoing**
  Nagaland University, Nagaland, India
  Thesis Title- Adsorption and Photocatalytic Studies on Activated Carbon and its Composite: An Experimental and Theoretical Insight to Understand the Mechanism

- **M.Sc. (Chemistry), 2019**
  Nagaland University, Nagaland, India

- **B.Sc. Chemistry (Hons.) with Physics, Chemistry, Mathematics, 2017**
  St. John College, Dimapur, Nagaland, India

Awards/ Honours/ Recognition

- **Research Excellence Award and Best Paper Award (with Cash Prize)**. Received at INNOST NANO 2025, SGT University, Gurugram, and Research Wheel Publishers from November 12–14, 2025.
- **Vice Chancellor's Award** for **Best Research Scholar** for 2025 at Nagaland University.
- **Extraordinary Contribution to the Conference.** Received during the 1st International Conference Innochem 25, organized by the Department of Chemistry, School of Sciences, Woxsen University, held from April 8-11, 2025.
- **Best Oral Presentation Award 2024.** Received at the National Conference organized by Department of Zoology, Nagaland University on 28-29 November 2024.
- **Best Oral (Cash) award and Best Paper Award 2024.** Received at the International Conference organized by Gram Bharti College, Ramgarh, Kaimur, Bihar, India under the flagship of Chemical Research Society of India in association with Research Plateau Publishers on 2-3 July 2024.
- **Shortlisted for Interview of CSIR-HRDG SRF- 2023.**

- **InSc Young Researcher Award 2023.**
- **Peer Reviewer for journals published by Springer Nature and Elsevier.**

Area of Research Interest

- Development of biomass-based materials for removal of organic, inorganic and biological pollutants from wastewater.
- Nanomaterials and composites for wastewater treatment.
- Activated carbon and its composite for various environmental applications.
- Photocatalytic studies for the removal of organic pollutants from water.

Conferences/Workshops/Seminars Attended/Paper Presented

1. Poster Presentation- International Conference on Chemistry in Multidisciplinary Research (ICCMR-2026), organized by Department of Chemistry, Nagaland University during March 25-27, 2025.

2. Oral Presentation- International Conference on Innovations in Nanomaterials, Nano Devices & Smart Technologies (INNOST NANO 2025), organized by SGT University, Gurugram, and Research Wheel Publishers from November 12–14, 2025.

3. Oral Presentation- 1st International Conference Innochem 25, organized by the Department of Chemistry, School of Sciences, Woxsen University, held from April 8-11, 2025.

4. Oral Presentation- International Conference on Chemistry in Multidisciplinary Research (ICCMR-2025) organized by Department of Chemistry, Nagaland University during March 25-27, 2025.

5. Oral Presentation- International Conference on CACSRE 2024 and NCCT 2024 jointly organized by Department of Chemistry, Industrial Chemistry, Chemistry (PUC), Mizoram University and the Association of Chemistry Teachers (ACT) during November 6-8, 2024.

6. Oral Presentation- National Conference on Recent Trends in Environmental Pollution and Health NCRTEPH 2024 organized by Department of Zoology, Nagaland University during November 28-29, 2024.

7. Oral Presentation- International Conference on ICCMEPR 2024 organized by Gram Bharti College, Ramgarh, Kaimur, Bihar, India under the flagship of Chemical Research Society of India in association with Research Plateau Publishers on July 2-3, 2024.

8. Oral Presentation- National Conference on “The Emerging Challenges in the Frontiers of Chemical Science” jointly organized by MU-CAA and Department of

Chemistry, Manipur University on March 29-30, 2023.

9. Oral Presentation- National Conference on "Trends in Multidisciplinary Research: Challenges and Applications" organized by M S Ramaiah College of Arts, Science and Commerce – Autonomous, Bengaluru on May 15-16, 2024.

10. Five-Day International Workshop on Sophisticated Instrumentation Techniques organized by the Department of Chemistry, School of Advanced Sciences (SAS), VIT-AP University in association with Institute of Physical sciences (ICF)-National Autonomous University of Mexico (UNAM) held during March 17-21, 2025.

11. Nagaland University Research Conclave- 2024 organized by the NEP and IQAC in coordination with NURSF, Lumami held on December 3-4, 2024.

12. 7-Days DST-SERB High-End workshop organized by Department of Physics, Nagaland University on March 20-26, 2024.

Invited lectures / Resource Person / Keynote Speaker/Co-ordinator

1. Resource Person- One Day Hands-on Workshop on "Essentials of SWAYAM" organized by Swayam Cell, Nagaland University on 21st November 2014.

2. Resource Person at the One Day Workshop on "Essentials of SWAYAM" organized by the SWAYAM Cell, Nagaland University, held on 21st November 2024 at Lumami Campus.

3. Student Coordinator- International Conference on Chemistry in Multidisciplinary Research (ICCMR-2025) organized by Department of Chemistry, Nagaland University during March 25-27, 2025.

4. Student Coordinator -International Conference on Medicinal Plants, Biodiversity Conservation, Natural Products for Health Care Needs in Traditional System of AYUSH Medicine (MBNHA 2025) held on 7th and 8th May 2025 organized by Department of Forestry, Nagaland University.

Master's Project Guidance

Total No.s' = 13

Responsibilities/ Assignments

1. Member, Academic Council, Nagaland University for the tenure of 6 months.
2. Research Scholar Hostel Prefect, Nagaland University, Lumami for the tenure of 6 months (2024).
3. Executive Member, Nagaland University Research Scholars' Forum, Lumami for

the tenure of 2 years (2022- 2024).

4. Students' Mentor, SWAYAM- MOOCs Course under the Department of Chemistry (Tenure: 2022 to 2026).

Research Publications

A. Paper Publications: 08 (WoS & Scopus indexed only)

1. **S. Sharma,** R.S. Umdor, I.T. Longchar, B. Singha, S.L. Ezung, P.C. Bhomick, D. Sinha, Highly efficient photocatalytic degradation of organic pollutants using novel carbon integrated ZrO_2–ZnO nanocomposites: kinetics, molecular docking, DFT simulation and real wastewater application, J. Mol. Liq. 436 (2025) 128260.

2. R.S. Umdor, **S. Sharma**, I.T. Longchar, D. Sinha, Enhanced adsorption of ciprofloxacin antibiotic using novel Rubus alceifolius activated carbon/MgAl LDH composite: Mechanistic insight, Chem. Eng. Sci. 313 (2025) 121723.

3. I.T. Longchar, **S. Sharma**, R.S. Umdor, P. Bora, D. Sinha, Utilization of activated Thysanolaena maxima biomass for the high-performance removal of tetracycline antibiotic from wastewater: experimental optimization and DFT simulation, Biomass Convers. Biorefin. 15 (2025) 15311–15326.

4. S.L. Ezung, M. Baruah, **S. Sharma**, R.S. Umdor, I.T. Longchar, B. Giridharan, U.B. Sinha, D. Sinha, Photocatalytic degradation of chlorpyrifos using Fe-doped ZnO/activated carbon nanocomposite, J. Mol. Struct. 1319 (2025) 139434.

5. I.T. Longchar, S. Kumar, R.S. Umdor, **S. Sharma**, P. Bora, D. Sinha, Evaluation of a novel activated carbon/graphene oxide as an efficient composite adsorbent for the removal of herbicide 2,4-dichlorophenoxyacetic acid: adsorption isotherm and kinetics study, J. Mol. Liq. 415 (2024) 126406.

6. **S. Sharma,** R.S. Umdor, I.T. Longchar, S.L. Ezung, D. Sinha, Exploring the adsorption of catechol and resorcinol onto Croton caudatus activated carbon: An integrated experimental and theoretical approach, Groundw. Sustain. Dev. 27 (2024) 101325.

7. R.S. Umdor, S.L. Ezung, **S. Sharma**, S. Kumar, I.T. Longchar, D. Sinha, Experimental and DFT study on the removal of sulfadiazine by activated carbon prepared from Rubus alceifolius, Biomass Convers. Biorefin. 15 (2025) 4551–4564.

8. **S. Sharma,** S.L. Ezung, A. Supong, M. Baruah, S. Kumar, R.S. Umdor, D. Sinha, Activated carbon adsorbent derived from waste biomass, Croton caudatus, for efficient removal of 2-chlorophenol from aqueous solution: kinetics, isotherm, thermodynamics and DFT simulation, Chem. Eng. Res. Des. 190 (2023) 777–792.

B. Patent Publication: 03

1. **S. Sharma**, R.S. Umdor, I.T. Longchar, B. Singha, D. Sinha, Carbon based ZrO_2–ZnO nanocomposite for 4-nitrophenol degradation, Indian Patent Appl. 202531037955 A, Published on 25 April 2025.

2. R.S. Umdor, **S. Sharma**, D. Sinha, S. Kumar, T.L. Imotila, System zur Synthese und Charakterisierung von aus *Rubus alceifolius* hergestellter Aktivkohle zur Entfernung von Sulfadiazin, German Utility Patent 20 2024 103 104, Published on 27 June 2024.

3. S.L. Ezung, M. Baruah, S. Kumar, **S. Sharma**, R.S. Umdor, B. Giridharan, D. Sinha, A process of preparation of Fe-doped ZnO/activated carbon nanocomposite for photocatalytic degradation of chlorpyrifos, Indian Patent Appl. 202331084822 A, Published 19 January 2024.

C. Book/Chapter Publication: 02

1. **S. Sharma**, R.S. Umdor, I.T. Longchar, D. Sinha, Water pollution studies, Chyren Publication House, India, 2025, 133–148. ISBN: 978-93-49076-02-0.

2. **S. Sharma**, R.S. Umdor, I.T. Longchar, D. Sinha, Current trends, future perspectives, and challenges in wastewater treatment, In: Advances in Wastewater Treatment: Cutting Edge Techniques and Sustainable Solutions, Nova Science Publishers, Inc., 2026, pp. 133–148. ISBN: 979-8-90134-007-3.

Additional Courses

Online certification course under SWAYAM

- Industrial Wastewater Treatment, NPTEL (12 weeks course- 3 credits)
- Analytical Chemistry, NPTEL (12 weeks course- 3 credits)

Chemical Engineering Research and Design 190 (2023) 777–792

Available online at www.sciencedirect.com

Chemical Engineering Research and Design

journal homepage: www.elsevier.com/locate/cherd

Activated carbon adsorbent derived from waste biomass, "*Croton caudatus*" for efficient removal of 2-chlorophenol from aqueous solution: Kinetics, isotherm, thermodynamics and DFT simulation

Shisak Sharma, Soremo L. Ezung, Aola Supong, Mridushmita Baruah, Suraj Kumar, Raplang Steven Umdor, Dipak Sinha *

Department of Chemistry, Nagaland University, Lumami 798627, Nagaland, India

ARTICLE INFO

Article history:
Received 22 September 2022
Received in revised form 2 January 2023
Accepted 3 January 2023
Available online 6 January 2023

Keywords:
Croton caudatus
Activated carbon
2-chlorophenol
Adsorption
Density functional theory
Water purification

ABSTRACT

The present study aims to prepare an activated carbon (AC) adsorbent developed from *Croton caudatus* biomass material for the adsorption of 2-chlorophenol (2CP) from wastewater. Activated carbon was prepared by KOH activation at 2:1 impregnation ratio and 700 °C temperature using a muffle furnace under self-generated atmosphere for 2 h. Several techniques and methodologies such as proximate analysis, ultimate (CHNS) analysis, BET, SEM, FT-IR, XRD and point of zero charge (pH_{pzc}) have been used to determine physicochemical properties of the activated carbon. Batch adsorption studies were conducted for 2-chlorophenol adsorption and the optimum adsorbent dose, initial concentration, pH, reaction time and temperature were found to be 0.15 g/L, 80 mg/L, 4, 60 min and 298 K, respectively. The equilibrium isotherm study for 2-chlorophenol adsorption was fitted well to the Langmuir model with the adsorption capacity of 53.619 mg/g, while the adsorption kinetics was best described by pseudo-second order model. Thermodynamic parameters demonstrated a negative ΔH (exothermic) and negative ΔG (spontaneous) values. Studies on regeneration have shown that saturated carbon can be recycled up to five times with considerable removal efficiency. Besides, density functional theory (DFT) simulation revealed that the adsorption of 2-chlorophenol onto AC adsorbent is favorable. Among the oxygen-containing functional groups, the carboxyl group appeared to have a greater influence on the adsorption process than the hydroxyl and carbonyl groups with the highest negative $E_{adsorption}$ of – 42.16 kJ/mol. Furthermore, the inclusion of three oxygen-containing functional groups improves the adsorption capacity of AC towards 2CP relative to a single functional group.

© 2023 Institution of Chemical Engineers. Published by Elsevier Ltd. All rights reserved.

Abbreviations: CCAC, *Croton caudatus* activated carbon; CP, chlorophenol; EPA, environmental protection agency; DFT, density functional theory; wt%, weight percentage; RMSE, Residual root mean error; AC, activated carbon; p_AC, pristine activated carbon; COOHAC, carboxyl functionalized activated carbon, OH(AC), hydroxyl functionalized activated carbon; CHOAC, carbonyl functionalized activated carbon; OH+CHO+COOHAC, hydroxyl, carboxyl and carbonyl functionalized activated carbon; pH_{zpc}, zero-point charge

* Corresponding author.
E-mail address: dipaksinha@gmail.com (D. Sinha).

https://doi.org/10.1016/j.cherd.2023.01.002
0263-8762/© 2023 Institution of Chemical Engineers. Published by Elsevier Ltd. All rights reserved.

Groundwater for Sustainable Development 27 (2024) 101325

Contents lists available at ScienceDirect

Groundwater for Sustainable Development

journal homepage: www.elsevier.com/locate/gsd

Research paper

Exploring the adsorption of catechol and resorcinol onto Croton caudatus activated carbon: An integrated experimental and theoretical approach

Shisak Sharma, Raplang Steven Umdor, Imotila T. Longchar, Soremo L. Ezung, Dipak Sinha *

Department of Chemistry, Nagaland University, Lumami, 798627, Nagaland, India

HIGHLIGHTS

- The adsorption capacity of AC towards resorcinol was higher than catechol.
- AC could be regenerated for upto fifth cycles.
- Effect of co-interfering ions changes in the following order: $CO_3^{2-} > SO_4^{2-} > NO_3^- > Cl^-$.
- DFT calculations indicated AC with COOH functionalization exhibits highest adsorption energies.

GRAPHICAL ABSTRACT

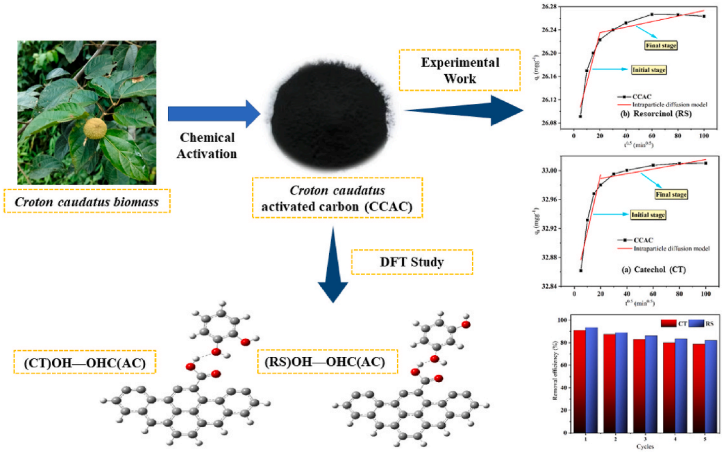

ARTICLE INFO

Keywords:
Croton caudatus biomass
Adsorption
Catechol
Resorcinol
Activated carbon
Density functional theory

ABSTRACT

The present work aimed to examine the process for adsorption of Catechol (CT) and Resorcinol (RS) onto activated carbon that was obtained from *Croton caudatus* biomass (CAB). Using a batch method, the maximum removal efficiencies of 99.23 % for CT and 98.68 % for RS was achieved at adsorbent dosage-0.2 g L^{-1}, reaction time-60 min; concentration-100 mgL^{-1} CT and 80 mgL^{-1} RS; and pH 6.0 CT and pH 4.0 RS, respectively. A maximum equilibrium adsorption of 56.05 mgg^{-1} and 61.85 mgg^{-1} was achieved at pH 6.0 and pH 4.0 for CT and RS. The adsorption behavior of both adsorbates on activated carbon were best described by the Langmuir model (correlation coefficients (R^2) = 0.996 for CT and 0.995 for RS) and the pseudo-second order kinetic model. The values of ΔG, ΔS, and ΔH suggest that the adsorption process is spontaneous and endothermic. Additionally, the adsorption process is easily reversible, enabling the reuse of the adsorbate even after fifth cycle. Further, density functional theory (DFT) simulations demonstrated that the CT and RS adsorption onto the AC adsorbent

Abbreviations: CAB, Croton caudatus biomass; CCAC, Croton caudatus activated carbon; AC, activated carbon; CT, catechol; RT, resorcinol; OFGs, oxygen functional groups; DFT, density functional theory; pHzpc, zero-point charge; PFO, pseudo-first order; PSO, pseudo-second order; ID, intraparticle diffusion; *AC, unmodified activated carbon; COOH(AC), carboxyl functionalized activated carbon; OH(AC), hydroxyl functionalized activated carbon; CHO(AC), carbonyl functionalized activated carbon.

* Corresponding author.
E-mail address: dipaksinha@gmail.com (D. Sinha).

https://doi.org/10.1016/j.gsd.2024.101325
Received 10 November 2023; Received in revised form 24 August 2024; Accepted 29 August 2024
Available online 31 August 2024
2352-801X/© 2024 Elsevier B.V. All rights are reserved, including those for text and data mining, AI training, and similar technologies.

Journal of Molecular Liquids 436 (2025) 128260

Contents lists available at ScienceDirect

Journal of Molecular Liquids

journal homepage: www.elsevier.com/locate/molliq

Highly efficient photocatalytic degradation of organic pollutants using novel carbon integrated ZrO_2-ZnO nanocomposites: kinetics, molecular docking, DFT simulation and real wastewater application

Shisak Sharma [a], Raplang Steven Umdor [a], Imotila T. Longchar [a], Basanta Singha [a], Soremo L. Ezung [a], Parimal C. Bhomick [b], Dipak Sinha [a,*]

[a] Department of Chemistry, Nagaland University, Lumami, 798627, Nagaland, India
[b] Bristol Composites Institute, Queen's Building, University of Bristol, Bristol BS8 1TR, UK

ARTICLE INFO

Keywords:
Nanocomposite
Photocatalysis
4-nitrophenol
Kinetics
UV irradiation

ABSTRACT

Photocatalysis serves as a promising alternative approach for the treatment of wastewater contaminated with organic pollutants. The method is advantageous owing to its ability for complete mineralization of toxic compounds, degradation of chemically stable pollutants and wide application. Herein, we report the synthesis of a CCAC/ZrO_2-ZnO nanocomposite *via* a hydrothermal method by anchoring ZrO_2-ZnO onto activated carbon derived from *Croton caudatus* biomass for 4-nitrophenol (4-NP) degradation. The nanocomposite was thoroughly characterized using advanced analytical techniques, including XRD, FT-IR, SEM/TEM with SAED and EDS, PL spectroscopy, BET surface area analysis, and XPS. Photocatalytic activity was evaluated through the 4-NP degradation under UV light, achieving an impressive 98.2 % degradation with a catalyst dosage of 0.07 g/L, initial concentration of 40 ppm, irradiation time of 80 min and pH 6. The degradation intermediates and pathway were identified using LC-MS analysis. The nanocomposite exhibited good recyclability, retaining 78.5 % efficiency after multiple cycles and achieved a notable 87.86 % degradation efficiency in real wastewater. Density Functional Theory (DFT) calculations were performed to investigate the chemical reactivity and formation mechanism of the prepared nanocomposite. The results indicated a significant enhancement in its reactivity, which contributed to improve the efficacy in the degradation of 4-NP. Subsequently, the molecular docking studies targeting DNA gyrase and DHFR revealed favorable binding energies (MolDock), providing a valuable theoretical framework for future *in vitro* and *in vivo* experimental validation. These findings may significantly aid in the rational design and development of next-generation antibacterial agents designed at combating the growing threat of antibiotic-resistant pathogens such as *Escherichia coli (E. coli)* and *Staphylococcus aureus (S. aureus)*.

1. Introduction

Nitrophenols are anthropogenic, inhibitory, and biorefractory organic molecules. They have been extensively applied in chemical industry for insecticides, medicines, and dyes [1,2]. 4- nitrophenol (4-NP) is a phenolic molecule that contains two functional groups on its benzene ring; nitro (NO_2) and hydroxyl (OH). European Economic Union and US Environmental Protection Agency considers 4-NP among priority contaminants due to its potential to negatively impact aquatic life, animals, and human beings at low amounts with the maximum allowable limit of 1 ppm [3]. The exposure of 4-NP also leads to a spectrum of acute and chronic health effects including gastrointestinal complication, respiratory tract problems, injury to organs like kidneys and liver, skin and eye irritant, and cardiovascular system problem. It may also lead to hypersalivation, suppression of hunger, breakdown of protein, and interference with the central nervous and circulatory systems [4,5]. In

Abbreviations: AOPs, Advanced Oxidation Processes; AC, Activated carbon; NP, Nitrophenol; DFT, Density functional theory; CCAC, *Croton caudatus* activated carbon; DHFR, Dihydrofolate reductase; TDS, Total dissolved solids; EC, Electrical conductivity; TH, Total hardness; BOD, Biological oxygen demand; TOC, Total organic carbon; MQW, Ultrapure Milli-Q water; MVD, Molegro virtual docker.

* Corresponding author.
E-mail address: dipaksinha@gmail.com (D. Sinha).

https://doi.org/10.1016/j.molliq.2025.128260
Received 15 April 2025; Received in revised form 9 July 2025; Accepted 30 July 2025
Available online 5 August 2025
0167-7322/© 2025 Elsevier B.V. All rights are reserved, including those for text and data mining, AI training, and similar technologies.

RSC Advances

PAPER

Check for updates

Cite this: *RSC Adv.*, 2026, **16**, 14107

Harnessing synergistic effects in porous carbon/Co-ZnO heterojunction for enhanced visible-light photocatalytic removal of bisphenol A

Shisak Sharma, Raplang Steven Umdor, Imotila T. Longchar, Partha Pratim Gogoi, Soremo L. Ezung and Dipak Sinha *

Endocrine-disrupting contaminants, particularly bisphenol A (BPA), are prevalent in aquatic environments, posing severe ecological and health risks that demand efficient remediation strategies. Photocatalysis has emerged as a promising enhanced oxidation technology for the mitigation of such recalcitrant organic pollutants. Herein, we report the hydrothermal synthesis of a CCAC/Co-ZnO nanocomposite, achieved by anchoring cobalt doped ZnO nanoparticles onto activated carbon obtained from Croton caudatus biomass. Characterization studies (XRD, SEM, EDS, HR-TEM, XPS, BET surface area, PL and UV-Vis DRS) validated the optimized nanostructure, and photocatalytic evaluations showed 99.67% BPA breakdown within 60 min under visible light irradiation at optimal conditions. The reaction obeyed pseudo-first-order kinetics ($t_{1/2}$ of 12.6 min and k_{ap} of 0.055 min^{-1}), dominated by hydroxyl radicals (•OH), and photogenerated holes (h^+) as primary reactive oxygen species (ROS). LC-MS identified intermediates enabled proposal of a plausible BPA degradation pathway, while reusability studies showed 77.63% efficiency over five cycles, confirming excellent photostability and reusability. Moreover, DFT calculations elucidated improved ROS generation mechanisms, providing mechanistic insights into the degradation processes. These findings provide a viable strategy for designing biomass-derived, visible-light-responsive photocatalysts for sustainable environmental remediation applications.

Received 24th January 2026
Accepted 10th March 2026

DOI: 10.1039/d6ra00641h

rsc.li/rsc-advances

1. Introduction

In recent times, the widespread occurrence of endocrine-disrupting chemicals (EDCs) in the aquatic environment has become a global concern. Bisphenol A (BPA) is one of the commonly detected EDCs in groundwater, surface water, industrial effluents, and landfill leachate. Its presence is primarily attributed to its wide-ranging application as a precursor in the production of epoxy resins, polycarbonate plastics and other polymers (*e.g.*, rubber antioxidants, food packaging containers, dental sealants, PCV pipes, and other fine chemical materials).[1–3] BPA is constituted of two phenolic rings joined by an acetone-derived bridge, from which its nomenclature is derived ('A' denotes acetone).[4] According to reports, 27 million tonnes of polymers containing BPA are produced globally each year, with 60% (approx.) of the world's BPA consumption coming from Asian countries.[5,6] Owing to its extensive use, BPA is ubiquitously released in the environment, posing adverse effects on both human health and the ecosystem. BPA also poses other health concerns, due to its potential carcinogenic and genotoxic implications.[7,8] Studies have indicated that exposure to BPA may promote the growth of cancer cells, especially in the tissues of the breast and prostate. Beyond this, BPA has been associated with various other health issues, including infertility, obesity, and developmental abnormalities.[9–11] The substantial toxicity of BPA is largely due to its unique physicochemical properties. These include high solubility in water (about 200 mg L^{-1} @ 25 °C), chemical stability, and resistance to biodegradation, allowing it to persist in aquatic environments even at very low concentrations (pM or nM).[12,13] Consequently, several nations and regions, including the European Union, Sweden, Canada, United States, Norway, India and China, have banned the usage of BPA.[14] Similarly, the USEPA has also included this compound on the Drinking Water Contaminant Candidate List 5.[15] As a result, there is an urgent need to develop highly efficient strategies for BPA removal from aqueous media.

To address the growing concern pertaining to emerging organic substances (*e.g.*, BPA) in wastewater, several methods of treatment have been investigated, including chemical oxidation, biological treatment, adsorption, membrane separation, electro-Fenton processes and photocatalysis.[16–18] Among these, heterogeneous photocatalysis has emerged as a promising approach in advanced oxidation processes (AOPs) over other conventional methods due to its mild operating conditions, eco-friendliness, reusability, long-term stability, high degradation efficiency, lack of secondary pollutants and wide

Department of Chemistry, Nagaland University, Lumami-798627, Nagaland, India. E-mail: dipaksinha@gmail.com

© 2026 The Author(s). Published by the Royal Society of Chemistry

Chemical Engineering Science 313 (2025) 121723

Contents lists available at ScienceDirect

Chemical Engineering Science

journal homepage: www.elsevier.com/locate/ces

Enhanced adsorption of ciprofloxacin antibiotic using novel *Rubus alceifolius* activated carbon/ MgAl LDH composite: Mechanistic insight

Raplang Steven Umdor, Shisak Sharma, Imotila T Longchar, Dipak Sinha *

Department of Chemistry, Nagaland University, Lumami 798627 Nagaland, India

ARTICLE INFO

Keywords:
Layered double hydroxide
Activated carbon
Adsorption
Ciprofloxacin
Pharmaceuticals

ABSTRACT

In this study, composites of layered double hydroxide (LDH) and activated carbon (AC) derived from *Rubus alceifolius* biomass were synthesized with varying amounts of AC using the co-precipitation method. The resulting composites were characterized using FTIR, BET, SEM, TEM, EDX, and XPS. The MgAl-AC3 composite exhibited a high BET surface area (568.87 $m^2\ g^{-1}$) compared to pure MgAl LDH (73.05 $m^2\ g^{-1}$). The adsorption models followed the Redlich-Peterson isotherm and pseudo-second-order kinetics, with thermodynamic analysis confirming a spontaneous, endothermic process. Post-adsorption studies indicated surface adsorption of ciprofloxacin rather than intercalation.

1. Introduction

Ciprofloxacin (CIP) is a widely used fluoroquinolone antibiotic and one of the most extensively used chemotherapeutic antibiotics in the world (Avcı et al., 2019). It was first commercialized in 1987 and is known for its broad-spectrum antibacterial activity, being very efficient towards gram-negative bacteria (Pham et al., 2020). CIP acts by inhibiting the enzyme topoisomerases of bacteria resulting in the disruption of cellular reproduction and ultimately compromising their proliferation (Sharma et al., 2010). This antibiotic is utilized to treat infections in both humans and animals. After being ingested, most of it is excreted unmetabolized through urine and feces, which then find their way into rivers, lakes, and other water sources (Jara-Cobos et al., 2023). According to reports, trace concentrations of CIP in drinking water could lead to gastrointestinal disturbances like nausea, vomiting, and diarrhea. Moreover, prolonged exposure to this antibiotic in aquatic ecosystems can result in the development of antibiotic-resistant bacteria which poses a substantial ecological threat (Danner et al., 2019; Liang et al., 2018). Therefore, the toxicity level of CIP in water sources should be controlled. Various conventional treatment methods, including ion exchange (Wang et al., 2017), chemical oxidation (Dou et al., 2020), biodegradation (Han et al., 2020), and membrane filtration (Liang et al., 2021), have been employed for CIP removal from wastewater. However, these methods often suffer from limitations such as high operational costs, generation of toxic by-products, and limited efficiency in handling low-concentration pollutants (Álvarez-Torrellas et al., 2016; Gao et al., 2012). Among these, adsorption has emerged as a promising alternative due to its simplicity, cost-effectiveness, and environmental sustainability. Numerous adsorbents, such as montmorillonite (Wu et al., 2010), activated sludge-derived AC (Kim et al., 2020), metal–organic frameworks (Moradi et al., 2016), and biochar (Li et al., 2018), have been explored for CIP removal. Nevertheless, many of these materials exhibit drawbacks, including limited adsorption capacities, slow adsorption kinetics, and poor reusability, necessitating the development of novel, high-performance adsorbents (Ji et al., 2021). In this context, LDHs have attracted extensive attention because of their high adsorption capacity, inexpensive precursor material, ease of synthesis, and ion exchange properties. These nanomaterials have proven to be highly effective in the removal of a wide range of contaminants from wastewater, making them a popular choice in environmental remediation efforts (Kuznetsova et al., 2017).

LDHs are two-dimensional nanomaterials that possesses layered arrangement, which comprises of positive divalent and trivalent metal hydroxides with anions and water molecules located in the interlamellar space. The general formula of LDH is $[M^{2+}_{1-x}M^{3+}_{x}(OH)^{2}]^{x+}(A^{n-})_{\frac{x}{n}}.yH_2O$, where $M^{2+}$and M^{3+} represents the divalent and trivalent metal cation. A^{n-} represents the anion in the interlayer spaces and x indicates the molar ratio of $[M^{3+}]/[M^{2+}] + [M^{3+}]$ (Gao et al., 2020; Zubair et al., 2017). Despite the extensive use of LDH as adsorbent for adsorption

Abbreviations: LDH, layered double hydroxide; AC, activated carbon; CIP, ciprofloxacin; eg, example; AICc, corrected Akaike Information Criterion.

* Corresponding author.
E-mail address: dipaksinha@gmail.com (D. Sinha).

https://doi.org/10.1016/j.ces.2025.121723
Received 17 January 2025; Received in revised form 9 April 2025; Accepted 23 April 2025
Available online 25 April 2025
0009-2509/© 2025 Elsevier Ltd. All rights are reserved, including those for text and data mining, AI training, and similar technologies.

Biomass Conversion and Biorefinery (2025) 15:15311–15326
https://doi.org/10.1007/s13399-024-06462-9

ORIGINAL ARTICLE

Utilization of activated *Thysanolaena maxima* biomass for the high-performance removal of tetracycline antibiotic from wastewater: experimental optimization and DFT simulation

Imotila T Longchar[1] · Shisak Sharma[1] · Raplang Steven Umdor[1] · Priyakshi Bora[1] · Dipak Sinha[1]

Received: 19 July 2024 / Revised: 9 December 2024 / Accepted: 17 December 2024 / Published online: 6 January 2025
© The Author(s), under exclusive licence to Springer-Verlag GmbH Germany, part of Springer Nature 2025

Abstract

The study focused on the adsorption of tetracycline (TC) using *Thysanolaena maxima* activated carbon (TMAC) in a batch experiment. TMAC was formed via a chemical activation process involving potassium hydroxide mixed in a 2:1 ratio with carbonized char. Various analytical techniques such as Fourier transform infrared spectroscopy (FT-IR), scanning electron microscopy–energy dispersive X-ray spectroscopy (SEM–EDX), X-ray diffraction (XRD) spectroscopy, and Brunauer–Emmett–Teller (BET) surface area analysis was performed to characterize the produced carbon. The TMAC possessed specific surface area, total pore volume, and average pore diameter values of 1065.011 m^2/g, 0.4443 cm^3/g, and 3.036 nm, respectively. The effect of various adsorbent dosage (0.15 g/L), initial TC concentration (20 mg/L), contact time (110 min), temperature (328 K), and pH (2) on TC adsorption was investigated, and the TMAC exhibited a high adsorption efficiency of 97%. Thermodynamic analysis revealed that the spontaneous adsorption process was endothermic. The Langmuir ($Q_m = 21.317$ mg/g) and the pseudo-second-order model ($R^2 = 0.9980$) provided the best fit for the adsorption isotherm and kinetic study. The fifth regeneration cycle of the adsorbent was successful, proving its ability to be reused multiple times. Density functional theory (DFT) simulations revealed that the carboxyl group appeared to have a greater impact on the adsorption process than the hydroxyl and carbonyl groups, with an E_{adsorp} value of − 47.99 kJ/mol. The results indicate that the produced TMAC effectively eliminated TC from aqueous solutions.

Keywords *Thysanolaena maxima* · Activated carbon · Tetracycline · Adsorption · Density functional theory

Abbreviations

TMAC	*Thysanolaena maxima* Activated carbon
TC	Tetracycline
DFT	Density functional theory
pH_{zpc}	Zero-point charge

1 Introduction

The tetracycline (TC) is an antibiotic used worldwide and has been reportedly found in both surface and groundwater with concentrations in the range of 0.11 to 4.20 µg/L in surface water [1]. Its presence in wastewater primarily stems from improper disposal of expired medications and human excretion [2, 3]. TC remains in the aquatic environment due to its slow degradation, impacting the growth of aquatic species and posing health risks through the food chain [4]. Even at low concentrations (< 1 mg/L) in natural water, TC's presence raises significant concerns about its toxicity [5]. Prolonged consumption of TC-contaminated water can lead to bacterial imbalances, gastrointestinal issues, and liver damage and can interfere with teeth and bone development [6–8]. Thus, the effective removal of tetracycline from aquatic systems has become a critical concern.

Activated carbon (AC) as an adsorbent has been widely expected to effectively eliminate various water pollutants in developing nations [9]. In the adsorption mechanism, ACs are well-known due to their high surface area, well-formed micropores, excellent thermal stability, ease of regeneration, and low production cost [10]. Considering this, numerous studies have been focused on using inexpensive and abundant raw materials, such as agricultural and waste biomass, to produce AC [11]. Several studies have also been conducted on TC removal from wastewater using AC, for

✉ Dipak Sinha
dipaksinha@gmail.com

[1] Department of Chemistry, Nagaland University, Lumami 798627, Nagaland, India

Journal of Molecular Structure 1319 (2025) 139434

Contents lists available at ScienceDirect

Journal of Molecular Structure

journal homepage: www.elsevier.com/locate/molstr

Photocatalytic degradation of chlorpyrifos using Fe-doped ZnO/activated carbon nanocomposite

Soremo L Ezung [a], Mridushmita Baruah [a], Shisak Sharma [a], Raplang Steven Umdor [a], Imotila T Longchar [a], Bupesh Giridharan [b], Upasana Bora Sinha [a,*], Dipak Sinha [a,*]

[a] Department of Chemistry, Nagaland University, Lumami, 798627, Nagaland, India
[b] Department of Forestry, Nagaland University, Lumami, 798627, Nagaland, India

ARTICLE INFO

Keywords:
Nanocomposite
Hydrothermal process
Activated carbon
Visible light irradiation
Degradation

ABSTRACT

The present research reports the synthesis of Iron-Zinc oxide nanocomposite supported on activated carbon synthesised from *Schima wallichii* biomass. The nanocomposite was produced using a hydrothermal process and its physicochemical characterization was carried out using several analytical methods such as Transmission Electron Microscope (TEM), X-Ray Diffractometer (XRD), Fourier Transform Infra-Red (FT-IR), Photoluminescence (PL), UV–Visible Diffuse Reflectance Spectroscopy (DRS) and BET analyser. The prepared material was assessed for its degradation efficiency on chlorpyrifos (CPs) under visible light irradiation. The photocatalyst demonstrated optimal conditions achieving 98 % CPs degradation with 0.05 g catalyst dosage, 150 ppm initial concentration, 60-min of irradiation, and pH 2. Furthermore, recycling studies indicated the material's promising reusability, maintaining 62.7 % efficiency even after multiple cycles.

1. Introduction

Over the last century, pesticides have played a pivotal role in increasing agricultural production and have also found use in urban households. This is because of their efficiency, affordability, and immediate toxicity [1]. However, it has been found that pesticides have negative impacts on species and can be harmful to human health [2–4]. For example, chlorpyrifos (organophosphorus pesticide) that is widely used to control insects and pests in various crops such as fruit, grain, vegetable, cotton, etc. as well as ornamental plants. The excessive use of chlorpyrifos can result in neurological disorders, growth abnormalities, brain cell replication and intracellular oxidative stress, and therefore interrupting normal cellular development and differentiation. Furthermore, exposure to chlorpyrifos during pregnancy may result in mental abnormalities in children. Pesticides containing chlorpyrifos are the most common pollutants found in water sources, harming not only farmers but also spreading over long distances due to their resistance towards degradation [5,6]. As a result, removing chlorpyrifos from water systems is of considerable importance [7]. Several techniques have been applied to remove chlorpyrifos pesticides from waste water. Among the different strategies available, photocatalysis has been described as the most effective and advantageous method for treating wastewater [8].

Semiconductor materials such as TiO_2 (Titanium dioxide), ZnO (Zinc oxide), ZrO_2 (Zirconium dioxide), etc., are often used photocatalysts for the degradation of organic pollutants [9–12]. ZnO is well-known as one of the most cost-effective and ecologically friendly wide bandgap semiconductor materials with exceptional features making it suitable for versatile applications such as organic pollutant photodegradation, optoelectronic devices, solar cells, and sensors [13–15]. However, only UV light which makes up around 5% of the solar spectrum can activate ZnO. Consequently, there have been various attempts to create an active ZnO photocatalyst that functions under visible light. A preferred methodology has been by doping ZnO with anionic non-metals and transition metals. Among these, doping ZnO with transition metal cations has been suggested as a useful technique for improving photocatalytic properties of the catalyst under visible light. Numerous studies have reported that Fe doped ZnO nanocrystalline particles have superior photocatalytic activity than pure ZnO. The presumption is that the inclusion of Fe (III) cations within the lattice of the photocatalyst acts as shallow traps, thereby reducing the rate at which electrons and holes recombined [16,17]. The best photocatalytic activities might be obtained by doping iron at a very low level. Besides their role as photocatalysts, both ZnO and its doped nanoparticles have been explored for their potential in degrading

* Corresponding authors.
E-mail addresses: upasanaborasinha@gmail.com (U.B. Sinha), dipaksinha@gmail.com (D. Sinha).

https://doi.org/10.1016/j.molstruc.2024.139434
Received 16 April 2024; Received in revised form 5 July 2024; Accepted 23 July 2024
Available online 25 July 2024
0022-2860/© 2024 Elsevier B.V. All rights are reserved, including those for text and data mining, AI training, and similar technologies.

Journal of Molecular Liquids 415 (2024) 126406

Contents lists available at ScienceDirect

Journal of Molecular Liquids

journal homepage: www.elsevier.com/locate/molliq

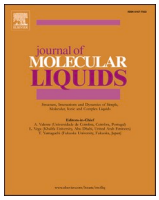

Evaluation of a novel activated carbon/graphene oxide as an efficient composite adsorbent for the removal of herbicide 2,4-Dichlorophenoxy-acetic acid: Adsorption isotherm and kinetics study

Imotila T Longchar, Suraj Kumar, Raplang Steven Umdor, Shisak Sharma, Priyakshi Bora, Dipak Sinha *

Department of Chemistry, Nagaland University, Lumami-798627, Nagaland, India

ARTICLE INFO

Keywords:
Thysanolaena maxima
Activated carbon
Graphene oxide
2,4-Dichlorophenoxyacetic acid
Adsorption

ABSTRACT

Thysanolaena maxima-derived activated carbon/graphene oxide (TMAC/GO) composite was synthesized through a one-step mixing process via ultrasonication and used as an adsorbent for the removal of 2,4-Dichlorophenoxy-acetic acid (2,4-D) herbicide from solution. Various analytical techniques, including Fourier-transform infrared spectroscopy (FTIR), Field emission scanning electron microscopy-energy dispersive X-ray spectroscopy (FESEM-EDX), X-ray diffractometer (XRD), Brunauer, Emmett, and Teller (BET) surface area analyzer, and Transmission electron microscopy (TEM) were employed to characterize the synthesized composite. Results showed that the TMAC/GO had a porous structure with a large surface area of 960 m^2/g, an average pore diameter of 2.658 nm, and a total pore volume of 0.6372 cm^3/g. A series of batch experiments were conducted for different adsorption parameters, which include TMAC/GO dosage (0.05–0.25 g/L), initial concentration (50–300 mg/L), pH (2–12), contact time (20–140 mins), and temperature (298–398 K). Adsorption thermodynamics, isotherm models, and kinetics were employed to understand the adsorption mechanism. The composite showed good adsorption ability with the Langmuir maximum adsorption capacity of 98.469 mg/g. When compared with TMAC, the composite exhibited higher removal efficiency under the same dosage, concentration, and temperature with variations in pH and time. The pseudo-second-order kinetics model justified the experimental results with an R^2 value of 0.997. Furthermore, the composite displayed good reusability performance up to 5 cycles. These findings, along with the cost-effectiveness of the material and its selectivity towards the herbicide, suggest its practical importance for water decontamination.

1. Introduction

2,4-Dichlorophenoxyacetic acid (2,4-D) is widely used to manage broad-leaved weeds and pests in agricultural fields due to its cost-effectiveness and adequate selectivity [1]. Nevertheless, 2,4-D presents considerable environmental concerns as a pollutant, primarily because it degrades slowly in the environment [2]. 2,4-D is classified as a phenoxy compound; it is regarded as moderately toxic and falls into a category of chemicals that could pose risks to human health due to its carcinogenic and mutagenic properties [3]. The herbicide's maximum permissible concentration in potable water is 100 ppb (0.1 mg/L) [4]. The concentration decreased below 3.13 mg/L can result in an unpleasant taste and odour, failing to meet the standards established by the World Health Organization (WHO, 2003) [5]. Environmental exposure to this herbicide, even in small amounts, can pose adverse health effects, particularly affecting vital organs in humans, such as the central nervous system, liver, and kidneys [6,7]. Besides that, the herbicide is associated with various reproductive health risks, including a higher incidence of abnormal sperm, sperm immobility, and sperm death, as well as an increase in lymphocyte levels and immune deficiency disorders. Studies on exposed animals have also reported fetal mortality, disorders of the urinary system, and congenital defects [8]. Furthermore, 2,4-D contributes to the degradation of soil and water resources because of its complex chemical composition, toxicity, and persistence in the environment [9]. Despite contamination risks, its use in agriculture will inevitably continue, adversely affecting water quality and human health [10]. Therefore, developing methods for the adsorption and removal of 2,4-D from soil, water, and wastewater is crucial for reducing

* Corresponding author.
E-mail address: dipaksinha@gmail.com (D. Sinha).

https://doi.org/10.1016/j.molliq.2024.126406
Received 29 June 2024; Received in revised form 22 October 2024; Accepted 1 November 2024
Available online 3 November 2024
0167-7322/© 2024 Elsevier B.V. All rights are reserved, including those for text and data mining, AI training, and similar technologies.

Biomass Conversion and Biorefinery (2025) 15:4551–4564
https://doi.org/10.1007/s13399-024-05488-3

ORIGINAL ARTICLE

Experimental and DFT study on the removal of sulfadiazine by activated carbon prepared from *Rubus alceifolius*

R. S. Umdor[1] · S. L. Ezung[1] · S. Sharma[1] · S. Kumar[1] · I. T. Longchar[1] · D. Sinha[1]

Received: 23 October 2023 / Revised: 27 February 2024 / Accepted: 4 March 2024 / Published online: 19 March 2024
© The Author(s), under exclusive licence to Springer-Verlag GmbH Germany, part of Springer Nature 2024

Abstract

This study describes the synthesis of activated carbon from locally derived biomass *Rubus alceifolius* using $ZnCl_2$ as an activating agent for sulfadiazine (SDZ) removal from wastewater. The adsorbent material was characterized by Fourier transform infrared (FTIR), powder X-ray diffraction (XRD), X-ray photoelectron spectroscopy (XPS), scanning electron microscope (SEM), N_2 adsorption–desorption isotherms, and zero-point charge (pH_{zpc}). Brunauer–Emmett–Teller (BET) surface area and total pore volume of the synthesized carbon were found to be 233 $m^2\ g^{-1}$ and 0.16 $cm^3\ g^{-1}$, respectively. Batch adsorption studies were carried out under varying initial concentrations, adsorbent dosage, temperature, contact time, and pH to comprehend the effects of different operating parameters on the removal efficiency for sulfadiazine from wastewater. The equilibrium isotherm study fitted well with the Langmuir model with maximum adsorption capacity (q_m) of 29.57 mg g^{-1}. The adsorption kinetic was best fitted by the pseudo-second-order model. Thermodynamic process of adsorption of SDZ onto activated carbon was found to be spontaneous and endothermic. Theoretical investigations using density functional theory (DFT) calculations suggested that the adsorption of SDZ onto functionalized activated carbon is favorable. Among the oxygen-containing functional groups, the carboxyl group appeared to have the largest effect on the adsorption process. However, DFT calculation showed that the presence of all three oxygen-containing functional groups enhanced the adsorption of SDZ, compared with pristine activated carbon.

Keywords *Rubus alceifolius* · Activated carbon · Adsorption · Sulfadiazine · Density functional theory

Abbreviations

RAAC	*Rubus alceifolius* activated carbon
SDZ	Sulfadiazine
DFT	Density functional theory
pH_{pzc}	Zero-point charge
AC	Activated carbon
AC_P	Pristine AC
AC_COOH	COOH functionalized AC
AC_OH	–OH functionalized AC
AC_CHO	–CHO functionalized AC
OH + CHO + COOH_AC	–OH, –COOH, –CHO functionalized AC

1 Introduction

Antibiotics are drugs that are commonly used as a preventative and therapeutic treatment for infections caused by microorganisms, by obstructing their metabolism via biochemical activities [1]. Due to the rapid increase in antibiotic use around the world, they are often found in urban wastewater, surface water, groundwater, and drinking water. This is a growing concern as antibiotic residue may give rise to the emergence of antibiotic-resistant microorganisms in marine environments [2, 3]. Antibiotics are divided into several classes, including nitroimidazoles, sulfonamides, tetracyclines, chloramphenicol, quinolones, and fluoroquinolones. Sulfadiazine belongs to the class of antibiotics called sulfonamides, and they are frequently used in aquaculture and animal husbandry [4]. Probably due to its high consumption and affordable cost which leads to its high consumption, it has been reported that SDZ has been detected at high concentrations in sewage treatment plants [5]. Consequently, SDZ antibiotics have garnered global attention for their negative role in

✉ D. Sinha
dipaksinha@gmail.com

[1] Department of Chemistry, Nagaland University, Lumami 798627, Nagaland, India

(12) PATENT APPLICATION PUBLICATION

(19) INDIA

(22) Date of filing of Application :21/04/2025

(21) Application No.202531037955 A

(43) Publication Date : 25/04/2025

(54) Title of the invention : Carbon based ZrO2-ZnO Nanocomposite for 4-Nitrophenol Degradation

(51) International classification :C02F1/72, C02F1/58
(86) International Application No :NA
Filing Date :NA
(87) International Publication No : NA
(61) Patent of Addition to Application Number :NA
Filing Date :NA
(62) Divisional to Application Number :NA
Filing Date :NA

(71)**Name of Applicant :**
1)Nagaland University
Address of Applicant :Nagaland University, Lumami Headquarters, Zunheboto district -India-798627 Zunheboto ---------- ----------
Name of Applicant : NA
Address of Applicant : NA
(72)**Name of Inventor :**
1)Shisak Sharma
Address of Applicant :Room No. 2 Kamnoi Hostel Nagaland University, Lumami Headquarters, Zunheboto district Zunheboto ---------- ----------
2)Raplang Steven Umdor
Address of Applicant :Room No. 9 Kamnoi Hostel Nagaland University, Lumami Headquarters, Zunheboto district Zunheboto ---------- ----------
3)Imotila T Longchar
Address of Applicant :Room No. 13 Aliper Hostel Nagaland University, Lumami Headquarters, Zunheboto district Zunheboto ---------- ----------
4)Basanta Singha
Address of Applicant :Room No. 14 Kamnoi Hostel Nagaland University, Lumami Headquarters, Zunheboto district Zunheboto ---------- ----------
5)Dipak Sinha
Address of Applicant :Room No. 11 Kinimi Apartment Nagaland University, Lumami Headquarters, Zunheboto district Zunheboto ---------- ----------

(57) Abstract :
The present invention relates to the synthesis of a CCAC/ZrO2-ZnO nanocomposite from Croton caudatus biomass for degrading 4-nitrophenol (4-NP) in wastewater. The nanocomposite is characterized using techniques like XRD, FT-IR, SEM/TEM, and BET surface area analysis. Its photocatalytic performance showed an impressive 98.2% degradation of 4-NP under UV light with a dosage of 0.07 g/L, initial concentration of 40 ppm, and pH 6 after 80 minutes. Degradation intermediates are identified via LC-MS, and recycling studies indicated 78.5% efficiency after multiple cycles. DFT calculations supported the findings, while in-silico docking suggested antibacterial potential, advocating further optimization. The invention highlights the CCAC/ZrO2-ZnO nanocomposite as a sustainable photocatalyst for water treatment.

No. of Pages : 26 No. of Claims : 6

Bundesrepublik Deutschland

Urkunde

über die Eintragung des
Gebrauchsmusters Nr. 20 2024 103 104

Bezeichnung:

System zur Synthese und Charakterisierung von aus Rubus Alceifolius hergestellter Aktivkohle zur Entfernung von Sulfadiazin

IPC:

B01L 99/00

Inhaber/Inhaberin:

NAGALAND UNIVERSITY, Zunheboto, Nagaland, IN
Raplang, Steven Umdor, Zunheboto, Nagaland, IN
Sharma, Shisak, Zunheboto, Nagaland, IN
Sinha, Dipak, Zunheboto, Nagaland, IN
Suraj, Kumar, Zunheboto, Nagaland, IN
Temjenwati, Imotila Longchar, Zunheboto, Nagaland, IN

Tag der Anmeldung:

11.06.2024

Tag der Eintragung:

27.06.2024

Die Präsidentin des Deutschen Patent- und Markenamts

Eva Schewior

Eva Schewior

München, 27.06.2024

Die Voraussetzungen der Schutzfähigkeit werden bei der Eintragung eines Gebrauchsmusters nicht geprüft.
Den aktuellen Rechtsstand und Schutzumfang entnehmen Sie bitte dem DPMAregister unter www.dpma.de.

(12) PATENT APPLICATION PUBLICATION
(19) INDIA
(22) Date of filing of Application :12/12/2023

(21) Application No.202331084822 A
(43) Publication Date : 19/01/2024

(54) Title of the invention : A PROCESS OF PREPARATION OF Fe-DOPED ZnO/ACTIVATED CARBON NANOCOMPOSITE FOR PHOTOCATALYTIC DEGRADATION OF CHLORPYRIFOS

(51) International classification :B01J0035000000, A01N0057160000, C02F0001300000, C02F0001320000, C02F0101300000
(86) International Application No :NA
Filing Date :NA
(87) International Publication No : NA
(61) Patent of Addition to Application Number :NA
Filing Date :NA
(62) Divisional to Application Number :NA
Filing Date :NA

(71)**Name of Applicant :**
1)NAGALAND UNIVERSITY
Address of Applicant :DEPARTMENT OF CHEMISTRY, NAGALAND UNIVERSITY ZUNHEBOTTO LUMAMI NAGALAND INDIA 798627 Lumami ---------- ----------
Name of Applicant : NA
Address of Applicant : NA
(72)**Name of Inventor :**
1)SOREMO L EZUNG
Address of Applicant :DEPARTMENT OF CHEMISTRY, NAGALAND UNIVERSITY, ZUNHEBOTTO LUMAMI NAGALAND INDIA 798627 Lumami ---------- ----------
2)MRIDUSHMITA BARUAH
Address of Applicant :DEPARTMENT OF CHEMISTRY, NAGALAND UNIVERSITY, ZUNHEBOTTO LUMAMI NAGALAND INDIA 798627 Lumami ---------- ----------
3)SURAJ KUMAR
Address of Applicant :DEPARTMENT OF CHEMISTRY, NAGALAND UNIVERSITY, ZUNHEBOTTO LUMAMI NAGALAND INDIA 798627 Lumami ---------- ----------
4)SHISAK SHARMA
Address of Applicant :DEPARTMENT OF CHEMISTRY, NAGALAND UNIVERSITY, ZUNHEBOTTO LUMAMI NAGALAND INDIA 798627 Lumami ---------- ----------
5)RAPLANG STEVEN UMDOR
Address of Applicant :DEPARTMENT OF CHEMISTRY, NAGALAND UNIVERSITY, ZUNHEBOTTO LUMAMI NAGALAND INDIA 798627 Lumami ---------- ----------
6)BUPESH GIRIDHARAN
Address of Applicant :DEPARTMENT OF FORESTRY, NAGALAND UNIVERSITY, ZUNHEBOTTO LUMAMI NAGALAND INDIA 798627 Lumami ---------- ----------
7)DIPAK SINHA
Address of Applicant :DEPARTMENT OF CHEMISTRY, NAGALAND UNIVERSITY, ZUNHEBOTTO LUMAMI NAGALAND INDIA 798627 Lumami ---------- ----------

(57) Abstract :
TITLE: A PROCESS OF PREPARATION OF Fe-DOPED ZnO/ACTIVATED CARBON NANOCOMPOSITE FOR PHOTOCATALYTIC DEGRADATION OF CHLORPYRIFOS APPLICANT: NAGALAND UNIVERSITY ABSTRACT The present invention relates to a process of photocatalytic degradation of Chlorpyrifos in wastewater using Fe-doped ZnO/Activated Carbon Nanocomposite. The process of the present invention comprises of following steps; a. preparation of Schima wallichii activated carbon; b. preparation of SWAC/Fe-ZnO nanocomposite; Characterized in c. photocatalytic degradation of chlorpyrifos in waste water.

No. of Pages : 41 No. of Claims : 2

CP/2025/ ESD/CH-13/1

CHYREN PUBLICATION

E-CERTIFICATE

of Publication

This is to certify that ***Shisak Sharma*** has published his/her chapter entitled ***Water Pollution Studies*** in the edited book on ***Environment & Sustainable Development @ 2025*** bearing "ISBN: "978-93-49076-02-0 " in January 2025.

ISBN 978-93-490-7602-0

9 789349 076020

CHYREN PUBLICATION

Chapter 18

Carbon-Based Nanoadsorbents for the Treatment of Industrial Wastewater

Tanisha Kathuria[1]
Anjali Mehta[1]
Sudhanshu Sharma[1]
and Sudesh Kumar[2,*]

[1]Department of Chemistry, Banasthali Vidyapith, Tonk, Rajasthan, India
[2]Department of Education in Science and Mathematics, National Council of Educational Research and Training (NCERT), Delhi, India

Abstract

Carbon-based nanoadsorbents, such as biochar, carbon nanotubes, graphene, and activated carbon, are widely used for wastewater remediation. Due to their large specific surface area (SURFACE AREA), mesoporous arrangement, excellent chemical stability, high adsorption capacity, availability of various functional groups that provide easy modification, ease of regeneration, and reusability, they have attracted special attention in environmental remediation. These characteristics enable them to resist extreme conditions encountered in wastewater, including acidic, basic, and salted conditions, even at elevated concentrations or temperatures. This chapter addresses various carbon Nanomaterials (NMs), as well as their morphologies, structures, and advantages for treating wastewater. A comprehensive analysis of issues associated with scalability, affordability, and environmental impact offers perspectives on future research areas and the advancement of environmentally friendly and more efficient wastewater treatment technologies.

Keywords: nanoadsorbents, wastewater treatment, adsorption mechanism, industrial wastewater

* Corresponding Author's Email: sudeshneyol@gmail.com

In: Advancements in Wastewater Treatment
Editors: Neha Agarwal, Maulin P. Shahl, Vijendra Singh Solankil et al.
ISBN: 979-8-90134-007-3
© 2026 Nova Science Publishers, Inc.

Contributor Copy